Transport properties of the three-dimensional topological insulator mercury telluride

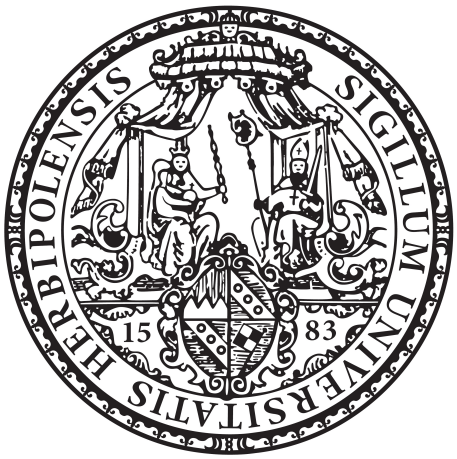

Dissertation zur Erlangung des
naturwissenschaftlichen Doktorgrades der
Julius-Maximilians-Universität Würzburg

vorgelegt von

Fabian Bernhard Schmitt

aus Aschaffenburg

Würzburg, 2021

Eingereicht am: 06.12.2021
bei der Fakultät für Physik und Astronomie

1. Gutachter: Prof. Dr. H. Buhmann
2. Gutachter: Prof. Dr. S. Höfling
3. Gutachter:
der Dissertation

Vorsitzende(r):
1. Prüfer: Prof. Dr. H. Buhmann
2. Prüfer: Prof. Dr. S. Höfling
3. Prüfer: Prof. Dr. G. Sangiovanni
im Promotionskolloquium

Tag des Promotionskolloquiums: 11.11.2022

Doktorurkunde ausgehändigt am: .....

Contents

Acronyms

2D	two-dimensional
3D	three-dimensional
ALD	atomic layer deposition
BG	back-gate
CM	clustering metals
CMT	cadmium mercury telluride ($Cd_{0.7}Hg_{0.3}Te$)
EBL	electron beam lithography
FFT	fast Fourier transformation
IBE	ion beam etching
ICP	inductively coupled plasma
LL	Landau level
LLF	Landau level fan-chart
MBE	molecular beam epitaxy
PECVD	plasma enhanced chemical vapor deposition
PMMA	polymethyl methacrylate
QH	quantum Hall
QHE	quantum Hall effect
QSHE	quantum spin Hall effect
SdH	Shubnikov-de Haas
SEM	scanning electron microscope
SL	sacrificial layer
TG	top-gate
TI	topological insulator
TRS	time-reversal symmetry
TS	trap states
TSS	topological surface state
UR	ungated regions
vdP	van der Pauw
VPS	Volkov-Pankratov state
WE	wet etching

1. Introduction: Motivation and description of contents

"The pen is mightier than the sword" - Edward Bulwer-Lytton, 1839.

The aim of physics is to understand and describe the world around us. To achieve this goal physicists create preferably simple models. On a large scale ($\geq$ mm), this already has been done several hundred years ago. For example, based on Newton's laws of the classical mechanics one can easily describe the movement of a car or sports phenomena like the trajectory of a ball in a soccer, baseball, or football match. In the field of condensed matter physics, the relevant physics takes place on much smaller length scale. The energies in such small dimensions usually are quantized and can be described by the Schrödinger equation for massive particles. Paul Dirac extended the Schrödinger equation to include relativity theory. The resulting equation is the Dirac equation for massless particles.

Due to its wide range of application, condensed matter physics is one of the largest fields in today's physical research. For instance, the miniaturization of switching electronics based on the progress in solid-state transistors has made computers available to everybody and therefore has changed our daily life completely. Another example of condensed matter physics in our everyday life is the charge coupled device [1], which is used for image processing in a digital camera. One of the most rapidly developing fields of research in condensed matter physics is represented by spintronics (portmanteau meaning spin transport electronics) in general, and research toward the realization of the quantum computer in particular [2]. At the moment, the most advanced approach for quantum computation is based on superconducting qubits. However, there also exist approaches on the basis of topological qubits, using either topological superconductivity [3] or so-called chiral qubits in topological semimetals [4].

Topological materials are a new class of material [5]. Due to their rich physics, topological insulators (TIs) represent particularly interesting representatives of this class. The first TIs have been realized in two dimensions in graphene [6] and a short time later in mercury telluride (HgTe) quantum wells [7]. Later, the concept was extended from two to three dimensions. The first experimental realizations of three-dimensional (3D) topological insulators were made in bismuth antimony and were proven via angle-resolved photoemission spectroscopy (ARPES) [8]. Eventually, based on transport measurement results, tensile

strained HgTe has proven to be a 3D TI [9]. These insulators are of major interest, since at their interface to trivial insulators they host two-dimensional (2D) conducting surface states, while being insulating in the bulk. Besides the massless topological surface states (TSSs) there exists the theoretical prediction of additional massive surface states, the so-called Volkov-Pankratov states (VPSs), named after their discoverers B. A. Volkov and O. A. Pankratov [10]. The massless surface states possess special transport properties, such as forbidden backscattering due to protection by time-reversal symmetry (TRS) and spin-momentum locking. This means that the charge carriers in these states have their spin locked at a right-angle to their momentum. Topological insulators offer the possibility of controllable spin transport and are therefore receiving increased attention in the research field of spintronics. Furthermore, it is predicted that as a result of spin-momentum locking, the symmetry-protected surface states can host Majorana particles if superconductivity is induced on the surface of a three-dimensional TI via proximity effects [11]. In the 2D case, the transport properties of surface states have already been investigated in detail and many interesting effects have been discovered. Particularly noteworthy are the quantum Hall effect (QHE) [12], the quantum spin Hall effect (QSHE) [7], and the quantum anomalous Hall effect (QAHE) [13]. In the three-dimensional case, however, despite the experimental realization of 3D TIs more than ten years ago, the transport properties of their surface states have hardly been studied so far. There are two main reasons for this. On the one hand, HgTe is the only known three-dimensional material system in which the surface states are accessible in the experiment due to the level of the Fermi energy, the high enough charge carrier mobility, and the possibility of sufficiently defect-free growth. On the other hand, the system is more complex due to its three-dimensionality, as multiple surface states localized at the interfaces to trivial insulators and the bulk material can contribute simultaneously to transport.

Based on earlier measurement results of our group "Experimental Physics III", it has become apparent that many physical properties of the 3D topological insulator mercury telluride still require in-depth exploration. This thesis focuses on the systematic investigations of the transport properties of three-dimensional HgTe-based TI samples. In addition to the contribution of massless surface states to transport, the contribution of massive surface states, which was not yet experimentally proven at the beginning of this PhD project, is to be studied. The aim is to contribute toward the applicability of this material system, for example in the field of spintronics, by extending the overall understanding of 3D TI HgTe and the possibilities of its manipulation. In order to be able to examine the transport properties, functional devices have to be fabricated first. Starting from the well-established lithography of two-dimensional HgTe samples [14], the lithographic processing is revised and enhanced to the three-dimensional case for structures ranging from hundreds of micrometers (macroscopic) down to a few micrometers in size (microscopic). Developments of this kind are crucial, since they are the key to exploiting the full potential of our high-quality mercury telluride layers. The transport properties of the surface states are investigated using two different sample

designs, namely the so-called macroscopic Hall bars and microscopic H-bars[1].

This thesis is organized as follows:

- After the introduction in chapter 1, chapter 2 deals with the fundamental characteristics which make HgTe a prime candidate for studying the transport properties of 3D topological insulator materials. These characteristics include the band structure of HgTe, the theoretical description of topological and massive surface states, and the behavior of these states in the presence of an external magnetic field. This knowledge represents an important element for the interpretation of the measurements and the data in the subsequent chapters. Chapter 2 further outlines the state of the art of lithography of macroscopic samples applied in our group and shows its shortcomings by means of transport measurements.

- Chapter 3 revises the lithographic steps for the fabrication of macrostructures. The possible origin of the observed unintentional doping of our samples during lithographic processing is elaborated as well. This chapter further presents a model, which can be used to predict the expected increase of the charge carrier density for a given device. Based on the experience and knowledge documented in chapter 3, a novel, improved standard recipe for the fabrication of macroscopic devices and a new procedure for the characterization of wafer materials have been introduced in our group.

- Chapter 4 investigates the behavior of the magnetoresistances of our samples at high magnetic fields ($B > 4\,\mathrm{T}$) and extremely low temperatures ($T \ll 1\,\mathrm{K}$). The observation of unexpected magnetoresistance fluctuations of the order of $\pm 10^2\,\mathrm{k\Omega}$, impeding meaningful interpretation of the data, indicates that certain regions of the devices may become insulating under these conditions. Chapter 4 deals with the exploration of this phenomenon. Based on the findings documented in chapter 4, it is shown that the unexpected signal fluctuations can be prevented by modifications regarding the growth of the samples, the sample lithography, or the measurement-setup. In this context, the ohmic contacts of the devices are also examined in detail. Specifically, the application of different contact structures is investigated and a newly developed fabrication process resulting in so-called clustering metals is specified.

- In chapter 5, magneto-transport measurements of samples containing manganese (Mn) dopants[2] fabricated using the modified lithography introduced in chapter 4 are studied. The results show unexpected sequences of quantum Hall plateaus. Chapter 5 describes the so-called re-entrant quantum Hall effect. It is revealed that the re-entrant QHE occurs due to an interplay of topological and massive surface states. It is also demonstrated that the counter-propagating quantum Hall edge states from these surface states

[1] The sample design is configured like the capital letter "H".

[2] Manganese functions as a paramagnetic dopant [15], which may affect the band structure of 3D HgTe [16].

inter-scatter and that the strength of inter-scattering is tunable via the dual-gate configuration. This chapter further discusses the influence of manganese doping on the transport properties of 3D topological insulator devices.

- Chapter 6 outlines the preference of the use of electron beam lithography (EBL) over optical lithography for the fabrication of microscopic three-dimensional TI samples. The necessary lithographic steps are also presented. These microstructures are required in order to achieve sample dimensions comparable to characteristic properties of the charge carriers involved in transport. Such properties include the mean free path and the spin relaxation length. Particular attention is given to the definition of the mesa of microscopic devices via etching, since this represents the most demanding fabrication step. Two different etching techniques, namely wet etching and the novel inductively coupled plasma etching as well as their advantages and disadvantages are discussed in detail.

- In chapter 7, the transport properties of microscopic 3D HgTe-based topological insulator devices are investigated using H-bar structures. A non-local resistance signal can be detected in transport measurements. Chapter 7 studies the behavior of this signal as a function of gate voltage, temperature, size of the H-bar structure, and magnetic field strength. It is shown that the non-local resistance signal can be attributed to the current-induced spin polarization of the topological surface states due to spin-momentum locking. In this context, the contribution of the massive surface states to the observed non-local signal is examined as well. This chapter further outlines the difference between spin transport in 2D and 3D H-shaped microstructures.

Finally, chapter 8 gives a summary of the results of this thesis.

2. The basics of the three-dimensional topological insulator HgTe

In order to investigate the transport properties of macroscopic and microscopic three-dimensional HgTe-based topological insulator samples, some basic knowledge of the material is essential. This knowledge will be applied to analyze the transport measurements and data in the subsequent chapters. In this context, this chapter presents the fundamentals which make mercury telluride a prime candidate for studying the transport properties of surface states of 3D TI materials. These fundamentals include the band structure of HgTe (Subsec. 2.1.1), the theoretical description of massless and massive surface states (Subsec. 2.1.2 and Subsec. 2.1.3), the growth of samples and the measurement-setup (Subsec. 2.2.1) as well as the presentation of two standard measurement techniques, namely magnetic field-dependent (Subsec. 2.2.2) and gate voltage-dependent measurements (Subsec. 2.2.3).

The next step is to fabricate the relevant functional devices. The samples are fabricated by lithographic processing. Due to the different fabrication processes, a distinction has to be made between macroscopic and microscopic structures. Microstructures require more challenging lithographic techniques, but are essential if the dimensions of samples are to be comparable to the mean free path and the spin relaxation length of charge carriers in the topological surface states (TSSs); both parameters are typically in the µm-range. Section 2.3 describes the state of the art of lithography of macroscopic devices applied in our group and shows its shortcomings on the basis of magneto-transport measurements.

2.1. The II-VI semiconductor HgTe

HgTe is a II-VI semimetal and its atoms are arranged in so-called zincblende crystal structure. A schematic sketch of the crystal structure of HgTe is shown in Fig. 2.1. The zincblende structure consists of two face-centered cubic (fcc) sublattices with an offset of $(\frac{1}{4}, \frac{1}{4}, \frac{1}{4})a_0$ in all spatial directions [17], where $a_0 = 6.46152\,\text{Å}$ is the lattice constant [18]. One of the sublattices can be assigned to the group II element (Hg) and the other to the group VI element (Te). In order to use the semimetal mercury telluride as a semiconductor, one has to consider its band structure. The description of the band structure of HgTe is subject of the following subsection.

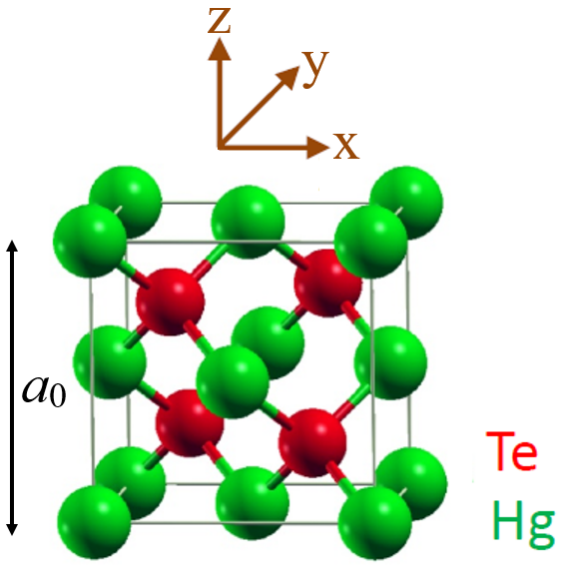

Figure 2.1.: Zincblende crystal structure of HgTe. The Hg and Te atoms are represented in green and red respectively. Adapted from [19], licensed under CC BY 4.0, `https://creativecommons.org/licenses/by/4.0/`.

2.1.1. Band structure of HgTe

The band structure of HgTe is presented in Fig. 2.2. The conduction and valence bands (Γ_8 bands) touch each other at the Γ point ($k = 0$, with k being the wavenumber), i.e. the material possesses no band gap. This makes mercury telluride a semimetal. The nomenclature reflects the symmetry properties of the bands, which are determined by the constitutions of the underlying atomic orbitals. The Γ_7 and Γ_8 bands are constituted of the Te p-like, while the Γ_6 band is composed of the Hg s-like band. Due to strong spin-orbit coupling in HgTe, the orbital character is defined by the total angular momentum quantum number $j = |l \pm s|$, where l represents the angular momentum number and $s = \pm\frac{1}{2}$ the spin. The projection of j is given by $|m_j| \leq j$. The Γ_6 band has a degeneracy of two with $j = \frac{1}{2}$ and $m_j = \pm\frac{1}{2}$ and is conventionally denominated as electron band. The Γ_8 band, however, has a degeneracy of four with $j = \frac{3}{2}$. The bands with $m_j = \pm\frac{3}{2}$ and $m_j = \pm\frac{1}{2}$ are called heavy hole (HH) and light hole (LH) bands respectively. The Γ_7 band is traditionally denominated as split-off band and has a degeneracy of two ($j = \frac{1}{2}$ and $m_j = \pm\frac{1}{2}$) [20]. The low energy part of the band structure of mercury telluride around the Γ point can be described by the Kane model, which can be written down either as a six band model only including the Γ_6 and Γ_8 bands or as an eight band model also including the Γ_7 band [21], depending on the desired accuracy of the calculated band structure.

From Fig. 2.2, one can see that the Γ_6 band is lower in energy than the Γ_8 bands. Sticking to the conventional definition of the band gap in semiconductors between the Γ_6 and Γ_8 bands, the band gap is defined as the energy difference $\Delta E = E_{\Gamma_6} - E_{\Gamma_8}$. In the case of

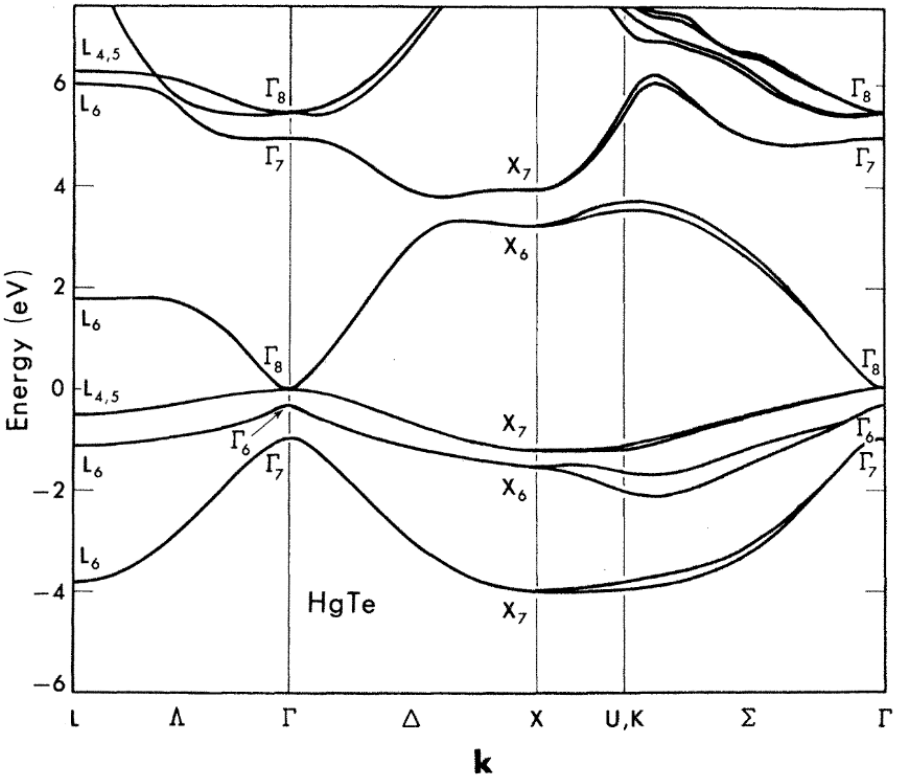

Figure 2.2.: The inverted band structure of mercury telluride: The Γ_6 band is lower in energy than the Γ_8 bands. At the Γ point and at the level of the Fermi energy ($E = 0$) the Γ_8 bands are touching, which makes HgTe a semimetal. Reprinted with permission from [22]. Copyright 1972 by the American Physical Society.

mercury telluride, we find $\Delta E_{\mathrm{HgTe}} \approx -300\,\mathrm{meV}$ at the Γ point. This makes HgTe a quadratic semimetal with an inverted band ordering indicated by a negative band gap. The inverted band structure of HgTe is caused by strong relativistic correction terms. The relativistic correction terms are determined by the large atomic mass of the mercury atoms and the pronounced spin-orbit interaction. The underlying mechanism is discussed in detail on the basis of the ordinary Hamiltonian at atomic level, for example in Ref. [23]. This band inversion is an important prerequisite for a material system to be a topological insulator. The requirements for the semimetal HgTe to become a TI are described next.

In general, there are two requirements for a given material system to be a three-dimensional topological insulator. First, it is necessary that the material has an inverted band structure. This is essential so that two-dimensional surface states are formed at the interfaces to trivial insulators, which have a non-inverted, topological trivial band ordering. A more detailed description of the formation of surface states is given in Subsec. 2.1.2. As already discussed, mercury telluride has an inverted band structure. Second, the material system has to possess a bang gap in the bulk [24]. If the level of Fermi energy lies in the band gap, the bulk is

insulating and transport happens exclusively through the surface states. Thus, a 3D TI is a system that is insulating in the bulk, while having conductive states at its surfaces. As can be seen in Fig. 2.2, in the case of HgTe, the Γ_8 bands are touching at $E = 0$. So there is no band gap. One possibility to open a band gap in the band structure of three dimensional mercury telluride is its tensile strained growth on a substrate with a larger lattice constant. By doing so, the lattice symmetry of HgTe breaks. As a result the degeneracy of the Γ_8 LH and HH bands is lifted. The resulting consequence is the opening of a band gap, as shown in Fig. 2.3.

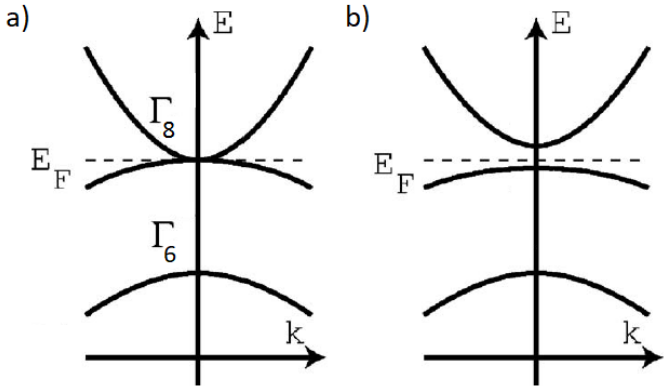

Figure 2.3.: Schematics of Γ_6 and Γ_8 bands around the Γ point for a) unstrained and b) tensile strained HgTe. In the case of applied tensile strain, the degeneracy of the Γ_8 bands is lifted and a band gap is formed. Adapted with permission from [25]. Copyright 2007 by the American Physical Society.

The substrate materials, which are used for all samples investigated in this thesis, are either pure cadmium telluride (CdTe) or a combination of n-doped gallium arsenide (GaAs) and cadmium telluride. To reduce the lattice mismatch of GaAs and CdTe and to avoid lattice relaxations, an additional zinc telluride (ZnTe) interlayer is grown in between. The thickness of this interlayer is usually only a few nanometers. Since cadmium telluride possesses a slightly larger lattice constant ($a_{\mathrm{CdTe}} = 6.4815\,\text{Å}$ [26]) compared to mercury telluride, the resulting lattice mismatch is $\varepsilon = (a_0 - a_{\mathrm{CdTe}})/a_{\mathrm{CdTe}} \approx -0.3\,\%$. Thus, we are able to apply the required tensile strain to the HgTe layer. Based on this lattice mismatch, one can estimate the energy of the tensile strain induced band gap at the Γ point to be $E_{\mathrm{gap}} = E_{\mathrm{LH}} - E_{\mathrm{HH}} = 22\,\mathrm{meV}$ [27]. At this point, it is worth mentioning that cadmium telluride has a non-inverted, topological trivial band ordering. This means that the Γ_6 band is higher in energy than the Γ_8 bands.

2.1.2. Topological and massive surface states

As shown above, the band structure of HgTe is inverted, implying a negative energy gap $\Delta E = E_{\Gamma_6} - E_{\Gamma_8}$ at $k = 0$. For many other materials, including conventional semiconductors

like CdTe and $Cd_xHg_{1-x}Te$[1] with cadmium (Cd) content $x = 0.7$, and even for the vacuum, the band order is not inverted and $\Delta E > 0$ applies. The energy gap of $Cd_xHg_{1-x}Te$, for instance, can be calculated via

$$\Delta E_{Cd_xHg_{1-x}Te}(x) = (-0.302 + 1.93x - 0.810x^2 + 0.832x^3)\,\text{eV} \tag{2.1}$$

for temperature $T = 0\,\text{K}$ [28]. In the case of cadmium content $x = 0.7$, one finds the energy gap to be $\Delta E_{CMT}(0.7) \approx 0.94\,\text{eV}$. Naturally, if an interface of two different materials 1 and 2 with $\Delta E_1 \cdot \Delta E_2 < 0$ is formed, there is a continuous connection of each band and therefore a band crossing has to take place at the interface. At this point, it is specified that in the following the interface is to be aligned parallel to the xy-plane.

For the example of a CMT/HgTe/CMT layer sequence, the behavior of the bands is sketched in Fig. 2.4a). With the Fermi energy lying between the Γ_6 and Γ_8 bands, mercury telluride is insulating in the bulk due to the band gap E_{gap}, whereas one obtains conductive states at the interfaces to CMT. These states are called massless or topological surface states. The charge carriers in the two-dimensional TSSs behave like massless relativistic particles - similar to the case of graphene, a monolayer of graphite. For this reason, the charge carriers do not obey the Schrödinger equation, what would result in a parabolic energy dispersion, but the Dirac equation. The energy of a topological surface state is described by the following

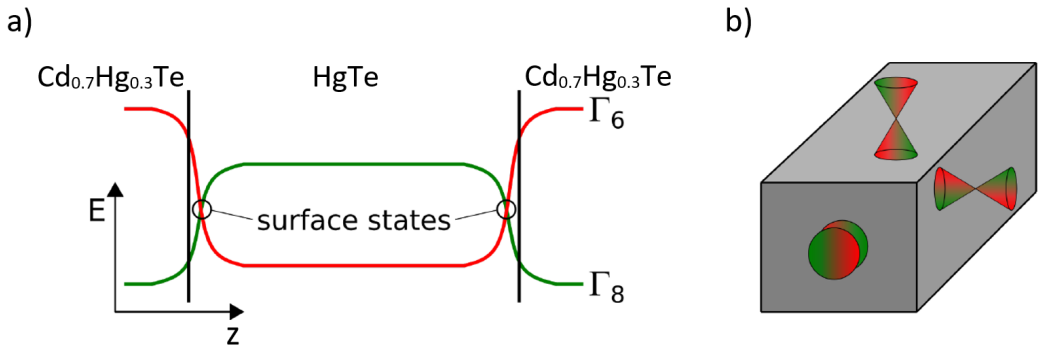

Figure 2.4.: a) Band structure of a $Cd_{0.7}Hg_{0.3}Te/HgTe/Cd_{0.7}Hg_{0.3}Te$ layer sequence. The continuity condition at interfaces forces band crossings at the material edges. The formed surface states are marked by black circles. b) A two-dimensional electron gas with linear energy-momentum dispersion relation is developed on each surface of a three-dimensional material slab. The linear dispersion relation is symbolized by red-green cones. Modified with permission from [29].

Hamiltonian:

$$H_{TSS} = -i\hbar v_F \vec{\sigma} \cdot \nabla, \tag{2.2}$$

where i is the imaginary unit, $\hbar$ the reduced Planck constant, v_F the Fermi velocity, and $\vec{\sigma} = (\sigma^x, \sigma^y)$ in terms of the Pauli matrices σ^x, σ^y, and σ^z [12]. The energy eigenvalues

[1] In the following, the abbreviation used for $Cd_{0.7}Hg_{0.3}Te$ is CMT.

resulting from this Hamiltonian are given by:

$$E = \pm\hbar v_{\mathrm{F}} \left|\overrightarrow{k}\right|, \tag{2.3}$$

with $\left|\overrightarrow{k}\right| = |(k_{\mathrm{x}}, k_{\mathrm{y}})|$ being the absolute value of the in-plane wave vector. The energy spectrum obtained by Eq. 2.3 is the so-called Dirac cone, which is sketched in Fig. 2.5a). The crossing point in the middle of a Dirac cone is referred to as Dirac point and represents the transition point from electron to hole transport. If an ashlar-formed 3D TI slap like in Fig. 2.4b) is considered, one can observe that always two surfaces of the slap have an identical spatial orientation, i.e. the surface normals of each two surfaces point in the same direction. Looking from a top view down on the slap, the closer surface is in the following called the top surface and the more distant one the bottom surface. Another characteristic of charge carriers in a TSS is the spin-momentum locking. This means that the spin of a fermion is locked at a right-angle to its momentum due to spin-orbit coupling. The spin-momentum locking can be read directly from Eq. 2.2 and is presented in Fig. 2.5b). For instance, if a fermion moves in the x-direction, then its spin has to point in y-direction and vice versa. The spin-momentum locking of charge carriers in the surface states is one of the reasons why topological insulators are of such great interest to current physical research and why they are promising candidates for the field of spintronics. The topological surface states can be

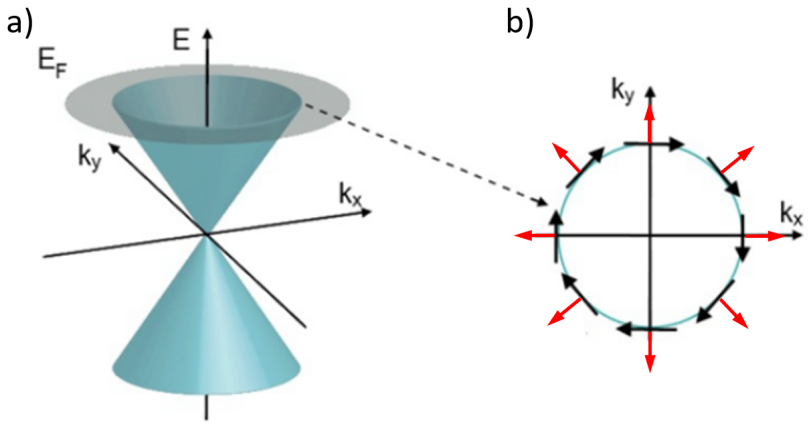

Figure 2.5.: a) Linear energy-momentum dispersion relation of a massless relativistic fermion. Due to its shape, the dispersion relation is called Dirac cone. b) Cut through the Dirac cone depicting the Fermi circle from the bird's eye view. The spin-momentum locking is indicated by red (momentum) and black (spin) arrows. Adapted with permission from [30]. Copyright 1969 by the Nature Publishing Group.

made experimentally visible via angle-resolved photoemission spectroscopy (ARPES), as it is shown for example in Refs. [8, 9, 31].

A different access to the nature of interface states of a $Cd_xHg_{1-x}Te$/HgTe layer stack is

given by B. A. Volkov and O. A. Pankratov [10]. Their model[2] uses a four band model with mutually inverted bands to predict the band structure of an inverted contact. One of the obtained results is a linear dispersing non-degenerate interface state. This state, which is independent of the cadmium content x, is called massless Volkov-Pankratov state (VPS) and is equivalent to the TSS described above. In addition to the massless VPS, massive surface states at the inverted interface are reported. These massive states have a quadratic dispersion relation, are spin degenerate and therefore double degenerate, and are called massive Volkov-Pankratov states. They are only formed at interfaces with a smooth variation of x. The band structure of such a smooth inverted contact is sketched in Fig. 2.6, where one can see the conduction band and valence band like massive VPSs marked in purple. The conduction band and valence band like Volkov-Pankratov states can be occupied by electrons (n-type) and holes (p-type) respectively. The energy scale of the band gap of the massive

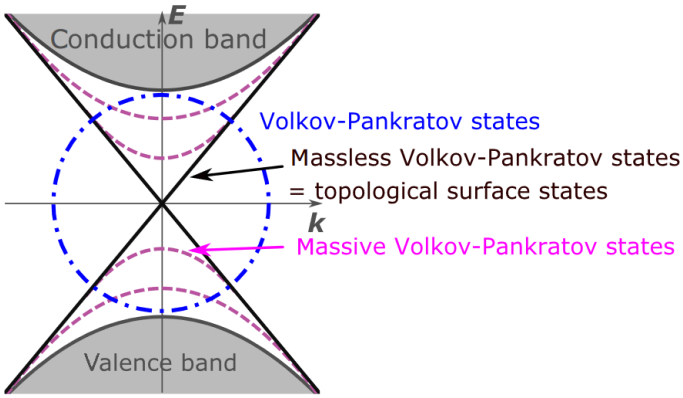

Figure 2.6.: Shown are the massive and massless Volkov-Pankratov states at the interface between two materials with mutually inverted bands. The massless states are also called topological surface states. Adapted from [32], licensed under CC BY 4.0, `https://creativecommons.org/licenses/by/4.0/`.

VPSs is related to the thickness of the smooth transition area. For a quite narrow transition area, as it is the case for our samples, it is expected that the massive surface states only exist at inaccessible high energies. However, the creation mechanism of massive VPSs is extended in Refs. [33, 34] by accounting for a smooth drop of electric potential over such an inverted interface. It is shown that the smooth electric potential drop is equivalent to a smooth Cd content x variation and leads to the formation of these additional massive Volkov-Pankratov states as well.

Similar electric field induced massive surface states were found in magneto-transport measurements done on compressive strained three-dimensional HgTe, which represents a Dirac semimetal [32]. In this reference, the electron transport is assigned to the massless topological surface states. Given that the Dirac points and the hole regimes of the TSSs are not

[2]The model is motivated by the material system $Sn_xPb_{1-x}Te$.

accessible in magneto-transport measurements, the hole transport cannot originate from the topological surface states. The p-type transport is explained by additional valence band like massive Volkov-Pankratov states, which form due to an applied (negative) gate voltage. The formation of massive VPSs is shown via $6\,\mathrm{x}\,6$ $k \cdot p$ calculations, which consider the applied gate voltage by a realistic Hartree potential. The band structures of tensile and compressive strained mercury telluride only differ slightly for small k and energy window around the energy where the quadratic band touching point would be for unstrained HgTe. Therefore, it is reasonable to assume that these additional massive Volkov-Pankratov states are formed in the three-dimensional topological insulator phase as well. In Sec. 2.2, it is shown that p-type and potentially even n-type massive VPSs can be observed in magneto-transport measurements of tensile strained 3D mercury telluride.

At this point, it should be mentioned that in the case of high electron densities, also n-type massive bulk states can be occupied in addition to the surface states. Note that the p-type bulk states of our 3D TI HgTe samples are not accessible in the experiment and therefore have not to be considered. Analogous to the VPSs, the massive n-bulk states have a quadratic dispersion relation and are spin degenerate and therefore double degenerate. Due to the possibility of an identical description of energy dispersion and spin degeneracy of n-type bulk and Volkov-Pankratov states, in the following, solely the term n-type massive states will be used and only if necessary a clear distinction will be made between n-bulk states and n-type VPSs. It should be noted, however, that the Volkov-Pankratov states are surface states, whereas the n-bulk states are localized in the bulk. If a distinction is required and it has to be determined whether n-bulk states or n-type VPSs are occupied first when more and more electrons are introduced into the system, then a separate consideration is necessary for each given device. For instance, already the individual layer thicknesses of the grown layer stack of a sample (cf. Subsec. 2.2.1) can be decisive. Different layer thicknesses affect the smooth drop of electric potential over the sample, which in turn influences the formation of massive Volkov-Pankratov states. To identify which states become populated first, dedicated self-consistent 8-orbital $k \cdot p$ band structure calculations are required for each wafer material[3]. A detailed description of the self-consistent $k \cdot p$ calculations can be found in Ref. [35]. On the basis of these calculations, it is also possible to specify the states accessible in our experiments. A layer sequence of $Cd_{0.7}Hg_{0.3}Te$/HgTe/$Cd_{0.7}Hg_{0.3}Te$ with typical layer thicknesses and the maximal and minimal chemical potential, which can be achieved experimentally, are used as inputs (cf. Appx. A.2 and cf. Sec. 2.2, respectively). Since two $Cd_{0.7}Hg_{0.3}Te$/HgTe interfaces exist, we include in our analysis two surface states referred to in the following as top and bottom surface states.

The results of the band structure calculations, and thus the experimentally accessible states in our three-dimensional HgTe-based samples, are presented in Fig. 2.7a). This figure

[3] In Chap. 5 and Chap. 7, such calculations are carried out and presented for wafer materials QC0464 and Q2982, respectively.

uses a simplified illustration of the bands. Without taking into account any hybridization effects between the surface states and the valence bands, the topological surface states can be modeled using a linear dispersion relation and the massive states can be modeled using a quadratic dispersion relation. Further, only the bands relevant for transport are shown in Fig. 2.7a). The calculations assume a larger charge carrier density for the top TSS (in

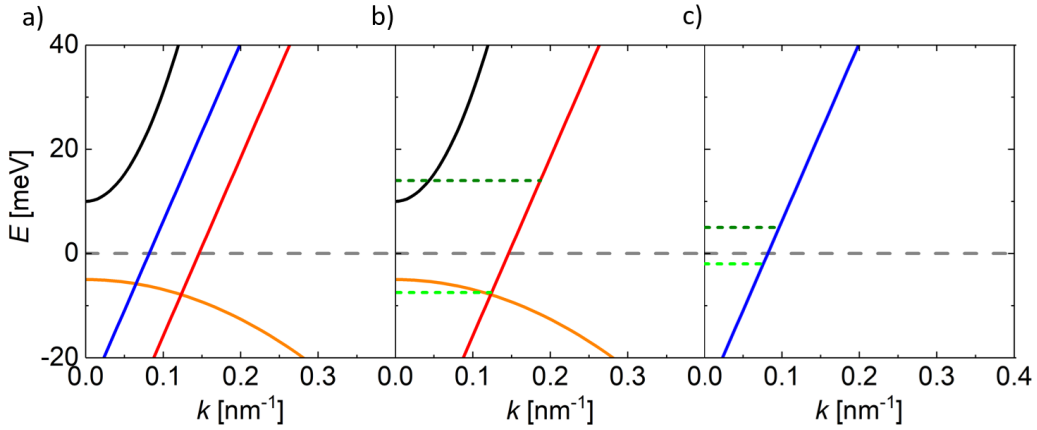

Figure 2.7.: a) Illustration of the massless and massive states experimentally accessible in our 3D TI devices. Shown are the topological surface states of the top (in red) and bottom (in blue) surfaces as well as the double degenerate n-type (in black) and p-type (in orange) massive Volkov-Pankratov states. The zero energy level is indicated via a dashed gray line. b) depicts the surface states accessible on the top surface using the experimentally accessible energy range determined by the minimal (dashed light green line) and maximal (dashed dark green line) achievable chemical potentials. In c), an analogous consideration as presented in b) is carried out, except now the bottom surface is considered. This figure was inspired by Ref. [35].

red) compared to the bottom one (in blue) in order to imitate our devices. This density difference and the resulting different energy levels of the topological surface states of the top and bottom surfaces at $k = 0$ are expected due to different electrostatic environments as explained in Subsec. 2.1.3 and Subsec. 2.2.1. The additional p-type Volkov-Pankratov states of the top surface are depicted in orange. The n-type massive states, which can be either n-type VPSs of the top surface or n-bulk states, are exemplarily represented by n-type Volkov-Pankratov states (in black) in Fig. 2.7. Minimal and maximal achievable chemical potentials, which are accessible in the experiment, are indicated by dashed light and dark green lines respectively. It can be seen that on the top surface, the n-type TSS as well as n-type and p-type massive Volkov-Pankratov states are experimentally accessible (cf. Fig. 2.7b)). On the bottom surface, however, only the n-type topological surface state is accessible (cf. Fig. 2.7c)). Hence, in the following, the Volkov-Pankratov states of the top surface are referred to just as VPSs without explicitly mentioning that they are located at the top surface. The different accessibility of the states located at the top and the bottom of

the 3D slab is determined by the layout of the devices. While the top surface is close to the sample surface, the bottom surface is buried deeper in the device (cf. Subsec. 2.2.1) making it difficult to manipulate the level of chemical potential (cf. Subsec. 2.2.3). Since the Dirac points of both surfaces and thus the hole regimes of the TSSs are not accessible in transport measurements, the p-type transport in our samples is completely assigned to the p-type massive VPSs. The n-type transport, on the other hand, is composed of the contributions from topological surface states (top and bottom) and n-type massive Volkov-Pankratov or bulk states. It is noted that in the experiment, the TSSs are always occupied whereas the n-type VPSs and the n-bulk states are only populated in the case of high electron densities.

The next step is to investigate how the massless and massive states behave in the presence of an external magnetic field which points perpendicularly to the interfaces of the CMT/HgTe/CMT layer sequence. Hereafter, this direction is defined as the z-direction.

2.1.3. Topological and massive states in the presence of an external magnetic field

In order to investigate the magnetic field dependence of topological and massive surface states, firstly, the behavior of a two-dimensional electron gas (2DEG) in the presence of an external magnetic field B is studied. Secondly, the relativistic magnetic field dependence of surface states is examined. The knowledge gained is then used to analyze the magneto-transport measurements described in the subsequent chapters.

Due to the restriction in z-direction, the charge carriers in the surface states defined parallel to the xy-plane are classified as a 2DEG. The carriers of a two-dimensional electron gas, which is perpendicularly penetrated by a magnetic field[4], are forced onto cyclotron orbits by the Lorentz force [36]. The resulting states are called Landau levels (LLs). Their energies are quantized to

$$E_{\mathrm{LL}} = (N + \frac{1}{2})\hbar\omega_{\mathrm{c}} = (N + \frac{1}{2})\hbar\frac{eB}{m_{\mathrm{eff}}}, \tag{2.4}$$

with $N = 0, 1, 2, ...$ being the Landau level index, $\omega_{\mathrm{c}} = eB/m_{\mathrm{eff}}$ the cyclotron frequency, e the elementary charge, and m_{eff} the effective mass of the charge carriers [12]. The degeneracy of these LLs is given by:

$$n_{\mathrm{LL}} = g_{\mathrm{s}} g_{\mathrm{v}} \frac{e}{h} B, \tag{2.5}$$

where g_{s} is the spin degeneracy, g_{v} the valley degeneracy, and h the Planck constant [37]. Eq. 2.5 shows that the degeneracy is directly proportional to the magnetic field B. The number of occupied Landau levels in a system is given by the so-called filling factor defined by:

$$\nu = \frac{n}{n_{\mathrm{LL}}} = \frac{n}{g_{\mathrm{s}} g_{\mathrm{v}}} \frac{h}{e} \frac{1}{B}, \tag{2.6}$$

[4] It is noted that in the case of a 3D slab (cf. Fig. 2.4b)), always two surfaces are perpendicularly penetrated by an external magnetic field.

with n being the charge carrier density. In a finite two-dimensional system, such as in a real sample, the energies of the LLs are locally enhanced at the edges due to the edge potential. This causes fully occupied Landau levels, which have lower energy values than the Fermi energy E_F in the bulk, to bend upwards. This results in crossing points with E_F at the edges of the sample. Since the crossing points are located at the edges of the sample, in the following, these states are called edge states and edge channels respectively. The transverse or Hall conductivity σ_{xy}[5] of the edge states is quantized and proportional to the number of occupied LLs in the bulk. It can be written down as [35]:

$$\sigma_{\mathrm{xy}} = \nu \frac{e^2}{h}. \tag{2.7}$$

This effect is called quantum Hall effect. The values of the Hall conductivity, which are given by Eq. 2.7 for different ν, are referred to as Hall plateaus. A more detailed description of the QHE can be found in Ref. [12]. Given that only fully occupied states are available in the bulk, the longitudinal conductivity σ_{xx} is zero as long as the level of E_F does not coincide with the energy of a LL. Consequently, not only the Hall conductivity, but also the transverse or Hall resistance R_{xy} is quantized. For the same reason, as long as the Hall resistance is quantized, the longitudinal resistivity ρ_{xx} and thus the longitudinal resistance R_{xx} have to be zero, making the system a perfect conductor. If the Fermi energy and the energy of a Landau level coincide, then backscattering in the bulk states is allowed and R_{xx} takes finite values. This oscillation like behavior of the longitudinal resistance is called Shubnikov-de Haas (SdH) oscillation and is a characteristic of the QHE as well [38].

Now, the relativistic case is to be considered. Assuming a magnetic field pointing in z-direction ($\overrightarrow{B} = B \cdot \hat{\mathrm{z}}$, with $\hat{\mathrm{z}}$ being the unit vector in z-direction), for the two relevant topological surface states[6], the Hamiltonian from Eq. 2.2 can be written as [9]:

$$H_{\mathrm{TSS}} = \hbar v_\mathrm{F} \begin{pmatrix} k_\mathrm{x}\sigma^\mathrm{y} - k_\mathrm{y}\sigma^\mathrm{x} & 0 \\ 0 & -(k_\mathrm{x}\sigma^\mathrm{y} - k_\mathrm{y}\sigma^\mathrm{x}) \end{pmatrix}. \tag{2.8}$$

This Hamiltonian can be solved with the help of creation and annihilation operators [9]. The resulting eigen-energies for the top and bottom topological surface states are given by

$$E_{\mathrm{TSS}}(B, N_{\mathrm{TSS},\beta}) = \pm\sqrt{2e\hbar v_\mathrm{F}^2 B N_{\mathrm{TSS},\beta}}, \tag{2.9}$$

where $N_{\mathrm{TSS},\beta} = 0, 1, 2, ...$ is the Landau level index of surface β and $\beta = \mathrm{I}, \mathrm{II}$ represents the two relevant surface states. Without loss of generality, in the following, we refer to

[5] The indices x and y indicate the direction with respect to a two-dimensional Cartesian coordinate system. The first index always indicates the direction of the current and the second index the direction of the resulting voltage.

[6] According to Subsec. 2.1.2, the relevant surfaces states, which are perpendicularly penetrated by the magnetic field, are called top and bottom surface states.

surface I as the top and to surface II as the bottom surface respectively. Thus, TSS,I is the topological surface state located at the top surface and TSS,II is the one located at the bottom surface of the 3D topological insulator. In the two Dirac cone model for two surface states, the Landau levels are double degenerate as long as no energy difference between these surface states is introduced. Positive energy values describe electrons, while a negative sign in Eq. 2.9 indicates that the charge carriers are holes. As already mentioned in Subsec. 2.1.2, the p-type transport regime of the TSSs of our samples is not accessible in the experiment since the Dirac point is energetically buried deep in the valence band. Therefore, Eq. 2.9 takes on only positive values. For $N_{\mathrm{TSS},\beta} = 0$ applies $E_{\mathrm{TSS}} = 0$. This particular LL is called zero-level.

Considering non-relativistic and relativistic cases, the major difference between the two is the shift by $\frac{1}{2}$. The consequence is that in contrast to the integer plateau values of the QHE, now half-integer values are taken. Hence, for one of the two topological surface states, the Hall conductivity of a quantum Hall (QH) plateau can be written as $\sigma_{\mathrm{xy}}^{\beta} = (N_{\mathrm{TSS},\beta} + \frac{1}{2})e^2/h$. In an ideal 3D TI, there is no energy difference between top and bottom surface states and the total Hall conductivity becomes $\sigma_{\mathrm{xy}}^{\mathrm{I+II}} = (2N_{\mathrm{TSS,I}} + 1)e^2/h$, where $N_{\mathrm{TSS,I}} = N_{\mathrm{TSS,II}}$ is valid. Therefore, a sequence of only odd quantum Hall plateaus should be visible in the experiment. In real samples, however, an energy difference is expected due to unequal electrostatic environments during measurement [9]. Hence, the total Hall conductivity has to be given by

$$\sigma_{\mathrm{xy}}^{\mathrm{I+II}} = (N_{\mathrm{TSS,I}} + N_{\mathrm{TSS,II}} + 1)\frac{e^2}{h} = \nu_{\mathrm{TSS}}\frac{e^2}{h}, \tag{2.10}$$

with $\nu_{\mathrm{TSS}} = N_{\mathrm{TSS,I}} + N_{\mathrm{TSS,II}} + 1$ being the total filling factor of top and bottom topological surface states.

The next step is to consider the consequence of the Zeeman effect on the model. The Zeeman Hamiltonian for a magnetic field in z-direction is given by

$$H_{\mathrm{Zeeman}} = \begin{pmatrix} g_{\mathrm{TSS}}^{*}\mu_{\mathrm{B}}B\sigma^{\mathrm{z}} & 0 \\ 0 & g_{\mathrm{TSS}}^{*}\mu_{\mathrm{B}}B\sigma^{\mathrm{z}} \end{pmatrix}, \tag{2.11}$$

where g_{TSS}^{*} is an effective g-factor for the topological surface states and μ_{B} the Bohr magneton [9]. The eigen-energies of the combined Hamiltonian $H = H_{\mathrm{TSS}} + H_{\mathrm{Zeeman}}$ can be calculated to

$$E_{\mathrm{TSS}}(B, N_{\mathrm{TSS},\beta}) = \sqrt{2e\hbar v_{\mathrm{F}}^2 B N_{\mathrm{TSS},\beta} + (g_{\mathrm{TSS}}^{*}\mu_{\mathrm{B}}B)^2}. \tag{2.12}$$

For $N_{\mathrm{TSS},\beta} = 0$, the result is $E_{\mathrm{TSS}}(B, N_{\mathrm{TSS},\beta} = 0) = g_{\mathrm{TSS}}^{*}\mu_{\mathrm{B}}B$. The two surface states are degenerate as long as no energy difference is introduced between them. As mentioned before (cf. Subsec. 2.1.2), it is very likely that in the real experiment there is an energy difference $\delta = E_{\mathrm{TSS,I}}(B = 0) - E_{\mathrm{TSS,II}}(B = 0)$ between top and bottom topological surface states. Thus, the degeneracy is lifted. This energy difference is a result of different charge carrier densities located in each of the surface states β. The influence of a certain carrier density

$n_{\mathrm{TSS},\beta}$ on the energy values of Landau levels can be described by $E_{\mathrm{TSS},\beta} = -\hbar v_{\mathrm{F}}\sqrt{4\pi n_{\mathrm{TSS},\beta}}$ [39], considering the energy at the band edges. Adding this energy shift to Eq. 2.12, the latter reads:

$$E_{\mathrm{TSS}}(B, N_{\mathrm{TSS},\beta}) = \sqrt{2e\hbar v_{\mathrm{F}}^2 B N_{\mathrm{TSS},\beta} + (g^*_{\mathrm{TSS}}\mu_{\mathrm{B}}B)^2} + E_{\mathrm{TSS},\beta}. \tag{2.13}$$

A simulation of the outcome of Eq. 2.13 is shown in Fig. 2.8, where the energy dispersion of the LLs for $N_{\mathrm{TSS},\beta} \leq 3$ is plotted as a function of the magnetic field for electron transport. The parameters for the plot are $g^*_{\mathrm{TSS}} = 20$ and $v_{\mathrm{F}} = 5 \cdot 10^5 \frac{\mathrm{m}}{\mathrm{s}}$, and are taken from Refs. [40, 41]. The assumed values for the charge carrier densities of top and bottom surfaces are $n_{\mathrm{TSS,I}} = 4 \cdot 10^{11} \frac{1}{\mathrm{cm}^2}$ and $n_{\mathrm{TSS,II}} = 2 \cdot 10^{11} \frac{1}{\mathrm{cm}^2}$ respectively.

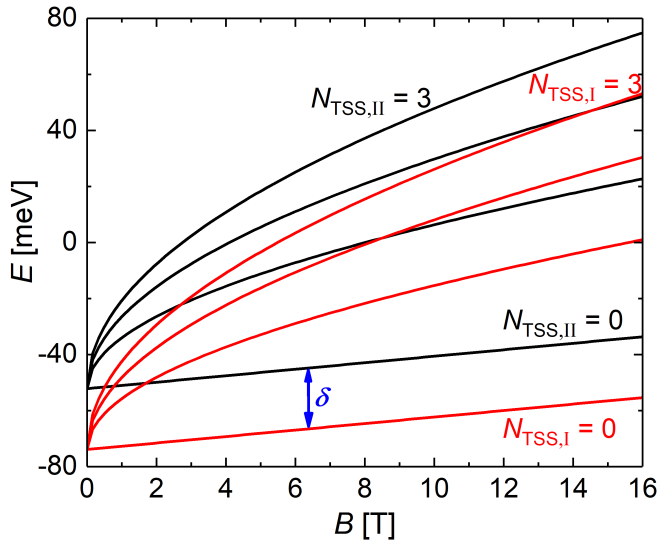

Figure 2.8.: Landau level dispersion of a two Dirac cone model in a magnetic field for electron transport. Only the levels for $N_{\mathrm{TSS},\beta} \leq 3$ are plotted. The different starting energies at $B = 0\,\mathrm{T}$ are a result of different carrier densities for top (in red) and bottom topological surface states (in black). δ indicates this energy difference. The two zero levels and the Landau levels having the highest energy are marked by their LL index $N_{\mathrm{TSS},\beta} = 0,\, 3$.

The massive Volkov-Pankratov as well as the n-bulk states are described by the Schrödinger equation. Considering the Zeeman effect, one obtains for the eigen-energies [15]:

$$E_{\mathrm{m}}(B, N_{\mathrm{m}}) = (N_{\mathrm{m}} + \frac{1}{2})\frac{\hbar e}{m_{\mathrm{eff}}}B \pm \frac{g^*_{\mathrm{m}}}{2}\mu_{\mathrm{B}}B, \tag{2.14}$$

with $N_{\mathrm{m}} = 0,\, 1,\, 2,\, ...$ being the Landau level index and g^*_{m} the effective g-factor for the massive states. Note that the index m represents either VPS or bulk, depending on which

massive states are occupied. The plus-minus sign indicates that the VPSs and bulk states are split in presence of a magnetic field due to their spin orientation (up, down). This lifts the spin degeneracy of these states. The occupied Landau levels from the VPSs and n-bulk states contribute to the Hall conductivity by $\sigma_{xy} = \pm\nu_m e^2/h$, with ν_m being the filling factor of the massive states. This time, the $\pm$-sign distinguishes between n-type and p-type states. Positive values indicate n-type VPSs or n-bulk states, while negative ones represent p-type Volkov-Pankratov states. Again, an energy shift of the massive states is caused by the charge carrier density n_m located in these states. The energy at the band edge for a certain carrier density is given by $E_{m,0} = -\frac{1}{2}\hbar^2\pi\,|n_m|\,/m_{eff}$ [15]. In the case of electron transport, $n_m > 0$ and $m_{eff} > 0$ are valid, while for hole transport $n_m < 0$ and $m_{eff} < 0$ apply. Adding this energy shift to Eq. 2.14 one finds:

$$E_m(B, N_m) = (N_m + \frac{1}{2})\frac{\hbar e}{m_{eff}}B \pm \frac{g_m^*}{2}\mu_B B + E_{m,0}. \tag{2.15}$$

In Fig. 2.9, the energy dispersion of the massive states is depicted. Only the Landau levels

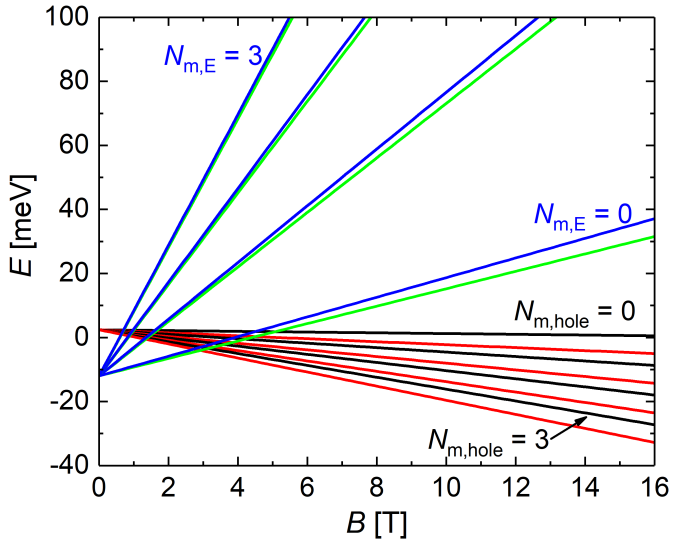

Figure 2.9.: Energy dispersion of the massive states in presence of a magnetic field B. Only the levels for $N_m \leq 3$ are plotted. The different spin orientation (up and down) of the subbands is represented in blue and green for electron transport and in black and red for hole transport. The Landau levels of the spin up subbands with indexes $N_m = 0$ and $N_m = 3$ are marked for the n-type regime as well as for the p-type regime.

for $N_m \leq 3$ are plotted as a function of the magnetic field for electron (in blue and green) and hole transport (in black and red). The used parameters are $n_{m,E} = 2\cdot 10^{11}\,\frac{1}{cm^2}$, $n_{m,hole} = -4\cdot 10^{11}\,\frac{1}{cm^2}$, $g_m^* = 6$, $m_{eff,E} = 0.02m_e$, and $m_{eff,hole} = -0.2m_e$, where m_e is the rest mass of

an electron [15].

Based on the considerations made above, one is able to conclude that the total Hall conductivity σ_{xy}^{tot} of a three-dimensional topological insulator can be noted as

$$\sigma_{xy}^{tot} = (\nu_{TSS} \pm \nu_m)\frac{e^2}{h}, \tag{2.16}$$

when the topological surface states of top and bottom surfaces as well as massive Volkov-Pankratov or bulk states are simultaneously contributing to transport. The corresponding total filling factor ν reads $\nu = \nu_{TSS} \pm \nu_m$. The theoretical considerations of this subsection are utilized in Ch. 4 and Ch. 5.

2.2. Preparation and transport characteristics of three-dimensional HgTe-based samples

The following subsections describe the growth of samples, the measurement-setup, and the two standard measurement techniques which are applied, namely magnetic field-dependent and gate voltage-dependent measurements. In addition, it is shown how the characteristic parameters that determine the transport behavior of the devices can be deduced from these standard measurements. In particular, the determination of characteristic sample properties such as charge carrier density n and mobility μ is demonstrated. The knowledge of these parameters provide the basis for the further evaluation of the transport measurements described in the subsequent chapters.

2.2.1. Growth of HgTe-based samples and measurement-setup

A sketch of the complete layer stack of our devices is given in Fig. 2.10. The sample wafer is grown via molecular beam epitaxy (MBE). For this purpose, a substrate is planted in a high-vacuum chamber. In the framework of this thesis, the substrate materials are either solely CdTe or a combination of n-doped GaAs, a ZnTe interlayer, and CdTe. The doped GaAs functions as a gate-electrode sitting beneath the HgTe layer [42]. This allows a gate voltage to be applied to the back of the sample. For this reason, it is called back-gate (BG). The ZnTe interlayer is used to reduce the lattice mismatch between GaAs and CdTe and to avoid lattice relaxations. The CdTe, typically about 4 µm thick, is chosen due to its lattice constant, which applies a tensile strain on the mercury telluride layer that is later grown on top of it. The tensile strain is required to turn the semimetal HgTe into a 3D topological insulator (cf. Subsec. 2.1.1). Before the HgTe is grown, a $Cd_{0.7}Hg_{0.3}Te$ buffer layer is grown first. This buffer layer usually has a thickness between 30 nm and 100 nm and passes the strain unaltered to the layers above. Afterwards the elementary materials (Hg and Te) are vaporized and vapor-deposited onto the buffer layer. It is also possible to replace some Hg atoms with Mn atoms in order to create a paramagnetic doping ($Hg_{1-y}Mn_yTe$, with y being

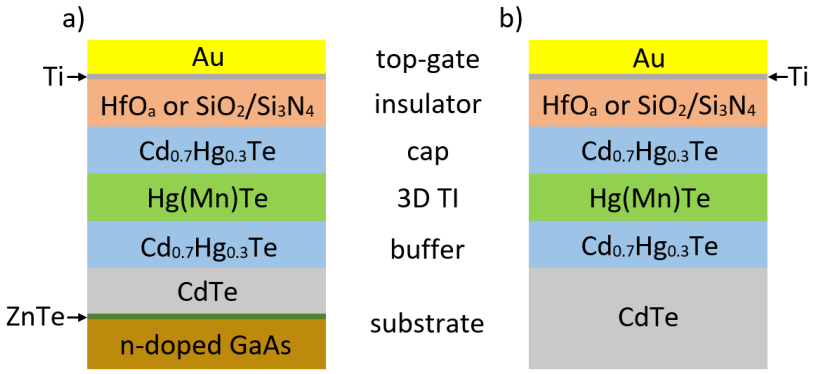

Figure 2.10.: Typical layer stacks of samples used in this thesis. The substrate material is either a) a combination of n-doped GaAs, a ZnTe interlayer, and CdTe or b) solely CdTe. In both cases, the layer stack consists of substrate, buffer, 3D TI, cap, insulator, and top-gate-electrode. Application of insulator and top-gate is done during lithography, while the rest of the layer stack is MBE grown. The layer thicknesses are not drawn to scale.

the manganese content). This special material system is discussed in chapter 5. The mercury telluride layer exhibits a thickness between 60 nm and 100 nm and represents the 3D topological insulator. For this reason, the HgTe layer is also called the active layer. It is worth mentioning that the thickness of the mercury telluride layer should not be much smaller than 60 nm, since otherwise the top and bottom surface states may interact, hybridize, and form a two-dimensional topological insulator. On the other hand, the thickness should not greatly exceed 100 nm, as otherwise, the HgTe layer relaxes and dislocation lines are formed. To protect the top surface from oxidation and other contaminations, another $Cd_{0.7}Hg_{0.3}Te$ layer (cap) is finally grown on top of the HgTe. The thickness of this layer typically is between 10 nm and 60 nm. Another advantage of the protective cap layer is that the mercury telluride layer now has a similar electrostatic potential at the top and the bottom. This leads to a symmetrization of the whole structure. Additionally, by growing a buffer and cap layer underneath and on top of the strained HgTe layer respectively, the overall quality of the mercury telluride layer and the charge carrier mobility in the system are increased [27]. A more detailed description of MBE growth and the vapor-deposition of individual layers can be found in Ref. [43].

The MBE grown wafers are then taken to a cleanroom, where the samples are processed into their final forms. During lithography, a sample piece can be structured in almost every desired design via physical and chemical treatment. In addition, top-gate-electrodes can be metallized onto the devices to vary the position of the Fermi energy E_F in the system. An insulation layer is deposited between the top-gate (TG) and the cap layer to electrically separate them from each other (cf. Fig. 2.10). Chap. 3 and Chap. 6 give a detailed description of the lithographic processing of the macrostructures and microstructures respectively.

The transport measurements have to be done at low temperatures in order to prevent optical phonons of the crystal lattice becoming relevant. Therefore, in the case of a mercury telluride heterostructure, the measurements must be carried out at temperatures of maximum 20 K [44]. In order to satisfy this condition, the measurements are performed either in a ^{4}He bath cryostat or in a ^{3}He/^{4}He dilution refrigerator. In the bath cryostat, one can achieve temperatures of around $T \approx 1.5\,\mathrm{K}$, while in the dilution refrigerator, temperatures of $T \approx 20\,\mathrm{mK}$ can be attained. Both systems are equipped with strong superconducting magnets capable of magnetic field strengths of up to $B = 14\,\mathrm{T}$ for the bath cryostat and $B = 16\,\mathrm{T}$ for the dilution refrigerator. In the framework of this thesis, some measurements also have been carried out in the *Laboratoire National des Champs Magnétiques Intenses* (LNCMI) in Grenoble, France. In this high magnetic field laboratory, magnetic fields of up to $B = 37\,\mathrm{T}$ can be reached.

The measurements are performed by applying a low-frequency AC-voltage excitation with constant amplitude. The resulting voltage drops between the contacts of the devices are measured with high impedance lock-in amplifiers. Small excitation voltages ($V_{\mathrm{exc}} \approx 200\,\mu\mathrm{V}$)

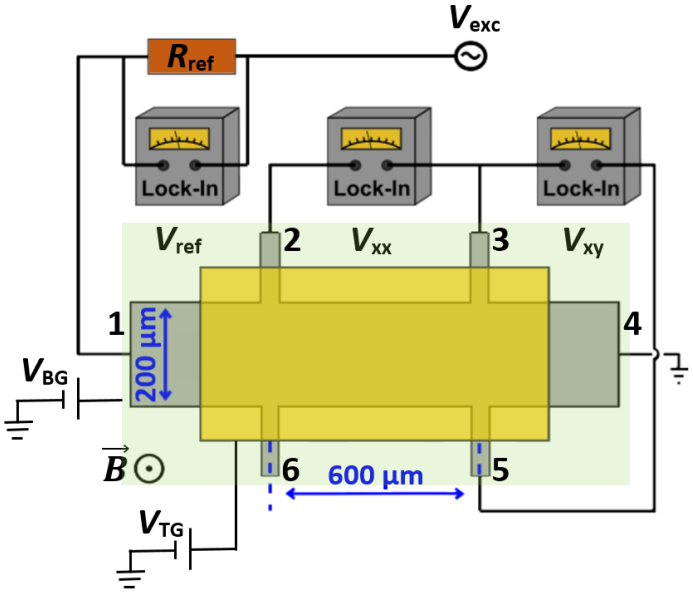

Figure 2.11.: A schematic of a 6-terminal Hall bar and the measurement-setup applied are shown. The six contacts of the Hall bar are numbered consecutively 1 to 6 in clockwise order. V_{exc} is the low-frequency excitation voltage, R_{ref} a well-defined reference resistor, V_{TG} the applied top-gate voltage, and V_{BG} the back-gate voltage. The TG is displayed in yellow and the BG in green. The measured voltages are the voltage drop over the reference resistor V_{ref}, the longitudinal voltage $V_{23} = V_{\mathrm{xx}}$, and the Hall voltage $V_{35} = V_{\mathrm{xy}}$. The size of the Hall bar is 600 x 200 $\mu\mathrm{m}^2$ and the whole structure is perpendicularly penetrated by a magnetic field $\vec{B}$.

are needed to stay in the linear response regime and to prevent the sample from heating.

Low excitation frequencies of $f_{\mathrm{exc}} = 17.73\,\mathrm{Hz}$ or $f_{\mathrm{exc}} = 37\,\mathrm{Hz}$ are used in order to ensure that the response of the investigated sample is only resistive. In general, the measured voltage is proportional to the impedance $Z = R + iX$, where R is the resistance, X the reactance, and i the imaginary unit. The reactance is due to the capacitance or inductance of the sample and is hence negligible for low frequencies. The current running through the device can be calculated using the voltage drop over a well-defined reference resistor with the help of Ohm's law $I = V_{\mathrm{ref}}/R_{\mathrm{ref}}$. The measured voltages V allow the resistances R of interest to be evaluated by the relation $R = V/I$. In order to characterize the samples, measurements are carried out on a Hall bar in the so-called four-point geometry. This geometry enables currentless voltage measurements and therefore resistance measurements utilizing lock-in amplifier techniques. A 6-terminal Hall bar design and the typical setup of a measurement in four-point geometry are sketched in Fig. 2.11. Using this configuration, the resistances of the contact leads have no influence on the measurement results, since no current runs through the voltage probes. The energetic position of the Fermi energy E_{F} can be controlled by applying a top-gate (V_{TG}) or back-gate voltage (V_{BG}) to the gate-electrodes located on top or bottom of the structure. This enables measurements with different charge carrier densities and types (electrons, holes) available in the system.

2.2.2. Magneto-transport measurements

In magneto-transport measurements, the magnetic field strength is increased constantly while the transverse and longitudinal voltages are recorded. The values of applied top-gate and back-gate voltages are constant during the measurements. These kind of measurements facilitate the determination of intrinsic sample properties like charge carrier density n and mobility μ. From the measurement results, one can determine which massless and massive surface states of the 3D HgTe-based TI samples are occupied and therefore contribute to transport. This knowledge is necessary in order to investigate the transport properties of surface states. The procedure is exemplified with magneto-transport measurements of sample QC0461 I. Details of this sample and wafer material QC0461 are given in Appx. A.1 and Appx. A.2, respectively. This sample has a slight manganese doping $\mathrm{Hg}_{1-y}\mathrm{Mn}_y\mathrm{Te}$, with $y = 0.011$. The possible influence of the Mn dopants is discussed in Ch. 5. The magneto-transport measurements of sample QC0461 I for applied top-gate voltages $V_{\mathrm{TG}} = 0\,\mathrm{V}$ and $V_{\mathrm{TG}} = -1\,\mathrm{V}$ are presented in Fig. 2.12a) and b) respectively. Both figures display the dependence of transverse resistance R_{xy} (in red) and longitudinal resistance R_{xx} (in black) as a function of the magnetic field B. It is noted that the back-gate was grounded during the measurements. The top-gate voltages were chosen in such a way that the electrons are the dominant carrier type with $V_{\mathrm{TG}} = 0\,\mathrm{V}$ and the holes the dominant carrier type with $V_{\mathrm{TG}} = -1\,\mathrm{V}$.

Examining the n-type transport first, one is able to observe that the Hall resistance R_{xy} forms a positive linear slope for small magnetic fields before quantum effects become visible

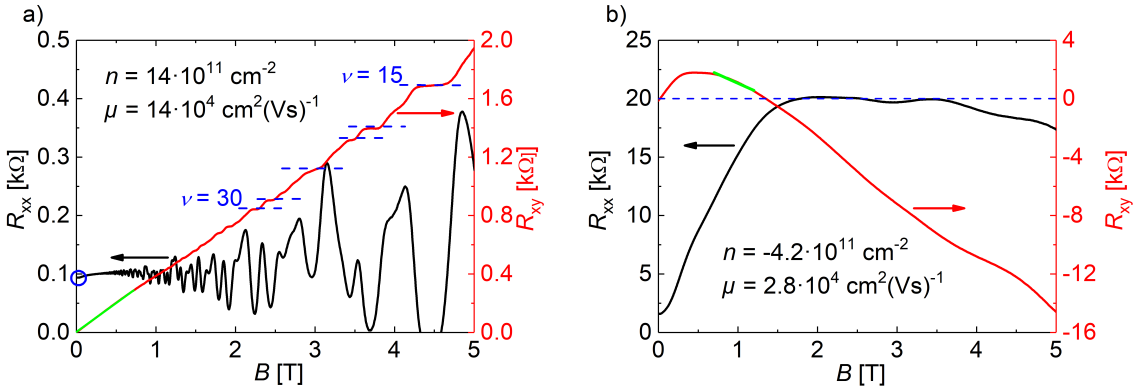

Figure 2.12.: Magneto-transport measurements of sample QC0461 I for a) $V_{\mathrm{TG}} = 0\,\mathrm{V}$ and b) $V_{\mathrm{TG}} = -1\,\mathrm{V}$ at $T \approx 100\,\mathrm{mK}$. The transverse resistance R_{xy} (in red) and longitudinal resistance R_{xx} (in black) are presented as a function of magnetic field B. In a), the linear slope of the semi-classical Hall regime for $B < 1\,\mathrm{T}$ and the value of the longitudinal resistance at zero field $R_{\mathrm{xx}}(B = 0\,\mathrm{T})$ are indicated by a straigh green line and a blue circle respectively. The expected QH plateau values for ν =15, 18, 19, 23, 28, 30 are delineated by dashed blue lines. In b), $R_{\mathrm{xy}} = 0$ is depicted via a dashed blue line. A sufficiently linear dependence on the magnetic field around 1 T used for the evaluation is marked by a straight green line.

for $B > 1.5\,\mathrm{T}$. This means that the transverse resistance develops quantum Hall plateaus, which are indicated by dashed blue lines. Not every plateau for each filling factor ν is visible. Missing quantum Hall plateaus imply the coexistence of at least two independent two-dimensional charge carrier systems, which are contributing to transport [9, 45]. Inferring from references [35] and [46], we assume that these systems are the TSSs of top and bottom surfaces and n-type massive states. Furthermore, only quantum Hall plateaus possessing large filling factors ν are depicted in Fig. 2.12a). This implies that the resistance values of the QH plateaus are very close to each other and hence it is difficult to resolve every single one in the measurement. The longitudinal resistance R_{xx} shows oscillations, which have minima if R_{xy} resides on a quantum Hall plateau and maxima if the transverse resistance performs a transition between two plateaus. These oscillations can be identified as Shubnikov-de Haas oscillations. Note that some minima of the SdH oscillations are non-zero. Each 2D charge carrier system involved in transport forms SdH oscillations, which develop their maxima and minima at different magnetic fields. If the oscillations are superimposed, then the minima can exhibit non-zero resistance values. Thus, the Hall resistance as well as the longitudinal resistance show the expected behavior described in Subsec. 2.1.3.

The semi-classical low magnetic field regime ($B < 1\,\mathrm{T}$) can be used to determine the charge carrier density n and mobility μ of the sample. It is worth mentioning that the mobility μ constitutes a good figure of merit for the quality of a device, since it is a measure for the

amount of impurities in the sample. The density n indicates how many charge carriers are present in the system. In addition, the influences of the top-gate and the back-gate on the mercury telluride layer can be investigated based on the changes in carrier density. In this thesis, electron densities are defined as positive, while hole densities are negative. To extract n and μ from magneto-transport measurements, the Drude model is used [36].

The resistivity $\rho(B)$ of a Hall bar in dependence of a magnetic field B can be written as

$$\rho = \begin{pmatrix} \rho_{\mathrm{xx}} & R_{\mathrm{xy}} \\ -R_{\mathrm{xy}} & \rho_{\mathrm{xx}} \end{pmatrix} = \begin{pmatrix} \frac{1}{\sigma_0} & \frac{B}{ne} \\ -\frac{B}{ne} & \frac{1}{\sigma_0} \end{pmatrix}, \tag{2.17}$$

where $\sigma_0 = \sigma_{\mathrm{xx}}(B = 0\,\mathrm{T}) = ne\mu$ represents the conductivity without magnetic field [36]. One can obtain from Eq. 2.17 that the semi-classical Hall resistance R_{xy} has to be:

$$R_{\mathrm{xy}} = \frac{1}{ne}B. \tag{2.18}$$

By fitting the linear slope of the transverse resistance R_{xy} in the semi-classical low magnetic field regime (cf. green line in Fig. 2.12a)) and using Eq. 2.18, the charge carrier density n can thus be determined. Putting in the numbers, we find the carrier density of sample QC0461 I to be $n = 14.1 \cdot 10^{11}\,\frac{1}{\mathrm{cm}^2}$ at $V_{\mathrm{TG}} = 0\,\mathrm{V}$.

The longitudinal resistivity at zero magnetic field $\rho_{\mathrm{xx}}(B = 0\,\mathrm{T})$ is also given by Eq. 2.17 and reads

$$\rho_{\mathrm{xx}}(B = 0\,\mathrm{T}) = \frac{1}{\sigma_0} = \frac{1}{ne\mu}. \tag{2.19}$$

The connection between the longitudinal resistivity ρ_{xx} and the longitudinal resistance R_{xx} is given by

$$R_{\mathrm{xx}} = \frac{l}{b} \cdot \rho_{\mathrm{xx}}, \tag{2.20}$$

where l/b is the ratio of sample length l to sample width b, also known as aspect ratio AR. For the Hall bar design presented in Fig. 2.11 this ratio is equal to three. However, other aspect ratios are possible for different sample designs. With the help of Eq. 2.19, Eq. 2.20, and the carrier density n, one can calculate the mobility μ of the system. The value of the longitudinal resistance at zero magnetic field is marked by a blue circle in Fig. 2.12a). Hence, we find the mobility to be $\mu = 14.2 \cdot 10^4\,\frac{\mathrm{cm}^2}{\mathrm{Vs}}$ at $V_{\mathrm{TG}} = 0\,\mathrm{V}$. The mobility not only contains information about the amount of scattering in the sample, but also about the band structure of the material itself. This is evident in the relaxation time approximation for the mobility given by:

$$\mu = \frac{e\tau}{m_{\mathrm{eff}}}, \tag{2.21}$$

with τ being the relaxation time. The effective mass m_{eff} is the renormalized mass accounting for the movement of a charge carrier through a crystal instead of vacuum and is given by the curvature of the respective band [35].

Another method for determining the charge carrier density is given by the analysis of the SdH oscillations. The inverse spacing of the Shubnikov-de Haas oscillation peaks $\Delta\,(1/B)$ can be used together with the definition of the filling factor ν (cf. Eq. 2.6) to identify the carrier density by

$$\Delta\left(\frac{1}{B}\right) = \frac{e}{h}\frac{g_\mathrm{s} g_\mathrm{v}}{n}. \tag{2.22}$$

If the longitudinal resistance R_{xx} is plotted against the inverse magnetic field instead of the magnetic field, one can use a mathematical tool such as fast Fourier transformation (FFT) and Eq. 2.22 to determine n. Ref. [35] expands on the FFT analysis technique regarding the usage of different FFT-windows and selected boundary conditions. The fast Fourier transformation analysis provides the densities of all charge carrier systems (n-type and p-type surface states, n-bulk states) contributing to transport, since each carrier system involved in transport develops SdH oscillations. The frequencies of the oscillations depend on the charge carrier densities of the respective massless and massive states. In contrast, the method of linear fitting of the Hall slope gives only the total density n_{tot} of the system, i.e. the combined density of all charge carrier systems involved in transport. In order to perform a meaningful FFT analysis, pronounced SdH oscillations are required. However, these only occur when a sufficient number of charge carriers are located in the massless and massive states and the sample possesses sufficient electron and hole mobilities. Therefore, the method of FFT analysis cannot always be applied (cf. e.g. Sec. 5.1).

To evaluate the magneto-transport measurement of sample QC0461 I at $V_{\mathrm{TG}} = 0\,\mathrm{V}$ using the fast Fourier transformation analysis, the longitudinal resistance R_{xx} has to be plotted as a function of inverse magnetic field B^{-1}. The measured data points in the experiment are equidistant in B. For the purpose of a distinct FFT, the data points should be equidistant in B^{-1}. For this reason, the R_{xx} data are linearly interpolated in B^{-1} to provide the necessary equidistant sampling points for the numerical FFT. The result is shown in Fig. 2.13a) for a magnetic field range of $0.25\,\mathrm{T} \leq B \leq 5\,\mathrm{T}$. The data points for $B < 0.25\,\mathrm{T}$ are removed from the evaluation, since in this regime the SdH oscillations are not resolved in the measurement. The fast Fourier transformation of this data gives a spectrum of the individual frequencies f_{FFT} of the Shubnikov-de Haas oscillations in B^{-1}. In this case, f_{FFT} has the unit of the magnetic field strength. For a more convenient presentation of the results, f_{FFT} can be transformed into the more intuitive charge carrier density n by means of $n = \frac{e}{h} f_{\mathrm{FFT}}$. The outcome of the FFT analysis as a function of n is presented in Fig. 2.13b). At this point, a remark is to be made: To be able to convert the x-axis of the fast Fourier transformation spectrum using $n = \frac{e}{h} f_{\mathrm{FFT}}$, non-degenerate bands have to be assumed. This implies that the valley and spin degeneracy are set $g_\mathrm{v} = g_\mathrm{s} = 1$. In the case of Hg(Mn)Te, all relevant bands are situated at the Γ point, which prevents any valley degeneracy, resulting in $g_\mathrm{v} = 1$. However, the value of the spin degeneracy g_s depends on the type of the underlying band. It can be either $g_\mathrm{s} = 1$ for the topological surface states or $g_\mathrm{s} = 2$ for the massive (Volkov-Pankratov and n-bulk)

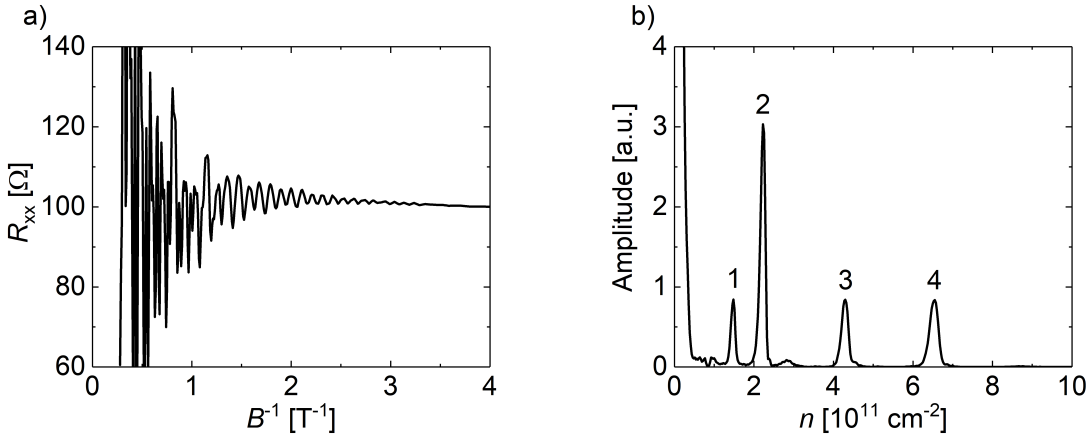

Figure 2.13.: a) The longitudinal resistance R_{xx} of sample QC0461 I at $V_{\mathrm{TG}} = 0\,\mathrm{V}$ is linearly interpolated to be equidistant in B^{-1} and plotted in dependence on inverse magnetic field B^{-1}. b) shows the fast Fourier transformation spectrum of the data from a) as a function of density n. The most pronounced peaks are numbered consecutively by 1, 2, 3, and 4.

states, if their spin degeneracy is not lifted. For the case of lifted spin degeneracy, $g_{\mathrm{s}} = 1$ also holds for the massive states. This means that one has to consider the degeneracy of the underlying band when determining the carrier density of a particular state using FFT analysis. If the underlying band is double degenerate the corresponding charge carrier density has to be doubled. The fast Fourier transformation spectrum of sample QC0461 I shows four pronounced peaks. According to Subsec. 2.1.2, we expect that these peaks represent the carrier densities originating from the TSSs (top, bottom) and either the n-type Volkov-Pankratov or n-bulk states with lifted spin degeneracy. The corresponding densities are $n_1 = 1.4 \cdot 10^{11}\,\frac{1}{\mathrm{cm}^2}$, $n_2 = 2.2 \cdot 10^{11}\,\frac{1}{\mathrm{cm}^2}$, $n_3 = 4.2 \cdot 10^{11}\,\frac{1}{\mathrm{cm}^2}$, and $n_4 = 6.4 \cdot 10^{11}\,\frac{1}{\mathrm{cm}^2}$, resulting in a total carrier density of $n_{\mathrm{tot}} = n_1 + n_2 + n_3 + n_4 = 14.2 \cdot 10^{11}\,\frac{1}{\mathrm{cm}^2}$. Additional higher order peaks with much smaller amplitudes are observed, for example at $n = 2.8 \cdot 10^{11}\,\frac{1}{\mathrm{cm}^2}$, which represents the second order peak of n_1. Using this total density and Eq. 2.19, we find the mobility to be $\mu = 14.1 \cdot 10^4\,\frac{\mathrm{cm}^2}{\mathrm{Vs}}$. The obtained results for total carrier density n_{tot} as well as mobility μ are in good agreement with the results obtained from the analysis of the Hall slope for small magnetic fields ($n = 14.1 \cdot 10^{11}\,\frac{1}{\mathrm{cm}^2}$, $\mu = 14.2 \cdot 10^4\,\frac{\mathrm{cm}^2}{\mathrm{Vs}}$), making both methods valid tools to characterize samples.

Next, the p-type transport is to be studied. Fig. 2.12b) displays the magneto-transport measurement of sample QC0461 I at $V_{\mathrm{TG}} = -1\,\mathrm{V}$ and $V_{\mathrm{BG}} = 0\,\mathrm{V}$. By altering the applied top-gate voltage, the energy position of the Fermi level in the system is changed, which may result in different charge carrier systems contributing to transport. When examining the transverse resistance (red curve in Fig. 2.12b), one is able to observe the distinct behavior of two different kinds of carriers, recognizable by the inversion of the Hall slope at low mag-

netic fields, $B < 2\,\mathrm{T}$. According to a two-band Drude model [47], the low field regime is dominated by highly mobile electrons. In this regime one can see a distinct n-type behavior up to $B \approx 0.5\,\mathrm{T}$, then p-type carriers are responsible for the formation of p-type quantum Hall states. Inferring from reference [48] and Subsec. 2.1.2, we assume that in the regime where we observe the p-type quantum Hall effect at high magnetic fields, three charge carrier systems are present in our samples: two n-type conducting topological surface states (top and bottom) and one (dominating) p-type massive Volkov-Pankratov state. The less-pronounced quantum Hall plateaus in p-type transport indicate the lower mobility of holes compared to electrons. For the same reason, the SdH oscillations of the longitudinal resistance (black curve in Fig. 2.12b)) are suppressed and it is difficult to identify resolved individual oscillations in the measurement. For this reason, the magneto-transport measurement at $V_{\mathrm{TG}} = -1\,\mathrm{V}$ cannot be evaluated using FFT analysis. In addition, it is also difficult to trace a linear slope in the R_{xy}-signal for small magnetic fields, since at $B \approx 0.5\,\mathrm{T}$ the dominant charge carrier type changes from electrons to holes and thus a reversal of slope occurs. For slightly larger magnetic fields (around 1 T), however, the Hall resistance exhibits a sufficient linear magnetic field dependence (cf. straight green line in Fig. 2.12b)), which in a good approximation represents the charge carrier density of the device. Using this slope and equations 2.18, 2.19, and 2.20, we are able to determine n and μ. For sample QC0461 I and $V_{\mathrm{TG}} = -1\,\mathrm{V}$, we find $n_{\mathrm{tot}} = -4.2 \cdot 10^{11}\,\frac{1}{\mathrm{cm}^2}$ and $\mu = 2.8 \cdot 10^4\,\frac{\mathrm{cm}^2}{\mathrm{Vs}}$.

Depending on applied top-gate voltage, different charge carrier systems can contribute to transport. This can be shown exemplarily based on fast Fourier transformation spectra of $R_{\mathrm{xx}}(B^{-1})$ for different TG voltages. The spectra of sample QC0461 I for $V_{\mathrm{TG}} = 0\,\mathrm{V}$, $V_{\mathrm{TG}} = -0.5\,\mathrm{V}$, and $V_{\mathrm{TG}} = -0.6\,\mathrm{V}$ are presented in Fig. a), b), and c), respectively. Fig. 2.14a) is a replot of Fig. 2.13b) to enable a direct comparison of all three FFT spectra. The BG was grounded for all measurements and the x-axes are transformed from frequency f_{FFT} into charge carrier density n assuming non-degenerate bands. First, the charge carrier densities obtained from the fast Fourier transformation spectra are to be compared to those deduced from the linear Hall slope $R_{\mathrm{xy}}(B)$ for small magnetic fields. For $V_{\mathrm{TG}} = 0\,\mathrm{V}$, this comparison has already been carried out above using Fig.2.13b) and Fig. 2.12a). Now, the FFT spectra from Fig. 2.14b) and c) ($V_{\mathrm{TG}} = -0.5\,\mathrm{V}$ and $V_{\mathrm{TG}} = -0.6\,\mathrm{V}$) are to be evaluated in the same way. For $V_{\mathrm{TG}} = -0.5\,\mathrm{V}$,

$$n_{\mathrm{tot,FFT}} = n_{1'} + n_{2'} + n_{3'} + n_{4'} = (0.5 + 0.9 + 1.4 + 2.3)\,\frac{1}{\mathrm{cm}^2} = 5.1\,\frac{1}{\mathrm{cm}^2}$$

and $n_{\mathrm{tot,Hall}} = 5.0\,\frac{1}{\mathrm{cm}^2}$. For $V_{\mathrm{TG}} = -0.6\,\mathrm{V}$, we find

$$n_{\mathrm{tot,FFT}} = n_{1''} + n_{2''} = (1.0 + 1.3)\,\frac{1}{\mathrm{cm}^2} = 2.3\,\frac{1}{\mathrm{cm}^2}$$

and $n_{\mathrm{tot,Hall}} = 2.4\,\frac{1}{\mathrm{cm}^2}$. Note that in determining $n_{\mathrm{tot,FFT}}$, it is assumed that all massless and

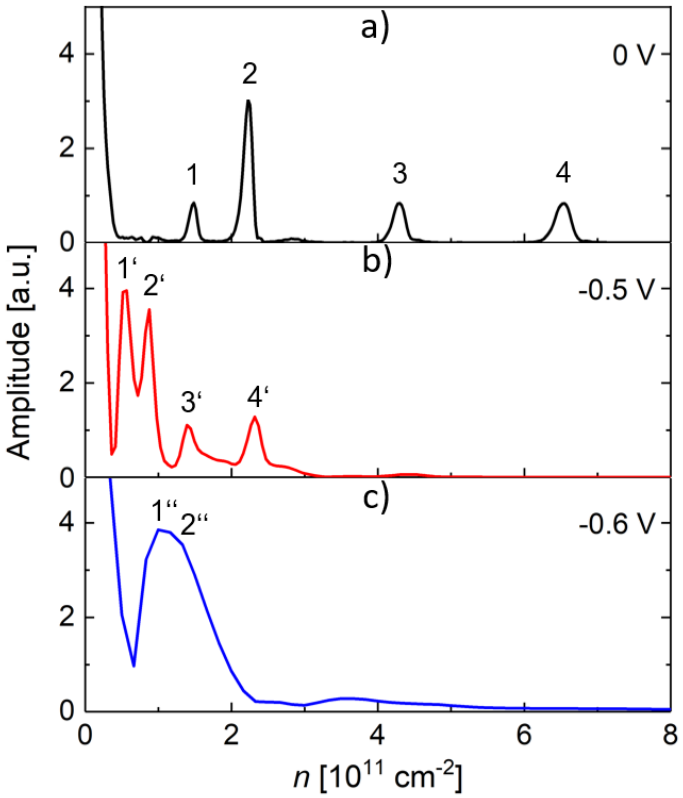

Figure 2.14.: The FFT spectra of $R_{xx}(B^{-1})$ for a) $V_{TG} = 0\,V$, b) $V_{TG} = -0.5\,V$, and c) $V_{TG} = -0.6\,V$ are shown in black, red, and blue respectively as function of charge carrier density n. The most pronounced peaks are numbered consecutively by a) 1, 2, 3, and 4, b) $1'$, $2'$, $3'$, and $4'$, and c) $1''$ and $2''$.

massive states involved in transport are n-type and non-degenerate. Overall, it can be stated that the charge carrier densities obtained from both methods are in good agreement. Second, the positions of the peaks change when applied TG voltage is altered. This implies that the number of charge carriers occupying the respective transport channels changes. By applying a negative top-gate voltage, the number of electrons populating the n-type massless and massive states is decreased. Below a certain top-gate voltage, some states are depopulated to the point that they no longer contribute to transport. This is the case for $V_{TG} = -0.6\,V$, at which only two peaks appear in the FFT spectrum. Since in our systems the topological surface states are always occupied by electrons within the experimentally accessible range of maximal and minimal achievable chemical potential (cf. Fig. 2.7), it is quite likely that the two TSSs (top, bottom) are the remaining transport channels. Note that for $V_{TG} = -0.6\,V$, the densities located at top and bottom surfaces are similar, wherefore the positions of the peaks in the fast Fourier transformation spectrum are very close to each other. This maintains to the double peak structure visible in Fig. 2.14c).

Given that we are able to tune the level of the Fermi energy E_F in the system via altering the applied top-gate or back-gate voltage, in the following subsection, TG-dependent and BG-

dependent measurements are investigated and analyzed. On the basis of these measurements one can determine, for instance, the level of Fermi energy E_F, at which the transition from n-type to p-type dominated transport occurs.

2.2.3. Gate voltage-dependent measurements

The general functionalities of top-gate and back-gate are shown in Fig. 2.15a) and b), respectively. The longitudinal resistances R_{xx} are presented as a function of top-gate V_{TG} and back-gate voltage V_{BG} for $B = 0\,\mathrm{T}$. Note that in each case the other gate voltage is set to zero. The

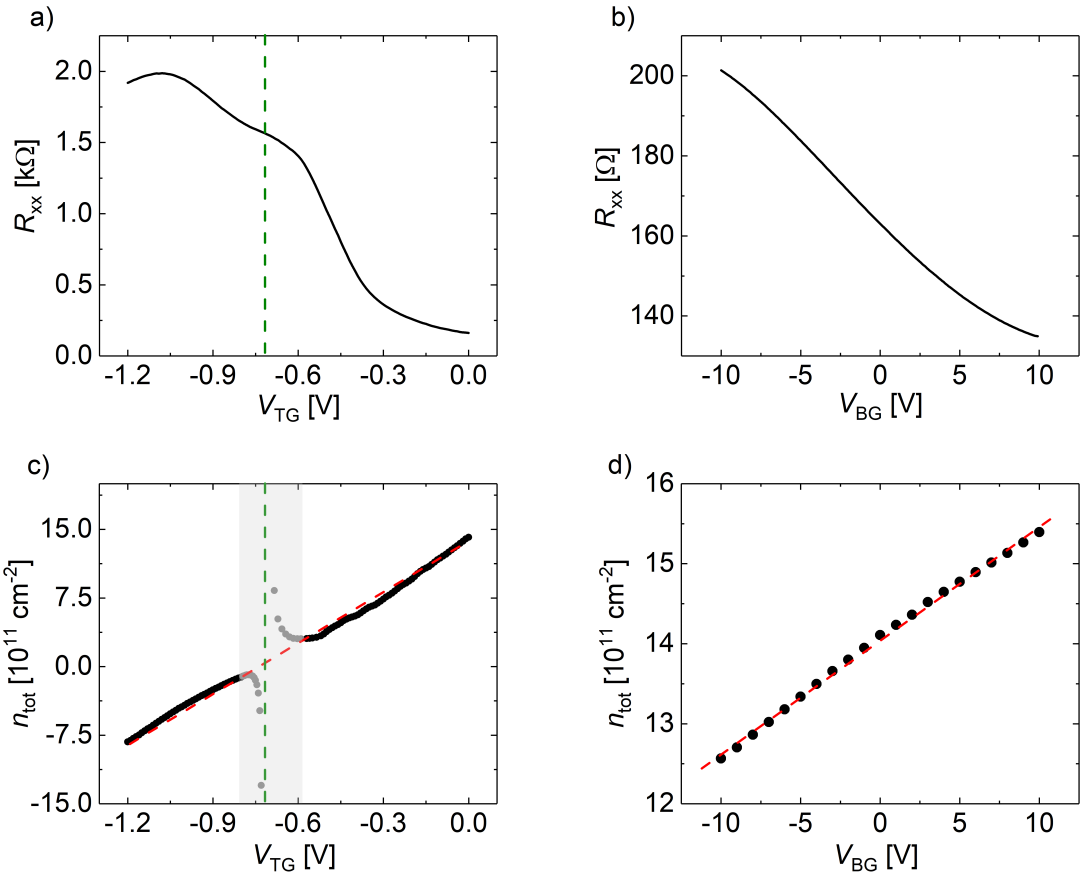

Figure 2.15.: The longitudinal resistance R_{xx} is presented for $B = 0\,\mathrm{T}$ as a function of a) top-gate voltage V_{TG} and b) back-gate voltage V_{BG} at $T \approx 100\,\mathrm{mK}$. In a), the expected value of V_{TG} for zero total density is depicted by a dashed olive line. The change in carrier density depending on applied TG and BG voltage is displayed in c) and d) respectively. Black circles represent the voltage values at which n_{tot} was determined. The non-analyzable top-gate range is marked in gray and the corresponding data points are drawn as gray circles. The dashed red lines indicate linear fits to determine the gate actions G_{TG} and G_{BG} of TG and BG respectively. In c), the top-gate voltage for zero total density estimated by the linear fit is shown as a dashed olive line.

applied TG voltage can vary the value of R_{xx} from $R_{xx}(V_{TG} = 0\,V) \approx 160\,\Omega$ to a maximum of $R_{xx}(V_{TG} = -1.08\,V) \approx 2.0\,k\Omega$ before it drops again to $R_{xx}(V_{TG} = -1.2\,V) \approx 1.9\,k\Omega$. However, the applied BG voltage only alters R_{xx} in a range between $R_{xx}(V_{BG} = 10\,V) \approx 130\,\Omega$ and $R_{xx}(V_{BG} = -10\,V) \approx 200\,\Omega$. The influence of the back-gate on the topological and massive states is therefore much smaller than the one of the top-gate. This corresponds to our sample structure: For sample QC0461 I, the spatial distance between active layer ($Hg_{1-y}Mn_yTe$) and top-gate is around 30 nm. The distance between active layer and back-gate though is roughly 4 µm (cf. Subsec. 2.2.1). A positive top-gate or back-gate voltage increases the number of electrons in the n-type massless and massive states contributing to transport. These additional carriers lead to a decrease in longitudinal resistance. By applying a more and more negative TG or BG voltage, the number of electrons in the transport channels is reduced, resulting in a growing R_{xx}. For the special case of the top-gate, when the applied negative voltage reaches a certain value, holes are introduced into the system and p-type Volkov-Pankratov states become populated. This is the case at $V_{TG} = -0.65\,V$, where a shoulder is visible in the R_{xx}-signal. At a slightly higher negative top-gate voltage, the number of electrons is equal to the number of holes. At this gate voltage, a transition happens and holes become the dominant carrier type. Henceforth, the transport is dominated by p-type massive Volkov-Pankratov states. In case of sample QC0461 I, this transition from n-type to p-type conductance occurs at $V_{TG} = -0.73\,V$ as indicated by a dashed olive line in Fig. 2.15a). It is notable that the transition point is not aligned with the maximum of R_{xx}. A possible explanation may be given by the different mobilities of electrons and holes. While the electrons are highly mobile, the mobility of the holes is rather small. By increasing the applied negative top-gate voltage, the number of highly mobile electrons decreases whereas the density of inert holes increases. This may cause a shift of the minimum of the longitudinal conductivity σ_{xx}, equivalent to a shift of the maximum of the longitudinal resistance R_{xx}, towards higher negative gate voltages. By increasing the applied negative top-gate voltage even further, the amount of holes in the system is also enhanced more and more, which at some point leads to a decreasing R_{xx} again. This behavior can be observed in Fig. 2.15a) for $V_{TG} < -1.08\,V$.

These changes in longitudinal resistances occur with varying total charge carrier densities from $n_{tot}(V_{TG} = 0\,V) = 14.1 \cdot 10^{11}\,\frac{1}{cm^2}$ to $n_{tot}(V_{TG} = -1.2\,V) = -8.3 \cdot 10^{11}\,\frac{1}{cm^2}$ for the TG and from $n_{tot}(V_{BG} = 10\,V) = 15.4 \cdot 10^{11}\,\frac{1}{cm^2}$ to $n_{tot}(V_{BG} = -10\,V) = 12.6 \cdot 10^{11}\,\frac{1}{cm^2}$ for the BG as shown in Fig. 2.15c) and d), respectively. For each gate voltage indicated by a black circle, the total carrier density n_{tot} was determined by a linear fit of the semi-classical Hall regime for small magnetic fields ($0\,T < B \leq 1.2\,T$) as described in Subsec. 2.2.2. At a certain value of top-gate voltage, holes become the dominant carrier type in the system and the Hall resistance R_{xy} has to change its sign from positive to negative. This means that in the case of a continuous top-gate voltage-dependent measurement R_{xy} performs a zero-crossing. For this reason, it seems like that the absolute value of total density $|n_{tot}|$ increases

enormously around this transition point $V_{\mathrm{TG}} = -0.73\,\mathrm{V}$, which is indicated by a dashed olive line. However, this is only an artifact of the used evaluation method (cf. Eq. 2.18). The non-analyzable top-gate voltage range of $-0.81\,\mathrm{V} < V_{\mathrm{TG}} < -0.59\,\mathrm{V}$ is marked as a gray area in Fig. 2.15c) and the corresponding data points are shown as gray instead of black circles.

The calculated densities allow the influence of the gates defined as $G_{\mathrm{TG}} = \Delta n_{\mathrm{tot}}/\Delta V_{\mathrm{TG}}$ for the top-gate and $G_{\mathrm{BG}} = \Delta n_{\mathrm{tot}}/\Delta V_{\mathrm{BG}}$ for the back-gate to be determined by using a linear fit. The linear fit is plotted in Fig. 2.15c) and d) as a dashed red line. It is noted that the top-gate voltages within the gray area are excluded from the fit. The obtained gate actions are $G_{\mathrm{TG}} = 18.6 \cdot 10^{11}\,\frac{1}{\mathrm{Vcm^2}}$ and $G_{\mathrm{BG}} = 0.14 \cdot 10^{11}\,\frac{1}{\mathrm{Vcm^2}}$ for TG and BG respectively. The linear fit in Fig. 2.15c) gives $V_{\mathrm{TG}} = -0.74\,\mathrm{V}$ for the charge neutrality point, which is in good agreement with the experimental observation ($V_{\mathrm{TG}} = -0.73\,\mathrm{V}$). The ratio of top-gate to back-gate efficiency $F_{\mathrm{gate}} = G_{\mathrm{TG}}/G_{\mathrm{BG}} = 132.9$ is almost identical to the factor of the inverse spatial distances of TG and BG from the active layer $F_{\mathrm{distance}} = 4\,\mu\mathrm{m}/30\,\mathrm{nm} = 133.3$. This strengthens the assumption that the different gate actions are predetermined by the diverse spatial arrangements of top-gate and back-gate.

In addition, we assume that the TG mainly influences the massless and massive states located at the top surface, while the BG only affects the topological surface states located at the bottom surface[7]. This assumption is based on the idea that the carriers located at top surface screen the electrostatic potential of the top-gate and therefore the charge carriers at the bottom surface only perceive a negligible change in potential when the TG voltage is altered. In the same manner, the carriers located at the bottom surface screen the electrostatic potential of the back-gate. This phenomenon is called Dirac-screening and is discussed in detail in Ref. [45].

2.3. Shortcomings in the state of the art of lithography of 3D HgTe-based devices revealed by transport measurements

Besides the theoretical knowledge about massless and massive surface states gained in the previous sections and the introduction of the standard measurement techniques, the fabrication of three-dimensional HgTe-based topological insulator samples represents another important cornerstone for the investigation of the transport properties. The MBE grown wafer has to be structured into the desired design through physical and chemical treatment. While the lithography of samples should meet the structural and experimental specifications as precisely as possible, the lithographic processing should change the intrinsic characteristics and properties of wafer materials in the least possible way. Only a predictable, reproducible, and well performing lithography can lead to devices which are able to contribute to the understanding of the material system Hg(Mn)Te in such a way as to enable the development

[7] The massive states at the bottom surface are not accessible in the experiment due to the small gate action of the back-gate (cf. Fig. 2.7).

of potential future applications. In order to achieve this goal, each individual fabrication step, like etching of the sample structure and metallization of certain sample areas, has to be optimized. In the past decade, great progress has been achieved in improving the lithography of Hg(Mn)Te samples. This holds especially for two-dimensional mercury telluride structures [14]. For the 3D case, however, the lithography has not yet been optimized and there is still potential for improvement.

The state of the art of lithography in our group starts from the standard recipe for the fabrication of macroscopic Hg(Mn)Te devices, the so-called *old 6-terminal standard recipe* (cf. Appx. B.1). It is emphasized that this standard recipe has now been replaced by a new one based on the knowledge gained in this thesis. The lithographic details and techniques of the *old 6-terminal standard recipe* are precisely described in chapter 3. Here only a brief overview is given. The recipe consists basically of three major steps:

- **Definition of the mesa:** In this step, the mesa of the sample is defined by etching off all wafer material around the desired mesa structure (cf. Fig. 2.16a)).
- **Insulator and top-gate application**: A gate insulator is applied on top of the mesa before the top-gate-electrode consisting of a titanium (Ti) sticking and a gold (Au) layer is metallized. The insulator acts as an additional dielectric layer between gate metals and Hg(Mn)Te layer (cf. Fig. 2.16b)).
- **Metallization of contact areas:** The contact areas of the sample are shortly etched to improve the metal-semiconductor contact and afterwards a gold germanium (AuGe) and a gold layer are subsequently applied on top (cf. Fig. 2.16c)).

Finally, the sample is glued into a chip-carrier so that it can be mounted in the measurement-setup. There are two types of glue for this purpose. The first type is the non-conductive *GE Varnish*, which has the advantage of drying quickly (approximately 10 h) and can be used directly from the storage vessel. The second type is a conductive silver glue, which has to be prepared from the components *EPO-TEK E4110-KIT 1 OZ Part A* and *EPO-TEK E4110-KIT 1 OZ Part B* in the ratio of 10:1. This glue is used for samples with back-gate, as its conductivity enables contacting the back-gate-electrode. However, due to the high liquid content, about 48 h are required for drying. The electrical connection between chip-carrier and sample is usually achieved via wedge-wedge bonding with a gold wire.

Sample QC0461 I was fabricated using the *old 6-terminal standard recipe* with one minor variance: It has a hafnium oxide (HfO_a[8]) gate-dielectric instead of an insulator consisting

[8]The atomic layer deposition of hafnium and oxide is performed at a temperature of $T = 303\,\mathrm{K}$. At this temperature, Hf can have an oxidation number of +2 or +4. Along with the oxidation number of oxygen (-2), HfO or HfO_2 can be formed during the deposition process. Until now, the exact chemical compound that is formed in our ALD-machine has not yet been investigated. Therefore, in the following, hafnium oxide is written with the index a, with a = 1 or 2.

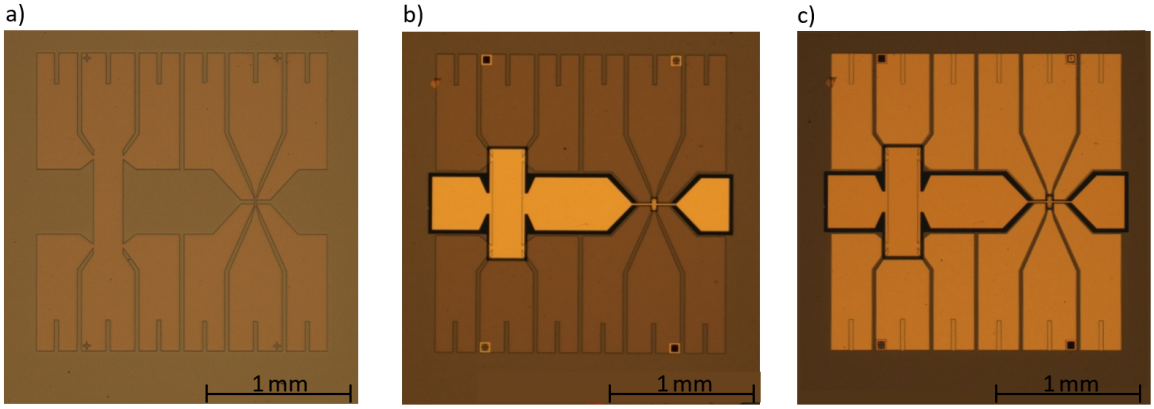

Figure 2.16.: The three major lithography steps for macroscopic sample fabrication. The steps are: a) definition of the mesa, b) insulator and top-gate application, and c) metallization of contact areas. In a), the defined 2 x 2 mm^2 mesa (light brown) can be distinguished from the etched substrate (khaki brown) by its color difference. The mesa design consists of two 6-terminal Hall bars of different size. Their dimensions are 600 x 200 μm^2 and 30 x 10 μm^2. In b), the top-gate-electrode is recognizable by its golden color. The insulator is visible as the black layer underneath the top-gate. In c), the contact areas are metallized with 50 nm AuGe and 50 nm Au.

of a silicon oxide/silicon nitride (SiO_2/Si_3N_4) superlattice. Fig. 2.17a) shows the same measurement as in Fig. 2.12a) up to a higher magnetic field B (16 T). This measurement shows two peculiarities, which are described below:

First, the longitudinal R_{xx} (in black) as well as the transverse resistance R_{xy} (in red) deviate strongly from the expectation for magnetic fields $B > 5\,T$. R_{xx} takes negative values and the Shubnikov-de Haas oscillations are noisy and deformed. The Hall resistance exhibits noisy and suppressed plateaus in the range $5\,T < B < 8\,T$ and starts to rise at $B \approx 8\,T$ reaching resistance values larger than 70 kΩ. Even more striking, for magnetic fields $B > 12\,T$, both magnetoresistance signals unexpectedly fluctuate in the $\pm 10^2$ kΩ-range. Fluctuations having such a large amplitude and showing both positive as well as negative values indicate a vanishingly small current flowing through the sample. Fig. 2.17b) presents the raw data of this measurement. Longitudinal voltage V_{xx} (in black), transverse voltage V_{xy} (in red) as well as the current I passing through the device (in blue) are displayed. As the magnetic field increases, the current approaches zero. For $B > 12\,T$, the current through the device is hardly measurable. This observation coincides well with the observed strong fluctuations in this magnetic field regime. Such low currents indicate that certain parts of the sample exhibit an insulating character under the given conditions ($B > 12\,T$ and $T \approx 100\,mK$).
The second peculiarity of this measurement is not immediately recognizable. However, if we determine the charge carrier density of sample QC0461 I for $V_{TG} = V_{BG} = 0\,V$, we obtain $n \approx 14 \cdot 10^{11}\,\frac{1}{cm^2}$. This value is remarkable, as the wafer QC0461 was grown without the intention of doping. Undoped HgTe-based samples grown in our MBE typically possess

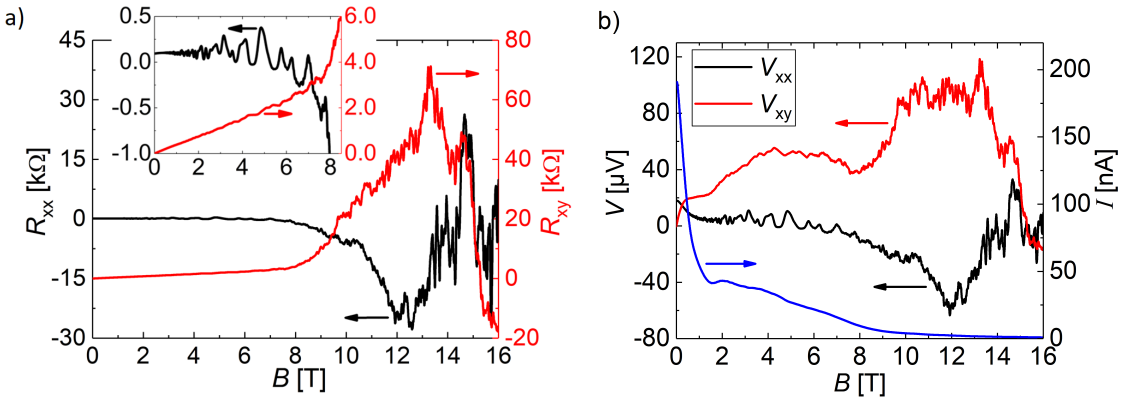

Figure 2.17.: a) Magneto-transport measurement of sample QC0461 I at $V_{TG} = V_{BG} = 0\,V$ and $T \approx 100\,mK$. Longitudinal resistance R_{xx} and transverse resistance R_{xy} are shown in dependence of magnetic field B and displayed in black and red respectively. The inset depicts R_{xx} and R_{xy} in higher magnification for $B \leq 8.5\,T$ and uses identical axis labels. b) presents the raw data of this measurement. The current I passing through the sample is plotted in blue, while longitudinal voltage V_{xx} and Hall voltage V_{xy} are depicted in black and red respectively.

charge carrier densities in the range of $|n| < 3 \cdot 10^{11}\,\frac{1}{cm^2}$, which is several times smaller than the density determined in the experiment. Since no gate voltage was applied to the sample during measurement and the carrier density of the device was therefore not manipulated, it is reasonable to assume that at least one of the lithographic processing steps causes n-type doping of the material system Hg(Mn)Te.

High n-type densities in the samples at $V_{TG} = V_{BG} = 0\,V$ complicate the experimental accessibility of the p-type surface states. Strong unexpected magnetoresistance fluctuations occurring at high magnetic fields make it impossible to evaluate the transport in the high field regime in a meaningful way. Therefore, before the transport properties of surface states of 3D Hg(Mn)Te devices can be studied and thus a deeper understanding of the material system can be obtained, these two phenomena have to be examined and explained first. In order to find the origin of the n-type doping and to be able to suggest possible solutions, the lithographic processing steps of the *old 6-terminal standard recipe* will be systematically investigated and revised. This is the topic of Chap. 3.

3. Unintentional increase of the n-type carrier density induced by lithographic processing

As shown in the previous chapter, the lithography of three-dimensional HgTe-based samples still exhibits shortcomings. Before the transport properties of our devices can be studied in the most effective manner, the lithographic processing has to be optimized and its possible consequences for the material system Hg(Mn)Te have to be understood first. One of the observed phenomena is an unexpectedly high n-type charge carrier density of the devices, which occurs without manipulating the level of the Fermi energy via the dual-gate configuration ($V_{\mathrm{TG}} = V_{\mathrm{BG}} = 0\,\mathrm{V}$). The high electron densities complicate the experimental accessibility of the p-type surface states and may thus affect the investigability of the transport properties of these states. For this reason, this phenomenon is to be studied.

Since the wafer materials are grown without any in situ doping, it is reasonable to assume that the n-type doping happens during lithographic processing. To verify this assumption, each individual fabrication step of the samples is scrutinized (Sec. 3.1). Based on the in-depth consideration of the lithographic processing of macroscopic 3D HgTe-based devices, many improvements for fabrication have been introduced. A listing of these improvements is given in Sec. 3.2. The last section (Sec. 3.3) of this chapter deals with the explanation of the lithography-induced increase of the electron density.

3.1. Examination of the lithographic processing of HgTe-based macrostructures to identify the doping-causing fabrication step

The recipe in question is the *old 6-terminal standard recipe* (cf. Appx. B.1). The starting point of the investigation is an untreated sample piece. The charge carrier density of this sample piece gives the density of the MBE grown wafer and is the benchmark of all subsequent analysis. The measurement method used for this was invented by Leo J. van der Pauw [49] and is topic of Subsec. 3.1.1. Each of the following subsections deals with the examination of devices which are fabricated up to a certain lithography step and measured subsequently in order to determine their densities. These steps are (i) definition of the mesa structure via

etching, (ii) fabrication of the ohmic contacts, and (iii) application of gate-dielectric and top-gate-electrode, and are described in detail in Subsec. 3.1.2, Subsec. 3.1.3, and Subsec. 3.1.4, respectively. It is noted that here, compared to the *old 6-terminal standard recipe*, steps (ii) and (iii) are presented in reverse order. The reason for this is that for some specific samples, due to their special designs, the ohmics have to be processed prior to the application of gate insulator and top-gate metals. By comparing the charge carrier densities of the wafer material and those of the samples at the various stages, the doping-causing lithography step can be identified. In addition, this procedure allows the magnitude of doping to be specified. Three different wafers QC0438, QC0478, and QC0479 were used in order to obtain enough data for the evaluation. Details of the wafer materials, such as their layer stacks, can be found in Appx. A.2.

Optical lithography is used to fabricate macroscopic structures measuring a few hundred micrometers in size. For the optical lithography, two types of photoresist are available, namely negative and positive. Our group uses the negative photoresist denoted by *ARN 4340* and the positive resist denoted by *ECI 3012*. The usage of both types of photoresist is presented in the following:

Negative resist: This resist consists of short molecule chains, which cross link under illumination and by applying heat. First, a drop of negative resist has to be spin-coated homogeneously across the sample surface. The spin-coating is done at 6000 rpm for 20 s. Afterwards, the resist is baked at 80 °C for 2 min to evaporate the solvent. The sample covered with negative resist is put in a mask-aligner. A thin layer of chromium manufactured on a glass plate represents the desired structures, which are supposed to be transferred onto the sample. This plate is put in between the sample and a mercury vapor lamp ($\lambda = 310$ nm to 440 nm). Only the uncovered parts of the glass are transparent, keeping the resist directly below the chromium unaffected. After a 20 s exposure ($P = 8$ W), the sample receives a post exposure baking (PEB) for 6 min at 80 °C. Throughout the PEB the exposure-activated short polymer chains are cross linked. The resist at the non-exposed areas beneath the chromium is then stripped during the 40 s development in *AR 300-47*, while the resist at previously exposed areas remains. Now, the negative resist is a negative image of the structure on the mask.

Positive resist: This resist consists of long molecule chains, which decay under illumination and can then be resolved by a proper developer, usually based on tetramethylammonium hydroxid. Again, the first process step is to spin-coat a drop of positive resist across the sample surface at 6000 rpm for 20 s. In addition, the subsequent baking at 80 °C for 2 min remains the same. The difference between positive and negative resist takes place in the mask-aligner and throughout development. The long polymer chains decay during the 7 s exposure ($P = 8$ W). The resist at the exposed areas is then stripped during the 22 s development in *AZ 726 MIF*. Resist at non-exposed areas remains. Note that for positive

resist no PEB is needed. At the end, the positive resist is a positive image of the structure on the mask.

If we assume that both photoresists are mechanically and chemically stable, anything done to the sample surface only affects the non-covered parts. After dissolving the remaining resist, the formerly covered parts of the sample are unaffected. The dissolving happens for both resist types chemically with acetone.

3.1.1. Van der Pauw method

First, untreated samples are investigated with the help of the van der Pauw (vdP) method. In order to use the vdP method, 3 x 3 mm^2 sample pieces have to be separated from the wafer materials, glued into chip-carriers with non-conductive glue (*GE Varnish*), and bonded with indium lumps and gold wires. By placing one bond in each of the corners, we obtain devices with four contacts. An example of such a sample can be seen in Fig. 3.1. In this figure, the contacts are numbered consecutively counter-clockwise by 1, 2, 3, and 4. Care should be taken to ensure that the shape of the sample piece is as close to a square as possible to increase the accuracy of the van der Pauw method. In addition, the indium dots used for attaching the Au wires should be as small as feasible and they should be positioned right in the corners of the quadratic sample piece. In reality, however, this goal can only be achieved to a limited extent, since the bonding procedure involves thermal heating and hardening of Indium, which is difficult to control.

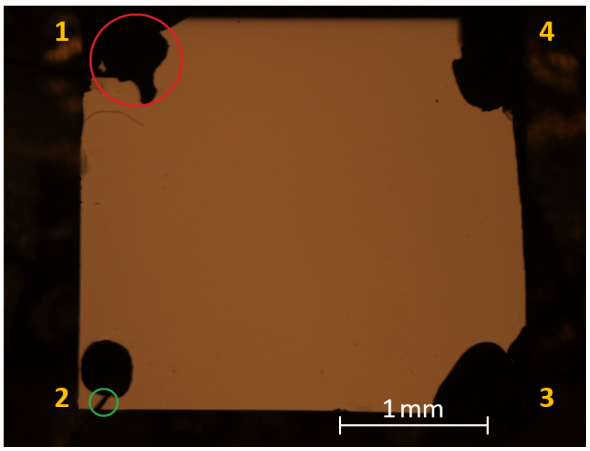

Figure 3.1.: Sample fabricated to determine the density n of wafer material QC0478 using the van der Pauw method. The quadratic sample is silhouetted in brown against the dark background. Indium lumps can be spotted at each of the four corners as black dots, with one of them marked by a red circle. An example of an Au wire, which connects the sample to the chip-carrier, is marked by a green circle. The corners are numbered consecutively counter-clockwise by 1, 2, 3, and 4.

To determine the charge carrier density n of samples using the van der Pauw method, two sets of measurements have to be carried out: one with a perpendicular magnetic field pointing

wafer	density n [$10^{11}\,\frac{1}{\mathrm{cm}^2}$]
QC0438	2.8
QC0478	2.6
QC0479	2.6

Table 3.1.: Charge carrier densities n determined using the vdP method for samples of wafer materials QC0438, QC0478, and QC0479.

in positive z-direction ($+B$) and one with a magnetic field of the same strength pointing in negative z-direction ($-B$). For each measurement, one has to send a current from one contact to another and measure the resulting voltage difference between the remaining two contacts. Both contact pairs should be arranged diagonally across the sample. By using the numbering of the contacts introduced in Fig. 3.1, one can, for instance, send a current from contact 1 to 3 (I_{13}) and measure the voltage difference between 2 and 4 ($V_{24} = V_2 - V_4$). This represents one possible measurement configuration. In order to increase the accuracy of the vdP method more configurations can be measured. For this thesis, four configurations are used for each magnetic field direction to calculate the carrier density n. These configurations are (I_{24},V_{31}), (I_{31},V_{42}), (I_{42},V_{13}), and (I_{13},V_{24}). Note that the absolute value of the current should be the same for all measurements. By doing so, $|I_{13}| = |I_{24}| = |I_{31}| = |I_{42}| \equiv I$ holds. The voltage differences V_{ij}, with ij being 13, 24, 31, or 42, have to be measured twice, once for $+B$ and once for $-B$. Then, the difference between these voltage differences for opposite magnetic field directions is calculated using the relation $\Delta V_{ij} = V_{ij}(+B) - V_{ij}(-B)$. The charge carrier density n is finally determined by

$$n = -\frac{8}{\sum \Delta V_{ij}} \frac{IB}{e}. \tag{3.1}$$

One should note that the sign of $\sum \Delta V_{ij}$ indicates the dominant carrier type in the system. If $\sum \Delta V_{ij} < 0$, the material is n-type, while positive values imply p-type conductance [49, 50].

Untreated samples of wafer materials QC0438, QC0478 and, QC0479 are investigated according to the van der Pauw method and Eq. 3.1. These wafers were grown without the intention of doping, i.e. they should possess carrier densities of the order of $|n| < 3 \cdot 10^{11}\,\frac{1}{\mathrm{cm}^2}$. The results are summarized in Tab. 3.1. One finds that the charge carrier densities of all samples are below $3 \cdot 10^{11}\,\frac{1}{\mathrm{cm}^2}$, which is within the expected range for undoped wafers. For this reason, as already assumed, the increase in n-type density has to happen during the lithographic processing of samples.

3.1.2. Definition of the mesa structure via etching

The first step of the sample fabrication process is the definition of the mesa. Most mesas are shaped as Hall bars, as this design facilitates the determination of sample properties of interest such as charge carrier density n and mobility μ. However, in principle, arbitrary

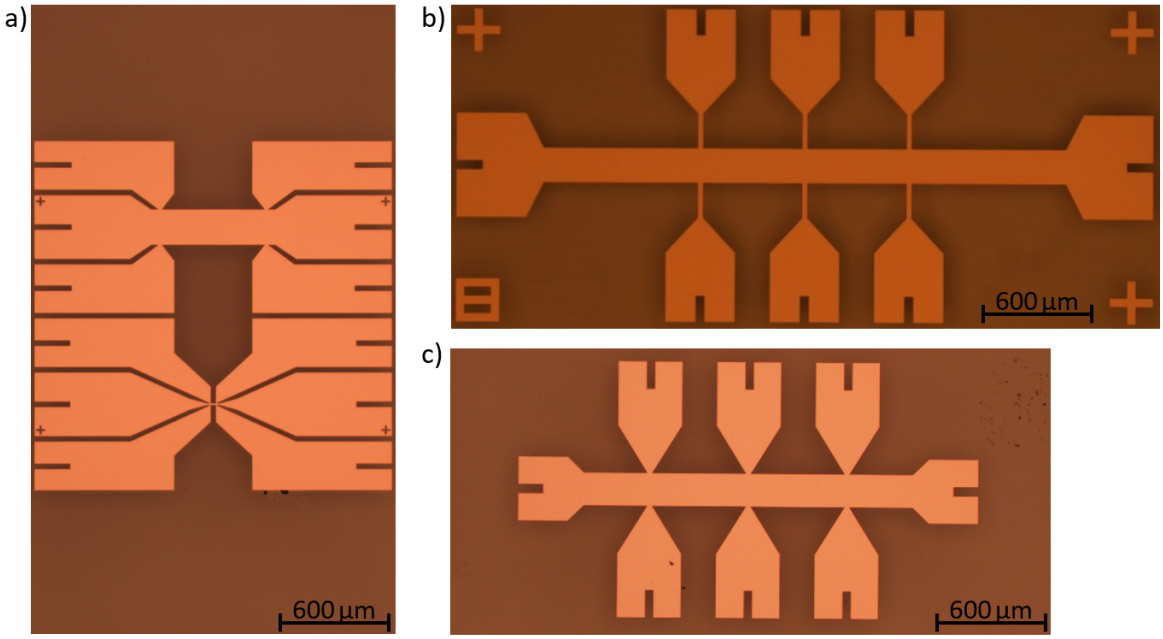

Figure 3.2.: Comparison of three different masks for Hall bar fabrication. The Hall bar design of the *old 6-terminal standard recipe* is shown in a), while b) displays an older 8-terminal design. In c), the novel 8-terminal Hall bar design is presented. Instead of two Hall bars of different sizes (600 x 200 µm^2 and 30 x 10 µm^2) next to each other, the old and novel 8-terminal designs consist of two equally sized Hall bars (600 x 200 µm^2 and 540 x 180 µm^2 respectively) in series.

device designs can be realized. For the evaluations of this chapter, we choose the Hall bar design. Since we have to bond the samples with indium lumps and gold wires, as described in Subsec. 3.1.1, the standard 2 x 2 mm^2 Hall bar design of the *old 6-terminal standard recipe* cannot be used. The reason for this is given by the extent of an indium lump used for bonding. The diameter of such a lump is approximately 300 µm to 500 µm (cf. Fig. 3.1). However, the width of a contact pad of the standard Hall bar design is only about 300 µm and the distance between two adjacent pads is 30 µm (cf. Fig. 3.2a)). Hence, the indium lumps would short cut the contacts of the sample. Instead, an older 8-terminal Hall bar design that is shown in Fig. 3.2b) is used. This design consists of two equally sized Hall bars (600 x 200 µm^2) in series. The contact pads have a diameter of 400 µm and the distance to an adjacent one is 200 µm, which allows for indium bonding. Another advantage of the design is the Hall bar duplication. Thus, the homogeneity of the sample piece can be determined by comparing the charge carrier densities and mobilities of both Hall bar structures. On the other hand, the dimensions of the 8-terminal design are larger (4 x 1.8 mm^2), which implies that less samples can be fabricated of a given wafer. For this reason, and based on the experience gained from the investigations of this section, a novel 8-terminal Hall bar design has been developed (cf. Sec. 3.2). The novel design retains all advantages of the old 8-terminal design, however, it is reduced in size (2.5 x 1.4 mm^2). This is presented in Fig. 3.2c).

To obtain the desired mesa structure the sample material around the design has to be removed at a certain height. The height of the mesa is determined by the thickness of the layer stack buffer/active layer/cap, which typically is less than 200 nm for our 3D TI Hg(Mn)Te samples. The removal of material is achieved via etching. All samples presented in this thesis are etched down to the substrate, i.e. the samples are etched completely through the cap, active, and buffer layer (cf. Fig. 2.10). There are three options for etching[1]: ion beam etching (IBE) with high-energy argon ions (Ar^+), wet etching (WE) with a KI $_{4.15\,g}$:$I_{2\ 0.1\,g}$:HBr $_{12.5\,ml}$:H_2O $_{37.5\,ml}$ solution, which is diluted in 200 ml deionized water (DIW), and the newly established inductively coupled plasma (ICP) etching with low-energy argon ions and reactive methane (CH_4). In the following, all three etching techniques are described.

Ion beam etching:
IBE uses accelerated Ar^+-ions to physically sputter material. The ion milling process usually is carried out for about three minutes in a high vacuum chamber at a base pressure of around $1 \cdot 10^{-9}$ mbar. The chamber is equipped with an ion gun, which is operated at an acceleration voltage of 1 kV and a total current of 8 mA. The exact etching time has to be calculated for each sample individually and depends on the thicknesses of cap d_{cap}, active $d_{\mathrm{Hg(Mn)Te}}$, and buffer layer d_{buffer}. For our tool, it can be determined via $t_{\mathrm{IBE}} = \frac{2}{3}(2d_{\mathrm{cap}} + d_{\mathrm{Hg(Mn)Te}} + 2d_{\mathrm{buffer}})\,\frac{\mathrm{s}}{\mathrm{nm}}$. A 100 nm thick barium fluoride (BaF_2) etch mask is applied on top of the sample to protect the desired mesa design. The application of the etch mask is accomplished by the use of negative photoresist and subsequent deposition of 100 nm BaF_2 in a high vacuum chamber. After etching, the barium fluoride mask is removed with DIW. It is worth mentioning that ion beam etching is almost completely anisotropic, i.e. the pattern of the etching mask is transferred unaltered to the sample. In addition, the etching is uniform across the whole sample piece and highly reproducible. Samples of the same wafer etched for the same amount of time possess similar etching profiles.

A schematic sketch of the IBE etching process with Ar^+-ions is given in Fig. 3.3a) to c). Since sputtered material hits the side surface of the active layer, it can be damaged during the etching process resulting in the formation of impurities along the whole side surface. These impurities disturb the potential landscape and can introduce backscattering of charge carriers in the surface states reducing their overall mobility. However, it has been shown that damage caused by ion beam etching depends strongly on the sample size and therefore usually has a greater effect on microscopic structures measuring a few micrometers in size [14]. This can be explained by the different side surface to volume ratio of the active layer for macroscopic and microscopic Hall bar devices. Due to reduced dimensions in x-direction and y-direction and an equal thickness of the Hg(Mn)Te layer (z-direction), this ratio is larger by a factor of

[1] Note that in the *old 6-terminal standard recipe* (cf. Appx. B.1) only ion beam etching is mentioned, since IBE was the standard etching technique at that time.

about 200 for microstructures. This means that as the sample size decreases, an increasing proportion of the active layer is damaged by the nearby etching with lateral impact, implying that the carrier mobility scales with the device size. In addition, numerous publications such

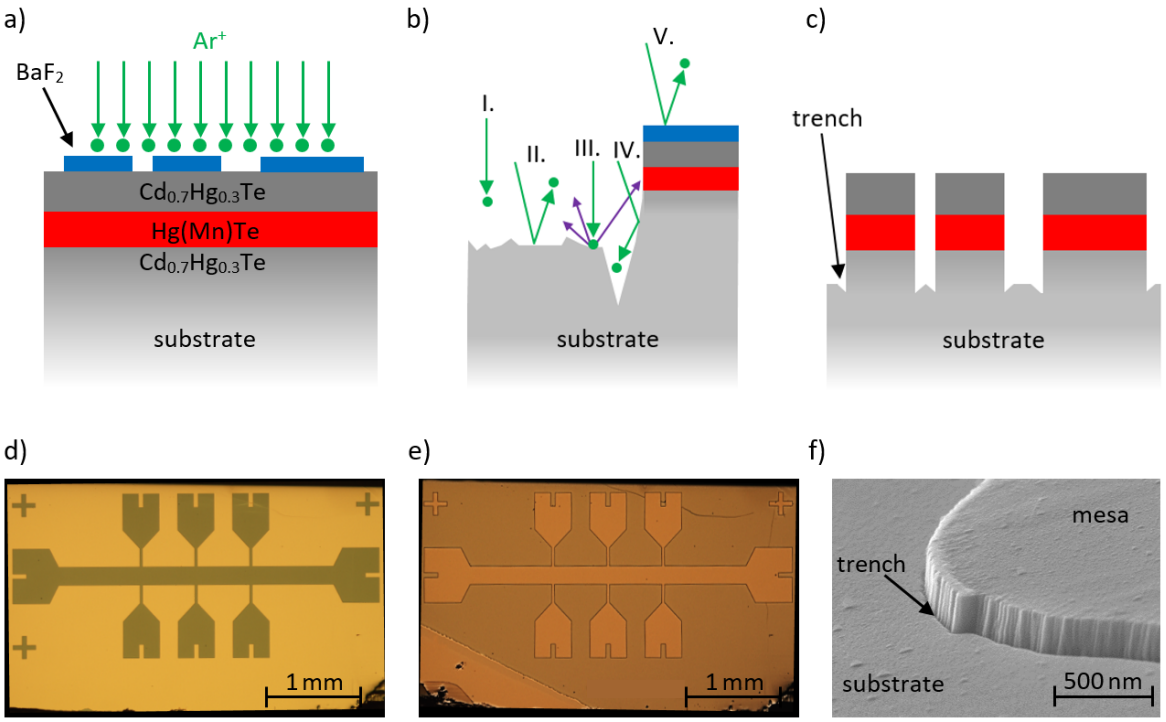

Figure 3.3.: A schematic of the IBE process is sketched in a) and b). The accelerated high-energy argon ions are indicated with green arrows and dots. The desired mesa structure is protected via a BaF_2 etch mask. The incoming Ar^+-ions (I.) hit the sample surface, sputter material, and are reflected afterwards (II. and III.). Violet arrows depict the sputtered material. Close-by the mesa structure, trenches are formed in the process (IV.). Argon ions hitting the BaF_2 mask do not sputter sample material (V.). c) displays the mesa structure after etching and removal of BaF_2. Optical microscope images of samples showing the BaF_2 etch mask and the etched mesa are presented in d) and e), respectively. In f), an SEM image of the etching profile is exhibited.

as [51] or [52] refer to the doping of (Cd,Hg)Te by ion milling. It is reported that the doping occurs due to Hg inter-diffusion. For our macroscopic three-dimensional samples, however, no IBE-related doping has been observed so far.

Close-by the mesa structure, not only incoming ions are hitting the sample surface, but also Ar^+-ions that are reflected at the side surface of the mesa. This increases the number of impacting ions per time unit at these areas, which results in the formation of characteristic trenches around the mesa. Optical microscope images of a sample covered with a BaF_2 mask and an etched mesa are shown in Fig. 3.3d) and e), respectively. Fig. 3.3f) displays a scanning electron microscope (SEM) image of an IBE profile, where the characteristic trench is visible as well.

Wet etching:

WE relies on purely chemical etching. The use of an aqueous solution of KI:I_2:HBr as an etchant for (Cd,Hg)Te has first been reported by Refs. [53, 54]. The etch rate is highly affected by variables such as temperature, activation energy of reaction, oxidation potential of the sample, viscosity of the etching solution, and composition of the etchant. The underlying chemistry process involves redox reaction, i.e. the exchange of charges between the etch solution and the sample surface. Electrons are being released after the oxidation of telluride

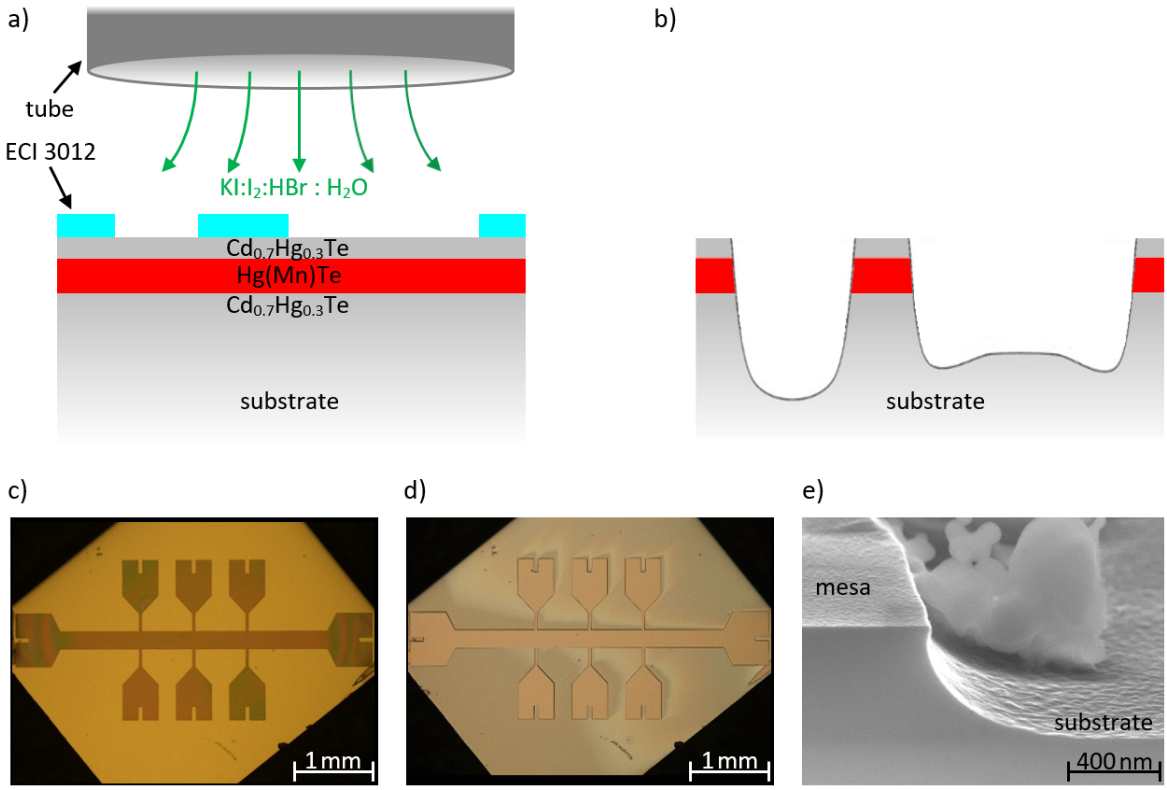

Figure 3.4.: A schematic of the wet etching process is shown in a). The aqueous solution KI:I_2:HBr performs redox reactions with Te, Cd, and Hg, and is pumped through a tube toward the sample surface. An etch mask consisting of photoresist *ECI 3012* protects the desired mesa. In b), the etched mesa structure after resist removal is depicted. Adapted with permission from [14], licensed under CC BY-SA 4.0, `https://creativecommons.org/licenses/by-sa/4.0/deed.de`. Optical microscope images of samples showing the etch mask and the etched mesa are presented in c) and d), respectively. If the flow of fresh etchant is not parallel to the surface normal but impinges on the sample surface at an angle, a shadow-like pattern is formed around the mesa (d)). In f), an SEM image of the etching profile is exhibited. The particles located in the background are leftovers from sample preparation.

(Te^{2-}) by triiodide (I_3^-) and consumed in the reduction of the metal ions Hg^{2+} and Cd^{2+}. Afterwards, the metal ions are chemically dissolved in hydrobromic acid (HBr). It has been

shown that the etch rate is strongly dependent on the iodine concentration of the etching solution. A higher iodine concentration results in a higher etch rate [55]. The concentration of our solution is KI $_{4.15\,g}$:$I_{2\ 0.1\,g}$:HBr $_{12.5\,ml}$:H_2O $_{37.5\,ml}$. In addition, the etchant is diluted in 200 ml deionized water. To achieve a constant flow of fresh etching solution towards the sample surface, the so-called pumping method is used. For this purpose, the etchant is pumped through a tube from a reservoir to the sample holder. The outlet of the tube should be placed directly above the sample and the elongation of the tube should be aligned parallel to the surface normal of the sample. Thus, the most uniform and reproducible etching result is obtained. The desired mesa structure is protected via an etch mask consisting of positive photoresist *ECI 3012*, which can be removed with acetone after etching. A schematic sketch of the wet etching process is depicted in Fig. 3.4a) and b), while optical images of devices are shown in c) and d). Fig. 3.4f) displays an SEM image of a wet etching profile. It is noted that the etching time for the presented sample was increased to exhibit the profile more explicit.

Compared to IBE, less lithography steps are required as the photoresist can be used as an etch mask. In addition, the side surfaces of samples cannot be damaged, since no physical etching component is involved during WE, making it a non-damaging etching technique. However, wet etching is a diffusion-controlled process. This means that the etch rate depends on the width of the structure to be etched due to diffusive trenching. Wide structures exhibit a lower etch rate compared to narrow ones. A calculated shape of an etched medium formed by the convection of a diffusion-controlled etch regime is presented in Fig. 3.5a). In Fig. 3.5b), a schematic of the etch depth dependence on the width of the etched structure is presented. Hence, it is difficult to set up a formula for the etching time. The best results can be achieved when the etching time is determined individually for each wafer and sample design via etching tests. As a rough estimate, it can be stated that for 3D Hg(Mn)Te macroscopic samples an etching time of 70 s leads to a depth of about 200 nm. Based on the

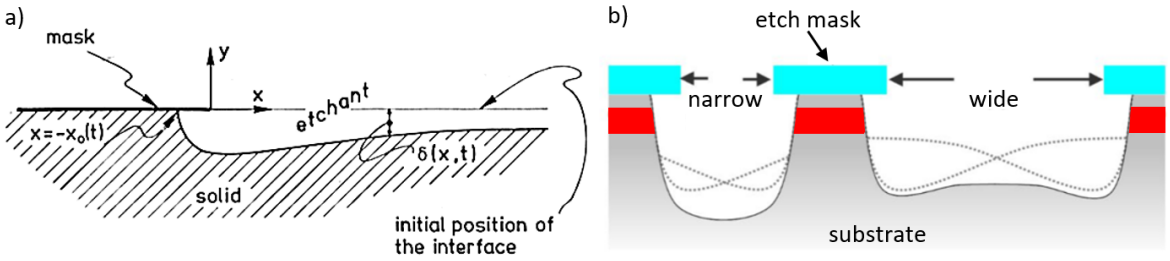

Figure 3.5.: a) shows the calculated etch profile of a diffusive controlled etch process. Reprintet with permission from [56], license granted by Copyright Clearance Center, Inc. In b), a schematic of the etch depth dependence on the width of the etched structure as a result of diffusive trenching is presented. Based on the isotropic nature of WE, lateral etching under the resist mask occurs. Adapted with permission from [14], licensed under CC BY-SA 4.0, `https://creativecommons.org/licenses/by-sa/4.0/deed.de`.

isotropic nature of WE, lateral etching under the resist mask occurs. Considering an isotropic

etching of about 200 nm, macroscopic structures possessing sample sizes of several hundred micrometers are almost unaffected by this phenomenon. In addition, since wet etching relies on many variables like the composition of the solution, temperature, and alignment of the tube, it is difficult to reproduce an etching result exactly.

Inductively coupled plasma etching:
Contrary to IBE and WE, which purely rely on physical and chemical etching respectively, ICP etching is a combination of physical and chemical etching. In a high vacuum chamber, argon atoms are ionized to an Ar^+-plasma in the presence of an electric field, which is inductively coupled to a magnetic field. The latter is generated by a radio frequency[2] (RF) voltage source, which powers a so-called ICP coil. The density of the plasma can be altered and is

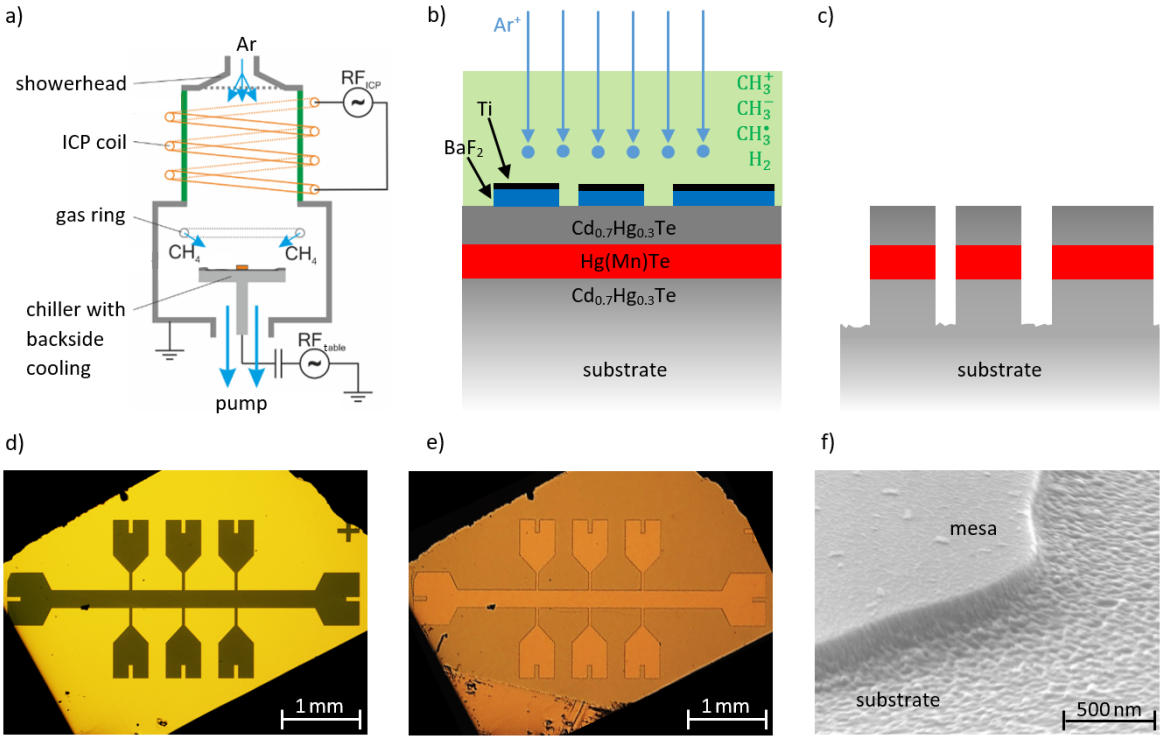

Figure 3.6.: The structure of an ICP etching chamber is sketched in a). Adapted with permission from [57]. In b), a schematic of the etching process is shown. Ar^+-ions (blue arrows and dots) are accelerated toward the sample surface and dissociate the CH_4 molecules (green area). The dissociation products CH_3^+, CH_3^-, H_2, and $CH_3^\bullet$ react with Hg, Cd, and Te. To protect the desired mesa structure, a BaF_2/Ti etch mask is applied. c) displays the mesa structure after removal of the etch mask. Optical microscope images of samples showing the etch mask and the etched mesa are presented in d) and e), respectively. In f), an SEM image of the etching profile is exhibited. The small particles on the mesa are most likely residues of the BaF_2/Ti mask.

[2]The used frequency is 13.56 MHz.

controlled by the RF source. Free lightweight electrons are attracted by a second RF voltage source located beneath the ICP coil, whenever its half period is positive. Due to capacitive coupling, electrons reaching the electrode of the radio frequency source remain there. This leads to negative DC bias in the mean over a period. This direct current bias usually has a value between 20 V and 30 V and accelerates the argon ions toward the sample surface, where they sputter sample material. However, the energy of the Ar^+-ions used for physical ICP etching is much lower than the energy of argon ions used for IBE, resulting in a more gentle process and less damage to the sample. In addition, the energy can be controlled by the power applied to the second RF source. The Ar^+-ions also dissociate the reaction gas CH_4, that is inserted into the high vacuum chamber via a ring located below the ICP coil, and supply energy to the sample surface. The latter acts as a catalyst for chemical reactions of the dissociation products of methane[3] with Hg, Cd, and Te. The resulting reaction products $Hg(CH_3)_2$, $Te(CH_3)_2$, $Cd(CH_3)_2$, and TeH_2 are removed from the chamber by pumping. During etching, the sample is located on a chiller, which is kept at a constant temperature of 0 °C to increase the sensitivity of chemical etching and reduce thermal load. The structure of an ICP etching tool is sketched in Fig. 3.6a).

To protect the desired mesa, a etch mask consisting of 100 nm BaF_2 and 10 nm titanium is used. The application of the etch mask is accomplished by the use of negative photoresist and the subsequent sequential deposition of BaF_2 and Ti in a high vacuum chamber. Barium fluoride is deposited by thermal evaporation, whereas titanium is evaporated by an e-gun. After etching for about 60 s, the mask is removed with DIW. Again, the exact etching time is depending on the thicknesses of cap, active, and buffer layer. The times for our ICP tool can be calculated via $t_{\mathrm{ICP}} \approx (2d_{\mathrm{cap}} + d_{\mathrm{Hg(Mn)Te}} + 2d_{\mathrm{buffer}})/5.76\,\frac{\mathrm{s}}{\mathrm{nm}}$. A schematic sketch of the ICP etching process is presented in Fig. 3.6b) and c), while optical images of samples are shown in d) and e). In Fig. 3.6f), an SEM image of an ICP etching profile is displayed.

Like ion beam etching, inductively coupled plasma etching is almost completely anisotropic, uniform across the whole sample piece, and highly reproducible.

After etching, the samples are bonded with heated indium lumps and gold wires. All three etching techniques are examined for the wafer materials QC0438[4], QC0478, and QC0479. As an example, the resulting samples fabricated of wafer QC0479 are shown in Fig. 3.7a), b), and c), representing IBE, WE, and ICP etching respectively. Magneto-transport measurements are performed to obtain the charge carrier densities n of the devices. The densities are determined by the linear slope of the semi-classical Hall resistance for small magnetic fields as described in Subsec. 2.2.2. The results are summarized in Tab. 3.2. One is able to observe that the charge carrier densities n for samples fabricated of the same wafer material are almost identical independent of the etching technique. Therefore, a mean density

[3] These are CH_3^+, CH_3^-, H_2, and the methyl radical $CH_3^\bullet$.
[4] Only IBE and WE samples were fabricated of wafer QC0438 due to lack of wafer material.

$\overline{n}_{\text{etch}} = (n_{\text{IBE}} + n_{\text{WE}} + n_{\text{ICP}})/3$ is calculated for each wafer and used for the subsequent investigations. Compared to the densities of untreated samples obtained by the vdP method, minor deviations can be found. However, none of the samples exhibits a carrier density larger than $10{\cdot}10^{11}\,\frac{1}{\text{cm}^2}$, as it is the case for sample QC0461 I ($n \approx 14{\cdot}10^{11}\,\frac{1}{\text{cm}^2}$ at $V_{\text{TG}} = V_{\text{BG}} = 0\,\text{V}$) observed in Sec. 2.3. Since the density deviations of the etched samples from the untreated wafers are rather small ($< 1 \cdot 10^{11}\,\frac{1}{\text{cm}^2}$), the minor variations are probably due to inhomogeneities within the underlying wafer materials. The distribution of impurities and the defect density is non-constant across the whole MBE grown wafer. As a result of this inhomogeneity, samples fabricated of the same wafer material may possess slightly different mobilities and densities. By comparing several identically built devices, it has been determined that the charge carrier density within a wafer can vary by about $1 \cdot 10^{11}\,\frac{1}{\text{cm}^2}$. All deviations found are in the range of this intrinsic density variation of a wafer. For this reason, it has to be assumed that etching does not affect the charge carrier density of samples. This means that one of the remaining two lithography steps is responsible for the increase of the electron density in the system. The next subsection covers the fabrication of the ohmic contacts.

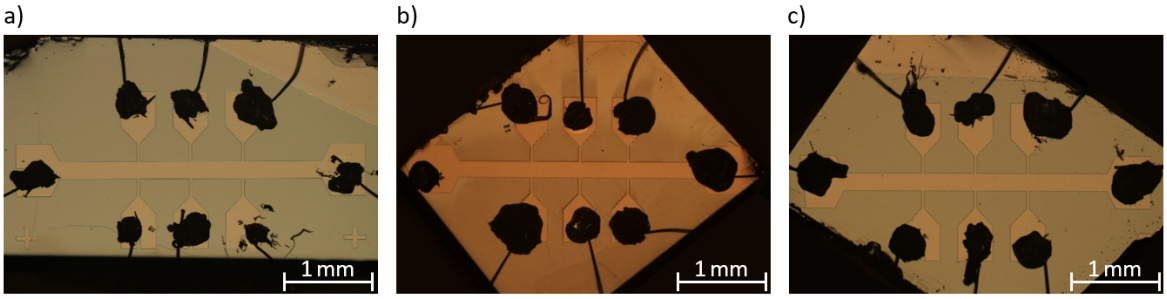

Figure 3.7.: Mesa structures fabricated using ion beam, wet, and inductively coupled plasma etching are shown in a), b), and c) respectively. The bonding is achieved via heated indium lumps and gold wires.

wafer	density n $[10^{11}\,\frac{1}{\text{cm}^2}]$				
	IBE	WE	ICP	$\overline{n}_{\text{etch}}$	vdP
QC0438	2.9	2.7	-	2.8	2.8
QC0478	2.6	2.7	2.7	2.7	2.6
QC0479	3.2	3.4	3	3.2	2.6

Table 3.2.: Determined charge carrier densities n for IBE, WE, and ICP etched samples fabricated of wafer materials QC0438, QC0478, and QC0479. The mean density $\overline{n}_{\text{etch}}$ for the three etching techniques and the densities of untreated samples obtained by the vdP method are also noted.

3.1.3. Fabrication of the ohmic contacts

During this lithography step, the ohmics are fabricated. For this purpose, a photomask consisting of negative resist is applied so that only the areas of the later ohmic contacts are affected in the following processes. First, an ion-milling step is carried out. The same high vacuum chamber as for IBE is used. This time, the ion gun is operated at only 0.4 kV and a total current of 8 mA resulting in an etch rate of 0.8 $\frac{\text{nm}}{\text{s}}$ for CMT. The aim is to etch approximately 20 nm close to the active layer, before 50 nm of gold germanium and 50 nm gold are deposited. The remaining cap layer thickness of 20 nm is chosen, since electrical characteristics of Hg(Mn)Te/CMT/Au interfaces are dominated by the indiffusion of Au into the semiconductors, thus doping the CMT p-type and forming an ohmic contact, as long as the thickness of the cap layer is not too large [58]. More detailed examinations of the metal-semiconductor contact CMT/Au can be found in Refs. [59, 60]. If the cap layer thickness of a sample is below 20 nm, then the etching time is set to 3 s to perform a short interface cleaning before the contact metals are deposited. The subsequent deposition of AuGe and Au happens in-situ, i.e. without exposing the sample to air to prevent any contaminations. The additional AuGe layer is required, since gold on its own exhibits a weak adhesion on CMT. Both metals are evaporated by an e-gun and deposited onto the sample. The beam of metal atoms is aligned parallel to the surface normal of the sample. It is worth mentioning that this method of metallization can lead to discontinuities of the metal layers over the mesa edges as shown in Fig. 3.8, since the height of the mesa is about 200 nm and only 100 nm of metal is deposited. The discontinuity of the metal layers can result in an electrical disconnection between the metal layers located on substrate and mesa respectively. After metallization, the lift-off process is carried out for 5 min in acetone at 50 °C. On the device, the metal layer remains solely at the areas of the ohmic contacts. Optical images of a sample showing the photomask and the metallized contacts are presented in Fig. 3.9a) and b) respectively. Due to the AuGe/Au layer, bonding of the samples can be performed using standard wedge-wedge bonding techniques with an Au-wire, thus avoiding the necessity of indium bonding. Therefore, the 6-terminal Hall bar design (cf. Fig. 3.2a)), which is the standard design in the *old 6-terminal standard recipe*, can be used for the investigation of this lithography step. This design is bonded directly on the ohmic contacts, preventing any influences of potential discontinuities of metal layers over the mesa edges. However, direct bonding on the contacts might damage them in the process and thus reduce their overall quality.

Before magneto-transport measurements of samples possessing metallized ohmic contacts are carried out, a short introduction to cross-sectioning techniques is to be given. An example of a cross-section at the mesa edge is shown in Fig. 3.8. The realization of cross-sections is achieved in a high vacuum chamber equipped with a dual-beam system, consisting of an electron and a gallium (Ga) ion source. First, during a preparation step, two platinum (Pt) layers are deposited onto the area of interest. Platinum deposition occurs by decomposing an organic platinum gas in either the electron beam (first layer) or the Ga-ion beam (second

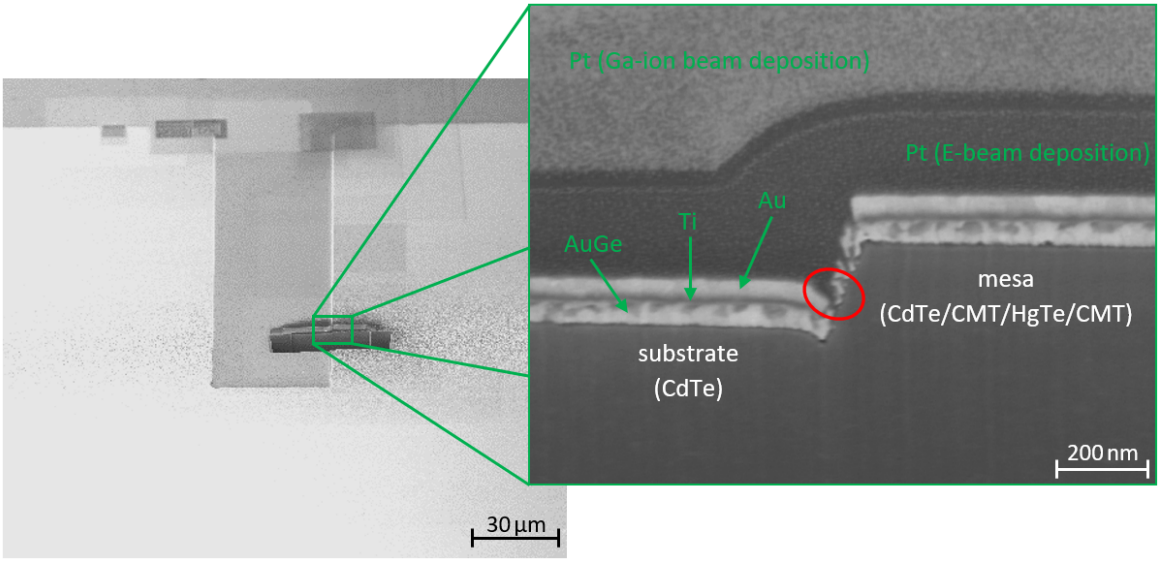

Figure 3.8.: SEM image of a cross-section of a metallized ohmic contact at the mesa edge. The inset shows the mesa edge at higher magnification. A clear discontinuity of the metal layers over the mesa edge can be observed (indicated by a red oval). During metallization, an additional 5 nm Ti layer was deposited between the AuGe and Au layers to clearly distinguish them from each other. The two protective Pt layers were applied onto the sample throughout a preparation step.

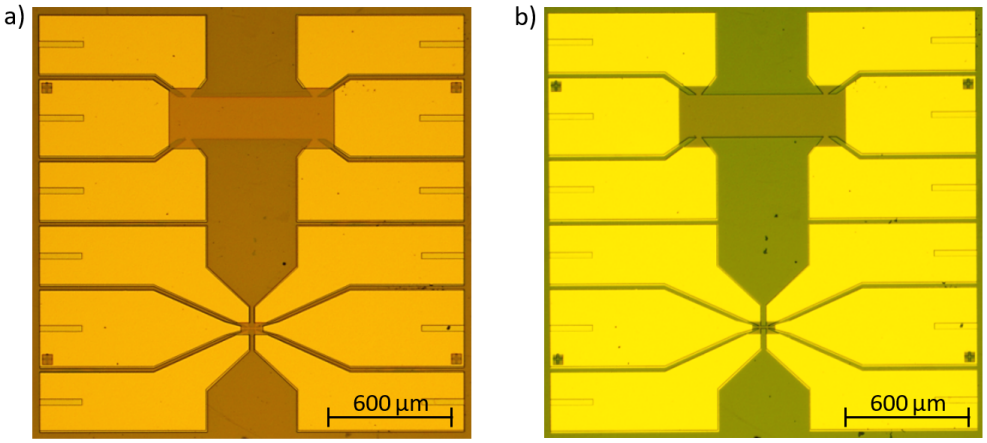

Figure 3.9.: Fabrication of the ohmic contacts: a) shows the applied photomask. Dark brown regions are covered with photoresist. b) displays the sample after ion milling, subsequent deposition of 50 nm AuGe and 50 nm Au, and removal of the remaining photoresist.

layer), while the beams are scanned over the preselected pattern. The e-beam source is operated at 2 kV and a total current of 2.7 nA, while the ion beam source is operated at 30 kV and 93 pA. This step is required, as the Pt layers protect the area of the later cross-section from abrasion by the gallium ion beam. To cut the sample next to the Pt layers open, a focused ion beam (FIB) of Ga-ions is used to mill the sample material. The parameters of the ion source used for this step are 30 kV and 0.28 nA. Subsequently, a polishing step of the cross-section is carried out. For this purpose, the Ga-ion beam is scanned slowly over a preselected pattern and the ion source is operated at 30 kV and a total current of only 28 pA. Finally, one is able to investigate the cross-section with the help of the electron beam, which is orientated under an angle of 52 ° respective to the surface normal of the sample. The best results are achieved if the electron source is operated at 5 kV and a total current of 43 pA. A detailed description of the FIB cross-sectioning technique can be found in Ref. [61].

Again, the wafer materials QC0438, QC0478, and QC0479 are investigated. It has been shown in subsection 3.1.2 that the charge carrier density does not depend on the etching technique. Therefore, only one sample per wafer material has to be examined.

Magneto-transport measurements are carried out to obtain the carrier densities of these samples. The charge carrier density is determined analog to Subsec. 3.1.2. The results are presented in Tab. 3.3. In comparison to the carrier densities of untreated samples (vdP) and the mean densities of etched mesa samples ($\overline{n}_{\mathrm{etch}}$), one can find a slight increase in carrier density. However, since the Hall bar structure is protected by a layer of photoresist during the fabrication of the ohmic contacts (cf. Fig. 3.9), it is unlikely that this lithography step induces the unintentional n-type doping. We thus assume that, analogous to Subsec. 3.1.2, inhomogeneities within the underlying wafer materials are responsible for the density variations. Since there is only one processing step left to complete the samples, this step has to cause the accumulation of electrons in the system resulting in observed densities $> 10 \cdot 10^{11}\,\frac{1}{\mathrm{cm}^2}$ at $V_{\mathrm{TG}} = V_{\mathrm{BG}} = 0\,\mathrm{V}$. In the following subsection, the final fabrication step, application of gate insulator and top-gate metals, is investigated.

wafer	density n $[10^{11}\,\frac{1}{\mathrm{cm}^2}]$		
	ohmic contacts	$\overline{n}_{\mathrm{etch}}$	vdP
QC0438	3.0	2.8	2.8
QC0478	2.7	2.7	2.6
QC0479	3.4	3.2	2.6

Table 3.3.: Determined charge carrier densities for samples of wafer materials QC0438, QC0478, and QC0479 after the fabrication of the ohmic contacts. $\overline{n}_{\mathrm{etch}}$ and the densities of untreated samples (vdP) are noted as well.

3.1.4. Application of gate-dielectric and top-gate-electrode

In order to control the level of the Fermi energy E_F in the system, a gate-electrode on top of the structure can be used. First, a gate-dielectric has to be applied in order to separate the electrode from the sample structure electrically. There are two possible options: A superlattice consisting of eleven alternating 10 nm thick SiO_2 and Si_3N_4 layers, which are applied to the sample via plasma enhanced chemical vapor deposition (PECVD), and a 15 nm thick atomic layer deposition (ALD) grown layer of HfO_a. The latter represents a novel method of insulator application in our group. In the following, both insulator types are described in detail.

Before a SiO_2/Si_3N_4 superlattice is deposited onto a sample, a short reactive ion etching using an oxygen plasma is performed to remove resist residues from the sample surface, which might have remained after mesa etch and fabrication of the ohmic contacts. In the following, this short cleaning step is referred to as miniclean. The PECVD of the insulator happens in a high vacuum chamber. To deposit the first 10 nm SiO_2 layer, the reaction gases silane (SiH_4) and nitrous oxide (N_2O) are injected into the chamber and dissociated in the presence of an electron plasma. The crucial dissociation products are silylene (SiH_2) and atomic oxygen (O). In addition to the radicals formed this way, the electron plasma also generates ions, which - together with the radicals - cause the deposition of silicon dioxide onto the sample by diffusion along the surface. To enable the diffusion process, the sample has to be heated to 80 °C. The other reaction products H_2 and N_2 are removed from the chamber via pumping. In an analogous manner, the first 10 nm Si_3N_4 layer is deposited. This time, the reaction gases are silane and ammonia (NH_3) and the reaction products are H_2 and Si_3N_4, which is deposited onto the SiO_2 layer at 80 °C. The whole procedure is repeated until six layers of SiO_2 and five of Si_3N_4 are deposited. Note that the insulator is not only applied to the area of the later top-gate-electrode, but across the whole sample piece. The reason for this is that due to the thickness (110 nm) and fracture toughness of the SiO_2/Si_3N_4 superlattice, the necessary lift-off process of the photomask would not be sufficiently feasible with this type of dielectric on top.

After insulator deposition, a photomask consisting of negative resist is applied. The sequential metallization of 5 nm Ti and 100 nm Au happens in a high vacuum chamber. Both metals are evaporated by an e-gun and deposited onto the sample. The beam of metal atoms is aligned parallel to the surface normal of the sample. This can once again lead to discontinuities of the metal layers over the mesa edges, which might disconnect the metal layer located on top of the Hall bar structure from the metal layer located on the substrate representing the bond pads of the top-gate-electrode. This implies the possibility that the top-gate cannot be used in measurements. The following lift-off process is carried out for 5 min in acetone at 50 °C. Optical images of a sample showing the applied SiO_2/Si_3N_4 insulator and the metallized gate-electrode are presented in Fig. 3.10a) and b) respectively. After metallization,

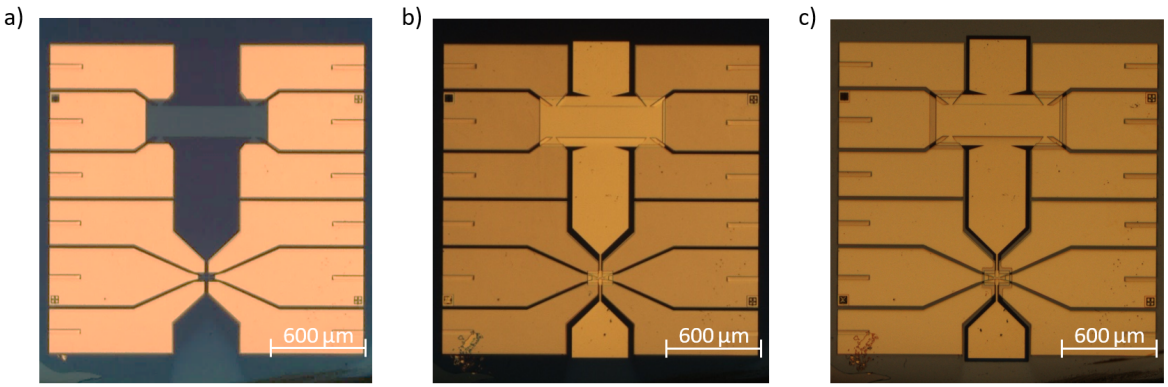

Figure 3.10.: Top-gate-electrode application process using a dielectric consisting of a 110 nm SiO_2/Si_3N_4 superlattice. a) shows the insulator covering the whole sample. In optical images, the SiO_2/Si_3N_4 superlattice can be recognized by its dark blue color. In b), the TG-electrode after metallization of 5 nm Ti and 100 nm Au is displayed. c) presents the sample after removal of excess insulator material covering the ohmic contacts.

the gate-dielectric has to be removed from the area of the ohmic contacts so that bonding is enabled. This is done by dipping the sample in hydrofluoric acid (HF) for 13 s. The used HF consists of concentrated hydrofluoric acid mixed with DIW in the ratio 1:1. To protect the insulator located beneath the top-gate-metals, a photomask consisting of positive resist is utilized. After etching, the photomask is stripped in acetone for about 5 min. An optical image of a completed sample is shown in Fig. 3.10c).

Before the HfO_a dielectric can be deposited onto the sample, a photomask consisting of negative resist has to be applied first, so that only the area of the later top-gate-electrode is covered with insulator. Then, a short miniclean is performed to remove any resist residues. Afterwards, the sample is taken to the high vacuum ALD chamber. To initiate the HfO_a insulator growth, the first gaseous precursor (H_2O) is injected into the reactor of the ALD chamber by a short pulse (200 ms). The H_2O-molecules react with the sample surface in a self-limiting way, so that the reaction terminates once all reactive sites on the surface are consumed (surface-saturation). In the process, hydroxy (OH) molecules are deposited onto the sample. Note that the reactor is heated to avoid precursor condensation and side reactions at the chamber wall. The sample stage, however, is kept constant at 30 °C via a liquid cooling system with thermal oil to reduce thermal load. Thereafter, the remaining precursor is purged by injecting an inert gas (Ar) into the reactor for 100 s. Now, a 50 ms pulse of the second precursor tetrakis(dimethylamido)hafnium(IV)[5] is inserted into the reactor. Again, the $[(CH_3)_2N]_4Hf$ molecules react with the hydroxy molecules in a self-limiting way until the surface is saturated. This results in the first HfO_a layer on the sample surface. As already mentioned in Sec. 2.3, during the reaction either HfO or HfO_2 can form. The thickness

[5] $[(CH_3)_2N]_4Hf$

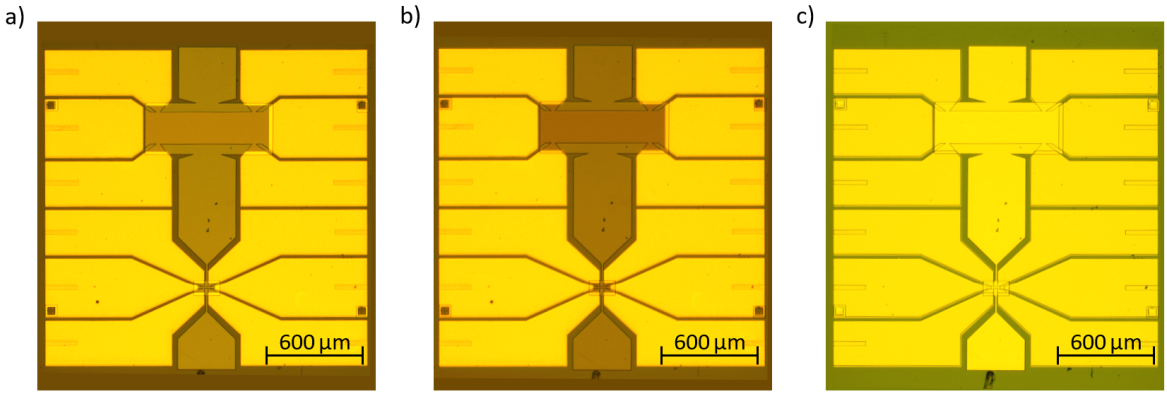

Figure 3.11.: Top-gate-electrode application process using an insulator consisting of 15 nm HfO_a. a) shows the applied photomask. The area of the sample that is not covered with photoresist can be identified by a lighter brown shade. In b), the sample after insulator growth is presented. c) displays the TG-electrode after metallization with 5 nm Ti as well as 100 nm Au and removal of the photomask.

of the HfO_a layer is about 1.7 Å. Once more, the remaining precursor is purged from the reactor by argon gas, which is injected into the chamber for 100 s. Now, the first growth cycle is completed. Since 90 cycles have to be grown in this manner, the whole process is quite time-consuming (about 6 h). Therefore, the growth of 15 nm HfO_a insulator is usually accomplished overnight.

After HfO_a deposition, the sample can be metallized with 5 nm Ti and 100 nm Au. This step is done in the same way as described for PECVD. The following lift-off process is carried out for 30 min in acetone at 50 °C. Optical images of a sample showing the applied photomask, the HfO_a insulator, and the metallized top-gate-electrode are presented in Fig. 3.11a), b), and c) respectively. Note that this time no insulator removal step is necessary, i.e. less lithography steps are required to fabricate the top-gate-electrode. Another advantage of the atomic layer deposition over the plasma enhanced chemical vapor deposition can be found by comparing their process temperatures. The ALD growth is carried out at 30 °C, whereas the PECVD is performed at 80 °C, which implies higher thermal load for the samples.

Finally, the samples are bonded via standard wedge-wedge bonding techniques with an Au-wire and are investigated in magneto-transport measurements. In the case of SiO_2/Si_3N_4 insulator type, for each wafer material (QC0438, QC0478, and QC0479) one sample was fabricated. However, in total, only one sample possessing a HfO_a insulator was built of these wafers (QC0478) due to the lack of material. The ICP etching technique was used to define the mesa of this particular device. Since the BaF_2-crucible was emptied during the deposition, less than 100 nm barium fluoride were applied onto the sample and the BaF_2 etch mask was perforated with tiny holes. Therefore, it is possible that parts of the Hall bar structure were exposed and hence affected throughout the etching process. On this account, the data

obtained from this particular sample are not trustworthy.

The charge carrier densities of the devices are determined analog to Subsec. 3.1.2 and are presented in Tab. 3.4. In addition, the results are visualized in Fig. 3.12. It is noted that the

wafer	density n $[10^{11}\,\frac{1}{\mathrm{cm}^2}]$				
	insulator and top-gate-electrode		ohmic contacts	$\overline{n}_{\mathrm{etch}}$	vdP
	SiO_2/Si_3N_4	HfO_a			
QC0438	11.7	-	3.0	2.8	2.8
QC0478	11.8	17.9	2.7	2.7	2.6
QC0479	12.1	-	3.4	3.2	2.6

Table 3.4.: Determined carrier densities n for samples of wafer materials QC0438, QC0478, and QC0479 after insulator deposition (SiO_2/Si_3N_4 superlattice or HfO_a) and top-gate-electrode application. The results from the previous subsections 3.1.1 (vdP), 3.1.2 ($\overline{n}_{\mathrm{etch}}$), and 3.1.3 (ohmic contacts) are also given.

top-gate was grounded in each measurement. This ensures that the experimentally observed increase of the n-type carrier density results solely from the lithographic treatment of the samples and is not caused by the application of a (positive) top-gate voltage. All devices possessing a SiO_2/Si_3N_4 insulator and a top-gate-electrode show a significantly increased charge carrier density compared to the samples without top-gate. The increase of the n-type density caused by the final lithography step is approximately $\Delta n \approx 9 \cdot 10^{11}\,\frac{1}{\mathrm{cm}^2}$ (increase of about 300 %) for all wafer materials under investigation, resulting in carrier densities $> 10 \cdot 10^{11}\,\frac{1}{\mathrm{cm}^2}$. The device possessing a HfO_a dielectric exhibits an even larger increase of the charge carrier density ($\Delta n \approx 15 \cdot 10^{11}\,\frac{1}{\mathrm{cm}^2}$). However, as mentioned earlier, the data obtained from this particular sample are not trustworthy. The investigation of more devices featuring an ALD grown insulator reveals that these samples show similar behavior to devices possessing a SiO_2/Si_3N_4 superlattice and fabricated of the same wafer (cf. Sec. 3.3). For this reason, it can be concluded that the lithography step of insulator and top-gate-electrode application is responsible for the increase of the n-type carrier density in the system.

In the investigations of Sec. 3.1, the lithography of macroscopic 3D HgTe-based samples was examined in detail and numerous possibilities for improvement were revealed in this context. This led to a revision of the *old 6-terminal standard recipe*. The following section lists the enhancements that eventually resulted in two new standard sample recipes for the fabrication of macroscopic mercury telluride devices. The subsequent Sec. 3.3 addresses the identification of the underlying mechanism leading to the lithography-induced increase of the n-type density.

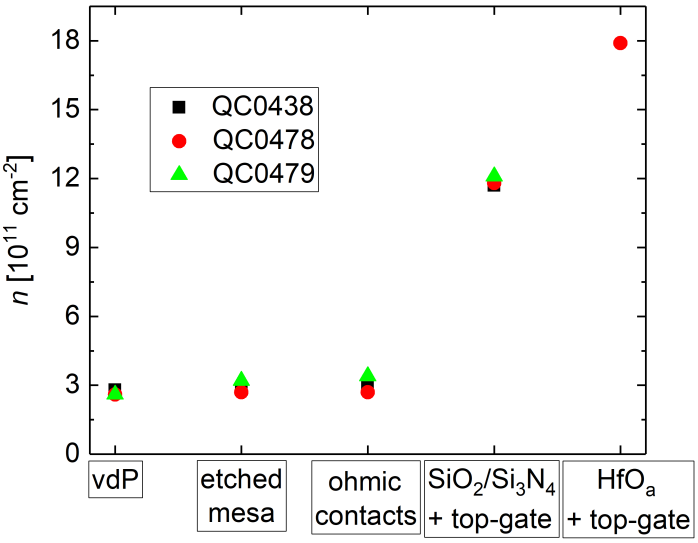

Figure 3.12.: The change in charge carrier density n during lithography is shown. Untreated samples (vdP) and the lithographic processing steps of mesa etching, ohmic contacts fabrication, and insulator (SiO_2/Si_3N_4 or HfO_a) and top-gate-electrode application were investigated. The samples were built of wafers QC0438 (black squares), QC0478 (red circles), and QC0479 (green triangles).

3.2. The novel 8-terminal standard recipes for the fabrication of macroscopic HgTe-based samples

The investigations of the previous section have revealed that the *old 6-terminal standard recipe* for the fabrication of macroscopic three-dimensional HgTe-based devices can be optimized. Such optimizations are crucial for the research in our group, since they are the key to exploiting the full potential of our high-quality molecular beam epitaxy grown CMT/Hg(Mn)Te/CMT heterostructures. The enhancements, which have been elaborated within the framework of this thesis, are presented in the following. Ultimately, this resulted in the development of two novel sample recipes, which are also presented below. These recipes represent the new standard recipes for the fabrication of macroscopic devices in our group.

- The novel 2.5 x 1.4 mm^2 8-terminal Hall bar design (cf. Fig. 3.2c)) consists of two equally sized Hall bars (540 x 180 μm^2) in series, which enhances the space for bonding. In addition, it allows the homogeneity of a sample piece to be determined by comparing the charge carrier densities and mobilities of both Hall bars. Due to the reduced dimensions of the novel design, more samples can now be fabricated of a given wafer.

- Given that physical etching can damage the Hg(Mn)Te layer, the novel standard recipes use the non-damaging wet etching technique. This etching technique is particularly

suitable for macroscopic devices, since the disadvantages of WE (cf. Subsec. 3.1.2) are negligible for structures of such size. In addition, wet etching requires less lithography steps than ion beam etching or inductively coupled plasma etching. The results are an increase in overall sample quality and a shortening of the fabrication process.

- Before the area of the later ohmic contacts is etched 20 nm close to the active layer, now an additional miniclean step is performed to remove resist residues. Using a larger mask for ohmic contact fabrication, which exceeds the dimensions of the mesa, allows for bonding on the substrate. This prevents possible damage to the ohmic contacts caused by bonding. To preclude discontinuities of metal layers over the mesa edges, the contact metals AuGe and Au are deposited under an alternating angle of $\pm 40\,^{\circ}$. The angle is altered every 10 nm of deposited metal.

- Since the application of insulator and top-gate-electrode increases the n-type carrier density in the system, samples for characterization purposes are fabricated without a top-gate. Now, the intrinsic properties of wafer materials, such as charge carrier density and mobility, can be determined in magneto-transport measurements. The quality of wafer materials determined in this manner provides important feedback for the growers. In addition, it can be specified whether a wafer material meets the requirements of the envisaged experiment. Due to their characterization purpose, these samples are called characterization Hall bars. The corresponding novel *8-terminal characterization Hall bar recipe* can be found in Appx. B.3 and represents one of the two newly established standard recipes.

- From now on, samples possessing a top-gate-electrode use an atomic layer deposition grown insulator as dielectric. The reduced thermal load and the fact that less lithography steps are required for fabrication make HfO_a the superior insulator type.

- Once again, to prevent discontinuities of metal layers over the mesa edges during top-gate metallization with 5 nm Ti and 100 nm Au, the metals are deposited under an alternating angle of $\pm 40\,^{\circ}$.

All these changes are included in the *new 8-terminal standard recipe*, which can be found in Appx. B.2 and represents the second newly established standard recipe. Optical images of samples fabricated according to the novel standard recipes are shown in Fig. 3.13. Figure 3.13a) displays a sample with top-gate-electrode (*new 8-terminal standard recipe*) and b) one without (*8-terminal characterization Hall bar recipe*).

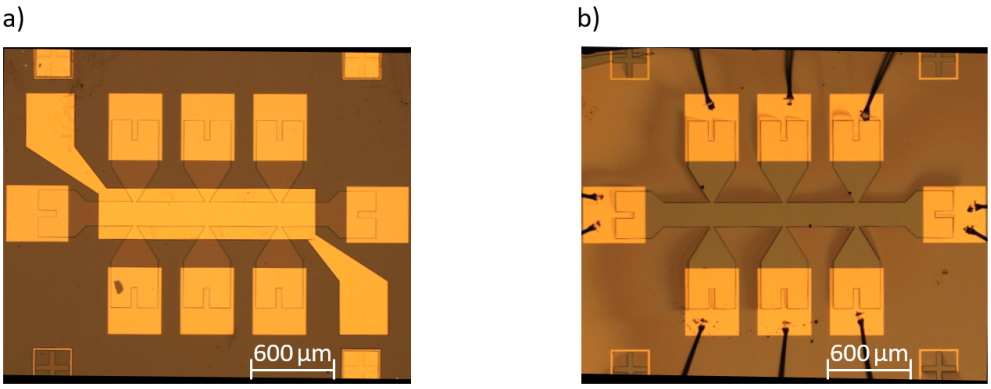

Figure 3.13.: Optical images of samples fabricated according to the novel standard recipes. a) shows a device with top-gate-electrode and b) one without. In addition, bonding on the metal layer located on the substrate is demonstrated in b).

3.3. Modeling of the lithography-induced increase of the n-type carrier density

This section is dedicated to the exploration of the underlying mechanism leading to the increase of the n-type carrier density in the system caused by lithography. The first step is the introduction of a purely classical model that describes the electrostatics in the system. In this context, it is assumed that the application of dielectric and top-gate-electrode on its own changes the electrostatics of the sample in such a way that electrons are accumulated in the active layer. The large work functions of the top-gate metals Ti and Au (compared to HgTe), which might affect the active layer similar to an applied positive top-gate voltage, play a decisive role here. This toy model is in the following called model I and is presented in Subsec. 3.3.1.

3.3.1. Increase of the electron density due to the large work functions of the top-gate metals: model I

To model the electrostatics in our system, we use the energy potential $U(z)$ sketched in Fig. 3.14. Note that z is the growth direction. At the position of the top-gate electrode ($z = z_{\mathrm{TG}}$), the energy potential is denoted by U_{TG}. U_{TG} can be caused by the application of a top-gate voltage or - as assumed in the context of model I - by the difference between the work functions of HgTe and the gate metals[6] ($\Delta W = W_{\mathrm{HgTe}} - W_{\mathrm{Ti,Au}}$). The energy potential $U(z)$ drops across the sample structure and takes the value U_{i} at the interface Hg(Mn)Te/CMT ($z = z_{\mathrm{top}} = 0.5 d_{\mathrm{TI}}$, where z_{top} is the z-coordinate of the top surface of the Hg(Mn)Te layer and d_{TI} is the thickness of the 3D TI). It should be mentioned that the slope of the drop is different for cap (CMT) and insulator layer (SiO_2/Si_3N_4 or HfO_a), since the relative permittivities ε_{r} of both materials are different. We assume that the spatial

[6]The values of the work functions of HgTe, Ti, and Au can be found in Tab. 3.5.

extent d_{SST} of the probability density of the surface states localized at the top surface reaches 10 nm into the active layer. This assumption is inferred from Ref. [45], where the probability

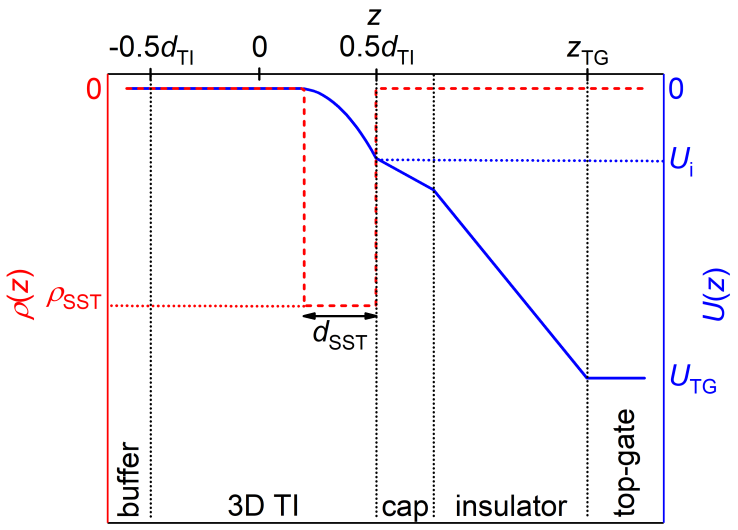

Figure 3.14.: Energy potential $U(z)$ and charge density $\rho(z)$ used to model the electrostatics in our devices are presented in blue and red, respectively. The charge density is constant ($\rho(z) = \rho_{\mathrm{SST}}$) in a region of thickness d_{SST} at the top surface of the 3D TI layer and zero otherwise. The energy potential is quadratic in this region and takes the value U_{i} at the interface. At the position of the top-gate-electrode ($z = z_{\mathrm{TG}}$), $U(z) = U_{\mathrm{TG}}$ holds.

densities of the top and bottom surface state wave functions are calculated for different values of top-gate voltage. In addition, it is assumed that the energy potential U_{i} is effectively screened by the mobile carriers located at the top surface [45]. Due to Dirac-screening, $U(z)$ takes the value zero for all $z < 0.5d_{\mathrm{TI}} - d_{\mathrm{SST}}$. The energy potential U_{i} at the interface causes a change in the number of charge carriers located in the top surface states. This variation in charge density is denoted as ρ_{SST}. Since there are no free charge carriers in the cap and insulator layer and the bottom surface state is screened, only the charge density in the top surface states is manipulated and $\rho(z)$ equals zero elsewhere. If a negative energy potential U_{TG} is applied to the sample, as shown in Fig. 3.14, the number of electrons populating the top surface states is increased, implying $\rho_{\mathrm{SST}} < 0$. Analogous, $U_{\mathrm{TG}} > 0$ would lead to $\rho_{\mathrm{SST}} > 0$. Note that the charge density $\rho(z)$ gives the variation of the amount of charge per unit volume. However, we are interested in the change in carrier density Δn. The relation between $\rho(z)$ and Δn is given by

$$\Delta n = -\frac{1}{e}\int_{z_1}^{z_2} \rho(z)\,\mathrm{d}z, \tag{3.2}$$

where z_1 and z_2 are the coordinates of the bottom and top of the sample structure, respectively. Due to

$$\rho(z) = \begin{cases} \rho_{\mathrm{SST}} & 0.5d_{\mathrm{TI}} - d_{\mathrm{SST}} \leq z \leq 0.5d_{\mathrm{TI}} \\ 0 & \text{elsewhere} \end{cases},$$

we define $\Delta n \equiv \Delta n_{\mathrm{SST}}$.

Now, we can use Maxwell's first equation (Gauss' law) to describe the electrostatics for our model. The association of electric field $\overrightarrow{E}$ to charge density ρ is defined by $\nabla \overrightarrow{D} = \rho$, involving the electric displacement field $\overrightarrow{D} = \varepsilon_0 \varepsilon_{\mathrm{r}} \overrightarrow{E}$, where ε_0 is the vacuum permittivity. The electric potential $V(z)$ satisfies $\overrightarrow{E} = -\nabla V$. The corresponding energy potential equals $U(z) = -eV(z)$. With the help of previous equations we find the Poisson equation for $U(z)$:

$$\partial_z [\varepsilon_{\mathrm{r}}(z)\, \partial_z U(z)] = \frac{e}{\varepsilon_0} \rho(z). \tag{3.3}$$

The solution of the Poisson equation can be obtained by two-fold integration

$$U(z) = \frac{e}{\varepsilon_0} \int_{z_0}^{z} \mathrm{d}z' \frac{1}{\varepsilon_{\mathrm{r}}(z')} \int_{z_0'}^{z'} \mathrm{d}z'' \rho(z''), \tag{3.4}$$

where z_0 and z_0' are arbitrary constants. In order to find a unique solution, we need to fix the two integration constants. This is done by imposing suitable boundary conditions. In the context of model I, we set $z_0 = z_0' = z_{\mathrm{bot}}$, where $z_{\mathrm{bot}} = -0.5d_{\mathrm{TI}}$ is the z-coordinate of the bottom surface of the 3D TI. Since the bottom surface is screened by the mobile carriers at the top surface, energy potential and electric field are set to zero at this location, resulting in $U(z_{\mathrm{bot}}) = 0$ and $\partial_z U(z_{\mathrm{bot}}) = 0$, respectively. Thus, we are able to rewrite Eq. 3.4 to

$$U(z) = -\frac{e^2 \Delta n_{\mathrm{SST}}}{\varepsilon_0} \int_{z_{\mathrm{bot}}}^{z} \mathrm{d}z' \frac{c(z')}{\varepsilon_{\mathrm{r}}(z')}, \tag{3.5}$$

with $c(z)$ being a coefficient depending on the shape of $\rho(z)$. If we choose the density profile to be uniform in the top surface region, i.e. $\rho(z) = -e\Delta n_{\mathrm{SST}}/d_{\mathrm{SST}}$ for $0.5d_{\mathrm{TI}} - d_{\mathrm{SST}} \leq z \leq 0.5d_{\mathrm{TI}}$, and $\rho(z) = 0$ elsewhere, as sketched in Fig. 3.14, we find

$$c(z) = \begin{cases} 1 & 0.5d_{\mathrm{TI}} < z < z_{\mathrm{TG}} \\ \frac{1}{2} & 0.5d_{\mathrm{TI}} - d_{\mathrm{SST}} \leq z \leq 0.5d_{\mathrm{TI}} \\ 0 & z < 0.5d_{\mathrm{TI}} - d_{\mathrm{SST}} \end{cases}.$$

For this choice of $\rho(z)$, the energy potential $U(z)$ is quadratic in the region of the top surface and linear for $0.5d_{\mathrm{TI}} < z < z_{\mathrm{TG}}$. Eq. 3.5 can be used to calculate the energy potential U_{i} at

the interface Hg(Mn)Te/CMT:

$$U_{\mathrm{i}} \equiv U\left(0.5 d_{\mathrm{TI}}\right) = -\frac{1}{2}\frac{e^2 \Delta n_{\mathrm{SST}}}{\varepsilon_0 \varepsilon_{\mathrm{SST}}} d_{\mathrm{SST}}, \tag{3.6}$$

where $\varepsilon_{\mathrm{SST}}$ is the relative permittivity of the top surface states. Given that there are no free charge carriers in the cap and insulator layer, the displacement field is constant for $z > 0.5 d_{\mathrm{TI}}$. Putting the top-gate-electrode on top of the insulator ($z = z_{\mathrm{TG}} \equiv 0.5 d_{\mathrm{TI}} + d_{\mathrm{CMT}} + d_{\mathrm{ins}}$, with d_{CMT} and d_{ins} being the thicknesses of cap and insulator layer respectively), we thus find the energy potential at the top-gate to be

$$U_{\mathrm{TG}} \equiv U\left(z_{\mathrm{TG}}\right) = -\frac{e^2 \Delta n_{\mathrm{SST}}}{\varepsilon_0}\left(\frac{1}{2}\frac{d_{\mathrm{SST}}}{\varepsilon_{\mathrm{SST}}} + \frac{d_{\mathrm{CMT}}}{\varepsilon_{\mathrm{CMT}}} + \frac{d_{\mathrm{ins}}}{\varepsilon_{\mathrm{ins}}}\right), \tag{3.7}$$

where $\varepsilon_{\mathrm{CMT}}$ and $\varepsilon_{\mathrm{ins}}$ are the relative permittivities of cap and insulator materials, respectively. Eq. 3.7 defines the relation between change in carrier density Δn_{SST} and energy potential U_{TG}.

Model I is based on the assumption that the energy potential at the position of the TG is a result of the application of the top-gate metals titanium and gold. Its value is determined by the difference between the work functions of HgTe and Ti/Au ($\Delta W = W_{\mathrm{HgTe}} - W_{\mathrm{Ti,Au}}$). Hence, equation 3.7 can be rewritten as

$$\Delta n_{\mathrm{SST}} = -\frac{\varepsilon_0 (W_{\mathrm{HgTe}} - W_{\mathrm{Ti,Au}})}{e^2}\left(\frac{1}{2}\frac{d_{\mathrm{SST}}}{\varepsilon_{\mathrm{SST}}} + \frac{d_{\mathrm{CMT}}}{\varepsilon_{\mathrm{CMT}}} + \frac{d_{\mathrm{ins}}}{\varepsilon_{\mathrm{ins}}}\right)^{-1}. \tag{3.8}$$

Due to $\Delta W < 0$, $\Delta n_{\mathrm{SST}} > 0$ applies, i.e. electrons are accumulated in the active layer. To experimentally determine the increase of the n-type density, two samples were fabricated for each wafer material under investigation, one with top-gate-electrode and one without, and measured afterwards. Since the value of $d_{\mathrm{ins}}/\varepsilon_{\mathrm{ins}}$ is different for SiO_2/Si_3N_4 and HfO_a insulator, both insulator types were used as gate-dielectric. The charge carrier densities of the samples are identified by magneto-transport measurements as described in Subsec. 2.2.2. The density change is calculated via $\Delta n_{\mathrm{SST}} = n_{\mathrm{with\ TG}} - n_{\mathrm{without\ TG}}$. Note that for samples possessing a top-gate-electrode, the TG was grounded during the measurements so that the change in carrier density can be attributed solely to the top-gate fabrication process. In total 17 different wafer materials are analyzed. The used wafers and their corresponding cap layer thicknesses d_{CMT} are listed in Appx. A.2. It should be mentioned that due to the shortage of some wafer materials not both insulator types can be investigated for all wafers. For sufficiently available wafer materials, more than one sample having a specific insulator type is examined to obtain more data and to verify reproducibility. Analogous to Subsec. 3.1.2, a density variance of $1 \cdot 10^{11}\ \frac{1}{\mathrm{cm}^2}$ within a wafer due to its growth-related inhomogeneity is assumed. For this reason, an error of $1 \cdot 10^{11}\ \frac{1}{\mathrm{cm}^2}$ is applied to both the

description	material	thickness d [nm]	relative permittivity ε_r	work function W [eV]
top-gate	Ti/Au	5/100		4.33/5.1
insulator type 1	SiO_2/Si_3N_4	60/50	3.9/7.5	
insulator type 2	HfO_a	15	23.9	
cap	CMT		12.44	
top surface states	Hg(Mn)Te	10	3	4.13

Table 3.5.: Parameters used to model the electrostatics in our devices. The thickness of the cap layer d_CMT is a variable depending on the underlying wafer (cf. Appx. A.2).

value of $n_{\text{with TG}}$ and the value of $n_{\text{without TG}}$. The error of Δn_SST results from Gaussian error propagation. Note that we are not able to specify the exact work function $W_\mathrm{Ti,Au}$ of a metal stack consisting of 5 nm Ti and 100 nm Au. However, as a first validity test of model I, it is sufficient to determine $\Delta n_\mathrm{SST,min}$ and $\Delta n_\mathrm{SST,max}$ and to check if the experimental obtained data are within this range. To calculate $\Delta n_\mathrm{SST,min}$ and $\Delta n_\mathrm{SST,max}$ the work functions of pure titanium W_Ti and gold W_Au are used, respectively. The actual value of $W_\mathrm{Ti,Au}$ has to be between these two. For a given insulator type, the only variable in Eq. 3.8 that differs from wafer to wafer is the thickness of the cap layer. Therefore, to apply model I to the experimentally obtained data, a plot of Δn_SST over d_CMT is applied. All other parameters required for Eq. 3.8 are listed in Tab. 3.5. The contribution of a SiO_2/Si_3N_4 superlattice dielectric can be determined via $d_\mathrm{ins}/\varepsilon_\mathrm{ins} = d_{SiO_2}/\varepsilon_{SiO_2} + d_{Si_3Ni_4}/\varepsilon_{Si_3Ni_4}$. It is noted that, inferred from Ref. [45], we do not use the relative permittivity of bulk HgTe ($\varepsilon_\mathrm{HgTe} = 21$) for the permittivity of the top surface states, but set $\varepsilon_\mathrm{SST} = 3$. Some of the used wafer materials possess Mn dopants in the HgTe layer. Since the manganese content is less than 3 % for all of them, we assume that $\varepsilon_\mathrm{SST,HgMnTe} \approx \varepsilon_\mathrm{SST,HgTe}$ and $W_\mathrm{HgTe} \approx W_\mathrm{HgMnTe}$ are valid.

The results for samples with HfO_a and SiO_2/Si_3N_4 insulators are shown as black squares in Fig. 3.15a) and b), respectively. Given that the device possessing a hafnium oxide insulator, which was fabricated of wafer QC0478, encountered issues during fabrication (cf. Subsec. 3.1.4), its corresponding data point is displayed as a gray diamond and removed from the evaluation. In both figures, $\Delta n_\mathrm{SST,max}$ and $\Delta n_\mathrm{SST,min}$ calculated according to Eq. 3.8 are drawn as a solid and dashed light green line respectively. Taking their errors into account, all data points for samples with HfO_a insulator are within $\Delta n_\mathrm{SST,max}$ and $\Delta n_\mathrm{SST,min}$. However, to consider model I as a satisfactory explanation for the experimentally observed increase of the n-type density, the data of the samples with SiO_2/Si_3N_4 insulator have to be within $\Delta n_\mathrm{SST,max}$ and $\Delta n_\mathrm{SST,min}$ as well. As can be seen from Fig. 3.15b), this is not the case. For devices possessing a SiO_2/Si_3N_4 insulator, there is only one data point within this range, even taking into account the errors. In the context of model I, a smaller n-type doping is expected for samples having a SiO_2/Si_3N_4 dielectric due to the greater layer thickness of the superlattice (110 nm) compared to the HfO_a insulator (15 nm). In the experiment, however,

it is revealed that the increase of electron density is comparable for both insulator types. For

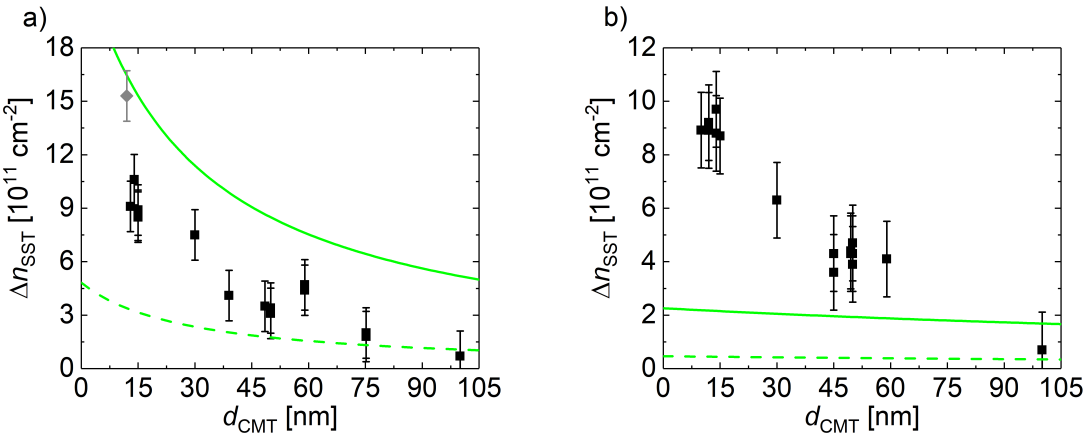

Figure 3.15.: Increase of the charge carrier density Δn_{SST} caused by top-gate application for a) HfO_a and b) SiO_2/Si_3N_4 insulators in dependence on the cap layer thickness d_{CMT}. The data points (black squares) are plotted together with their corresponding errors determined by Gaussian error propagation. $\Delta n_{\mathrm{SST,max}}$ and $\Delta n_{\mathrm{SST,min}}$ are calculated according to Eq. 3.8 and drawn as a solid and dashed light green line respectively. The data point removed from the evaluation is displayed as a gray diamond.

this reason, model I has to be discarded as a possible explanation for the lithography-related doping of our devices. The fact that the increase of the charge carrier density is only slightly (or possibly not at all) dependent on the type of insulator suggests that a (still unknown) mechanism underneath the dielectric layer contributes significantly to the accumulation of electrons in the active layer. This approach is discussed using a model extended to include quantum mechanical aspects in Subsec. 3.3.2. In particular, the extension includes the possible tunneling of electrons through the cap into the Hg(Mn)Te layer.

Although model I fails in determining the actual density of gated samples at $V_{\mathrm{TG}} = 0\,\mathrm{V}$, it may be possible to correctly predict the change of the charge carrier density Δn_{SST} for $V_{\mathrm{TG}} \neq 0$ using the introduced description of electrostatics. More precisely, model I may allow us to calculate the response of the carrier density to an applied top-gate voltage. For this purpose, the same modeling and assumptions as before can be used. Thus, together with the relation $U_{\mathrm{TG}} = -eV_{\mathrm{TG}}$, Eq. 3.7 can be rewritten as:

$$\Delta n_{\mathrm{SST}} = \frac{\varepsilon_0 V_{\mathrm{TG}}}{e} \left(\frac{1}{2} \frac{d_{\mathrm{SST}}}{\varepsilon_{\mathrm{SST}}} + \frac{d_{\mathrm{CMT}}}{\varepsilon_{\mathrm{CMT}}} + \frac{d_{\mathrm{ins}}}{\varepsilon_{\mathrm{ins}}} \right)^{-1}. \tag{3.9}$$

Note that $\Delta n_{\mathrm{SST}} = n\,(V_{\mathrm{TG}}) - n\,(0\,\mathrm{V})$ now describes the change in density in dependence on applied top-gate voltage V_{TG}. Based on Eq. 3.9, a theoretical top-gate action G_{TG} can be

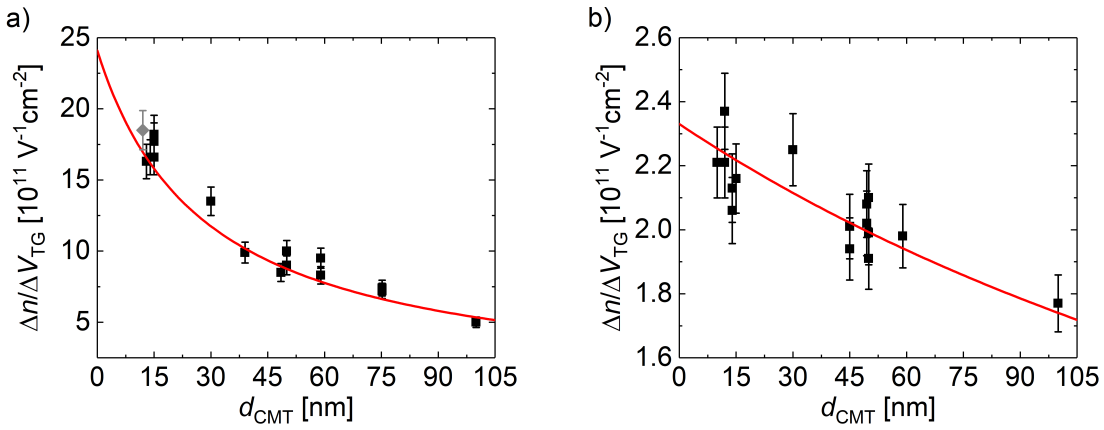

Figure 3.16.: Top-gate action $\Delta n/\Delta V_{\mathrm{TG}}$ in dependence on the thickness of the cap layer d_{CMT} for samples with a) HfO_a and b) SiO_2/Si_3N_4 insulators. The experimentally determined data points are shown in black. The TG action predicted by Eq. 3.10 is displayed as a red line in both graphs. The data point removed from the evaluation is depicted as a gray diamond.

derived for the samples as a function of insulator type and cap layer thickness:

$$G_{\mathrm{TG}} = \frac{\Delta n}{\Delta V_{\mathrm{TG}}} = \frac{\varepsilon_0}{e}\left(\frac{1}{2}\frac{d_{\mathrm{SST}}}{\varepsilon_{\mathrm{SST}}} + \frac{d_{\mathrm{CMT}}}{\varepsilon_{\mathrm{CMT}}} + \frac{d_{\mathrm{ins}}}{\varepsilon_{\mathrm{ins}}}\right)^{-1}, \tag{3.10}$$

where $\Delta n = n\left(V_{\mathrm{TG},2}\right) - n\left(V_{\mathrm{TG},1}\right)$ is the response of the carrier density to an altered top-gate voltage $\Delta V_{\mathrm{TG}} = V_{\mathrm{TG},2} - V_{\mathrm{TG},1}$. It is noted that Δn is independent of $n\left(0\,\mathrm{V}\right)$ due to the consideration of differences. Again, a reduced effect is expected for the SiO_2/Si_3N_4 superlattice due to the greater thickness of this insulator layer. In order to be able to compare Eq. 3.10 with experimental data, the same samples considered above are examined. For this purpose, the TG action G_{TG} is determined for each device possessing a top-gate-electrode as described in Subsec. 2.2.3. The parameters required for the theoretical prediction of the top-gate actions can be found in Tab. 3.5 and Appx. A.2.

The results for samples with HfO_a and SiO_2/Si_3N_4 insulators are shown as black squares in Fig. 3.16a) and b), respectively. The corresponding errors of the experimentally obtained data are calculated by Gaussian error propagation. The top-gate action $G_{\mathrm{TG}}\left(d_{\mathrm{CMT}}\right)$ predicted by Eq. 3.10 is delineated as a red line in both graphs. One is able to observe that the experimentally obtained data and the model prediction coincide for both insulator types in good manner. This is especially the case if the error bars are taken into account. As expected, based on Eq. 3.10, the measured samples having a SiO_2/Si_3N_4 dielectric exhibit lower top-gate actions due to the greater thickness of the superlattice. However, it is conspicuous that some of the samples with hafnium oxide insulator exhibit a slightly larger top-gate action than it is predicted by model I. An explanation for this observation might be given by the used thickness of the HfO_a dielectric layer $d_{\mathrm{ins}} = 15\,\mathrm{nm}$. After its growth in an ALD chamber,

the insulator should have a thickness of 15 nm. However, tests have shown that the actual thickness of the insulator lies between 13 nm and 15 nm. A reduced value of d_{ins} in Eq. 3.10 would result in increased values of G_{TG}.

Analogous to the top-gate action, the back-gate action G_{BG} of samples grown on n-doped GaAs substrates can be determined by describing the electrostatics in the system. For this purpose, the same modeling and assumptions can be used. In this case, the relevant layers of the device to model the electrostatics when a back-gate voltage V_{BG} is applied are ZnTe interlayer, CdTe substrate, CMT buffer, and the active layer (cf. Subsec. 2.2.1). Furthermore, it is assumed that the spatial extent d_{SSB} of the probability density of the surface state located at the bottom surface reaches 10 nm into the Hg(Mn)Te layer as well. The relative permittivity of the bottom surface state is set in analogy to the one of the top surface states to $\varepsilon_{\mathrm{SSB}} = 3$. Thus, the back-gate action can be calculated by (cf. Eq. 3.10)

$$G_{\mathrm{BG}} = \frac{\Delta n}{\Delta V_{\mathrm{BG}}} = \frac{\varepsilon_0}{e}\left(\frac{1}{2}\frac{d_{\mathrm{SSB}}}{\varepsilon_{\mathrm{SSB}}} + \frac{d_{\mathrm{CMT,buffer}}}{\varepsilon_{\mathrm{CMT}}} + \frac{d_{\mathrm{CdTe}}}{\varepsilon_{\mathrm{CdTe}}} + \frac{d_{\mathrm{ZnTe}}}{\varepsilon_{\mathrm{ZnTe}}}\right)^{-1}, \tag{3.11}$$

with $\Delta n = n\,(V_{\mathrm{BG},2}) - n\,(V_{\mathrm{BG},1})$ being the response of the charge carrier density to an altered back-gate voltage $\Delta V_{\mathrm{BG}} = V_{\mathrm{BG},2} - V_{\mathrm{BG},1}$, $d_{\mathrm{CMT,buffer}} \sim 10\,\mathrm{nm}$ the thickness of the CMT buffer layer, $d_{\mathrm{CdTe}} \approx 4\,\mu\mathrm{m}$ the thickness of the CdTe substrate with relative permittivity $\varepsilon_{\mathrm{CdTe}} = 10.2$, and $d_{\mathrm{ZnTe}} \sim$ nm the thickness of the ZnTe interlayer with relative permittivity $\varepsilon_{\mathrm{ZnTe}} = 10.4$. Since $d_{\mathrm{CdTe}} \gg d_{\mathrm{SSB}}, d_{\mathrm{CMT,buffer}}, d_{\mathrm{ZnTe}}$ applies, Eq. 3.11 can be simplified to

$$G_{\mathrm{BG}} \approx \frac{\varepsilon_0 \varepsilon_{\mathrm{CdTe}}}{e d_{\mathrm{CdTe}}}. \tag{3.12}$$

Therefore, the BG action of our three-dimensional topological insulator samples is almost independent of the thickness of the buffer layer and hence nearly independent of the underlying wafer. Small deviations between devices fabricated of different wafer materials can be derived from the differences in buffer and cadmium telluride layer thicknesses. By substituting the numbers, we find the back-gate action to be $G_{\mathrm{BG}} \approx 0.14 \cdot 10^{11}\,\frac{1}{\mathrm{Vcm^2}}$. This value is in good agreement with the experimental determined BG action of sample QC0461 I (cf. Subsec. 2.2.3). In fact, both values are identical.

3.3.2. Increase of the charge carrier density via tunneling electrons: model II

The next step in explaining the lithography-induced density increase is to extend model I to include quantum mechanical aspects. In this context, we assume that quasi-unbound electrons at the interface CMT/insulator, which are generated by the application of dielectric and top-gate-electrode, can tunnel through the cap into the active layer. The positively charged atomic cores left behind at the interface cause an accumulation of electrons in the mercury telluride layer, similar to an applied positive top-gate voltage. This toy model, hereinafter referred to as model II, is described in detail below:

Since the CMT cap layer of each sample possesses a finite extent, there are dangling bonds at the surface of the layer. If the CMT layer is not covered by a different material, surface reconstructions take place to minimize the internal energy of the system. However, if the cap is covered by another material, like the top-gate-dielectrics HfO_a and SiO_2/Si_3N_4, the surface reconstructions are disturbed and the dangling bonds remain at the interface CMT/insulator. The formation of covalent bonds between tellurium and either hydroxy (ALD) or silylene (PECVD) results in an unpaired electron per Te atom. These electrons are referred to as quasi-free radicals and are easy to remove from the tellurium atom. The disentanglement may be enabled by the changed electrostatic environment after application of the top-gate metals titanium and gold or by thermal excitation. During the lithographic fabrication process, macroscopic as well as microscopic samples are heated to 80 °C (cf. Appx. B and Appx. C), which is equivalent to applying a thermal excitation of about $E_{\mathrm{thermal}} \approx 30\,\mathrm{meV}$. In the context of model II, we assume that the quasi-free electrons (QFE) are able to tunnel through the CMT cap into the active layer leaving behind positively charged atomic cores at the interface. Tunneling back is extremely unlikely and therefore negligible. The result of this mechanism is similar to an applied positive top-gate voltage and leads to an increase of the electron density in the Hg(Mn)Te layer. Given that charge carriers can be trapped at the interface CMT/insulator due to the existence of dangling bonds and positively charged atomic cores, the states at this interface are referred to as trap states (TS) in the following. The positively charged atoms left behind lead to an energy potential $U_{\mathrm{TS}} < 0$ at the TS.

To model the electrostatics in the system, the energy potential sketched in Fig. 3.17 is used. Note that z still indicates the growth direction. The comparison of the energy potentials $U(z)$ used for the modeling of the electrostatics for model I and model II (cf. Figs. 3.14 and 3.17) shows similar profiles in the regions of cap and active layer. The difference is that in model II the energy potential U_{i} at the interface Hg(Mn)Te/CMT ($z = 0.5d_{\mathrm{TI}}$) is determined by U_{TS} at the position of the trap states ($z = z_{\mathrm{TS}} \equiv 0.5d_{\mathrm{TI}} + d_{\mathrm{CMT}}$) instead of U_{TG} at $z = z_{\mathrm{TG}}$. In addition, since the TS are located at the interface CMT/insulator, it is not required to include the dielectric layer in the consideration. It is noted that the value of U_{TS} may nevertheless depend on the insulator type, as the number and transmission probability of quasi-free electrons may be different for HfO_a and SiO_2/Si_3N_4. One possible explanation for the difference would be that the unpaired electrons are bound slightly differently to the Te atoms. Using the same assumptions made for model I, we are able to calculate the increase of the charge carrier density Δn_{SST} due to application of gate-dielectric and top-gate metals as a function of energy potential U_{TS} to (cf. Eq. 3.7)

$$\Delta n_{\mathrm{SST}} = -\frac{\varepsilon_0 U_{\mathrm{TS}}}{e^2}\left(\frac{1}{2}\frac{d_{\mathrm{SST}}}{\varepsilon_{\mathrm{SST}}} + \frac{d_{\mathrm{CMT}}}{\varepsilon_{\mathrm{CMT}}}\right)^{-1}. \tag{3.13}$$

The next step is to determine the energy potential U_{TS}. Given that U_{TS} is related to tunneling electrons, we need to calculate the tunnel probability. For this purpose, some simplifying

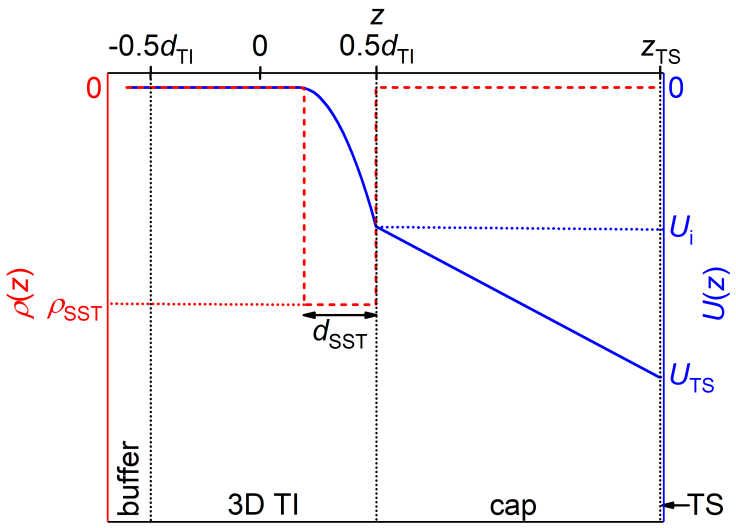

Figure 3.17.: Energy potential $U(z)$ and charge density $\rho(z)$ used to model the electrostatics for model II are shown in blue and red, respectively. The charge density is constant ($\rho(z) = \rho_{\mathrm{SST}}$) in a region of thickness d_{SST} at the top surface of the 3D TI layer and zero otherwise. The energy potential is quadratic in this region and takes the value U_{i} at the interface 3D TI/cap layer. At the position of the trap states ($z = z_{\mathrm{TS}}$), $U(z) = U_{\mathrm{TS}}$ holds.

assumptions are made. First, we assume that all quasi-free electrons that are able to tunnel have exactly the same energy E_{QFE}. We use this energy as an energetic reference point for our calculations and set $E_{\mathrm{QFE}} = 0$. In the case of a rectangular potential barrier of height $U_{\mathrm{B},0}$, the transmission probability T is in good approximation given by

$$T \approx e^{-\frac{2}{\hbar}\sqrt{2m_{\mathrm{eff}}(U_{\mathrm{B},0}-E)}d}, \tag{3.14}$$

where d is the thickness of the tunnel barrier, m_{eff} is the effective mass, and E the energy of the tunneling particle. To calculate the transmission probability of an arbitrary shaped potential barrier $U_{\mathrm{B}}(z)$, the so-called Wentzel-Kramers-Brillouin (WKB) approximation is used [62]. The arbitrary potential is approached by placing many narrow rectangles one behind the other. Using an infinite amount of infinitesimal rectangles, we find the transmission probability to be

$$T \approx e^{-\frac{2}{\hbar}\int_0^d \sqrt{2m_{\mathrm{eff}}[U_{\mathrm{B}}(z)-E]}\mathrm{dz}}. \tag{3.15}$$

The next simplifying assumption to be made is that the potential barrier $U_{\mathrm{B}}(z)$ has the same height for all tunneling quasi-free electrons. In the actual device, the height of $U_{\mathrm{B}}(z)$ changes with each tunneled electron, i.e., by choosing an invariant potential barrier, we basically use an averaged barrier height. Since the quasi-free electrons tunnel from the trap states through the CMT cap into the active layer, the potential barrier is located in the region $0.5d_{\mathrm{TI}} \leq z \leq z_{\mathrm{TS}}$ and its height is denoted by E_{CMT}. Due to the linear drop of E_{CMT}

across the cap layer, we obtain a triangular shaped potential barrier, which can be written as

$$U_{\mathrm{B}}(z) = \frac{E_{\mathrm{CMT}}}{d_{\mathrm{CMT}}}(z - 0.5 d_{\mathrm{TI}}). \tag{3.16}$$

At this point it should be mentioned that the value of E_{CMT} may differ slightly for both insulator types. The reason for this is that the energy of the quasi-free electrons E_{QFE} may depend on the choice of dielectric and the height of the potential barrier is considered relative to this energy. As the quasi-free electrons originate from tellurium atoms of the CMT layer, which is also the tunnel barrier, we expect the barrier height to be significantly smaller than, for example, the band edge offset between CMT and HgTe ($\approx 0.5\,\mathrm{eV}$ [63]), i.e. that $E_{\mathrm{CMT}} \ll 0.5\,\mathrm{eV}$ applies. In addition, we assume that the tunnel mechanism is independent of the manganese content y in the active layer, as long as $y \leq 3\,\%$ holds. Thus, after integration, we are able to rewrite Eq. 3.15 to

$$T \approx e^{-\frac{4}{3\hbar}\sqrt{2 m_{\mathrm{eff}} E_{\mathrm{CMT}}} d_{\mathrm{CMT}}} = e^{-k d_{\mathrm{CMT}}}, \tag{3.17}$$

with m_{eff} being the effective mass of the quasi-free electrons and $k = 4\sqrt{2 m_{\mathrm{eff}} E_{\mathrm{CMT}}}/(3\hbar)$ a constant wave number. The number of tunneling electrons N_{tunnel} is determined by $N_{\mathrm{tunnel}} = N_{\mathrm{total}} T$, where N_{total} is the total number of quasi-free electrons that are able to tunnel through the cap into the active layer. Each tunneled particle leaves behind a positively charged atomic core. The top layers of the sample can now be considered as a capacitor, whereat the TS represent one plate, the top surface states the other and the CMT layer the dielectric in between. Then the relation between energy potential U_{TS} and the number of positively charged atomic cores is given by

$$U_{\mathrm{TS}} = -\frac{e^2 N_{\mathrm{total}} T}{C}, \tag{3.18}$$

with C being the capacitance of the capacitor. This capacitance can be calculated via

$$C = \varepsilon_0 A \left(\frac{1}{2}\frac{d_{\mathrm{SST}}}{\varepsilon_{\mathrm{SST}}} + \frac{d_{\mathrm{CMT}}}{\varepsilon_{\mathrm{CMT}}} \right)^{-1}, \tag{3.19}$$

where A is the area of the capacitor. Thus, we find the energy potential to be

$$U_{\mathrm{TS}} = -\frac{e^2}{\varepsilon_0} n_{\mathrm{total}} \left(\frac{1}{2}\frac{d_{\mathrm{SST}}}{\varepsilon_{\mathrm{SST}}} + \frac{d_{\mathrm{CMT}}}{\varepsilon_{\mathrm{CMT}}} \right) e^{-k d_{\mathrm{CMT}}}, \tag{3.20}$$

with $n_{\mathrm{total}} = N_{\mathrm{total}}/A$ being the density of quasi-free electrons that are able to tunnel through the cap into the Hg(Mn)Te layer. Substituting Eq. 3.20 into Eq. 3.13, we get

$$\Delta n_{\mathrm{SST}} = n_{\mathrm{total}} e^{-k d_{\mathrm{CMT}}}. \tag{3.21}$$

According to model II, the number of tunneling particles is directly proportional to the ac-

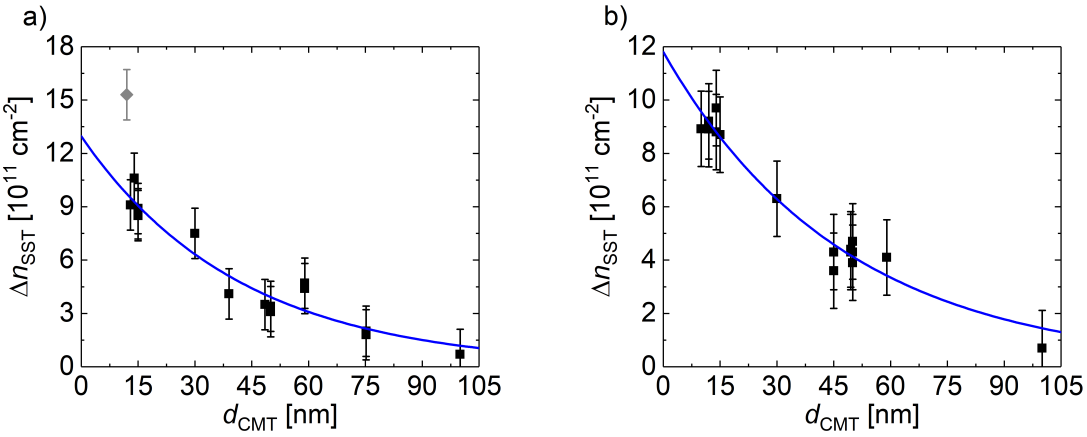

Figure 3.18.: Application of model II to the experimentally obtained data already presented in Fig. 3.15. The dependence of the lithography-induced density increase Δn_{SST} for a) HfO_a and b) SiO_2/Si_3N_4 insulators on the cap layer thickness d_{CMT} is shown. Fits according to Eq. 3.21 are displayed as blue lines.

insulator	fit parameter	
	n_{total} [10^{11} $\frac{1}{\mathrm{cm}^2}$]	k [$\frac{1}{\mathrm{nm}}$]
HfO_a	12.96±0.86	0.0239±0.0025
SiO_2/Si_3N_4	11.80±0.41	0.0210±0.0013

Table 3.6.: List of the parameters used to fit the experimentally obtained data according to Eq. 3.21.

cumulation of electrons in the active layer. Such a result is in line with our expectation, since each quasi-free electron that tunnels through the cap into the Hg(Mn)Te layer increases the carrier density in the latter by one. The next step is to apply this toy model to the experimentally obtained data. For this purpose, the same data already presented in Subsec. 3.3.1 (cf. Fig. 3.15) are used. It should be mentioned that the values of n_{total} and k are unknown and may differ for the two insulator types. For this reason, the data are fitted by exponential functions, whereat we set appropriate upper and lower bounds for the parameters n_{total} and k. For all samples possessing the same dielectric, the fit parameters have to be identical, since the mechanisms at the interface CMT/insulator are independent of the layer thicknesses underneath and thus of the wafer material used.

The outcome is shown in Fig. 3.18a) and b) for samples with HfO_a and SiO_2/Si_3N_4 insulators, respectively. The values of the fit parameters for both insulator types are listed in Tab. 3.6. It can be seen that, taking into account the errors, all data points are on the fit curve. This is valid for both types of dielectric. Since the experimental data can be described in a good manner by model II, the fit parameters obtained are to be analyzed next. As expected, the values of n_{total} and k are slightly different for HfO_a and SiO_2/Si_3N_4 insulators. We speculate that the unpaired electrons, which are generated when the dielectrics

are applied to the sample, are bound to the Te atoms to slightly different degrees depending on the insulator type. This can lead to a minor deviation in density and energy of the quasi-free electrons, which in turn would affect the values of n_{total} and E_{CMT}. By means of the relation $k = 4\sqrt{2m_{\mathrm{eff}}E_{\mathrm{CMT}}}/(3\hbar)$ the height of the tunnel barrier can be derived. If the effective mass of the electrons is set in analogy to Subsec. 2.1.3 $m_{\mathrm{eff}} = 0.02m_{\mathrm{e}}$, then $E_{\mathrm{CMT}}^{\mathrm{HfO_a}} = (0.61 \pm 0.13)\,\mathrm{meV}$ and $E_{\mathrm{CMT}}^{\mathrm{SiO_2/Si_3N_4}} = (0.474 \pm 0.059)\,\mathrm{meV}$ are obtained. The calculated barrier heights are therefore about three orders of magnitude smaller than typical band edge offsets in our devices, which is in line with the expectation as well. Based on the crystal structure of HgTe (cf. Sec. 2.1 and Fig. 2.1), the density of the tellurium atoms at the surface of the CMT layer can be roughly estimated to $n_{\mathrm{Te}} \approx a_0^{-2} = 2.4{\cdot}10^{14}\,\frac{1}{\mathrm{cm}^2}$. Since it is extremely unlikely that every unpaired electron per Te atom turns into a quasi-free electron with sufficient energy for tunneling, $n_{\mathrm{total}} < n_{\mathrm{Te}}$ should be valid. Tab. 3.6 shows that $n_{\mathrm{Te}}/n_{\mathrm{total}} \approx 200$ applies and therefore $n_{\mathrm{total}} < n_{\mathrm{Te}}$ is also fulfilled. Hence, we suppose that electrons can tunnel from the trap states, which form at the interface CMT/insulator, through the cap into the Hg(Mn)Te layer. The application of this hypothesis allows a qualitative plausible description and a correct quantitative prediction of the experimentally found lithography-induced density increase in our devices. The underlying tunnel mechanism is described by model II using simplifying assumptions. Since the increase of the carrier density can therefore be attributed solely to physical processes, we conclude that the lithographic fabrication steps do not unintentionally react chemically with our heterostructures, thus avoiding a reduction in the quality of the active layer.

By determining the fit parameters n_{total} and k, another method for verifying the applicability of model II is given. For this purpose, the experimentally obtained values for the energy potential U_{TS} have to be compared with those calculated by the model. To find the former, one can use Eq. 3.13 and substitute for Δn_{SST} the experimentally derived density increase of each investigated wafer due to gate-dielectric and top-gate-electrode application. The model prediction is specified via Eq. 3.20. The required parameters can be found in Tab. 3.5 and Tab. 3.6. The quantities subject to error are the measured increase of the charge carrier density and the thickness of the CMT cap layer[7]. The error of the energy potential results from Gaussian error propagation. In Fig. 3.19, U_{TS} is plotted as a function of the cap layer thickness d_{CMT}. a) shows the experimentally obtained data (black squares) for HfO_a insulator, while b) presents the data for SiO_2/Si_3N_4 dielectric. The prediction of model II calculated according to Eq. 3.20 is drawn as a blue line in both graphs. It can be seen that model II again coincides well with the experimentally obtained data within the limits of the errors. Since the energy potential can be written as $U_{\mathrm{TS}} = c_1 e^{-kd_{\mathrm{CMT}}} + c_2 d_{\mathrm{CMT}} e^{-kd_{\mathrm{CMT}}}$ (cf. Eq. 3.20), where c_1 and c_2 are two negative constants, $|U_{\mathrm{TS}}|$ increases for small d_{CMT} and approaches zero for $d_{\mathrm{CMT}} \to \infty$. This characteristic is given by the counteracting of

[7] It is assumed that the X-ray measurement, which is used to determine the thickness of the CMT layer, has an inaccuracy of 1 nm.

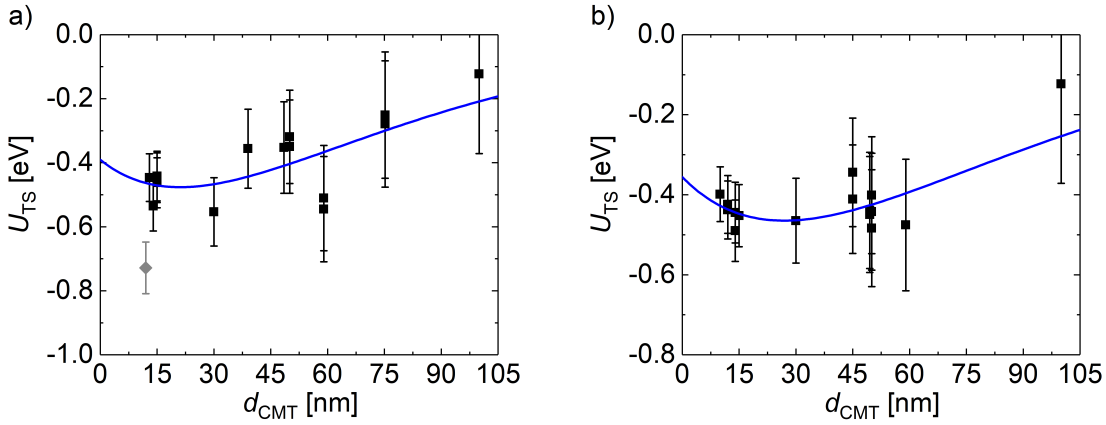

Figure 3.19.: Energy potential U_{TS} at the trap states in dependence on the thickness of the cap layer d_{CMT} for samples with a) HfO_a and b) SiO_2/Si_3N_4 dielectrics. The experimentally obtained data points are presented in black. The prediction of model II calculated according to Eq. 3.20 is displayed by a blue line. The data point removed from the evaluation is depicted as a gray diamond.

the inverse capacitance C^{-1} of the capacitor TS/top surface states (increases with d_{CMT}) and the transmission probability T of the quasi-free electrons (decreases with d_{CMT}), as $|U_{\mathrm{TS}}| \sim TC^{-1}$ (cf. Eq. 3.18) applies. The fact that this behavior can also be observed for the experimentally determined values of U_{TS} is another indication that model II is likely to be a simplified description of the actual mechanism leading to the n-type density increase in our devices due to lithographic processing.

To reduce the lithography-induced n-type doping, one can grow thicker cap layers. As it is shown in Fig. 3.18, the increase of the density Δn_{SST} decreases with increasing cap thickness d_{CMT}. For example, the value of Δn_{SST} is already halved when the thickness of the CMT layer is changed from 14 nm to about 40 nm. This applies to both insulator types. In addition, according to reference [57], an increased d_{CMT} also improves the overall quality of three-dimensional HgTe layers. This improvement results in enhanced charge carrier mobilities of the samples. Hence, the growth of an at least 30 nm thick cap layer is suggested. One has to consider, however, that the 3D topological insulator phase can only be realized when a tensile strain is applied to the Hg(Mn)Te layer (cf. Subsec. 2.1.1). Once the active layer reaches a certain critical thickness, strain is released by the formation of different types of lattice defects such as dislocations lines. It has been shown that the total thickness of the layer stack CMT/Hg(Mn)Te/CMT grown on a CdTe substrate should not exceed 250 nm [64]. Therefore, for a typical active layer thickness of 70 nm, a CMT cap layer of the order of 100 nm should be feasible without strain relaxation.

Another experimental indication of the existence of trap states can be found in the so-called hysteresis behavior of top-gate voltage-dependent measurements. For this purpose, we once

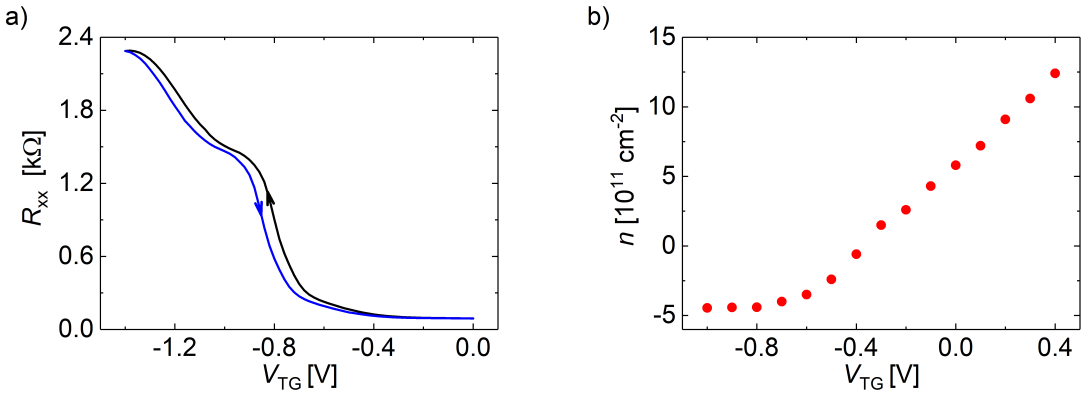

Figure 3.20.: a) Top-gate voltage-dependent measurements of sample QC0461 I at $T \approx 1.5\,\mathrm{K}$. The longitudinal resistance R_{xx} is presented as a function of V_{TG}. The black curve displays R_{xx} measured for $0\,\mathrm{V} \rightarrow -1.4\,\mathrm{V}$, while the blue curve shows the inverse sweep direction ($-1.4\,\mathrm{V} \rightarrow 0\,\mathrm{V}$). b) depicts the dependence of the charge carrier density n of sample Q2982 II on the applied TG voltage V_{TG}.

again examine sample QC0461 I. The longitudinal resistance R_{xx} is presented as a function of TG voltage V_{TG} for $V_{BG} = 0\,\mathrm{V}$ and $B = 0\,\mathrm{T}$ in Fig. 3.20a). The black curve represents R_{xx} for a continuous decrease in V_{TG} from 0 to -1.4 V[8], while the blue curve depicts the longitudinal resistance for the inverse sweep direction. One can observe that both curves are slightly shifted against each other. This phenomenon is called hysteresis behavior and can be explained by filling and depleting of the TS with charge carriers. When an increasingly negative TG voltage (black curve) is applied, not only is the n-type density in the active layer reduced and the p-type density increased respectively, but positive charge carriers are accumulated in the trap states as well. The filling depends heavily on the applied top-gate voltage. Higher negative TG voltages lead to a stronger charging of the TS. This results in an alteration of the energy potential $\Delta U_{TS}(V_{TG})$ located at the trap states. The trapped charge carriers remain there after the measurement is finished. If the TG voltage is then increased again (blue curve), the positive charge carriers located in the trap states partially screen the energy potential of the top-gate. This means that the active layer perceives a less negative effective top-gate voltage $V_{TG}^{eff}(V_{TG}) = V_{TG} + \Delta V_{TS}(V_{TG})$, where $\Delta V_{TS} = -\Delta U_{TS}/e > 0$ and $V_{TG} < 0$. The consequence is a shift of the $R_{xx}(V_{TG})$ curve by $-\Delta V_{TS}$. As the TG voltage increases, the TS are slowly depleted, i.e. V_{TG}^{eff} approaches V_{TG} again. In order to empty the trap states completely, it may be necessary to apply positive top-gate voltages.

It should be noted that in the case of high positive or negative applied top-gate voltages, V_{TG}^{eff} can become constant. An increase in applied TG voltage above a certain positive or negative value only leads to an increasing filling of the TS, which completely screens the

[8]It is noted that the sample experienced several thermal cycles between the identical measurements represented by Fig. 2.15a) and Fig. 3.20a) (black curve). As a result, the shape and the maximum value of the longitudinal resistance have slightly changed.

change in energy potential of the top-gate-electrode. In this case, $V_{\mathrm{TG}}^{\mathrm{eff}}$ and therefore the carrier density in the Hg(Mn)Te layer remain unchanged despite the alteration of V_{TG}. This phenomenon can be observed in Fig. 3.20b) starting from $V_{\mathrm{TG}} < -0.8\,\mathrm{V}$. Fig. 3.20b) shows the charge carrier density n of sample Q2982 II in dependence on applied top-gate voltage V_{TG}. Details about this sample can be found in Appx. A.1. The densities were determined by magneto-transport measurements at $T \approx 1.5\,\mathrm{K}$ as described in Subsec. 2.2.2. In contrast, since the filling of the trap states is strongly dependent on the applied top-gate voltage, $V_{\mathrm{TG}}^{\mathrm{eff}} \approx V_{\mathrm{TG}}$ applies in good approximation for a certain TG voltage range. In this window, the response of the carrier density Δn to a change in top-gate voltage ΔV_{TG} is approximately linear (cf. Fig. 3.20b) for $V_{\mathrm{TG}} > -0.6\,\mathrm{V}$). Thus, within this TG voltage range, the trap states do not affect the gate actions of the samples and the descriptions of G_{TG} and G_{BG} introduced in the context of model I (cf. Subsec. 3.3.1) hence remain valid. The corresponding top-gate voltage window is also referred to as hysteresis-free region and can be of particular interest for TG voltage-dependent measurements.

In this chapter, the state of the art of macroscopic sample fabrication in our group was revised and improvements were introduced along the way. Particularly noteworthy are the development of an optimized 8-terminal Hall bar design, the change from ion beam etching to non-damaging wet etching, and the metallization of the samples at an angle in order to avoid discontinuities of the metal layers over the mesa edges. This ultimately led to the introduction of a new procedure for the characterization of wafer materials and a novel standard recipe for the lithographic processing of HgTe-based macrostructures in our group. Due to the enhancements of this recipe, all macroscopic devices analyzed in the subsequent chapters were fabricated according to the novel standard recipe, unless otherwise specified.

In addition, it was shown that the gate actions of our samples are influenced by the type of gate-dielectric used as well as by the layer stack. Furthermore, it was found that trap states, which form at the interface CMT/insulator due to the fabrication of the top-gate, are responsible for the unintentional increase of the n-type density in the Hg(Mn)Te layer. The magnitude of this doping depends on the thickness of the CMT cap layer and can therefore be reduced by the growth of thicker caps. Lastly, it was established that the lithographic fabrication steps do not unintentionally react chemically with our MBE grown heterostructures, thus avoiding a degradation of the quality of the active layer.

The next step is to explore the origin of the strong, unexpected magnetoresistance fluctuations occurring at high magnetic fields (cf. Sec. 2.3 and Fig. 2.17). Understanding this phenomenon is crucial so that developments to avoid the appearance of these fluctuations can be introduced. This is necessary to enable a meaningful investigation and evaluation of the high-field transport behavior of our 3D TI samples. The implementation is carried out

in the following chapter.

4. Magnetoresistances in high magnetic fields and at low temperatures

As shown by preliminary transport measurements (cf. Sec. 2.3 and Fig. 2.17), under certain experimental conditions our devices can exhibit strong, unexpected magnetoresistance fluctuations, impeding a meaningful evaluation of the high magnetic field data. First, the issues related to the magnetoresistance signals observed at high magnetic fields and low temperatures are to be described in detail. In transport measurements performed under these conditions,

- the R_{xx}-signal may be strongly non-zero or negative even in the regions of magnetic field where the Hall resistance is quantized,
- the SdH oscillations may be noisy and deformed,
- the R_{xy}-signal may be noisy and exhibit suppressed quantum Hall plateaus,
- the quantum Hall plateaus formed may deviate significantly from the expected values,
- and in the extreme case, both magnetoresistance signals may show fluctuations, which can possess amplitudes of the order of $\pm 10^2\,\mathrm{k}\Omega$.

In the following, the occurrence of one or more of these features is referred to as signal issues. In order to investigate the high magnetic field transport properties of our samples in a meaningful way, the origin of the signal issues has to be found so that preventive measures can be developed. Two possibilities, which were considered the source of these issues, were explored in parallel. On the one hand, we assumed that the leads to the ohmic contacts may become insulating at high magnetic fields and low temperatures due to the low charge carrier density in these regions. The measurements which led to this assumption and the resulting conclusions are presented in Sec. 4.1. In the following section (Sec. 4.2), modifications regarding the growth of samples, the lithographic processing of samples, and the measurement-setup leading to an increase of the carrier density in the leads are described. On the other hand, we suspected that in the presence of strong magnetic fields and at low temperatures, the contacting of our devices using the standard contact structure AuGe/Au might be insufficient. In Sec. 4.3, the application of the alternative contact structures Ti/Au, In/Ti/Au, and Al/Ti/Au is examined. Inspired by gallium arsenide samples where the contact quality is significantly improved when indiffusion of contact metals into the mesa occurs [65],

Sec. 4.3 additionally presents a novel lithographic process for the fabrication of the ohmics that reproduces this behavior with our standard contact structure.

4.1. Low charge carrier densities in the contact leads as origin of the signal issues

To identify the origin of the signal issues, various measurement parameters such as temperature and applied top-gate and back-gate voltages were varied in order to study the dependency of the issues on these parameters. First, the temperature dependence is investigated. Fig. 4.1 shows two magnetotransport measurements of sample QC0461 I, one was carried out in a ^{4}He bath cryostat at $T \approx 1.5\,\mathrm{K}$ (Fig. 4.1a)) and the other one in a ^{3}He/^{4}He dilution refrigerator at $T \approx 100\,\mathrm{mK}$ (Fig. 4.1b)). To ensure the comparability of the measurements, the applied TG voltage was adjusted for the measurements, so that the total charge carrier densities are approximately $6 \cdot 10^{11}\,\frac{1}{\mathrm{cm}^2}$ in both cases. Note that the back-gate was grounded during these measurements. It can be recognized that only the measurement performed in the ^{3}He/^{4}He dilution refrigerator exhibits signal issues. Similar to the characterization measurement of sample QC0461 I (cf. Fig. 2.17), the signal issues start to emerge at about $B \approx 5.5\,\mathrm{T}$. This means that the occurrence of the issues related to the magnetoresistances is temperature-dependent and therefore they are only observable at extremely low temperatures ($T \ll 1\,\mathrm{K}$).

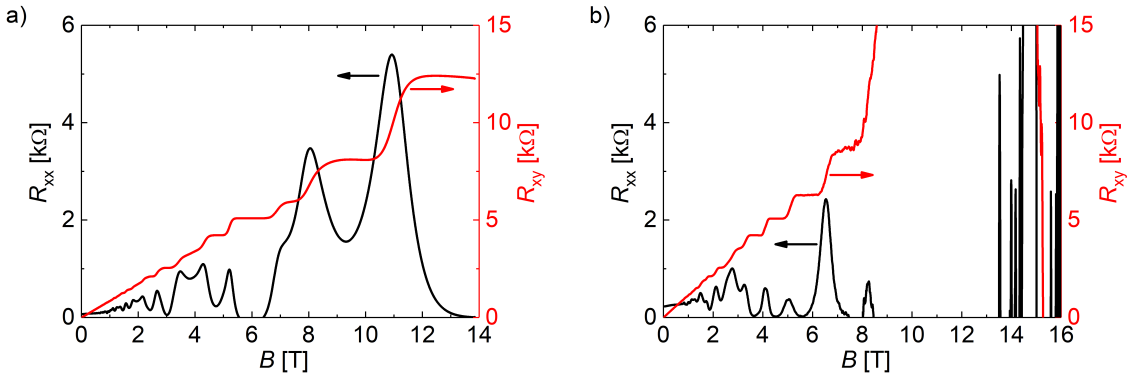

Figure 4.1.: Magneto-transport measurements of sample QC0461 I. a) was carried out in a ^{4}He bath cryostat at $T \approx 1.5\,\mathrm{K}$ and b) in a ^{3}He/^{4}He dilution refrigerator at $T \approx 100\,\mathrm{mK}$.

The dependency of magnetoresistance on applied top-gate voltage is tested by maintaining the applied BG voltage ($V_{\mathrm{BG}} = 10\,\mathrm{V}$) while altering the TG voltage in magnetotransport measurements. The examination of the dependence on the back-gate is carried out exactly the other way around ($V_{\mathrm{TG}} = -1\,\mathrm{V}$). To keep the graphs clearly laid out, only the signals of the transverse resistances are plotted in the following, since it is easier to localize the

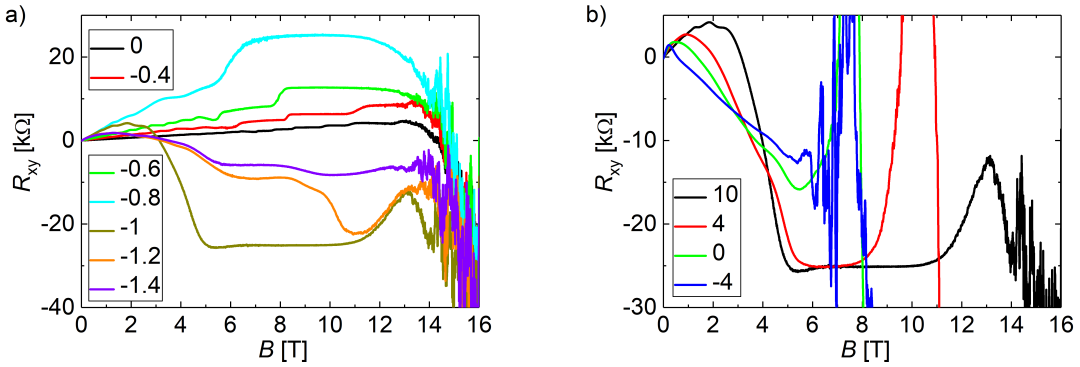

Figure 4.2.: Magneto-transport measurements of sample QC0461 I for different values of applied a) top-gate voltage V_{TG} and b) back-gate voltage V_{BG} at $T \approx 100\,\mathrm{mK}$. The applied values of TG and BG voltages are given (in the unit of volt) in the graphs.

magnetic field B_{s} at which the signal issues start to emerge in R_{xy}. The results can be found in Fig. 4.2a) and b), respectively. It is noted that in Fig. 4.2a) $V_{\mathrm{TG}} = -0.2\,\mathrm{V}$ is not displayed to keep the graph clearly laid out and readable. First, it can be detected that the signal issues are visible for all applied top-gate and back-gate voltages and occur in n-type as well as p-type transport. According to Eq. 2.6 (cf. Subsec. 2.1.3), the filling factor ν can be calculated from the ratio between charge carrier density n and Landau level degeneracy n_{LL}. Thus, for a given carrier density, the filling factor and the corresponding quantum Hall plateau are determined for each value of magnetic field. B_{s} is identified as the magnetic field at which the transverse resistance R_{xy} starts to deviate from the expected quantum Hall plateau. The values of B_{s} can be extracted for the top-gate and back-gate voltages under consideration from Fig. 4.2a) and b), respectively. Due to finite spacing between acquired data points and the difficulty of pinpointing the exact magnetic field at which R_{xy} deviates from the expected plateau (B_{s} is taken from the graphs by eye), we assume an error in reading of 3 % ($\Delta B_{\mathrm{s}} = 3B_{\mathrm{s}}/100$). The outcomes are shown in Tab. 4.1 and Tab. 4.2 for the dependency on TG and BG respectively. For each voltage applied, the corresponding total charge carrier density n_{tot} is also given. The values of n_{tot} are determined as described in Subsec. 2.2.2 and represent the carrier densities located in the sample structure underneath the top-gate-electrode. It is noted that this density may not be present in all regions of the device. One is able to recognize that B_{s} remains almost constant when the applied top-gate voltage V_{TG} is altered, despite changing the total carrier density from $15.89 \cdot 10^{11}\,\frac{1}{\mathrm{cm}^2}$ to $-8.62 \cdot 10^{11}\,\frac{1}{\mathrm{cm}^2}$. Only for low densities $|n_{\mathrm{tot}}| \leq 2.01 \cdot 10^{11}\,\frac{1}{\mathrm{cm}^2}$, we find a minor deviation in B_{s}. These two outliers will be discussed later in more detail. If, in the first instance, the outliers are removed from evaluation and it is taken into account that the values of B_{s} are only determined by eye, then it is very likely that the magnetic field, at which the signal issues start to emerge, is independent of applied TG voltage for sample QC0461 I. In

V_{TG} [V]	0	-0.2	-0.4	-0.6	-0.8	-1	-1.2	-1.4
n_{tot} [$10^{11}\,\frac{1}{\mathrm{cm}^2}$]	15.89	13.12	8.82	5.08	1.99	-2.01	-5.27	-8.62
B_{s} [T]	11.2	11.1	11.2	11.0	10.6	10.6	11.1	11.0

Table 4.1.: Dependence of the magnetic field B_{s} at which the signal issues start to emerge on the applied top-gate voltage V_{TG}. For each value of V_{TG}, the corresponding charge carrier density n_{tot} is also noted.

V_{BG} [V]	10	4	0	-4
n_{tot} [$10^{11}\,\frac{1}{\mathrm{cm}^2}$]	-2.01	-2.71	-3.22	-3.47
B_{s} [T]	10.6	7.7	5.6	4.5

Table 4.2.: Dependence of B_{s} on the applied back-gate voltage V_{BG}. For each value of V_{BG}, the corresponding carrier density n_{tot} is also noted.

contrast, B_{s} strongly depends on applied BG voltage. To explain the different dependencies on the two gate types, we have to consider the distinct layout of top-gate and back-gate. As already mentioned in Subsec. 2.2.3, TG mainly influences the surface states located at the top of the Hg(Mn)Te layer, while BG mainly affects the surface states at the bottom of this layer. However, what is more, top-gate and back-gate possess different spatial dimensions. Since the n-doped substrate GaAs functions as a BG, the back-gate is a global gate. This means that the whole mesa structure is influenced by the BG. The TG, on the other hand, covers and therefore affects only the Hall bar structure and small parts of the contact leads. Hence, there are regions of the mesa that are neither covered by the top-gate metals titanium and gold nor by the contact metals gold germanium and gold. In the following, these areas are referred to as ungated regions (UR) and can be seen in Fig. 4.3 (marked by a green rectangle). It is noted that the *old 6-terminal standard recipe* (cf. Appx. B.1) as well as the *new 8-terminal standard recipe* (cf. Appx. B.2) feature ungated regions in their designs. Given that the UR are not influenced by the top-gate but by the back-gate, we assume that the signal issues are related to these regions. This assumption is based on the consideration that the ohmic contacts covered by AuGe/Au are ideal, which implies that they are excellent conductors [66] and therefore can be excluded as the originator of the signal issues.

We know from the investigations of Sec. 3.3 that the untreated wafer material QC0461 possesses a charge carrier density of $n_0 = 1.02 \cdot 10^{11}\,\frac{1}{\mathrm{cm}^2}$. Since application of gate-dielectric and top-gate metals is the only lithographic step which alters the density in the system (cf. Sec. 3.1) and the ungated regions are not affected by this step, we assume that the UR of sample QC0461 I still exhibit a carrier density of $n_{\mathrm{UR}} = n_0 = 1.02 \cdot 10^{11}\,\frac{1}{\mathrm{cm}^2}$. Note that n_{UR} may deviate strongly from the carrier density located in the Hall bar structure n_{tot} depending on applied top-gate voltage. Surface states having such low electron densities enter their quantum limit already at magnetic field strengths readily accessible in the experiment. In the quantum limit of 3D TI samples, only the lowest (= zeroth) Landau level of each

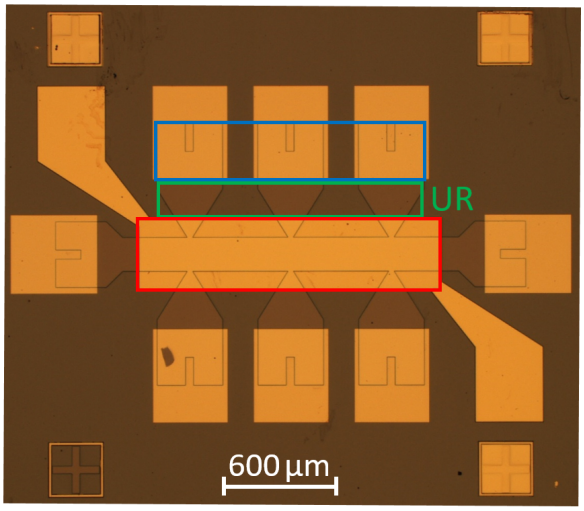

Figure 4.3.: Device fabricated according to the *new 8-terminal standard recipe*. All standard sample designs used in our group can be divided into three areas relevant to this chapter: the ohmic contacts (blue rectangle), the Hall bar structure (red rectangle), and the contact leads also referred to as ungated regions (green rectangle).

topological surface state (TSS,I and TSS,II) is occupied [35, 39]. This results in a total filling factor of $\nu = \nu_{\mathrm{TSS}} = 1$ (cf. Subsec. 2.1.3) and in the formation of one edge state ($\sigma_{\mathrm{xy}} = e^2/h$). Note that a filled zeroth Landau level contributes to σ_{xy} by $e^2/(2h)$ and an empty zeroth LL by $-e^2/(2h)$ [67]. If the spin and valley degeneracies are considered to be $g_{\mathrm{s}} = g_{\mathrm{v}} = 1$, the required magnetic field strength B_{QL} to enter the quantum limit can be estimated by (cf. Eq. 2.6)

$$B_{\mathrm{QL}} = \frac{h}{e}\,|n|\,. \tag{4.1}$$

For the ungated regions of sample QC0461 I, we find $B_{\mathrm{QL}} \approx 4.2\,\mathrm{T}$. When the applied magnetic field strength is increased beyond B_{QL}, we assume that one of the topological surface states starts to be depopulated. At a certain magnetic field ($> B_{\mathrm{QL}}$), the TSS is completely depopulated (associated zeroth LL is empty), turning the total filling factor into $\nu = \nu_{\mathrm{TSS}} = 0$ and introducing a compensation of the edge channel conductivity [$\sigma_{\mathrm{xy}} = (1/2 - 1/2)e^2/h$] [15, 68]. At this point, transport can happen exclusively through the bulk material, since the surface states are insulating. The assumption is supported by references [69] and [70], in which magnetic field-induced insulating states in graphene are reported. According to references [9] and [45], however, we expect HgTe to be a surface-dominated topological insulator system with suppressed bulk conductance. This is particularly the case, when the temperature in the system is extremely low ($T \ll 1\,\mathrm{K}$) and therefore the bulk carriers should freeze out [71]. Thus, they are unable to contribute to transport in this temperature regime. It is plausible that this behavior explains the temperature-dependent occurrence of the signal issues (cf. Fig. 4.1): It is only at sufficiently low temperatures ($T \ll 1\,\mathrm{K}$) that bulk conduction due to thermally activated bulk dopants can be completely excluded and the transport properties

of the system are determined solely by the surface states.

Starting from the magnetic field B_{QL}, an increase in magnetic field strength results in an increasing depopulation of one of the TSS, which, in combination with extremely low temperatures, leads to a rapidly decreasing conductance in the ungated regions. Poorly conducting ungated regions result in an extremely low current flowing through the sample (cf. Fig. 2.17). Moreover, the ungated regions are part of the trajectories of the edge states. This means that the measuring signals have to be transported through the UR, since the ungated regions connect the Hall bar structure to the ohmic contacts. Therefore, poorly conducting UR can lead to transverse resistance R_{xy} and longitudinal resistance R_{xx} deviating from expectations, being extremely noisy, and forming suppressed plateaus and deformed SdH oscillations. Above a certain magnetic field, the depopulation of one of the lowest Landau levels is sufficiently advanced so that the ungated regions exhibit an almost insulating behavior. In this regime, the magnetoresistance fluctuations of the order of $\pm 10^2\,\mathrm{k\Omega}$ occur. The value of magnetic field B_{s} at which the signal issues start to emerge should coincide with a certain critical value of the filling factor $0 < \nu_{\mathrm{c}} < 1$. At this point, the depopulation of the topological surface state has progressed to a sufficient extent so that the quality of the measurement is affected. Obviously, $B_{\mathrm{s}} > B_{\mathrm{QL}}$ has to be valid. In addition, it should be mentioned that the same chain of thought can be applied to the case of low p-type densities located in the ungated regions. Then, in the quantum limit, only the lowest LL of the p-type Volkov-Pankratov state (VPS) is occupied. The corresponding total filling factor can be written as $\nu = -\nu_{\mathrm{VPS}} = -1$. Again, we assume that this Volkov-Pankratov state starts to become depopulated when the applied magnetic field exceeds B_{QL}, leading to a significant decrease in conductance in the ungated regions. When the Landau level is completely depopulated, $\nu = 0$ is valid and the surface state becomes insulating. This time, $0 > \nu_{\mathrm{c}} > -1$ applies to the critical filling factor ν_{c}.

The considerations made above are not only true for low charge carrier densities n_{UR} located in the UR, they apply equally to low carrier densities n_{tot} located in the Hall bar structure. The conductance of the Hall bar itself can be decreased enormously when the magnetic field strength exceeds a critical value, since the lowest occupied Landau level starts to be depopulated. This LL can be either one of the zeroth Landau levels of the TSSs ($\nu = 1$) or the lowest LL of the p-type VPS ($\nu = -1$), depending on the sign of n_{tot}. For this reason, the origin of the deviations from expected values of R_{xx} and R_{xy} observed in magnetotransport-measurements may also be found in the Hall bar structure. Under the condition $|n_{\mathrm{tot}}| < |n_{\mathrm{UR}}|$, the Hg(Mn)Te layer of the Hall bar structure will enter the quantum limit first ($B_{\mathrm{QL,Hall\,bar}} < B_{\mathrm{QL,UR}}$) and therefore the signal issues start to emerge at smaller magnetic fields than expected from the ungated regions. In order to ensure that no signal issues occur in the measurement, $B \leq \min\left(B_{\mathrm{QL,Hall\,bar}}, B_{\mathrm{QL,UR}}\right)$ has to apply due to the edge transport. Based on the dependence of B_{QL} on the charge carrier density (cf. Eq. 4.1), it is reasonable to assume that B_{s} depends on $\min\left(|n_{\mathrm{tot}}|, |n_{\mathrm{UR}}|\right)$ as well. A larger

$\min(|n_{\mathrm{tot}}|, |n_{\mathrm{UR}}|)$ results in higher values of B_{s} and vice versa. Given the spatial dimensions of top-gate and back-gate, it is known that n_{tot} can be manipulated by both gates, whereas n_{UR} is only back-gate-tunable.

In order to verify our assumption, we determine n_{tot}, n_{UR}, ν_{c}, and B_{QL} for each value of applied back-gate voltage and compare the latter to B_{s}. The carrier density of the ungated regions is calculated by the relation (cf. Subsec. 2.2.3)

$$n_{\mathrm{UR}} = n_0 + G_{\mathrm{BG}} V_{\mathrm{BG}} = (1.02 + 0.14 \frac{1}{\mathrm{V}} \cdot V_{\mathrm{BG}}) 10^{11} \frac{1}{\mathrm{cm}^2}, \tag{4.2}$$

and B_{QL} according to Eq. 4.1. The critical filling factor ν_{c} can be estimated using (cf. Eq. 2.6):

$$\nu_{\mathrm{c}} = \frac{hn}{eB_{\mathrm{s}}}. \tag{4.3}$$

In Eq. 4.1 as well as Eq. 4.3, n is either substituted by n_{UR} or n_{tot}, depending on the one which possesses the smaller absolute value. In determining n (cf. Subsec. 2.2.2), we assume an inaccuracy of $\Delta n = 0.1 \cdot 10^{11} \frac{1}{\mathrm{cm}^2}$. The resulting error of ν_{c} is calculated using Gaussian error propagation. If our assumption of the depopulation of the lowest Landau levels being responsible for the signal issues is correct, the required magnetic field strength to enter the quantum limit B_{QL} should be smaller than B_{s}. However, both values should not deviate largely, i.e. they should be within the same order of magnitude. The case $V_{\mathrm{TG}} = -1\,\mathrm{V}$ and $V_{\mathrm{BG}} = 0\,\mathrm{V}$ (green curve in Fig. 4.2b)) is considered as an example. The density in the Hall bar structure equals $n_{\mathrm{tot}} = -3.22 \cdot 10^{11} \frac{1}{\mathrm{cm}^2}$. Since no BG voltage was applied during the measurement, the density in the ungated regions is $n_{\mathrm{UR}} = 1.02 \cdot 10^{11} \frac{1}{\mathrm{cm}^2}$. With $n_{\mathrm{UR}} < |n_{\mathrm{tot}}|$, $B_{\mathrm{QL}} \approx 4.2\,\mathrm{T}$ is obtained. The magnetic field strength at which the signal issues start to emerge in the measurements is 5.6 T. This agrees well with our assumption. The calculated value of the critical filling factor is $\nu_{\mathrm{c}} = 0.753 \pm 0.084$. Other values of the back-gate voltage listed in Tab. 4.2 are investigated analogously. The results are shown in Tab. 4.3. In the case of very low carrier densities located in the two topological surface states (top and bottom), i.e. $n_{\mathrm{TSS}} = n_{\mathrm{TSS,I}} + n_{\mathrm{TSS,II}} < 1 \cdot 10^{11} \frac{1}{\mathrm{cm}^2}$, the response of the electron density to an applied negative BG voltage might differ from the expected value of back-gate action G_{BG}. This can be recognized by the variation of the carrier density in the Hall bar structure n_{tot}, when changing the back-gate voltage from $V_{\mathrm{BG}} = 0\,\mathrm{V}$ to $V_{\mathrm{BG}} = -4\,\mathrm{V}$. The measured change in charge carrier density ($\Delta n_{\mathrm{tot}} = -0.25 \cdot 10^{11} \frac{1}{\mathrm{cm}^2}$) is smaller than expected from $G_{\mathrm{BG}} = 0.14 \cdot 10^{11} \frac{1}{\mathrm{Vcm}^2}$. Nevertheless, in order to be able to specify n_{UR} for the back-gate voltage $V_{\mathrm{BG}} = -4\,\mathrm{V}$, we assume that the same density change occurs in the ungated regions as in the Hall bar structure when going from 0 V to -4 V. Thus, we obtain $n^*_{\mathrm{UR}}(V_{\mathrm{BG}} = -4\,\mathrm{V}) = 0.77 \cdot 10^{11} \frac{1}{\mathrm{cm}^2}$, which, together with the resulting values of B^*_{QL} and ν^*_{c}, is also listed in Tab. 4.3. Note that these values are used for the subsequent evaluations.

For the top-gate voltages investigated (cf. Tab. 4.1), $V_{\mathrm{BG}} = -10\,\mathrm{V}$, $n_{\mathrm{UR}} = 2.42 \cdot 10^{11} \frac{1}{\mathrm{cm}^2}$, and $B_{\mathrm{QL,UR}} = 10.0\,\mathrm{T}$. As long as $|n_{\mathrm{tot}}| > n_{\mathrm{UR}}$ holds, we expect the same value for B_{s}, since

V_{BG} [V]	n_{tot} [$10^{11}\,\frac{1}{\mathrm{cm}^2}$]	n_{UR} [$10^{11}\,\frac{1}{\mathrm{cm}^2}$]	B_{QL} [T]	B_{s} [T]	ν_{c}
10	-2.01	2.42	8.3	10.6	-(0.784±0.088)
4	-2.71	1.56	6.5	7.7	0.838±0.093
0	-3.22	1.02	4.2	5.6	0.753±0.084
-4	-3.47	0.46	1.9	4.5	0.423±0.047
		0.77	3.2		0.708±0.079

Table 4.3.: Dependence of B_{s} on the applied back-gate voltage V_{BG}. For each value of V_{BG}, the carrier densities located in the Hall bar structure n_{tot} and the ungated regions n_{UR}, the associated value of B_{QL}, and the critical filling factor ν_{c} are noted. The last row represents the adjusted values of n^*_{UR}, B^*_{QL}, and ν^*_{c} for $V_{\mathrm{BG}} = -4\,\mathrm{V}$.

n_{UR} is independent of V_{TG}. This is in fact the case within the scope of error (assumed error in reading $\Delta B_{\mathrm{s}} = 3B_{\mathrm{s}}/100$), as can be seen from Tab. 4.1. Now, we are able to explain why the values of B_{s} for $V_{\mathrm{TG}} = -0.8\,\mathrm{V}$ and $V_{\mathrm{TG}} = -1.0\,\mathrm{V}$ show a minor deviation from those of the other TG voltages. For these two particular top-gate voltages, $|n_{\mathrm{tot}}| < n_{\mathrm{UR}}$ is valid. This in turn results in a smaller value of B_{QL} and thus of B_{s} compared to the other V_{TG}. Since $n_{\mathrm{tot}} \approx 6{\cdot}10^{11}\,\frac{1}{\mathrm{cm}^2}$ and $n_{\mathrm{UR}} = 1.02{\cdot}10^{11}\,\frac{1}{\mathrm{cm}^2}$ ($B_{\mathrm{QL,UR}} = 4.2\,\mathrm{T}$) apply in the magneto-transport measurement of Fig. 4.1b), according to Tab. 4.3, B_{s} should be approximately 5.6 T. This can indeed be observed in the measurement.

Hence, we find $B_{\mathrm{QL}} < B_{\mathrm{s}}$ for all examined top-gate and back-gate voltages. The difference $B_{\mathrm{s}} - B_{\mathrm{QL}}$ ranges from 1.0 T to 2.3 T, which is significantly less than an order of magnitude and therefore within the expected range. Moreover, a larger value of $\min(|n_{\mathrm{tot}}|, |n_{\mathrm{UR}}|)$ and thus of B_{QL} results in higher B_{s}. The absolute value of the critical filling factor $|\nu_{\mathrm{c}}|$ reads about 0.8 for all investigated back-gate voltages (cf. Tab. 4.3). This applies regardless of whether the lowest Landau levels are n-type or p-type. It thus seems that only the occupation of the lowest LLs is decisive. As soon as the occupation drops to approximately 80 %, the signal issues start to emerge in the measurements.

Overall, it can be stated that every magneto-transport measurement of sample QC0461 I, which was carried out in a ^{3}He/^{4}He dilution refrigerator, shows quite good agreement with our assumption. This means that it is likely that low charge carrier densities located in certain regions of the sample (Hall bar structure, ungated regions) are responsible for the issues related to the magnetoresistance signals observed at high magnetic fields and extremely low temperatures. The requirement of extremely low temperatures ($T \ll 1\,\mathrm{K}$) is due to the resulting suppression of bulk conduction and thus to the presence of pure surface state transport. Low carrier densities, on the other hand, lead to depopulation of the lowest Landau levels with associated filling factors $\nu = \pm 1$ initiating already at magnetic field strengths readily accessible in the experiment. As the magnetic field continues to increases, the relevant surface states are continuously depopulated, resulting in the conductance of these regions to

decrease more and more. As soon as the absolute value of the filling factor becomes smaller than a critical value ($|\nu_c| \approx 0.8$), the signal issues can be observed. Above a certain magnetic field, the conductance of these regions is sufficiently low so that the sample exhibits an insulating behavior. In this regime, the resistance fluctuations featuring amplitudes of the order of $\pm 10^2\,\mathrm{k}\Omega$ occur. Other 3D TI devices, which were fabricated of different wafer materials and possess ungated regions in their designs, show the idem qualitative behavior and an analogous evaluation leads to comparable results. This further strengthens our assumption.

Since we are able to identify that the occurrence of the signal issues is closely related to low filling factors at high magnetic fields, the next step is to find possible solutions to the signal issues. Due to the low charge carrier densities in the ungated regions, these issues often occur before the filling factor of the Hall bar structure reaches its critical value (cf. Eq. 4.3), as in most cases $|n_{\mathrm{tot}}| > |n_{\mathrm{UR}}|$ applies. For this reason, methods for increasing the carrier density in the UR and thus B_{s} are presented in the following section. These developments are crucial so that the high magnetic field data of our samples can be evaluated in a meaningful way.

4.2. Possible solutions to the signal issues

Our devices should naturally be measurable under the experimental conditions of high magnetic fields ($B > 10\,\mathrm{T}$) and extremely low temperatures ($T \ll 1\,\mathrm{K}$) in order to exploit the full potential of our measurement-setups. Since these are the experimental conditions at which we observe the signal issues, modifications affecting the growth of samples (MBE), their fabrication process (lithography), or the measurement-setup have to be developed. These modifications ensure that our samples are functional under the given conditions and are discussed in detail below.

MBE growth:
Instead of using commercial CdTe substrates, the samples can be grown on a combination of n-doped GaAs, a ZnTe interlayer, and CdTe. Due to the doping, the GaAs functions as a back-gate-electrode (cf. Subsec. 2.2.1). As described above, the BG is a global gate and enables the manipulation of the charge carrier density n_{UR} located in the ungated regions. This allows B_{QL} and thus B_{s} to be shifted towards higher values of magnetic field. However, it should be considered that since the back-gate is a global gate, an applied BG voltage affects the carrier density n_{tot} located in the Hall bar structure as well.

Another possibility to improve the signal quality at high magnetic fields is given through the growth of additional modulation doping layers. A modulation doping layer is an approximately 10 nm thick CMT layer in which some of the tellurium atoms are replaced by iodine atoms. Since tellurium only has six and iodine seven valence electrons, the latter acts as an electron donor, which means that positive charges accumulate in the CMT:I layer. This results in a negative energy potential at the doping layer [72], that leads to an increased

electron density in the active layer. This is reminiscent of the effect of a gate-electrode, however, the modulation doping induces a static density shift that cannot be changed in-situ. The CMT:I layer can be grown beneath, on top of, or symmetrically around the Hg(Mn)Te. Experiments have shown that each doping layer increases the carrier density in the active layer by about $1 \cdot 10^{11}\ \frac{1}{\mathrm{cm}^2}$ to $2 \cdot 10^{11}\ \frac{1}{\mathrm{cm}^2}$. The doping layers are grown across the whole wafer, therefore they affect the entire mesa structure including the ungated regions. Hence, both n_{tot} and n_{UR} are enhanced. For example, in a simple picture, a CMT:I layer sitting beneath the Hg(Mn)Te layer can be seen as a back-gate to which a positive voltage is applied. A more detailed discussion on modulation doping and magneto-transport measurements of devices possessing CMT:I layers can be found in Refs.[35, 57].

Lithography:
If the spatial dimension of the TG is enlarged so that the top-gate-electrode overlaps with the ohmic contacts, there are no more ungated regions in the sample design. Then, n_{UR} becomes equal to n_{tot} and as in the case of the back-gate, B_{QL} and B_{s} can now be controlled via the applied TG voltage. For this purpose, the only change to be made during sample fabrication is the use of an enlarged gate-mask. Since (at the moment) no sufficiently large mask-design exists to obtain an overlapping top-gate for the novel 8-terminal standard Hall bar, the old 6-terminal standard Hall bar was used instead for this project. The recipe to fabricate samples possessing an overlapping top-gate-electrode can be found in Appx. B.4. This recipe is referred to as *6-terminal overlapping top-gate recipe* and is identical to the *new 8-terminal standard recipe* (cf. Appx. B.2) except for two minor differences: The first difference is the usage of a 6-terminal Hall bar design instead of the novel 8-terminal design. The second difference is that the ohmic contacts and the top-gate are fabricated in reverse order. To obtain an overlapping layout, the ohmics have to be fabricated first. For the non-overlapping case, the top-gate-electrode can be applied first to reduce the amount of lithography that the Hall bar structure undergoes before the protective insulator layer is deposited. Sample QC0464 OG I was built according to the *6-terminal overlapping top-gate recipe* with one minor exception: the definition of the mesa was accomplished via inductively coupled plasma etching instead of wet etching. Optical images of sample QC0464 OG I showing the enlarged top-gate-mask and the completed device are shown in Fig. 4.4a) and b), respectively. The details of this sample are listed in Appx. A.1.

The magneto-transport measurements carried out on sample QC0464 OG I are used in order to verify if our assumptions from Sec. 4.1 is also valid for devices possessing an overlapping top-gate. In section 4.1, it is conjectured that the depopulation of the lowest Landau levels with associated filling factors $\nu = \pm 1$ progressing with increasing magnetic field is responsible for the observed signal issues. In this regard, the measured signals of the longitudinal resistance R_{xx} and the transverse resistance R_{xy} should not exhibit any issues until the applied magnetic field exceeds B_{QL} by a certain extent. In addition, we should not be able to ob-

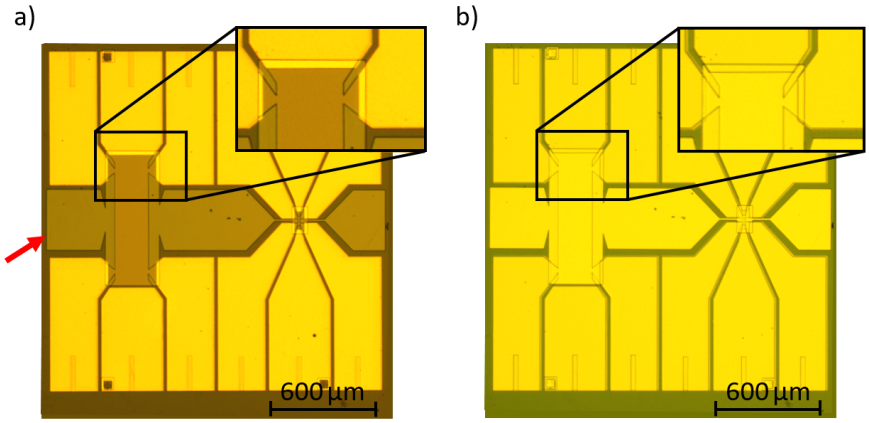

Figure 4.4.: Optical images of sample QC0464 OG I showing a) the enlarged top-gate mask indicated by a red arrow and b) the completed device. Both insets present the overlapping TG design more explicitly.

serve signal issues starting to emerge before the $\nu = \pm 1$ quantum Hall plateau develops. The corresponding total carrier densities n_{tot} for each value of applied top-gate voltage V_{TG} are determined as described in Subsec. 2.2.2. These densities can be used together with Eq. 4.1 to calculate B_{QL}. In addition, the critical filling factor ν_{c} is determined for each applied TG voltage on the basis of n_{tot}, B_{s}, and Eq. 4.3. Figure 4.5a) shows magneto-transport measurement results carried out on sample QC0464 OG I for applied top-gate voltages in the range of $-1.2\,\mathrm{V} \leq V_{\mathrm{TG}} \leq 0\,\mathrm{V}$. The corresponding total charge carrier densities are in the range of $-9.12 \cdot 10^{11}\,\frac{1}{\mathrm{cm}^2} \leq n_{\mathrm{tot}} \leq 13.31 \cdot 10^{11}\,\frac{1}{\mathrm{cm}^2}$. The back-gate was grounded during all measurements. It is noted that not all top-gate voltages investigated are presented in Fig. 4.5a) and only the transverse resistance R_{xy} is displayed to keep the graph clearly laid out and readable. The measurements were carried out in a ^{3}He/^{4}He dilution refrigerator at around 100 mK and at magnetic fields of up to 16 T. To have access to even higher magnetic fields, we travelled to France to measure at the *Laboratoire National des Champs Magnétiques Intenses* (LNCMI) in Grenoble. There, magnetic field strengths of up to 30 T are available. Again, the measurements were performed without applying a back-gate voltage and at $T \approx 100\,\mathrm{mK}$. The measured total carrier densities are in the range of $-6.31 \cdot 10^{11}\,\frac{1}{\mathrm{cm}^2} \leq n_{\mathrm{tot}} \leq 11.93 \cdot 10^{11}\,\frac{1}{\mathrm{cm}^2}$. The measurements carried out at the LNCMI are presented in Fig. 4.5b).

Before we evaluate the measurements regarding signal issues, it is relevant to mention another important phenomenon first. The curves of some p-type densities show an unexpected behavior. Since the absolute value of the filling factor $|\nu|$ of each surface state that contributes to transport is proportional to $1/B$ (cf. Subssec. 2.1.3 and Eq. 2.6), one would expect that the total filling factor decreases with increasing magnetic field B (as it is the case for all n-type measurements). However, if we examine the orange curve ($n_{\mathrm{tot}} = -3.54 \cdot 10^{11}\,\frac{1}{\mathrm{cm}^2}$) in Fig. 4.5a), we find a $\nu = -1$ quantum Hall plateau that develops at about 3 T which unexpectedly turns into a $\nu = -2$ QH plateau for magnetic fields $B > 6\,\mathrm{T}$ and then re-enters

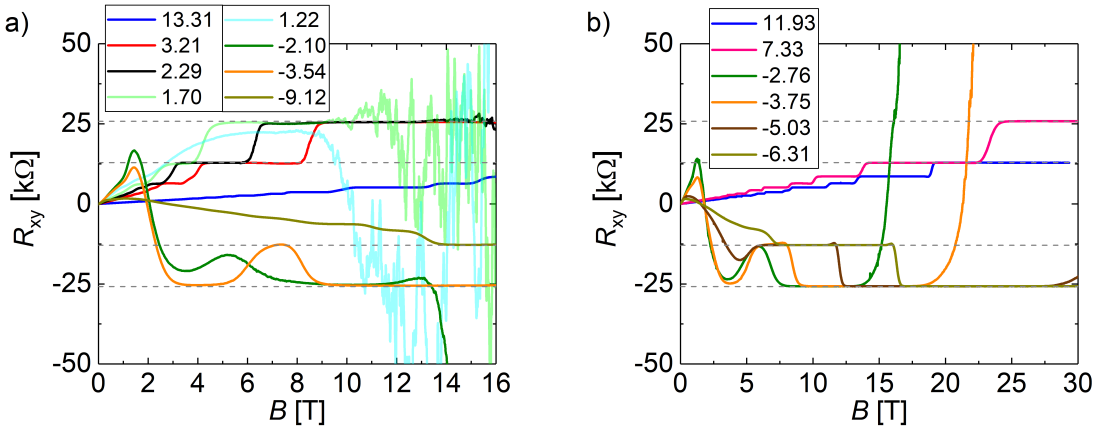

Figure 4.5.: Magneto-transport measurements of sample QC0464 OG I carried out in a) Würzburg and b) Grenoble at $T \approx 100\,\mathrm{mK}$. The transverse resistance R_{xy} is shown in dependence on the magnetic field B for different values of total charge carrier density n_{tot}. The densities are given in the unit of $10^{11}\,\frac{1}{cm^2}$ in both graphs. The theoretical values of quantum Hall plateaus with filling factors $\nu = -2$, -1, 1, and 2 are indicated by dashed gray lines.

n_{tot} $[10^{11}\,\frac{1}{cm^2}]$	13.31	6.52	3.21	2.29	1.70	1.22	-2.10	-3.54	-4.76	-9.12
B_{QL} [T]	55.1	27.0	13.3	9.5	7.0	5.0	8.7	14.6	19.7	37.7
B_s [T]	>16	>16	>16	12.0	9.0	6.8	10.9	>16	>16	>16
ν_c	-	-	-	0.789 ± 0.088	0.781 ± 0.087	0.742 ± 0.083	-(0.797 ± 0.089)	-	-	-

Table 4.4.: Dependence of B_s on the total carrier density n_{tot} located in the active layer. The values of B_{QL} and ν_c are determined according to Eq. 4.1 and Eq. 4.3, respectively. The data presented in this table were recorded in Würzburg.

n_{tot} $[10^{11}\,\frac{1}{cm^2}]$	11.93	7.33	-2.76	-3.75	-5.03	-6.31
B_{QL} [T]	49.3	30.3	11.4	15.5	20.8	26.1
B_s [T]	>29.3	>30	13.1	17.7	27.1	>30
ν_c	-	-	-(0.871±0.097)	-(0.876±0.098)	-(0.768±0.086)	-

Table 4.5.: Dependence of B_s on the total density n_{tot} located in the active layer. The values of B_{QL} and ν_c are calculated according to Eq. 4.1 and Eq. 4.3, respectively. The data presented in this table were recorded in Grenoble.

the $\nu = -1$ state for fields $B > 9\,\mathrm{T}$. The same behavior can be found in Fig. 4.5b). The dark green curve ($n_{\mathrm{tot}} = -2.76 \cdot 10^{11}\,\frac{1}{\mathrm{cm}^2}$), for example, shows a $\nu = -1$ QH plateau developing at approximately $B \approx 3\,\mathrm{T}$ that turns into a $\nu = -2$ quantum Hall plateau for $B > 5.5\,\mathrm{T}$ and re-enters the $\nu = -1$ state for $B > 7.5\,\mathrm{T}$. In the following, this phenomenon is referred to as re-entrant quantum Hall effect and its explanation is topic of Chap. 5.

Now, we present the evaluation referring to Fig. 4.5. We start by calculating the magnetic field strengths for sample QC0464 OG I required to be in the quantum limit $B_{\mathrm{QL}}\,(n_{\mathrm{tot}})$. These values can be compared to the magnetic field B_{s} at which the signal issues start to emerge. In addition, we calculate the critical filling factors $\nu_{\mathrm{c}}\,(n_{\mathrm{tot}}, B_{\mathrm{s}})$ and compare these values to the ones of sample QC0461 I. The results of the measurements carried out in Würzburg and Grenoble are presented in Tab. 4.4 and Tab. 4.5, respectively. It is noted that if B_{s} cannot be determined because it exceeds the maximum magnetic field strength available in the measurement-setup, then ν_{c} cannot be determined either. The corresponding cells in Tab. 4.4 and Tab. 4.5 are marked by "-" signs. One is able to observe that for most values of total charge carrier density n_{tot} no signal issues can be identified in the measurements. For the experimental setup in Würzburg, the signal issues in the measurements can be detected only if $|n_{\mathrm{tot}}| \leq 2.29 \cdot 10^{11}\,\frac{1}{\mathrm{cm}^2}$. For the experimental setup in Grenoble, $|n_{\mathrm{tot}}|$ has to be $\leq 5.03 \cdot 10^{11}\,\frac{1}{\mathrm{cm}^2}$ for the signal issues to be observed. Since $B_{\mathrm{QL}} < B_{\mathrm{s}}$ holds, this can be explained by the fact that B_{QL} is directly proportional to $|n_{\mathrm{tot}}|$ and therefore, for high absolute values of total carrier density, B_{s} may exceed the maximum available magnetic field strength of the measurement-setup (16 T in Würzburg, 30 T in Grenoble). In the low-density regime, the behavior of B_{s} is correlated to $|n_{\mathrm{tot}}|$. Larger absolute values of n_{tot} imply higher values of B_{s} and vice versa. In addition, the absolute values of the critical filling factor are approximately the same for all investigated top-gate voltages. Analogous to sample QC0461 I, we find $|\nu_{\mathrm{c}}| \approx 0.8$. This observation is to be clarified by plotting $|\nu_{\mathrm{c}}\,(n)|$ against the charge carrier density n. The result is shown in Fig. 4.6. The data points of sample QC0461 I (cf. Tab. 4.3) are presented in black, while the data points of sample QC0464 OG II (cf. Tabs. 4.4 and 4.5) are depicted in red. It can be recognized that all values of $|\nu_{\mathrm{c}}|$ are close to each other. A horizontal linear fit of the data points (dashed blue line in Fig. 4.6) results in $|\nu_{\mathrm{c}}|_{\mathrm{fit}} = 0.786 \pm 0.016$. Within the scope of their errors, all experimentally determined values of the critical filling factor are compatible with $|\nu_{\mathrm{c}}|_{\mathrm{fit}} = 0.786$. Thus, independent of the top-gate design used, underlying sample, and carrier type (n-type or p-type), the signal issues start to emerge as soon as the population of the lowest LLs drops to around 80 % with increasing magnetic field. Consequently, for samples possessing an overlapping top-gate layout, B_{s} can be predicted by (cf. Eq. 4.3)

$$B_{\mathrm{s}} \approx \frac{h}{0.8e}\,|n_{\mathrm{tot}}|\,, \tag{4.4}$$

when the total charge carrier density n_{tot} is known. Furthermore, signal issues are only

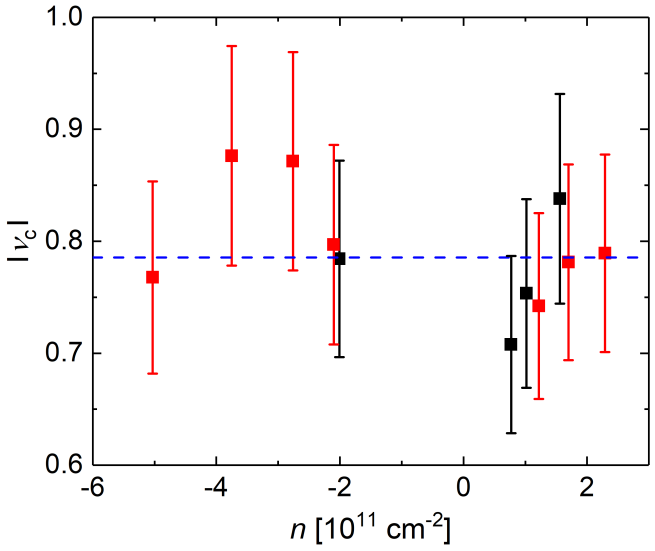

Figure 4.6.: Absolute value of the critical filling factor $|\nu_c|$ in dependency of the charge carrier density n. The black squares represent data points of sample QC0461 I, while red ones depict data points of sample QC0464 OG II. $|\nu_c|_{\text{fit}} = 0.786$ is indicated via a dashed blue line.

observable when the transverse resistance has already developed the quantum Hall plateau with associated filling factor $\nu = \pm 1$. This also corroborates our assumption.

Overall, sample QC0464 OG II featuring an overlapping top-gate confirms our explanation for the signal issues observed at high magnetic fields and extremely low temperatures (cf. Sec. 4.1). Under these experimental conditions, an overlapping TG ensures that the magnetoresistance signals R_{xx} and R_{xy} can be meaningfully evaluated until the device enters the low-density regime and becomes a poor conductor itself in the presence of strong magnetic fields.

Measurement-setup:

The last modification that can be made is related to the measurement-setup. Investigations have shown that the charge carrier density in the active layer can be altered by light-emitting diode (LED) illumination [73]. The photon energy of such a LED is approximately between 1 eV and 3 eV depending on its color. Since this energy is much larger than the bandgap between conduction band and valence band of HgTe (≈ 22 meV), charge carriers can be excited by photons and contribute to transport. To enable this method, one has to mount a LED in the cryostat directly above the sample. Fig. 4.7 shows the change in carrier density as a function of the illumination time for a sample with a top-gate-electrode (blue squares) and one without a top-gate-electrode (red squares). The device possessing a top-gate was illuminated by a blue LED to which a voltage of 3.9 V was applied. The sample without a

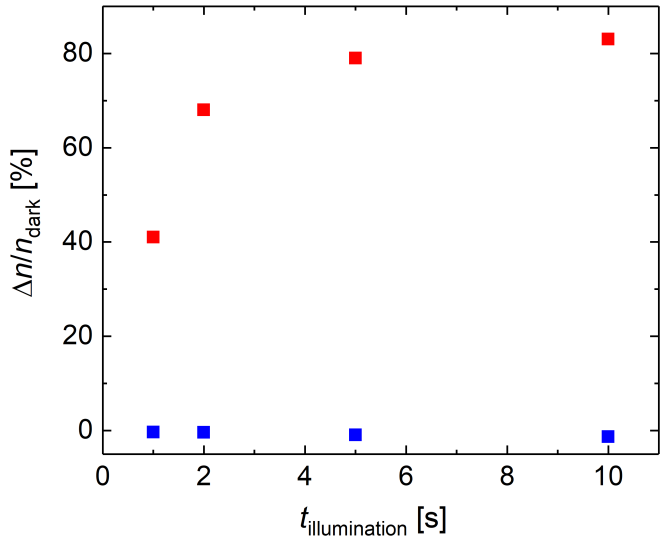

Figure 4.7.: Change of the charge carrier density $\Delta n/n_{\mathrm{dark}}$ as a function of the illumination time $t_{\mathrm{illumination}}$ for samples with and without top-gate-electrode. The device possessing a TG (blue squares) was illuminated by a blue LED, while the sample without top-gate (red squares) was illuminated by a red LED. The data points were taken with permission from [73].

top-gate was illuminated by a red LED operated at a voltage of 1.9 V. The illumination times chosen were 1 s, 2 s, 5 s, and 10 s. The change in charge carrier density is calculated using $\Delta n = n_{\mathrm{LED}} - n_{\mathrm{dark}}$, where n_{LED} is the carrier density in the active layer after illumination and n_{dark} is the density without illumination. It can be established that the carrier density in the active layer does not change significantly during illumination if the Hall bar structure is covered by a top-gate-electrode, i.e. $\Delta n/n_{\mathrm{dark}} \approx 0$ for all measured illumination times $t_{\mathrm{illumination}}$. This can be explained by the screening effect of the top-gate, since it is quite unlikely that a photon is able to penetrate the Ti and Au layers and reach the Hg(Mn)Te layer underneath. However, in the absence of a top-gate-electrode, the carrier density of the sample strongly depends on $t_{\mathrm{illumination}}$. With increasing illumination duration, the density in the active layer also increases until a saturation is reached. In our case, we find $n_{\mathrm{LED,max}} \approx 1.8 n_{\mathrm{dark}}$. Thus, the charge carrier density of the device can approximately be doubled.

Given that the ungated regions are not covered by top-gate metals, LED illumination increases the density located in these regions, whereas the charge carrier density in the Hall bar structure, which is covered by top-gate-electrode, is not significantly affected. For this reason, one is able to enhance n_{UR} and therefore B_{s} to a certain extent without altering the level of Fermi energy E_{F} in the Hall bar structure to be investigated.

4.3. Clustering metals in the ohmic contacts

In the previous two sections it was shown that the signal issues observed at high magnetic fields and extremely low temperatures can be attributed to low filling factors $|\nu| < 1$ in the leads to the ohmic contacts or the Hall bar structure. Therefore, it can be concluded that the standard contact structure AuGe/Au is fully functional within the experimental limits of our measurement-setups. Nevertheless, the research concerning our ohmics carried out in parallel to the investigations described in Sec. 4.1 and Sec. 4.2 is to be presented. Sec. 4.3 is intended to demonstrate what is possible when fabricating the ohmic contacts and to provide an excellent starting point for future research.

First, it is to be specified why we considered the ohmic contacts as a possible source of the signal issues emerging at high magnetic fields and extremely low temperatures. We suspected that a possible cause for the observed issues might be magnetic freeze-out [74], which strongly decreases the conductance of the ohmics under these conditions and, in the extreme case, makes them completely insulating. Hence, in order to improve the quality of the ohmic contacts and to prevent the possibility of magnetic freeze-out, two diverse approaches were taken. First, different contact metals replacing the standard AuGe/Au layer stack were tested. Second, new lithographic processes for the fabrication of the ohmics were investigated. The aim was to reproduce the condition of the contacts of gallium arsenide (GaAs) samples: The heating of GaAs devices to over 400 °C results in an annealing of the contact metals leading to an intermixing of the metal layers and strong indiffusion of metal into the GaAs layer [75]. The indiffusion is even visible in SEM images in the form of metal-fingers 10 nm to 50 nm thick, which penetrate into the GaAs bulk. Hence, in the following, this phenomenon is referred to as fingering. Fig. 4.8 shows the intermixing and fingering of Pt/Ti/Pt/Au contact structures on GaAs. Figures a) to c) represent a series of heating temperatures (450 °C to 490 °C), which in turn generate intermixing and fingering of different intensity. From the figures, it can be deduced that the strength of both effects increases with increasing temperature. For the material system GaAs, only through intermixing and fingering of metal ohmic contacts are obtained. It has been shown that the contact quality is significantly improved by the annealing procedure [65]. Hereafter, we will refer to the combination of intermixing of metal layers and fingering of metal into the bulk solely as clustering metals (CM).

It is recalled that the standard process for contacting our samples as described in Subsec 3.1.3 neither leads to noticeable intermixing of the AuGe and Au layers nor shows visible fingering of metal into the mesa (cf. Fig. 3.8). Therefore, we attempted to obtain clustering metals by applying the tow approaches mentioned above. It is emphasized that in the case of our $Hg_{1-x}Cd_xTe$ heterostructures, the heating and annealing of contact metals to temperatures $T \geq 400$ °C is not an option because mercury tends to evaporate out of the material for temperatures above 80 °C [29].

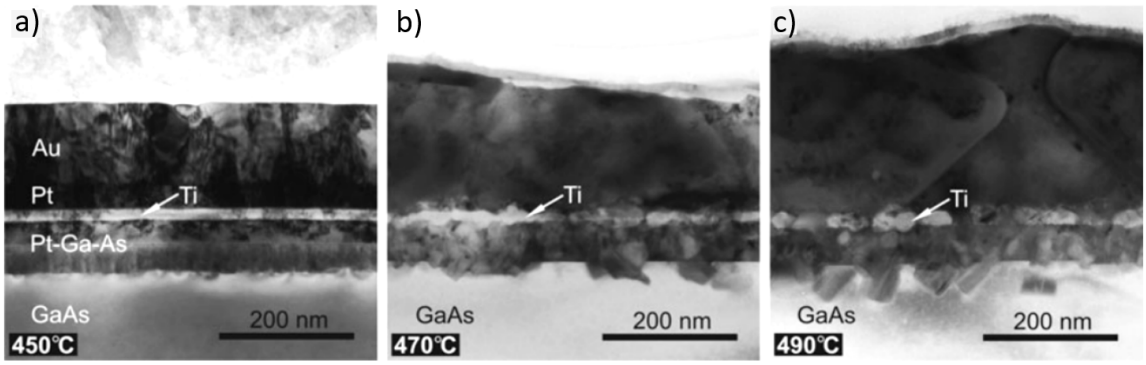

Figure 4.8.: Cross-section images of a GaAs device showing the condition of the contacts for different heating temperatures of a) 450 °C, b) 470 °C, and c) 490 °C . Annealing of contact structures at 450 °C causes the reaction of Pt with components Ga and As and the formation of Pt-Ga-As interlayers. Annealing at 470 °C and 490 °C results in an intermixing of metal layers and fingering of metal into the GaAs layer (visible as dark spots in the bright GaAs bulk). Reprinted with permission from [75], license granted by John Wiley & Sons and Copyright Clearance Center, Inc.

In the following, the results obtained by use of different metals for contacts are presented. The contacts were fabricated as explained in Subsec. 3.1.3. However, the e-gun evaporation of 50 nm AuGe and 50 nm Au described in this subsection was replaced by the evaporation of different metals. The alternative contact structures are Ti/Au (30 nm/70 nm), In/Ti/Au (70 nm/5 nm/25 nm), and Al/Ti/Au (70 nm/5 nm/25 nm). The additional 5 nm Ti layers have been chosen in analogy to the contact structure of GaAs samples. They also facilitate the differentiation of each individual metal layer in SEM images. For the condition of the contacts to be examined, SEM images of cross-sections are taken. The results are presented in Fig. 4.9a) to c), where the contact structures Ti/Au, In/Ti/Au, and Al/Ti/Au are displayed in a), b), and c) respectively. Since the metals were not deposited under an angle (cf. Sec. 3.2), all samples show discontinuities of the metal layers over the mesa edges. In addition, the deposition of indium (Fig. 4.9b)) and aluminum (Fig. 4.9c)) does not result in a smooth layer, but exhibits a layer that varies in thickness across the sample surface. Last and most important, none of the samples shows indications of the desired clustering metals at all. From the above it can be concluded that it was not possible for us to create CM by the use of different contact metals.

The second approach of developing new fabrication techniques for the ohmic contacts is based on the attempt to create clustering metals through chemical processes and reactions. In the following, we present and discuss the sample recipe, which creates clustering AuGe and Au layers on the mesa. This recipe is called *8-terminal Hall bar clustering metals recipe* and can be found in Appx. B.5. Two fundamental conditions are necessary to obtain clustering

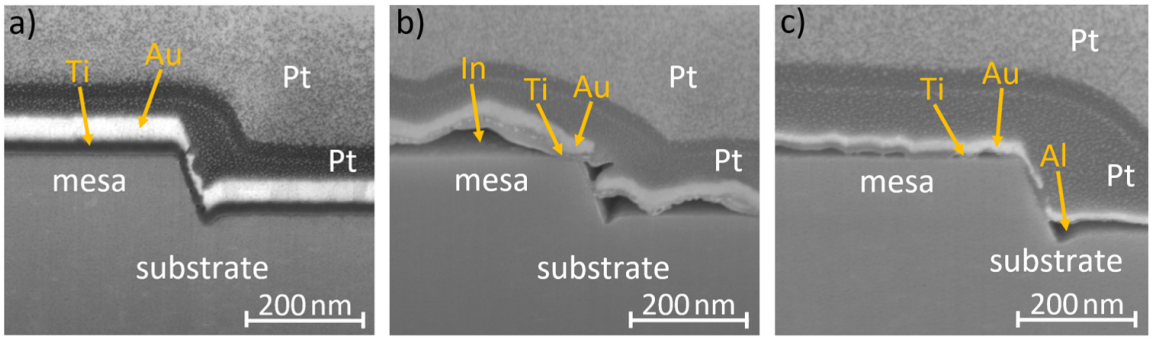

Figure 4.9.: Cross-section images of devices possessing different contact structures. The structures are a) Ti/Au (30 nm/70 nm), b) In/Ti/Au (70 nm/5 nm/25 nm), and c) Al/Ti/Au (70 nm/5 nm/25 nm).

metals:

- The wafer material has to contain a modulation doping layer, which is grown on top of the active layer. The presence of iodine atoms is of particular importance here.
- Those areas of the mesa, on which clustering should take place afterwards, have to be in direct contact with titanium, that in turn has to be stripped later using hydrofluoric acid (HF).

The exact chemical and physical mechanisms behind the formation of clustering metals are not yet fully understood. However, for this thesis, the result is of major interest. For this reason, the *8-terminal Hall bar clustering metals recipe* is discussed below using sample Q3097 II with the relevant optical and SEM images. In addition, a sample specimen Q3097 VI fabricated according to the *new 8-terminal standard recipe* (Appx. B.2) is compared to the sample Q3097 II in order to highlight the differences between the two recipes. Details regarding wafer material Q3097 and the above-mentioned devices can be found in Appx. A.2 and Appx. A.1, respectively. Since this wafer material possesses a modulation doping layer containing iodine grown on top of the active layer, it satisfies the first condition stated above.

We now consider the second condition. The simplest method to get the sample surface in direct contact with titanium is the usage of a titanium etch mask to define the mesa. However, the entire mesa structure and not only the areas of the ohmics would be affected by the chemical and physical processes causing clustering metals. In order to reduce the amount of lithography to which the Hall bar structure is subjected and to protect its surface, a 10 nm thick SiO_2 is applied across the whole sample piece at the beginning of processing. This layer is called sacrificial layer (SL) and its vapor deposition is performed in the PECVD (cf. Subsec. 3.1.4). To remove the SL from the areas of the later ohmics, a mask consisting of positive photoresist is used to expose these areas. Afterwards, the sample is dipped for 10 s into buffered oxide etch (BOE[1]), also known as buffered HF, whereby the removal happens.

[1]The BOE we use is diluted in deionized water at a ratio of 1:7.

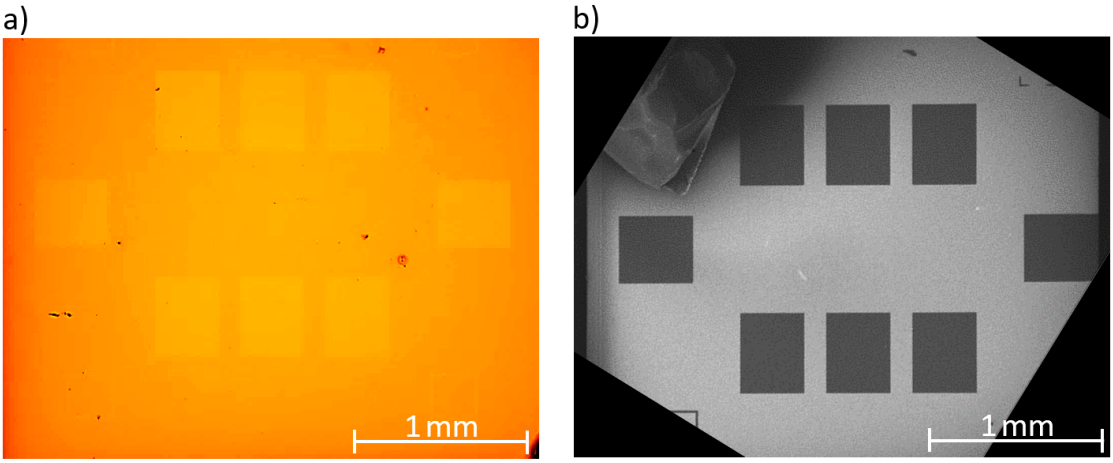

Figure 4.10.: a) optical and b) SEM images of sample Q3097 II showing the sacrificial layer, which has been removed from the areas of the later ohmic contacts. Using an optical microscope, the SL can hardly be distinguished from the sample surface. In an electron microscope, the SiO_2 (light gray) stands out clearly from the dark sample surface. In the top left corner of b), the clamp keeping the device in position is observable.

The lift-off is carried out for 5 min in acetone at 50 °C. An optical and a scanning electron microscope image showing the SL are presented in Fig. 4.10a) and b), respectively. In the next step, the 15 nm thick titanium etch mask is deposited. For this purpose, a mask consisting of negative photoresist is used. Again, the lift-off process is carried out for 5 min in acetone at 50 °C. An optical image of sample Q3097 II presenting the titanium etch mask is shown in Fig. 4.11. It is clearly visible at which areas of the mesa design the sacrificial layer was removed before Ti deposition. To enable the mesa etch, the sacrificial layer has to be removed around the titanium mask. This step can be achieved in our ICP tool. Since titanium is not a sufficient etch mask for wet etching, ion beam etching or inductively coupled plasma etching[2] have to be used. The etching is done as described in Subsec. 3.1.2. Stripping of the titanium etch mask happens by placing the sample for 45 s in hydrofluoric acid, which is diluted in deionized water (DIW) at a ratio of 1:10. An optical image showing the etched mesa of sample Q3097 II is presented in Fig. 4.12a). The wet etched mesa of the comparison specimen is depicted in Fig. 4.12b). On closer inspection and additional adjustment of brightness, contrast, and saturation, a difference between the two samples can be detected. While the surface condition of sample Q3097 VI is uniform across the entire area of the later ohmics, the surface texture of Q3097 II varies across the contacts. The transition line, at which the surface condition starts to change, coincide with the boundary of the sacrificial layer. At those areas, where the sacrificial layer was removed before deposition of the Ti-mask, the mesa possesses a different surface texture. This is a first indication that the later ohmic contacts of sample Q3097 II are of diverse appearance and condition. It is noted that

[2]So far, only IBE has been tested, however, comparable results should be obtainable via ICP etching.

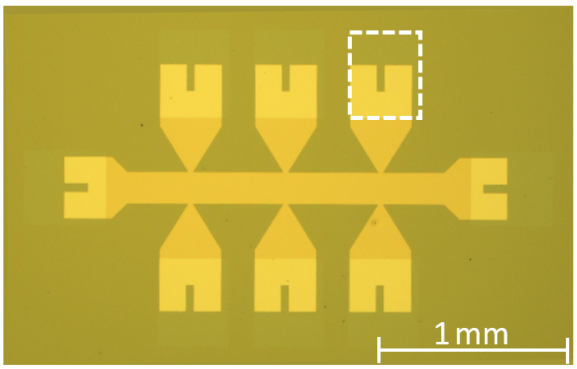

Figure 4.11.: Optical image of sample Q3097 II showing the titanium etch mask. One of the areas where the sacrificial layer was removed before the application of Ti is marked by a dashed white rectangle. The Ti deposited directly on the sample surface is brighter than the Ti deposited on top of the SL.

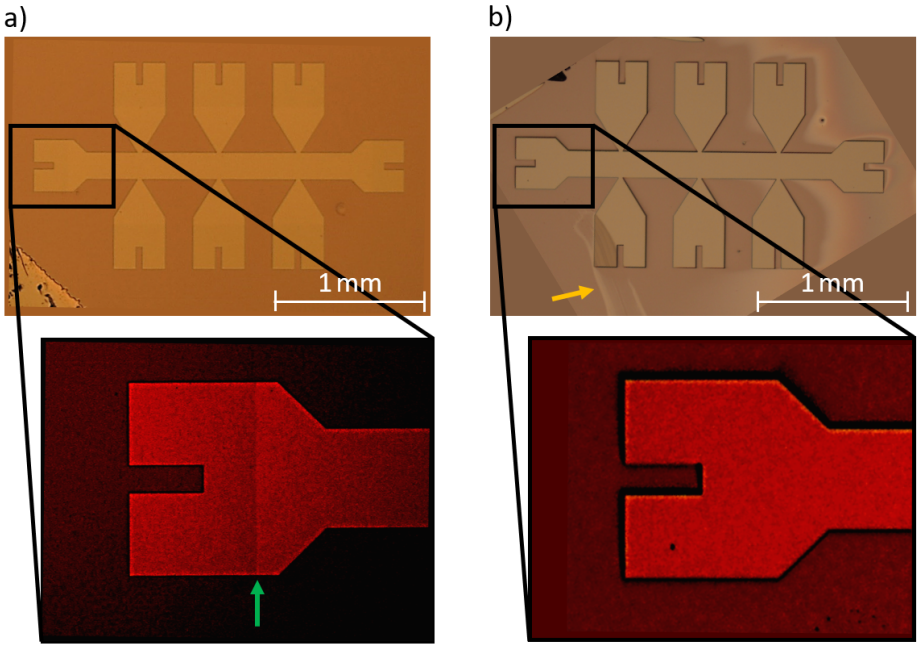

Figure 4.12.: Optical images of the mesa structures of devices a) Q3097 II and b) Q3097 VI. For each sample, one contact is magnified and the brightness, contrast, and saturation have been changed to present the difference between the devices more clearly. The point at which the surface condition of sample Q3097 II changes is marked by a green arrow and can be recognized by a slight variation in color. In b), an impurity of the wafer (indicated by an orange arrow) can be seen.

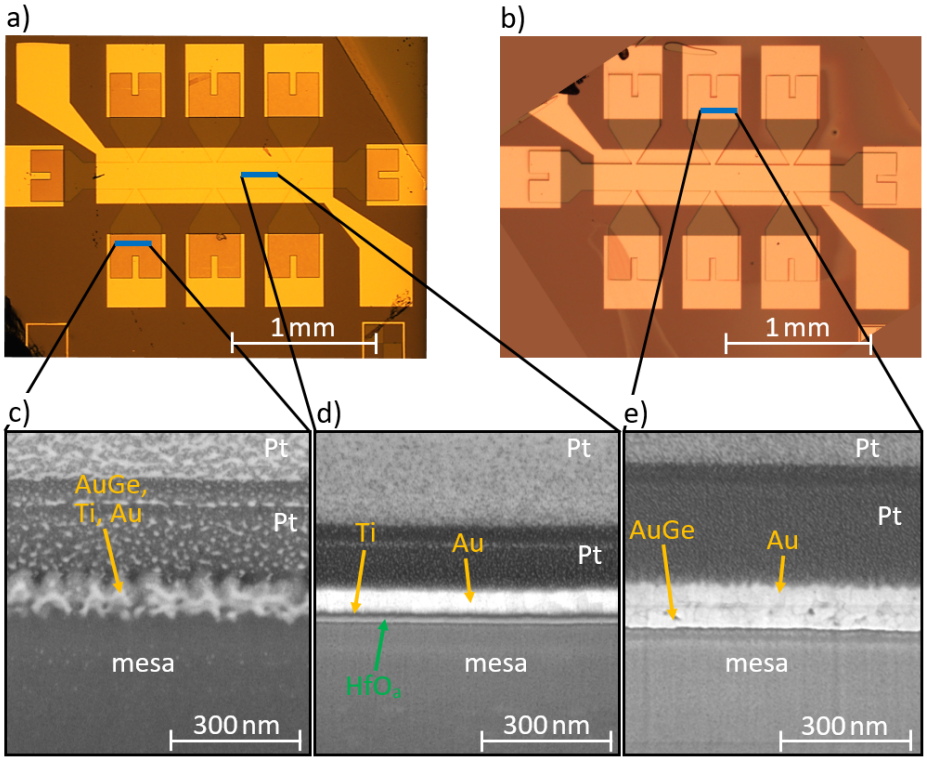

Figure 4.13.: Optical images showing the completed samples a) Q3097 II and b) Q3097 VI. The positions, at which cross-sections were made, are marked by blue stripes. The corresponding cross-section images are depicted in c), d), and e).

the diverse appearances of the Hall bar structures of devices Q3097 II and Q3097 VI result from the different operating modes that were used to take the pictures. Fig. 4.12a) shows the unaltered optical image, while in Fig. 4.12b) the so-called Nomarski interference contrast mode was applied. This mode, by using two Wollaston prisms and two polarizing filters, gives the two-dimensional image a three-dimensional character.

The subsequent lithographic steps "fabrication of ohmic contacts" and "gate-dielectric and top-gate application" (cf. Subsec. 3.1.3, Subsec. 3.1.4, and Sec. 3.2) are identical for samples Q3097 II and Q3097 VI except for one minor deviation: The difference can be found during metallization of the contacts. In the *8-terminal Hall bar clustering metals recipe*, an additional 5 nm Ti layer is deposited between the 50 nm AuGe and 50 nm Au layers. Again, this additional layer is chosen on account of the contact structure of GaAs samples and facilitates the differentiation of each individual metal layer in SEM images of cross-sections. Optical images of the completed devices Q3097 II and Q3097 VI are presented in Fig. 4.13a) and b), respectively. The different conditions of the ohmics of these two samples can already be detected based on their optical pictures. Since the optical microscope utilizes the principle of specular reflectance for imaging, smooth surfaces appear brighter than rough ones. If the surface is smooth, it is likely that the incoming photons are reflected back to the objective lens. However, if the surface is rough, the incoming photons are reflected in different di-

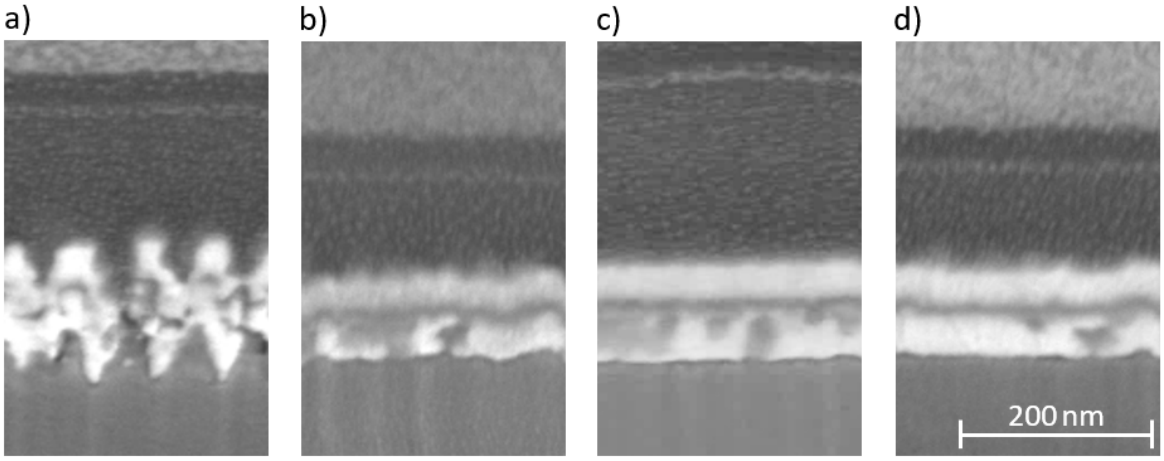

Figure 4.14.: SEM images of cross-sections of four dummy samples showing the conditions of the ohmic contacts. The depicted layers are (from bottom to top): mesa structure, 50 nm AuGe, 5 nm Ti, 50 nm Au, Pt (e-beam deposition), and Pt (Ga-ion beam deposition). The scale presented in d) is valid for all images.

rections and less photons reach the objective lens. For this reason, in optical pictures, the roughened metal layers of clustering metals appear darker than the smooth metal layers of non-clustering ones. The different conditions of the ohmic contacts is also visible in the corresponding SEM images of cross-sections. Sample Q3097 II built according to *8-terminal Hall bar clustering metals recipe* shows CM (cf. Fig 4.13c)), whereas sample Q3097 VI fabricated according to *new 8-terminal standard recipe* exhibits neither intermixing of metal layers nor fingering of metal into the mesa (cf. Fig. 4.13e)). The effect of the SiO_2 sacrificial layer with its protective function can be seen in Fig. 4.13d): Despite the usage of a wafer possessing a modulation doping layer grown on top of the active layer, a titanium etch mask, and hydrofluoric acid, the surface quality of the Hall bar structure remains smooth and unchanged. Thus, we have been able to develop a sample recipe that only modifies the condition of the ohmic contacts and preserves the rest of the device structure in an unaltered state.

The necessity of the presence of the two fundamental conditions (modulation doping layer containing iodine above active layer and titanium etch mask) to obtain clustering metals is presented in Fig. 4.14. Figure 4.14a) to c) depict devices fabricated of the same wafer material which contains a modulation doping layer grown on top of the active layer. The layer stack of the sample that is displayed in d) does not contain this additional doping layer, i.e. no iodine atoms are existent above the HgTe layer. Samples a) and d) were built exactly according to the *8-terminal Hall bar clustering metals recipe*, whereas the fabrication processes of the devices presented in b) and c) were slightly altered at a certain point of this recipe. In b), the sacrificial layer was not removed before Ti deposition and in c), the titanium etch mask was replaced by a BaF_2 etch mask. One can observe that only the ohmic contacts of the sample, which was fabricated exactly according to the *8-terminal Hall bar clustering metals recipe* and contains a modulation doping layer grown on top of the active layer, exhibit clustering

metals.

The next logical step would be to test the novel contacts in comparison to our standard contacts to figure out if an improved contact quality is obtained. For this purpose, two samples have to be built of the same wafer material, one according to the *8-terminal Hall bar clustering metals recipe* and the other one according to the *new 8-terminal standard recipe*. Subsequently, the quality of magneto-transport measurements of these two devices can be compared with each other. However, these tests have not been carried out to date. There are two reasons: First, after all the attempts necessary to achieve clustering metals, there was no sufficient wafer material left to fabricate more samples possessing CM. The only completed sample showing clustering metals (Q3097 II) should not be used for examinations, as this sample was exposed several times to high-energy electrons and ions and its mesa was cut open at several places. Second, in the meantime, we have been able to establish that the signal issues emerging at high magnetic fields and extremely low temperatures are caused by low filling factors $|\nu| < 1$ in the leads or the Hall bar structure and not by the ohmics (cf. Sec. 4.1). Since the assumption of ohmic contacts being responsible for this signal issues was the main motivation for the creation of clustering metals, the interest in modifying our standard contact structure diminished. If it should become necessary to improve the quality of the ohmics in the future after all, then the investigations and results of this section represent an excellent starting point for further research.

In this chapter, the behavior of the magnetoresistances of our three-dimensional HgTe-based devices at high magnetic fields and extremely low temperatures was investigated. Based on the magnetoresistance signals it could be demonstrated that the leads to the ohmic contacts may become insulating under these conditions due to the low charge carrier density present there. As soon as the population of the lowest Landau levels reaches a critical point, a strong reduction of the conductance of the leads occurs, impeding a meaningful evaluation of the high-field data of our samples. The absolute value of the critical filling factor $|\nu_c| \approx 0.8$ was found to be independent of the devices under consideration and the type (n-type or p-type) of the lowest LLs. In addition, it was shown that the carrier density in the leads can be increased by the growth of modulation doping layers, a back-gate-electrode, LED illumination, and the application of an overlapping top-gate design.

In order to improve the quality of our ohmics, alternative contact structures were investigated. However, no improvement compared to the standard contact structure AuGe/Au was found. Furthermore, inspired by the condition of the contacts in GaAs samples, a lithographic process was developed causing an intermixing of the AuGe and Au layers as well as fingering of metal into the mesa. The extent of the quality of the ohmic contacts possessing these so-called clustering metals has yet to be fully established. The innovations presented

in this thesis concerning the ohmics are therefore to be considered as an excellent starting point for future research.

The revised lithographic processing of macroscopic 3D HgTe-based devices and the related development of improvements make it possible to study the transport properties of our high-quality MBE grown heterostructures to a new extent. For this purpose, based on the results of this chapter, the full potential of our measurement-setups can now be utilized. The next chapter (Chap. 5) deals with the contributions of topological and massive states to transport. In particular, results of magneto-transport measurements carried out on 3D Hg(Mn)Te macrostructures will be consistently explained.

5. Interplay and tunable inter-scattering between quantum Hall edge states from topological and massive surface states in Hg(Mn)Te

Based on magneto-transport measurements, it was already demonstrated in Chap. 2 that in our three-dimensional HgTe-based devices several independent charge carrier systems can contribute to transport simultaneously. The indications were missing quantum Hall plateaus in the measurements and the inversion of the Hall slope at low magnetic fields for p-type dominated transport (cf. Subsec. 2.2.2). Now, we want to develop a method that allows us to determine the occupied topological and massive surface states in a sample for a given level of Fermi energy accurately. In addition, the interplay of topological surface states and Volkov-Pankratov states (Sec. 5.1) and a possible inter-scattering of these transport channels is to be investigated (Sec. 5.2). The inter-scattering could result from counter-propagating n-type and p-type quantum Hall edge states in the Hg(Mn)Te layer due to imposed opposite chirality of electrons and holes. This knowledge could give us access to previously unexplained transport phenomena.

An example of such an unexplained transport phenomenon was introduced in the previous chapter. There, an unexpected sequencing of QH plateaus is observed. In the p-type regime, for certain top-gate voltages, the magneto-transport measurements of sample QC0464 OG I show a sequence of the filling factor ν of $-1 \rightarrow -2 \rightarrow -1$ with increasing magnetic field strength (cf. Sec. 4.2 and Fig. 4.5). This phenomenon is referred to as re-entrant quantum Hall effect. A similar behavior is known from HgTe/CMT double quantum wells [76], but our observation is the first regarding three-dimensional topological insulators and therefore is to be investigated in detail.

A further difference to previously studied double quantum wells is that sample QC0464 OG I is doped with manganese. Magnetic dopants like Mn affect the band structure of HgTe as investigated in early times in bulk materials [16] and recently in quantum wells [77]. An altered band structure compared to undoped HgTe devices might lead to a different population of n-type and p-type states and thus to changed transport properties of the system. For this reason, it is to be determined whether manganese doping is required in order to observe the re-entrant quantum Hall effect. Note that the essence of topology, the band

inversion of the Γ_6 and Γ_8 bands (cf. Subsec. 2.1.1), is preserved as long as the manganese concentration does not exceed a critical value of $y \approx 7.5\,\%$ [78]. In general, magnetic dopants are able to create profound effects, since they can break time-reversal symmetry. In contrast to magnetically doped bismuth-based topological insulators [79], $Hg_{1-y}Mn_yTe$ is isoelectric and paramagnetic, and therefore, in the absence of an applied external magnetic field B, the magnetization is zero [78]. In the presence of (large) external magnetic fields, however, doping with manganese atoms leads to an enhanced Zeeman effect. In 2D HgTe-based samples, the resulting increased energetic splitting of the Landau levels causes an early onset of the $\nu = -1$ quantum Hall plateau already at onset fields as low as 50 mT [77]. In this context, the influence of magnetic doping in the form of manganese atoms on the transport properties of macroscopic three-dimensional HgTe-based Hall bar structures is to be studied using magneto-transport measurements.

It should be noted that parts of the following data and results are prepared for publication and based on the collaboration with Valentin Müller documented elsewhere (Ref. [57]).

5.1. Re-entrant quantum Hall effect

To investigate the re-entrant quantum Hall effect in more detail, we examine the manganese-doped sample QC0464 OG I. First, top-gate voltage-dependent and magneto-transport measurements carried out at different applied magnetic fields and TG voltages respectively are to be considered. Both measurements are shown in Fig. 5.1. It is noted that the back-gate was grounded for all measurements and that in Fig. 5.1b), only the transverse resistance R_{xy} is displayed to keep the graph clearly laid out and readable. One can observe that the top-gate-dependent as well as the magneto-transport measurements exhibit the expected behavior as it is qualitatively described in Subsec. 2.2.3 and Subsec. 2.2.2, respectively. The $R_{xy}(B = 3\,\mathrm{T}, V_{TG})$ trace (red curve in Fig. 5.1a)) represents a convenient method to determine the value of the top-gate voltage, at which the transition from n-type to p-type conductance occurs. Around the transition point, one of the carrier types predominates the transport on either side, implying that the transverse resistance possesses different signs. At this point, $R_{xy} = 0$ has to be valid. This can be unambiguously identified in the measurement. In our case, we find the transition voltage to be $-0.77\,\mathrm{V}$. On this account, we introduce V^*_{TG}, which is calculated via $V^*_{TG} = V_{TG} + 0.77\,\mathrm{V}$. Now, the charge neutrality point is aligned to $V^*_{TG} = 0\,\mathrm{V}$. The n-type regime of QC0464 OG I ($V^*_{TG} > 0\,\mathrm{V}$) shows well-defined quantization, manifesting the good quality of this sample. Whereas for $V^*_{TG} < 0\,\mathrm{V}$, the transverse resistance exhibits the expected coexistence of n-type and p-type carriers. The behavior at small magnetic fields ($B \leq 0.5\,\mathrm{T}$) is dominated by highly mobile electrons, while at high fields ($B \geq 2\,\mathrm{T}$), holes featuring lower mobility are the dominant carrier type. Using a two-band Drude model [47], we estimate the mobilities to be $\mu_E = 12.6 \cdot 10^4\,\frac{\mathrm{cm}^2}{\mathrm{Vs}}$ and $\mu_{hole} = 2.9 \cdot 10^4\,\frac{\mathrm{cm}^2}{\mathrm{Vs}}$. As described in Subsec. 2.2.2, this leads to less-pronounced quantum

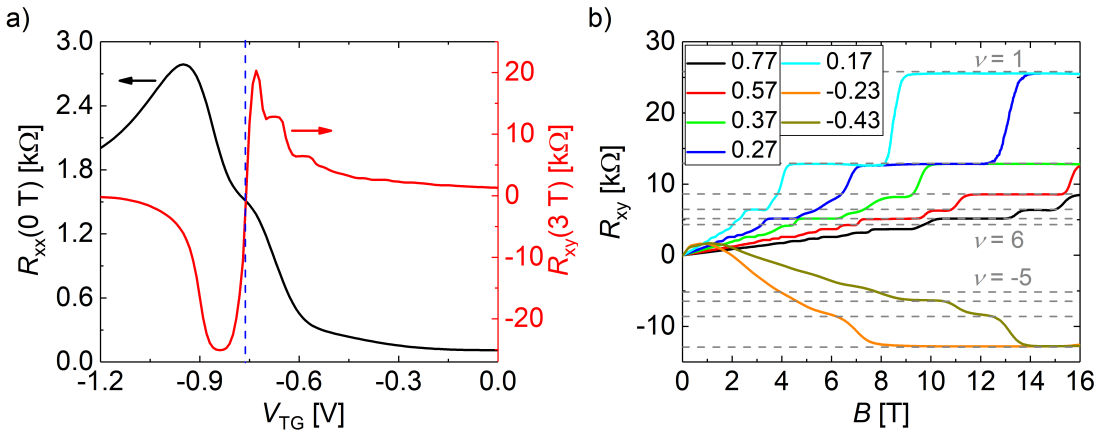

Figure 5.1.: Transport measurements of sample QC0464 OG I at $T \approx 100\,\mathrm{mK}$. a) shows the longitudinal resistance R_{xx} at $B = 0\,\mathrm{T}$ (in black) and the transverse resistance R_{xy} at $B = 3\,\mathrm{T}$ (in red) as a function of applied top-gate voltage V_{TG}. The blue dashed line indicates the transition from n-type to p-type conductance. b) displays magneto-transport measurements at different values of V_{TG}. The applied values are denoted in the unit of volt. The dashed gray lines mark the theoretical predictions of $R_{xy} = h/(e^2\nu)$ for QH plateaus with filling factors ν =-5, -4, -3, -2, 1, 2, 3, 4, 5, and 6.

Hall plateaus in p-type transport. The first observation to be made is that the doping with manganese atoms does not destroy the sample quality. In addition, one is able to find that none of the R_{xy}-traces shows signal issues (cf. chap. 4) despite measuring at extremely low temperatures ($T \approx 100\,\mathrm{mK}$) and magnetic fields of up to 16 T. The explanation is given by the design of sample QC0464 OG I. Since this sample was fabricated with an overlapping top-gate, the quality of the measurement signals solely depends on the total charge carrier density located in the active layer (cf. Sec. 4.2). The smallest value of $|n_{tot}|$ is taken at $V^*_{TG} = 0.17\,\mathrm{V}$ ($n_{tot}\,(V^*_{TG} = 0.17\,\mathrm{V}) = 3.3 \cdot 10^{11}\,\frac{1}{\mathrm{cm}^2}$). Thus, we find $B_{QL}\left(n_{tot} = 3.3 \cdot 10^{11}\,\frac{1}{\mathrm{cm}^2}\right) = 13.6\,\mathrm{T}$ and $B_s\left(n_{tot} = 3.3 \cdot 10^{11}\,\frac{1}{\mathrm{cm}^2}\right) \approx 17.1\,\mathrm{T}$(cf. Eq. 4.1 and Eq. 4.4). Since $B_s \approx 17.1\,\mathrm{T}$ is valid, we do not expect to observe signal issues when measuring up to 16 T.

At certain top-gate voltages ($V^*_{TG} < 0\,\mathrm{V}$), we find an unexpected behavior of the transverse resistance. Fig. 5.2a) displays the magneto-transport measurement at a top-gate voltage of $V^*_{TG} = -0.17\,\mathrm{V}$. The back-gate was grounded during this measurement. The corresponding total charge carrier in the Hg(Mn)Te layer is equal to $n_{tot} = -3.2 \cdot 10^{11}\,\frac{1}{\mathrm{cm}^2}$. One is able to observe that the $\nu = -1$ quantum Hall plateau develops at about 4 T which unexpectedly turns into a $\nu = -2$ QH plateau for fields $B > 6\,\mathrm{T}$ and then re-enters the $\nu = -1$ state for fields $B > 11\,\mathrm{T}$. As already mentioned in Subsec. 2.2.2, we assume that in the regime where we observe the p-type QHE at high magnetic fields, three carrier systems are present in our samples: two n-type conducting topological surface states (TSS,I and TSS,II) and one p-type massive Volkov-Pankratov state (VPS). Given such an unusual phenomenon and a negative top-gate voltage, we expect these three surface states to contribute to the total filling factor ν.

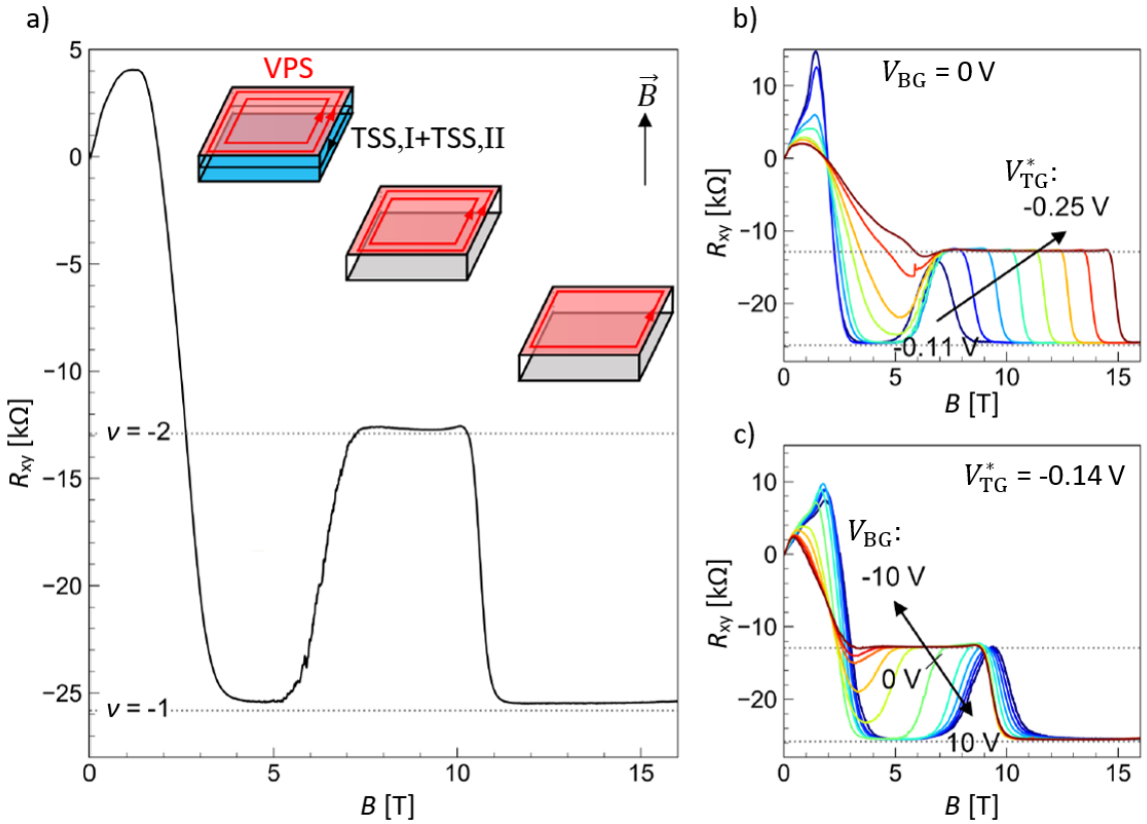

Figure 5.2.: Typical re-entrance of $\nu = -1$ displayed in transverse resistance R_{xy} as a function of magnetic field B at different values of V^*_{TG} and V_{BG}, measured at $T \approx 20\,\text{mK}$. In a), $V^*_{TG} = -0.17\,\text{V}$ is valid. The inset depicts cartoons to illustrate the evolution of quantum Hall edge states on a slab-like sample subject to a perpendicular magnetic field. b) presents top-gate tuning of R_{xy} as a function of B, evenly stepped (step size 0.02 V) from -0.11 V (navy) to -0.25 V (dark red). c) shows back-gate tuning of R_{xy} as a function of B, evenly stepped (step size 2 V) from -10 V (dark red) to 10 V (navy). In all graphs, the theoretical values of the QH plateaus with filling factors $\nu = -2$ and -1 are indicated via dotted gray lines.

To verify our assumption, we perform self-consistent 8-orbital ($|\Gamma_6, \pm\frac{1}{2}\rangle$, $|\Gamma_8, \pm\frac{3}{2}\rangle$, $|\Gamma_8, \pm\frac{1}{2}\rangle$, and $|\Gamma_7, \pm\frac{1}{2}\rangle$) $k \cdot p$ calculations for this sample. Thus, the level of the Fermi energy E_F in the system and which massless and massive states are occupied and therefore contribute to transport can be determined for defined values of applied top-gate voltage. The investigated values of V_TG^* are 0.27 V, 0.12 V, 0.07 V, and -0.03 V. The results are presented in Fig. 5.3a), b), c), and d), respectively. In a), the band structure for applied energy potential $U_\mathrm{i} = 0\,\mathrm{meV}$ at the interface Hg(Mn)Te/CMT is shown. For this energy potential, all states are double degenerate. The corresponding value of V_TG^* reads 0.27 V. It is noted that it is necessary to apply a negative top-gate voltage to the sample ($V_\mathrm{TG} = V_\mathrm{TG}^* - 0.77\,\mathrm{V} = -0.5\,\mathrm{V}$) to obtain $U_\mathrm{i} = 0\,\mathrm{meV}$, since the application of gate-dielectric and top-gate-electrode itself creates an energy potential $U_\mathrm{TS} < 0$ (cf. Subsec. 3.3.2), which has to be removed first. In addition, one is able to recognize that the valence band maximum is not at the Γ point, but occurs at finite momentum due to the combined effects of band inversion and hybridization [45, 77], referred to as camel back [48]. As the top-gate voltage decreases (Fig. 5.3b)), electrons from the top topological surface state (TSS,I) will be depleted gradually, while the bottom TSS (TSS,II) is expected to remain almost unaffected due to the screening effect (cf. Subsec. 2.2.3). At a certain TG voltage $V_\mathrm{TG}^* \leq 0.07\,\mathrm{V}$ (Fig. 5.3c) and d)), a massive p-conducting VPS will appear at the top surface and contribute to transport. The large density of states of the Volkov-Pankratov state leads to a pinning of the Fermi level to this state from now on [57]. This means that applied top-gate voltages $V_\mathrm{TG}^* < 0.07\,\mathrm{V}$ will mainly affect the number of charge carriers in the VPS, while the occupation of TSS,I remains nearly unaffected. This effect is also known as Fermi level pinning [42]. Thus, our assumption of three carrier systems being involved in transport at $V_\mathrm{TG}^* = -0.17\,\mathrm{V}$ is supported by the $k \cdot p$ calculations. By using the back-gate electrode, the population of the surface states on the bottom surface can be influenced. However, since the efficiency of the BG is much lower ($G_\mathrm{BG} \ll G_\mathrm{TG}$)[1], the bottom surface states can only be manipulated to a certain degree (cf. Subsec. 2.2.3). We find $n_\mathrm{tot}\,(V_\mathrm{BG,max}) - n_\mathrm{tot}\,(V_\mathrm{BG,min}) \approx 1.8 \cdot 10^{11}\,\frac{1}{\mathrm{cm}^2}$. Hence, in the experiment, only the topological surface state is accessible at the bottom surface (cf. Subsec. 2.1.2).

Now, we want to examine actual top-gate-dependent and back-gate-dependent measurements of sample QC0464 OG I. The corresponding measurements are presented in Fig. 5.2b) and c) for TG and BG dependency respectively. Starting at a top-gate voltage of $V_\mathrm{TG}^* = -0.11\,\mathrm{V}$, where the low-field $\nu = -1$ plateau is well-developed, the applied TG voltage is tuned to $V_\mathrm{TG}^* = -0.25\,\mathrm{V}$ while keeping the back-gate grounded. For lower top-gate voltages, the low-field $\nu = -1$ plateau gradually vanishes and at the same time, the transition from $\nu = -2$ to high-field $\nu = -1$ moves to higher magnetic fields. Both observations can be explained with the knowledge gained above and on basis of Eq. 2.6 ($\nu \sim n_\mathrm{tot} B^{-1} = (n_\mathrm{TSS,I} + n_\mathrm{TSS,II} + n_\mathrm{VPS}) B^{-1}$). When the top-gate voltage is decreasing from $-0.11\,\mathrm{V}$ to

[1] The top-gate and back-gate actions of sample QC0464 OG I are $G_\mathrm{TG} = 18.2 \cdot 10^{11}\,\frac{1}{\mathrm{Vcm}^2}$ and $G_\mathrm{BG} = 0.12 \cdot 10^{11}\,\frac{1}{\mathrm{Vcm}^2}$.

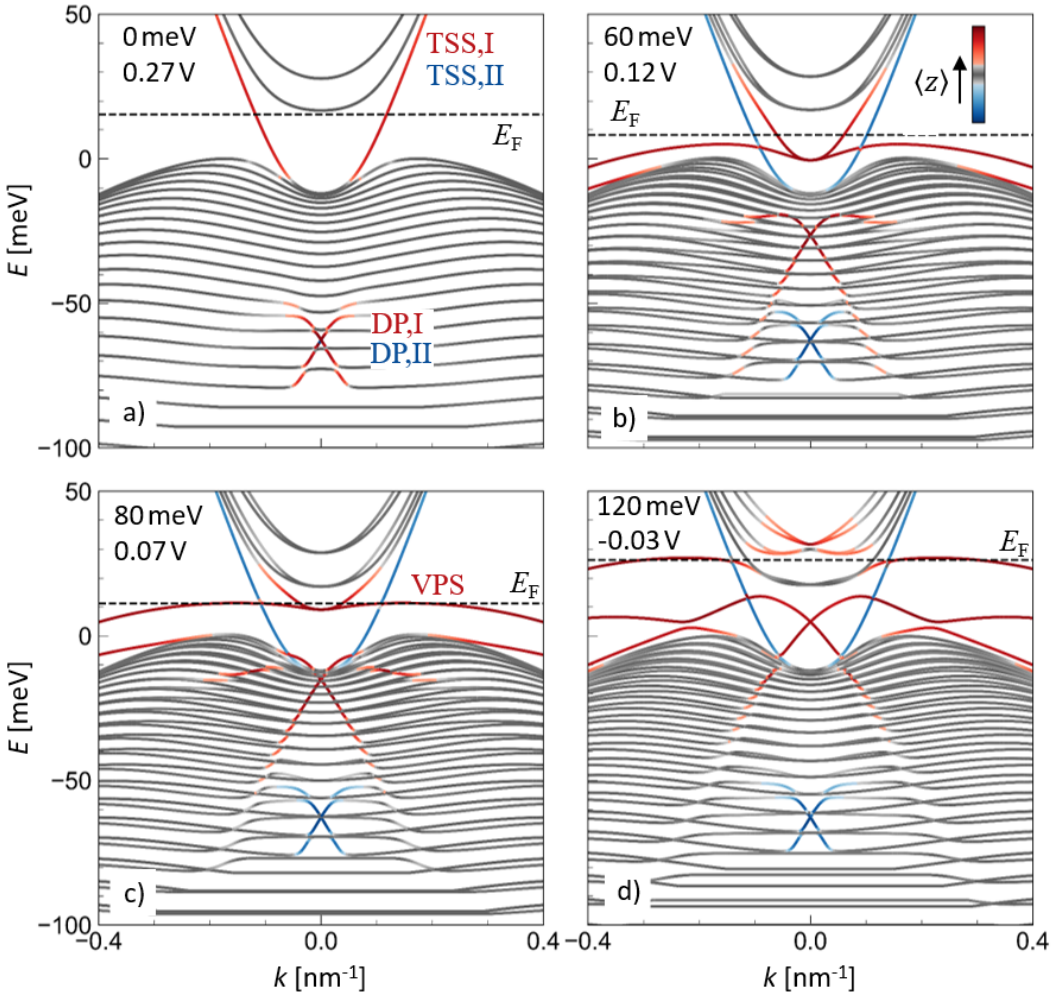

Figure 5.3.: Band structures from 8-orbital $k \cdot p$ calculations for sample QC0464 OG I using different applied energy potentials U_i at the interface Hg(Mn)Te/cap layer. The energy potentials under consideration are a) 0 meV, b) 60 meV, c) 80 meV, and d) 120 meV. The corresponding values of V_{TG}^* are also noted. In addition, indicated are top and bottom surface states (TSS,I and TSS,II), the respective Dirac points (DP,I and DP,II), Volkov-Pankratov states (VPS), the Fermi energy E_F via a dashed black line, and a color code (legend in b)), which depicts the wave function location (expectation value $\langle z \rangle$): top surface (red), bottom surface (blue) or elsewhere (gray).

$-0.25\,\mathrm{V}$, more and more holes are introduced into the system and the occupation of the VPS is increased, whereas the n-type densities located in TSS,I and TSS,II are almost unaffected. Consequently, higher Volkov-Pankratov Landau levels will become populated and the low-field $\nu = -1$ quantum Hall plateau will gradually disappear. In addition, the higher population of the VPS shifts the transition to the high-field $\nu = -1$ state to higher magnetic fields. In Fig. 5.2c), the TG was fixed at $V_{\mathrm{TG}}^{*} = -0.14\,\mathrm{V}$ while the BG was varied between -10 V and 10 V. It can be seen that positive back-gate voltages broaden the low-field $\nu = -1$ quantum Hall plateau, while negative BG voltages narrow the low-field $\nu = -1$ plateau. Since the back-gate mainly affects the TSS,II (cf. Subsec. 2.2.3), n_{VPS} as well as $n_{\mathrm{TSS,I}}$ are nearly constant during these measurements. An applied positive BG voltage increases the occupation of the bottom TSS, while a negative one decreases $n_{\mathrm{TSS,II}}$. A higher electron density will elongate the low-field $\nu = -1$ QH plateau up to higher fields. On the contrary, a lower electron density within the bottom surface state will cause an early depopulation of the topological surface states, which favors the dominance of the p-type Volkov-Pankratov state ($\nu = -\nu_{\mathrm{VPS}} = -2$) at lower magnetic fields.

Taking the above theoretical calculations and experimental evidences into account, it is clear that an interplay of three surface states can give rise to the re-entrant behavior. As we already know, in a 3D TI system, in which two topological surface states as well as one p-type massive Volkov-Pankratov state are occupied, the quantized total Hall conductivity can be written as $\sigma_{\mathrm{xy}}^{\mathrm{tot}} = (\nu_{\mathrm{TSS}} - \nu_{\mathrm{VPS}})e^2/h$, with integer total filling factor $\nu = \nu_{\mathrm{TSS}} - \nu_{\mathrm{VPS}}$ (cf. Subsec. 2.1.3). Intuitively, this may readily explain the appearance of the low-field $\nu = -1$ plateau as a combination of contributions from VPS ($\nu_{\mathrm{VPS}} = 2$), TSS,I and TSS,II ($\nu_{\mathrm{TSS}} = 1$) to the total $\sigma_{\mathrm{xy}}^{\mathrm{tot}} = \nu e^2/h$. Analogous to the assumptions made in chapter 4 (cf. Sec. 4.1), we speculate that one of the TSSs becomes depopulated, turning the associated filling factor into $\nu_{\mathrm{TSS}} = 0$ and introducing a compensation of the topological edge channel conductivity, when the magnetic field continues to increase. Therewith, solely the massive VPS is responsible for the observed quantum Hall effect, $\nu = 0 - 2 = -2$. At even higher magnetic fields, the second lowest Landau level from the massive Volkov-Pankratov state is expected to be depopulated, completing the transition from the $\nu = -2$ to the $\nu = -1$ QH plateau, as schematically sketched in Fig. 5.2a) by a cartoon.

An experimental method to make the occupied Landau levels of a given three-dimensional TI system visible is facilitated by the so-called Landau level fan-chart (LLF). To generate a LLF, for each value of applied magnetic field B one has to perform a top-gate voltage-dependent measurement. The back-gate voltage V_{BG} should be fixed during these measurements. The closer two adjacent magnetic field values are to each other, the better the Landau level fan-chart will be resolved. Typically, the step size of the magnetic field is chosen to be between 20 mT and 40 mT. Thus, by interpolating the data points, one is able to determine R_{xx}, R_{xy}, σ_{xx}, and σ_{xy} at each point in the (V_{TG}^{*},B) parameter space. The longitudinal and transverse

conductivities can be determined by

$$\sigma_{\mathrm{xx}} = \frac{\frac{R_{\mathrm{xx}}}{AR}}{\frac{R_{\mathrm{xx}}^2}{AR^2} + R_{\mathrm{xy}}^2} \tag{5.1}$$

and

$$\sigma_{\mathrm{xy}} = \frac{R_{\mathrm{xy}}}{\frac{R_{\mathrm{xx}}^2}{AR^2} + R_{\mathrm{xy}}^2}, \tag{5.2}$$

respectively, where AR is the aspect ratio of the sample (cf. Subsec. 2.2.2). The measured LLF of device QC0464 OG I is shown in Fig. 5.4. In Fig. 5.4a) and Fig. 5.4b), the values of R_{xx} and $\sigma_{\mathrm{xx}}^{1/3}$ are displayed at each point in the (V_{TG}^*,B) parameter space with the help of a color code. The representation of the longitudinal resistance R_{xx} shows the regimes of top-gate voltage V_{TG}^* and magnetic field B, in which the surface states of the sample become insulating. In the measurement, this behavior is manifested by resistance values much larger than 200 kΩ. It is noted that by using high impedance lock-in amplifiers, we are not equipped to measure such large resistances. Therefore, output resistances in the triple-digit kΩ-range indicate an insulating behavior of the sample. This is in good agreement with the previous chapter. We find the regimes to be at low charge carrier densities (around $V_{\mathrm{TG}}^* = 0\,\mathrm{V}$) and high magnetic fields ($B > 8.5\,\mathrm{T}$). Larger values of $|n_{\mathrm{tot}}|$ (increased $|V_{\mathrm{TG}}^*|$) lead to higher required magnetic fields to enter the insulating surface states. On the other hand, the representation of $\sigma_{\mathrm{xx}}^{1/3}$ is chosen to depict the positions of the occupied Landau levels. Large values of $\sigma_{\mathrm{xx}}^{1/3}$ (yellow and green) represent the positions of occupied LLs contributing to transport, while $\sigma_{\mathrm{xx}}^{1/3} = 0$ (blue) indicates the positions of quantum Hall plateaus. The cubic root is chosen to display the Landau levels in the graph more clearly. Since for small magnetic fields ($B < 2\,\mathrm{T}$) adjacent LLs are close to each other in energy (cf. Subsec. 2.1.3), it is difficult to resolve all Landau levels in the measurement in this magnetic field regime. Due to the low mobility of holes ($\mu_{\mathrm{hole}} = 2.9 \cdot 10^4\,\frac{\mathrm{cm}^2}{\mathrm{Vs}}$), the regime of high p-type densities ($V_{\mathrm{TG}}^* < -0.2\,\mathrm{V}$) also exhibits poor resolution. Thus, in the following evaluations, we will focus on the well-resolved parts of the LL fan-chart. The crossing points of electrochemical potential $\mu(B)$ and Landau levels indicate a change in the total filling factor of quantum Hall plateaus by $\Delta\nu = \pm 1$, depending on whether a p-type or an n-type LL is crossed. For instance, if we examine $V_{\mathrm{TG}}^* = -0.17\,\mathrm{V}$ (dashed black line in Fig. 5.4b)), we find crossings at $B \approx 11.2\,\mathrm{T}$, 6.3 T, and 4.2 T (from high to low magnetic fields). The latter crossing point is difficult to determine, since the poor resolutions of the regimes of low magnetic fields and high p-type densities already start to occur. At these values of magnetic field, the transverse resistance R_{xy} should perform a transition between two QH plateaus. Considering the corresponding magneto-transport measurement (cf. Fig. 5.2a)), we find the transitions between quantum Hall plateaus to be at $B \approx 11.0\,\mathrm{T}$, 6.2 T, and 3.9 T, which coincide well with the values determined from the LLF. On the basis of this magneto-transport measurement, one is able to identify the positions of the high-field $\nu = -1$ and $\nu = -2$ QH plateaus in the Landau

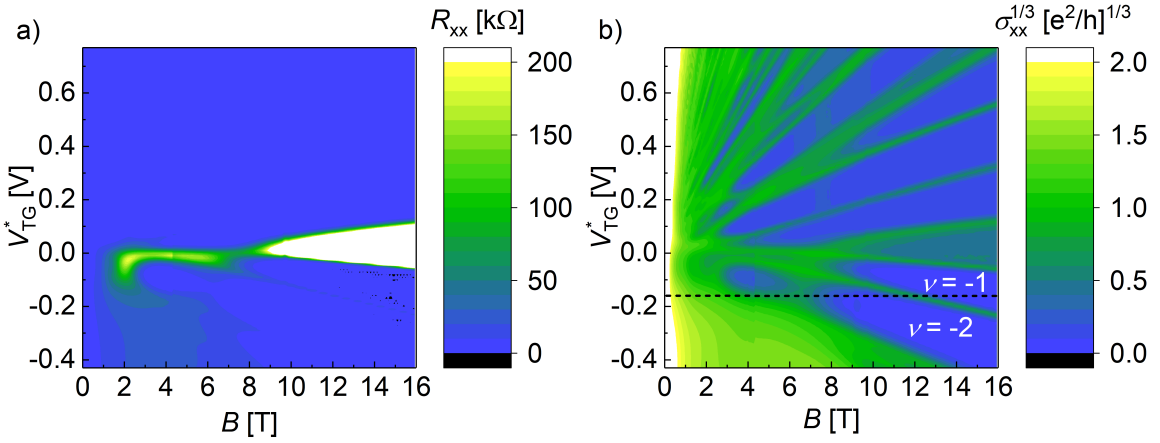

Figure 5.4.: Landau level fan-chart of sample QC0464 OG I measured at $T \approx 100\,\mathrm{mK}$ and $V_{BG} = 0\,\mathrm{V}$. The color code represents the value of a) R_{xx} and b) $\sigma_{xx}^{1/3}$ at each point in the (V^*_{TG},B) parameter space. In b), the positions of the high-field $\nu = -1$ and $\nu = -2$ quantum Hall plateaus are indicated in white. $V^*_{TG} = -0.17\,\mathrm{V}$ is delineated by a dashed black line. In both graphs, two measurement artifacts are visible: First, since the step size of the magnetic field was increased at about 4.3 T to reduce the total measuring time, a vertical line is observable at this field. Secondly, a dislocation line is apparent at $B \approx 9.6\,\mathrm{T}$ due to the fact that the LLF is composed of two sets of measurements.

level fan-chart. At this point, however, we are not able to assign the observed Landau levels to their underlying carrier systems. An n-type LL, for instance, can originate from n-bulk states, n-type VPSs, TSS,I or TSS,II (cf. Subsec. 2.1.2). Therefore it is not possible to identify which transport channel contributes to transport and thus to the total filling factor ν.

Hence, in order to gain detailed insight into the transport properties of the three-dimensional topological insulator Hg(Mn)Te, we have developed a toy model. We denote this model *four-band model* since four carrier systems are included in the calculations: the two topological surface states, one p-type Volkov-Pankratov state, and one n-type massive state, which can be either an additional VPS or a bulk state. In the following, we want to describe how the model works before it is applied to sample QC0464 OG I. First, we assume the Landau level dispersion for massless Dirac fermions for TSS,I and TSS,II and the LL dispersion for conventional parabolic-bands for Volkov-Pankratov and bulk states. The corresponding equations for the eigen-energies are given by (cf. Subsec. 2.1.3, Eq. 2.13 and Eq. 2.15)

$$E_{\mathrm{TSS}}(B, N_{\mathrm{TSS},\beta}) = \sqrt{2e\hbar v_{\mathrm{F}}^2 B N_{\mathrm{TSS},\beta} + (g^*_{\mathrm{TSS}}\mu_{\mathrm{B}}B)^2} - \hbar v_{\mathrm{F}}\sqrt{4\pi n_{\mathrm{TSS},\beta}} \tag{5.3}$$

and

$$E_{\mathrm{m}}(B, N_{\mathrm{m}}) = (N_{\mathrm{m}} + \frac{1}{2})\frac{\hbar e}{m_{\mathrm{eff}}}B \pm \frac{g^*_{\mathrm{m}}}{2}\mu_{\mathrm{B}}B - \frac{\hbar^2\pi}{2m_{\mathrm{eff}}}\left|n_{\mathrm{m}}\right|, \tag{5.4}$$

for topological surface and massive states, respectively. Here, for simplicity, we do not consider any coupling between n-type and p-type surface states. In addition, it is easily justifiable that the top and bottom TSSs do not hybridize in our 3D systems, since the thickness of the active layer ($d_{\mathrm{HgMnTe}} \approx 70\,\mathrm{nm}$) is much larger than the localization lengths of the surface states [39]. Furthermore, we consider an impurity-induced broadening of the Landau levels at a given magnetic field B via a Gaussian function $F(E)$. The total density of states DOS of the system is then described by

$$DOS(E) = \frac{Be}{h} \sum_{\ell} c_\ell F(E) = \frac{Be}{h\sigma\sqrt{2\pi}} \sum_{\ell} c_\ell e^{-\frac{(E-E_\ell)^2}{2\sigma^2}}, \tag{5.5}$$

where σ defines the broadening of the Gaussian function in units of energy and the sum runs over all Landau levels ℓ with associated energy E_ℓ. This includes the LLs from topological surface states as well as massive states. c_ℓ is a constant reflecting the character of the underlying Landau level. $c_\ell = 1$ for all LLs except the $N_{\mathrm{TSS},\beta} = 0$ Landau levels for the TSSs. The lowest LL of a topological surface state is responsible for the half-integer filling factor (cf. Subsec. 2.1.3). Therefore, we use $c_\ell = \frac{1}{2}$ for these particular Landau levels. For simplicity, we set σ constant in a varying magnetic field and assume the same σ for all LLs. For further calculations, we need to define an evenly spaced grid of (E, B) first and carry out calculations throughout this grid. To define the grid, the intervals of E and B are set to be 1 meV and 25 mT, respectively. Given the carrier densities from each state, we immediately know the total charge carrier density n_{tot} as follows:

$$n_{\mathrm{tot}} = n_{\mathrm{TSS,I}} + n_{\mathrm{TSS,II}} + n_{\mathrm{m}}^{\mathrm{p-type}} + n_{\mathrm{m}}^{\mathrm{n-type}}, \tag{5.6}$$

with $n_{\mathrm{TSS,I}}$, $n_{\mathrm{TSS,II}}$, $n_{\mathrm{m}}^{\mathrm{n-type}} > 0$ and $n_{\mathrm{m}}^{\mathrm{p-type}} < 0$ being valid. We can use n_{tot} to define the electrochemical potential μ for the entire system. This step includes the calculation of the integrated density of states $IDOS(E)$ as a function of energy:

$$IDOS(E) = \int_{-\infty}^{E} DOS_{\mathrm{TSS,I}}\left(E'\right) \mathrm{d}E' + \int_{-\infty}^{E} DOS_{\mathrm{TSS,II}}\left(E'\right) \mathrm{d}E' - \int_{E}^{+\infty} DOS_{\mathrm{m}}^{\mathrm{p-type}}\left(E'\right) \mathrm{d}E'$$
$$+ \int_{-\infty}^{E} DOS_{\mathrm{m}}^{\mathrm{n-type}}\left(E'\right) \mathrm{d}E', \tag{5.7}$$

where $DOS_{\mathrm{i}}^{\mathrm{j}}$ refers to the part of Eq. 5.5 which includes only Landau levels from the TSSs (TSS,I or TSS,II), p-type massive VPS, or n-type massive state (n-type Volkov-Pankratov or n-bulk state). We calculate $IDOS(E)$ for each B point on the defined grid and therefore obtain the value of $IDOS(E, B)$ at each point of the grid. To find the electrochemical potential $\mu(B)$ as a function of magnetic field B, we need to solve the equation $IDOS(\mu, B) = n_{\mathrm{tot}}$

at each B point. Now, we can derive the Landau levels crossed by the electrochemical potential $\mu(B)$ and thus know which bands are occupied at a given magnetic field B. Instead of plotting Landau levels in energy, one is able to plot LLs in density n by converting energy values to density values one by one via $IDOS(E,B) = n(E)$ at each B point. Then it is straightforward to determine the crossings of the electrochemical potential with the LLs, since the position of the electrochemical potential is given by $n = n_{\mathrm{tot}}$. If we feed the carrier densities $n_{\mathrm{TSS,I}}$, $n_{\mathrm{TSS,II}}$, $n_{\mathrm{m}}^{\mathrm{n-type}}$, and $n_{\mathrm{m}}^{\mathrm{p-type}}$ into our model as inputs at each top-gate voltage V_{TG}, a plot of Landau levels in the (V_{TG},B) parameter space can be constructed. This plot corresponds to the experimentally obtained Landau level fan-chart. Obviously, one has to be able to determine the respective charge carrier densities for each TG voltage of interest and the finer the steps between adjacent top-gate voltages are chosen, the more accurate the model becomes.

Now, the *four-band model* is to be applied to sample QC0464 OG I. For this purpose, we first have to determine the values of $n_{\mathrm{TSS,I}}$, $n_{\mathrm{TSS,II}}$, $n_{\mathrm{m}}^{\mathrm{n-type}}$, and $n_{\mathrm{m}}^{\mathrm{p-type}}$. These charge carrier densities can be extracted from fast Fourier transformation (FFT) analysis based on the periodicity of Shubnikov-de Haas oscillations in B^{-1} as described in Subsec. 2.2.2. Fig. 5.5 shows the results of the FFT analysis for this sample. When considering the fast Fourier transformation analysis of sample QC0464 OG I, one can observe a different quality for n-type ($V_{\mathrm{TG}}^{*} > 0\,\mathrm{V}$) and p-type ($V_{\mathrm{TG}}^{*} < 0\,\mathrm{V}$). For high n-type densities ($V_{\mathrm{TG}}^{*} > 0.47\,\mathrm{V}$), four pronounced peaks are visible representing the carrier systems of the two TSSs and the n-type massive state (Volkov-Pankratov or n-bulk state) with lifted spin degeneracy. If the top-gate voltage is decreased below $V_{\mathrm{TG}}^{*} = 0.47\,\mathrm{V}$, two of the peaks disappear gradually. Once only two peaks remain in the spectrum, only the carriers in TSS,I and TSS,II contribute to transport. In contrast, in p-type, it is difficult to recognize a well-resolved peak at all. The reason can be found in the low hole mobility ($\mu_{\mathrm{hole}} = 2.9 \cdot 10^{4}\,\frac{\mathrm{cm}^2}{\mathrm{Vs}}$) of this sample and in the combination of a moderate electron mobility ($\mu_{\mathrm{E}} = 12.6 \cdot 10^{4}\,\frac{\mathrm{cm}^2}{\mathrm{Vs}}$) paired with the fact that for $V_{\mathrm{TG}}^{*} < 0\,\mathrm{V}$, only a small number of electrons are involved in transport. Hence, the SdH oscillations for small magnetic fields $B < 2\,\mathrm{T}$ (mainly caused by electrons) as well as those for larger fields $B > 2\,\mathrm{T}$ (mainly caused by holes) are poorly resolved. Without pronounced Shubnikov-de Haas oscillations, a FFT analysis will most likely not provide any usable results. Since we are most interested in top-gate voltages $V_{\mathrm{TG}}^{*} < 0\,\mathrm{V}$ to recreate the experimentally observed re-entrant quantum Hall effect with the help of our model, the best we can do is to guess reasonable values of $n_{\mathrm{TSS,I}}$, $n_{\mathrm{TSS,II}}$, and $n_{\mathrm{m}}^{\mathrm{p-type}}$ for a top-gate voltage at which we observe the re-entrant QHE in the measurement. As already mentioned above, only three carrier system contribute to transport for $V_{\mathrm{TG}}^{*} < 0\,\mathrm{V}$ and therefore we do not have to include the n-type massive state in our considerations. The estimation of reasonable values of $n_{\mathrm{TSS,I}}$, $n_{\mathrm{TSS,II}}$, and $n_{\mathrm{m}}^{\mathrm{p-type}}$ is done taking into account the findings of undoped 3D HgTe-based devices for which we were able to determine the individual carrier densities in the p-type regime. $n_{\mathrm{TSS,I}} = 0.2 \cdot 10^{11}\,\frac{1}{\mathrm{cm}^2}$, $n_{\mathrm{TSS,II}} = 1.0 \cdot 10^{11}\,\frac{1}{\mathrm{cm}^2}$, and $n_{\mathrm{m}}^{\mathrm{p-type}} = -3.5 \cdot 10^{11}\,\frac{1}{\mathrm{cm}^2}$

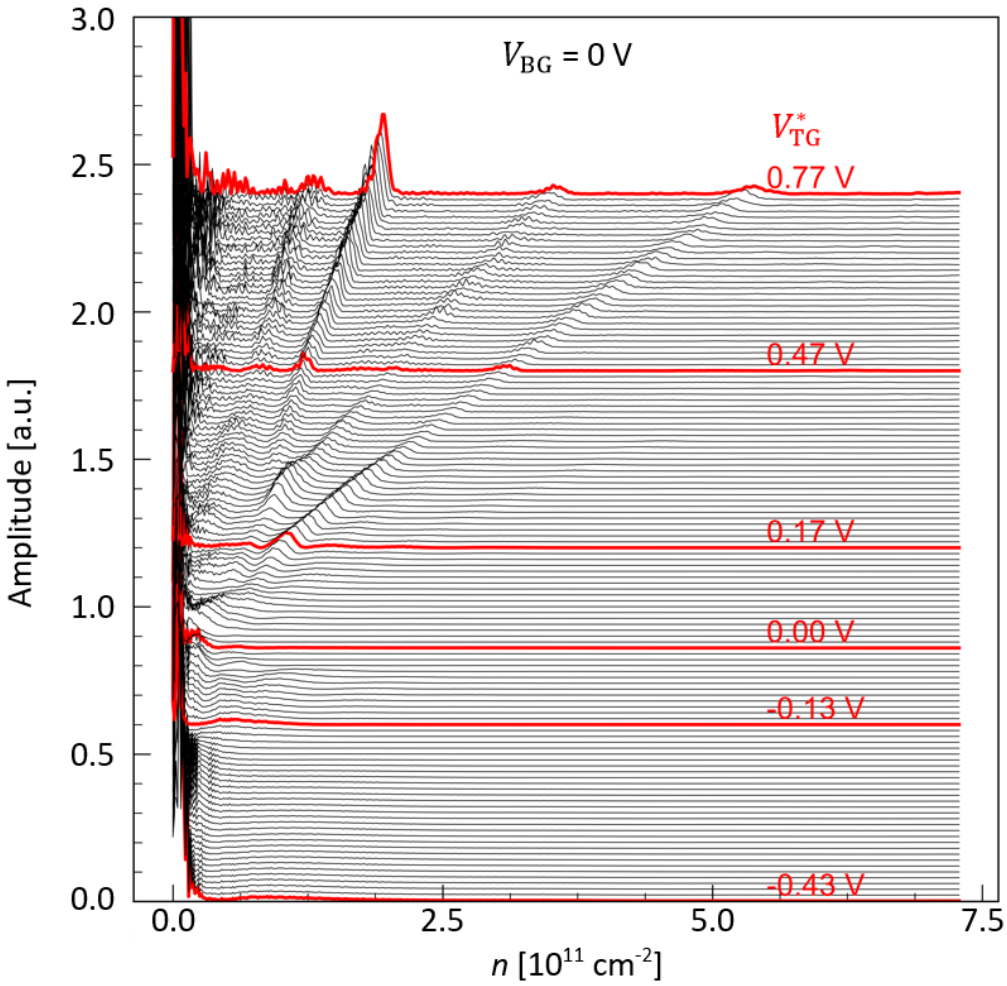

Figure 5.5.: The fast Fourier transformation analysis of sample QC0464 OG I is shown as a function of density n. The investigated top-gate voltages range from $V^*_{TG} = 0.77\,V$ to $V^*_{TG} = -0.43\,V$ in steps of 0.01 V. An offset of 0.02 is used between adjacent curves to make the graph more readable. For the same reason, six curves are highlighted in red.

represent such a set of charge carrier densities. Using Eq. 5.6, we find $n_{\mathrm{tot}} = -2.3 \cdot 10^{11}\,\frac{1}{\mathrm{cm}^2}$. This total charge carrier density is associated to $V_{\mathrm{TG}}^{*} = -0.12\,\mathrm{V}$ in the experiment. Since the re-entrant quantum Hall effect can be observed at this top-gate voltage (cf Fig. 5.2b)), we use the densities given above as input to feed the *four-band model*. Now, we are able to calculate the Landau level dispersion at this top-gate voltage. The results are presented in Fig. 5.6a) and b). a) shows the position of Landau levels in the (E,B) parameter space, while in b), the energy E has been converted into total carrier density n_{tot}. Since the number of occupied LLs approaches infinity at low magnetic fields, we need to set a cut-off field $B = 1\,\mathrm{T}$ to perform the calculation numerically. This means we carry out the calculation in the range 1 T to 16 T. The parameters used for the calculation are $v_{\mathrm{F}} = 5 \cdot 10^5\,\frac{\mathrm{m}}{\mathrm{s}}$, $g_{\mathrm{TSS}}^{*} = 28$, $g_{\mathrm{m}}^{*} = 6$, $m_{\mathrm{eff}} = -0.2 m_{\mathrm{e}}$, and $\sigma = 1\,\mathrm{meV}$ and are taken from Ref. [15]. The large effective g-factor g_{TSS}^{*} is assumed due to the doping with manganese. On the basis of these plots, we can determine the occupied Landau levels and therefore the total filling factor at each value of magnetic field B. With increasing field, whenever the electrochemical potential $\mu\,(B)$ crosses with LLs, the total filling factor changes by -1 or +1, depending on whether an n-type or a p-type Landau level is crossed, respectively. We find the high-field crossing to be at $B = 3.8\,\mathrm{T}$, 5.9 T, 6.7 T, and 9.8 T. In the regime of small magnetic fields ($B < 3.8\,\mathrm{T}$), the crossings of the electrochemical potential with LLs are too close to each other to carry out a meaningful evaluation. Thus, we can specify the value of the total filling factor $\nu = \nu_{\mathrm{TSS}} - \nu_{\mathrm{VPS}}$ as a function of the magnetic field B as follows: $\nu = 1 - 3 = -2$ for $3.8\,\mathrm{T} < B < 5.9\,\mathrm{T}$, $\nu = 1 - 2 = -1$ for $5.9\,\mathrm{T} < B < 6.7\,\mathrm{T}$, $\nu = 0 - 2 = -2$ for $6.7\,\mathrm{T} < B < 9.8\,\mathrm{T}$, and $\nu = 0 - 1 = -1$ for magnetic fields $B > 9.8\,\mathrm{T}$. At this point, one is already able to recognize that our model successfully recreated the re-entrant quantum Hall effect behavior observed in the experiment.

To compare the result of our model with the experimentally obtained data of sample QC0464 OG I, we can use the Landau level fan-chart (cf. Fig. 5.6c)) as well as the magneto-transport measurement, for which $V_{\mathrm{TG}}^{*} \approx -0.12\,\mathrm{V}$ applies (cf. Fig. 5.2b)). Since we only have one set of densities ($n_{\mathrm{TSS,I}}$, $n_{\mathrm{TSS,II}}$, and $n_{\mathrm{m}}^{\mathrm{p-type}}$) to feed the model, it can recreate just one top-gate voltage ($V_{\mathrm{TG}}^{*} = -0.12\,\mathrm{V}$) of the LLF. If we compare the calculated high-field crossings of $\mu\,(B)$ with Landau levels (marked as colored circles in Fig. 5.6c)) with the positions of the LLs in the Landau level fan-chart, we find a good agreement. This is especially the case if it is taken into account that the input charge carrier densities are only estimated values and the real densities may deviate slightly. Furthermore, we are able to compare the simulated positions of the quantum Hall plateaus and their associated values of the total filling factor with those found in the experiment. For this purpose, we consider Fig. 5.2b). The TG voltages $V_{\mathrm{TG}}^{*} = -0.11\,\mathrm{V}$ (navy curve) and $V_{\mathrm{TG}}^{*} = -0.13\,\mathrm{V}$ (blue curve) are of most interest, since they are the closest to $V_{\mathrm{TG}}^{*} = -0.12\,\mathrm{V}$. Examining $V_{\mathrm{TG}}^{*} = -0.13\,\mathrm{V}$, for instance, we find $\nu = -1$ for $3.6\,\mathrm{T} < B < 4.8\,\mathrm{T}$, $\nu = -2$ for $7.0\,\mathrm{T} < B < 8.1\,\mathrm{T}$ and $\nu = -1$ for $B > 9.9\,\mathrm{T}$. The comparison to the calculations ($\nu = -1$ for $5.9\,\mathrm{T} < B < 6.7\,\mathrm{T}$, $\nu = -2$ for $6.7\,\mathrm{T} < B < 9.8\,\mathrm{T}$,

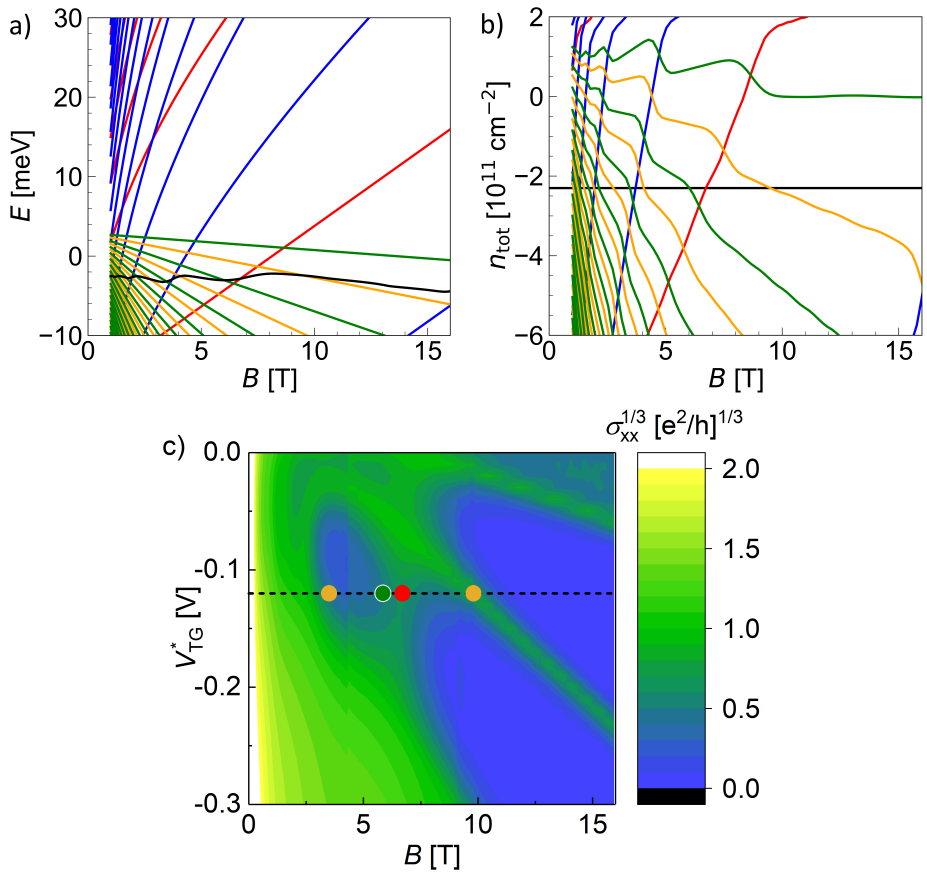

Figure 5.6.: Landau level dispersions in the a) (E,B), b) (n_{tot},B), and c) (V_{TG}^*,B) parameter space. a) and b) are results of the *four-band model* obtained from input densities $n_{\mathrm{TSS,I}} = 0.2 \cdot 10^{11}\,\frac{1}{\mathrm{cm}^2}$, $n_{\mathrm{TSS,II}} = 1.0 \cdot 10^{11}\,\frac{1}{\mathrm{cm}^2}$, and $n_{\mathrm{m}}^{\mathrm{p-type}} = -3.5 \cdot 10^{11}\,\frac{1}{\mathrm{cm}^2}$. The colors used in a) and b) are associated to the underlying carrier system as follows: TSS,I (red), TSS,II (blue), VPS spin-up (green), and VPS spin-down (yellow). The electrochemical potential is delineated as a black line. c) represents the experimentally obtained LLF of sample QC0464 OG I from Fig. 5.4b) with reduced range of top-gate voltage V_{TG}^*. $V_{\mathrm{TG}}^* = -0.12\,\mathrm{V}$ is indicated by a dashed black line. The calculated positions of the high-field crossings of the electrochemical potential with Landau levels are extracted from b) and sketched in c) using the same colors.

and $\nu = -1$ for $B > 9.8\,\mathrm{T}$) shows a satisfactory match between model and measurement. This is particularly noticeable by the good alignment of the high-field $\nu = -2$ and $\nu = -1$ quantum Hall plateaus. The different elongation of the $\nu = -2$ QH plateau can be explained by thermal and impurity-induced broadening of the Landau levels in the experiment. For this reason, a smooth transition between adjacent plateaus within a finite extent of magnetic field is performed in the measurement. However, when evaluating the calculations of the *four-band model*, a specific magnetic field value was taken for each of the crossings of $\mu\,(B)$ with the LLs. This would correspond to a step-shaped transition between adjacent quantum Hall plateaus and thus result in longer elongations of plateaus. The deviation of the positions of the low-field $\nu = -1$ plateaus may be the result of estimated input densities varying slightly from the unknown actual values at $V_{\mathrm{TG}}^{*} = -0.12\,\mathrm{V}$. In addition, slightly different top-gate voltages are considered ($V_{\mathrm{TG}}^{*} = -0.12\,\mathrm{V}$ and $V_{\mathrm{TG}}^{*} = -0.13\,\mathrm{V}$, respectively), which may also lead to small deviations between model result and magneto-transport measurement.

Thus, we can conclude that our *four-band model* is able to recreate the experimentally observed re-entrant quantum Hall effect. The comparison between simulation and actual data shows a satisfactory match. In this context, the model is not only able to determine the positions of the Landau levels, but it also allows the assignment of each LL to its underlying topological or massive state. It can be demonstrated, for instance, that in order to obtain the re-entrant QH effect, first a Landau level originating from the TSS,I and subsequently one originating from the p-type VPS with spin-down have to be crossed (cf. Fig. 5.6c)). Furthermore, the contribution of each carrier system to the total filling factor $\nu = \nu_{\mathrm{TSS}} \pm \nu_{\mathrm{m}}$ can be determined, since the *four-band model* allows the number and type of the occupied LLs for each point in the (V_{TG},B) parameter space to be identified. Hence, it can be verified that, as assumed, the re-entrant QHE results from an interplay of two topological surface states and one p-type massive Volkov-Pankratov state. However, there are also small deviations between model and experimental results. These deviations may be explained by the fact that our model neglects any influence of temperature and is fed by parameters v_{F}, g_{TSS}^{*}, g_{m}^{*}, and m_{eff}, which may not be known exactly for a given 3D TI system. In addition, the broadening of the Landau levels observed in the experiment results in a smooth transition between quantum Hall plateaus and thus in less elongated plateaus compared to the model prediction. Lastly, the fast Fourier transformation analysis of sample QC0464 OG I shows no evaluable results in the interesting top-gate voltage regime ($V_{\mathrm{TG}}^{*} < 0\,\mathrm{V}$), wherefore the required input charge carrier densities cannot be determined. Instead, estimated values, which may differ from the actual ones, were used.

The next step would be to apply our *four-band model* to a high mobility sample that exhibits pronounced Shubnikov-de Haas oscillations in the entire range of top-gate voltage in magneto-transport measurements. Thus, one is able to determine the input densities $n_{\mathrm{TSS,I}}$, $n_{\mathrm{TSS,II}}$, $n_{\mathrm{m}}^{\mathrm{n-type}}$, and $n_{\mathrm{m}}^{\mathrm{p-type}}$ for all values of top-gate voltage and therefore the whole Landau

level fan-chart can be reconstructed. In Ref. [57], the model is applied to a high mobility 3D TI sample (averaged carrier mobility is of the order of $\mu \approx 60 \cdot 10^4 \, \frac{\mathrm{cm}^2}{\mathrm{Vs}}$), which, additionally, has a CMT:I modulation doping layer grown beneath the active layer to increase the electron density in TSS,II (cf. Sec. 4.2). Since this topological surface state is almost unaffected by the top-gate, it is ensured that a sufficient number of electrons, which contribute to transport, are available for each value of applied top-gate voltage. The combination of high mobility and doping layer leads to pronounced SdH oscillations in magneto-transport measurements, which can be evaluated by FFT analysis to extract the required input densities. Also for this sample, the LLF simulated using the *four-band model* shows good agreement with its experimentally obtained counterpart. The positions of the Landau levels in the (V_{TG},B) parameter space as well as the values of the total filling factor ν coincide satisfactorily. In addition, the model is able to recreate the re-entrant QH effects appearing in the magneto-transport measurements of the high-mobility device. Thus, our toy model is sufficient to provide a qualitative understanding of the experimental results. Obviously, it is not a perfect quantitative match. A better fit would certainly require a more computationally heavy approach based on fully self-consistent $k \cdot p$ calculations. The analysis of the measurements of the Mn-doped (QC0464 OG I) and the high-mobility samples confirm our assumption that the re-entrant QHE is actually a phenomenological result of alternating population and depopulation of LLs originating from n-type topological surface states and a p-type massive Volkov-Pankratov state. Therefore, we are able to conclude that the observed re-entrance of quantum Hall plateaus is a direct consequence of the interplay of massless and massive surface states. In addition, using the *four-band model*, we are able to determine the occupied states in the device for each level of Fermi energy E_{F}. The associated knowledge of the corresponding filling factors (ν_{TSS}, ν_{m}) allows us to gain a profound understanding of magneto-transport measurements and the possibility of accessing previously unexplained transport phenomena of three-dimensional HgTe-based TI samples.

The high-mobility sample investigated in Ref. [57] also shows the re-entrant quantum Hall effect, which can be explained by the contribution of three independent charge carrier systems (TSSs of top and bottom surfaces and p-type VPS) to transport. Since this sample is not doped with manganese atoms, Mn-doping can be excluded as the origin of the re-entrant QHE. However, in three-dimensional manganese-doped devices, we observed a particularly pronounced re-entrant quantum Hall effect featuring a $-1 \rightarrow -2 \rightarrow -1$ sequencing of QH plateaus. We therefore speculate that this distinctive plateau sequencing originates from the band structure of HgTe being affected by magnetic dopants. Especially the enhanced Zeeman splitting in the presence of an external magnetic field may be a decisive factor here. In contrast to the 3D case, the influence of Mn-doping has already been proven in two-dimensional HgTe samples [77]. There, the increased Zeeman effect resulting from the doping causes a stronger splitting of the Landau levels, leading to an early onset of the $\nu = -1$ quantum

Hall plateau. The observation of the pronounced $-1 \rightarrow -2 \rightarrow -1$ re-entrant QHE in three-dimensional $Hg_{1-y}Mn_yTe$ samples is discussed as the condensed-matter realization of the parity anomaly in 3D topological insulators [15, 80].

To keep the *four-band model* as simple as possible, we assumed that there is no coupling between the Landau levels originating from the different carrier systems. In addition, it has not been taken into account so far that the n-type and p-type states, which propagate in opposite directions at the edge of a sample due to imposed opposite chirality of electrons and holes, may inter-scatter into each other. Therefore, in the following section, the inter-scattering between n-type and p-type quantum Hall edge states is to be investigated. For this purpose, a scattering model based on Büttiker's original idea, the Landauer-Büttiker formalism [66, 81], is introduced. Thus, by comparing equal and unequal numbers of edge states in each direction, we gain insights into the formation of counter-propagating quantum Hall edge states.

5.2. Tunable inter-scattering between counter-propagating quantum Hall edge states

A complex scattering model to describe the tunable inter-scattering between counter-propagating quantum Hall edge states can be found in Ref. [82]. Here, we solely want to present a simplified description of the modeling and emphasize on the results.

To describe the transport in the quantum Hall regime, one has to consider the Landauer-Büttiker formalism. The basic input for this formalism are the transmission probabilities T between voltage probes, which in our case are represented by the six contacts of the Hall bar device QC0464 OG I. Within the general Landauer-Büttiker formalism, in the case of edge channel transport, the current-energy potential relationship in a 6-terminal Hall bar structure can be expressed as

$$I_i = \frac{e}{h} \sum_j (N_{ji} T_{ji} U_i - N_{ij} T_{ij} U_j), \tag{5.8}$$

where I_i is the current flowing out of the ith electrode into the sample, U_i (U_j) is the energy potential on the ith (jth) electrode, T_{ji} (T_{ij}) is the transmission probability and N_{ji} (N_{ij}) is the number of QH edge channel propagating from the ith (jth) to the jth (ith) electrode [81, 83]. It is noted that at this point, to keep the model simple, we assume that all quantum Hall edge channels propagating in the same direction between two adjacent electrodes have the same transmission probability. If all QH edge channels contributing to transport propagate in the same direction, then $T = 1$ is valid due to the lack of reverse-propagating channels [66]. In contrast, referring to Ref. [82], we know that inter-scattering between counter-propagating states can have a pronounced influence on the transmission probabilities, resulting in $T < 1$.

If neither $j = i-1$ nor $j = i+1$ applies, i.e. the electrodes are not adjacent ones, then $T = 0$ holds. Without loss of generality, we refer to counter-clockwise moving quantum Hall edge channels as forward-moving (index f) and to clockwise moving edge channels as backward-moving (index b). In addition, for the sake of simplicity, we assume that forward-moving QH edge channels possess the same transmission probability T_f between all six electrodes. An analogous assumption is made for the transmission probabilities T_b of the backward-moving edge channels. By doing so, we neglect the fact that the distance between adjacent electrodes of the Hall bar device can vary (cf. Fig. 2.11), which in turn may affect the transmission probability. Obviously, the number of forward-moving and backward-moving quantum Hall edge states is unchanged across the Hall bar structure. The relation between energy potential and electric potential is given by $U = -eV$. Taking the considerations made above into account, we are able to rewrite Eq. 5.8 to

$$\begin{pmatrix} I_1 \\ I_2 \\ I_3 \\ I_4 \\ I_5 \\ I_6 \end{pmatrix} = \frac{e^2}{h} \begin{pmatrix} \alpha & \beta & 0 & 0 & 0 & \gamma \\ \gamma & \alpha & \beta & 0 & 0 & 0 \\ 0 & \gamma & \alpha & \beta & 0 & 0 \\ 0 & 0 & \gamma & \alpha & \beta & 0 \\ 0 & 0 & 0 & \gamma & \alpha & \beta \\ \beta & 0 & 0 & 0 & \gamma & \alpha \end{pmatrix} \begin{pmatrix} V_1 \\ V_2 \\ V_3 \\ V_4 \\ V_5 \\ V_6 \end{pmatrix}, \tag{5.9}$$

with $\alpha = -N_f T_f - N_b T_b$, $\beta = N_f T_f$, and $\gamma = N_b T_b$. Using the definition of contact numbers introduced in Fig. 2.11, in our experiments, we send the current I from electrode 1 to 4. This implies that $I_1 = -I$, $I_4 = I$, and $I_{i\neq 1,4} = 0$. Putting these values into Eq. 5.9, we find the longitudinal and the transverse resistance to be

$$R_{\mathrm{xx}} = \frac{V_2 - V_3}{I} = \frac{h}{e^2} \frac{N_f T_f N_b T_b}{(N_f T_f)^3 + (N_b T_b)^3} \tag{5.10}$$

and

$$R_{\mathrm{xy}} = \frac{V_2 - V_6}{I} = \frac{h}{e^2} \frac{N_f T_f - N_b T_b}{(N_f T_f)^2 + (N_b T_b)^2 - N_f T_f N_b T_b}, \tag{5.11}$$

respectively. On the basis of Eq. 5.10 and Eq. 5.11, we are able to determine the longitudinal and transverse conductivities as follows (cf. Eq. 5.1 and Eq. 5.2):

$$\sigma_{\mathrm{xx}} = \frac{e^2}{h} \frac{(N_f T_f)^4 N_b T_b + N_f T_f (N_b T_b)^4}{(N_f T_f)^4 + (N_b T_b)^4 - (N_f T_f N_b T_b)^2} \tag{5.12}$$

and

$$\sigma_{\mathrm{xy}} = \frac{e^2}{h} \frac{(N_f T_f)^5 - (N_b T_b)^5 - (N_f T_f)^3 (N_b T_b)^2 + (N_f T_f)^2 (N_b T_b)^3}{(N_f T_f)^4 + (N_b T_b)^4 - (N_f T_f N_b T_b)^2}. \tag{5.13}$$

The next step is to compare the results obtained from the model (Eq. 5.12 and Eq. 5.13) with the experimental results. For this purpose, we once more examine the data of sample QC0464 OG I. Fig. 5.7 shows σ_{xy} at each point in the (V_{BG},V^*_{TG}) parameter space at fixed

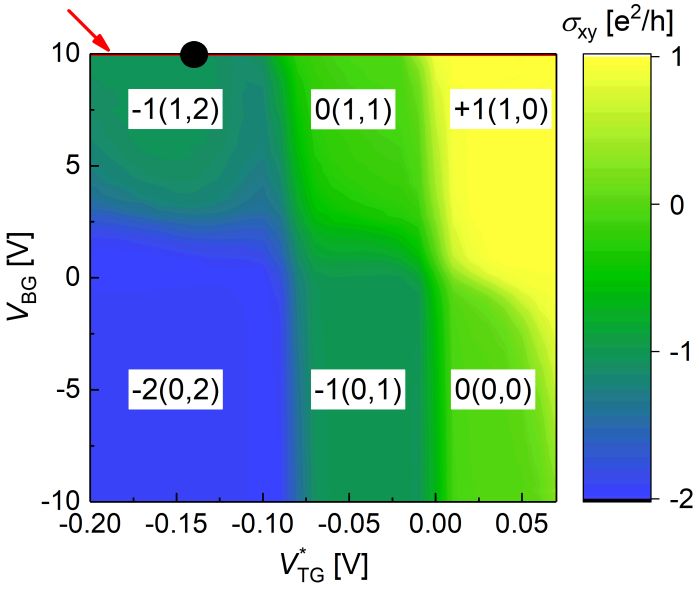

Figure 5.7.: σ_{xy} is presented for sample QC0464 OG I at each point in the (V_{BG},V^*_{TG}) parameter space at $B = 8\,T$ by means of a color code. The total filling factor ν, ν_{TSS}, and ν_{VPS} are displayed in the form $\nu(\nu_{TSS},\nu_{VPS})$ for each quantum Hall plateau visible in the measurement. The data plotted in Fig. 5.8 are extracted at $V_{BG} = 10\,V$ (marked by red line and arrow). A black dot indicates the point $(10\,V,-0.14\,V)$.

magnetic field $B = 8\,T$ and temperature $T \approx 100\,mK$ using a color code. The value of the total filling factor ν at each point in the (V_{BG},V^*_{TG}) parameter space can be determined by $\sigma_{xy} = \nu e^2/h$. In order to identify which carrier systems contribute to transport and thus to the total filling factor in each case, the evaluations of the previous section can be used. In studying the re-entrant quantum Hall effect, it was found that at $V^*_{TG} = -0.14\,V$, $V_{BG} = 10\,V$, and $B = 8\,T$ (cf. Fig. 5.2), the two n-type topological surface states (TSS,I and TSS,II) and one p-type massive Volkov-Pankratov state are occupied. The corresponding filling factors are $\nu_{TSS} = 1$ and $\nu_{VPS} = 2$. Based on this point (marked as a black dot in Fig. 5.7), ν_{TSS} as well as ν_{VPS} and therefore the total filling factor $\nu = \nu_{TSS} - \nu_{VPS}$ can be specified for each QH plateau. Since the back-gate mainly affects the topological surface state at the bottom surface (TSS,II), a reduced applied BG voltage leads to a depopulation of this state. Thus, it can be found that the applied back-gate voltage determines the presence of the n-type quantum Hall edge state ($\nu_{TSS} = 0$, 1). The top-gate on the other hand mainly influences the surface states at the top surface. By changing the applied TG voltage it is possible to alter the population of the VPS and therefore modulate the number of p-type QH edge states involved in transport ($\nu_{VPS} = 0$, 1, 2). The reason that the top-gate-electrode almost exclusively affects the population of the massive Volkov-Pankratov state is the pinning of the Fermi level to this state (cf. Sec. 5.1), which takes place in the investigated

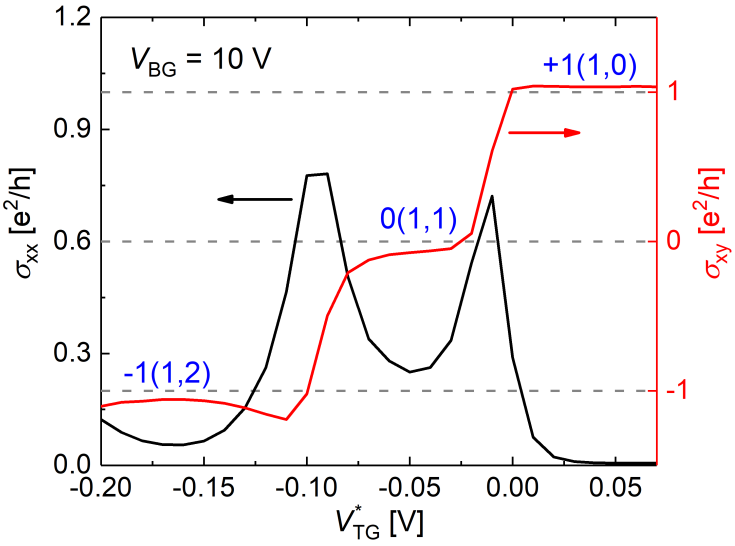

Figure 5.8.: Longitudinal conductivity σ_{xx} (in black) and transverse conductivity σ_{xy} (in red) as a function of top-gate voltage V^*_{TG} at fixed back-gate voltage $V_{BG} = 10\,\mathrm{V}$. For each quantum Hall plateau, the total filling factor ν, ν_{TSS}, and ν_{VPS} are displayed in the form $\nu(\nu_{TSS}, \nu_{VPS})$. Dashed gray lines indicate integer values of σ_{xy}.

range of top-gate voltage. Hence, it can be recognized that the occupations of topological and massive surface states, and thus ν_{TSS} and ν_{VPS}, are independently tunable by the dual-gate configuration. It is noted that due to the independent manipulation of n-type and p-type states, it is possible to obtain identical total filling factors based on different values of ν_{TSS} and ν_{VPS}. For example, $\nu = 0$ can be derived from $\nu_{TSS} = 1$ and $\nu_{VPS} = 1$ or from $\nu_{TSS} = 0$ and $\nu_{VPS} = 0$ (cf. Fig. 5.7). The varying transport properties of these two states are discussed in detail in Ref. [82].

In order to compare the model with the experimental results, traces of σ_{xy} as function of top-gate voltage have to be extracted from Fig. 5.7 for different values of back-gate voltage. Fig. 5.8, for instance, shows $\sigma_{xy}\,(V^*_{TG})$ for $V_{BG} = 10\,\mathrm{V}$. In addition, the associated trace of $\sigma_{xx}\,(V^*_{TG})$ is plotted. The traces of σ_{xx} as well as σ_{xy} appear edged due to the spacing between two adjacent points in top-gate voltage being 0.01 V. $V_{BG} = 10\,\mathrm{V}$ is chosen since the transverse conductivity exhibits all three cases of interest: First, quantum Hall edge states propagating exclusively in the same direction (1,0); second, an equal number of counter-propagating edge states (1,1); third, an unequal number of counter-propagating QH edge states (1,2). At this point, we associate forward-moving edge states with n-type bands and backward-moving states with p-type bands. Thus, in the case of all quantum Hall edge states propagating in the same direction (1,0) we get $N_f = 1$ and $N_b = 0$. Due to the lack of reverse-propagating channels, we set $T_f = T_b = 1$ and obtain $(\sigma_{xx}, \sigma_{xy}) = (0, 1)e^2/h$ from Eq. 5.12 and Eq. 5.13. In the experiment, we find $(\sigma_{xx}, \sigma_{xy}) = (0.01, 1.03)e^2/h$, which is in

good agreement with the prediction of the model.

Next, consider the case of an equal number of counter-propagating quantum Hall edge states (1,1). If we assume perfect transmission ($T_f = T_b = 1$), the calculation with $N_f = 1$ and $N_b = 1$ results in $(\sigma_{xx}, \sigma_{xy}) = (2, 0)e^2/h$. This situation is reminiscent of the quantum spin Hall effect [7] already mentioned in chapter 1. There, the elastic back-scattering between the two counter-propagating edge states with spin polarized oppositely is strongly suppressed due to spin conservation [84], leading to the 4-terminal conductivity of $2e^2/h$. The experimentally found values, however, are $(\sigma_{xx}, \sigma_{xy}) = (0.25, -0.04)e^2/h$. While the transverse conductivity is close to zero as well, the value of the longitudinal conductivity deviates strongly from $2e^2/h$. Motivated by Refs. [85, 86], in which the possibility of inelastic scattering between counter-propagating edge states in a TI system have been investigated, we believe that it is necessary to introduce inter-scattering between counter-propagating QH edge states to explain the observed σ_{xx}. In contrast to the quantum spin Hall state, we therefore allow the carrier systems to inter-scatter without restriction. An introduced inter-scattering will decrease the values of the transmission probabilities T_f and T_b. The transmission probabilities can be determined by comparing the experimental data with equations 5.12 and 5.13. For the case of $N_f = N_b = 1$, we find $T_f = 0.12$ and $T_b = 0.13$. Since these values are significantly smaller than one, there has to be strong inter-scattering between the two counter-propagating QH edge states. According to our simplified model, the edge states in the case under consideration possess an average transmission probability between the electrodes of only about 10 %. In addition, we find $T_f \approx T_b$. This suggests that the two transmission probabilities are correlated, i.e. the inter-scattering affects both simultaneously and to the same extent.

The last case is represented by an unequal number of counter-propagating edge channels (1,2), implying $N_f = 1$ and $N_b = 2$. Assuming perfect transmission, the model predicts $(\sigma_{xx}, \sigma_{xy}) = (18/13, -27/13)e^2/h$, which again differs strongly from the experimental values $(\sigma_{xx}, \sigma_{xy}) = (0.06, -1.05)e^2/h$. This time, an estimation of the transmission probabilities results in $T_f = 0.06$ and $T_b = 0.52$. Thus, there is one forward-moving quantum Hall edge channel with $T_f = 0.06$ and two backward-moving edge channels with $T_b = 0.52$. The system as a whole therefore behaves as if one p-type ($N_b T_b = 1.04$) and no n-type quantum Hall edge channel ($N_f T_f = 0.06$) contribute to transport. This behavior can also be found in the experimentally measured values of σ_{xx} and σ_{xy}. It seems that one forward-moving and one backward-moving edge channel cancel each other and only the unpaired QH edge channel determines the transport properties. In fact, investigations of other three-dimensional TI samples and considerations of different unequal numbers of counter-propagating edge states have yielded the same result [82]: It seems that $|N_f - N_b|$ unpaired quantum Hall edge states propagate dissipationless along the edge despite intense inter-scattering occurring between paired others. In a simple picture, an equal amount of forward-moving and backward-moving channels cancel each other and only the net number of states $N_f - N_b$ determines the transport

properties of the 3D topological insulator system as a whole. Hence, it appears that the strength of inter-scattering is robust against changing the number of unpaired QH edge channels.

It is noted that the scattering model described in this thesis represents a simplified model. A more specific model to address inter-scattering exclusively is given in Ref. [82]. There, for instance, the spatial variation of scattering probabilities is included. In contrast, in our model, a constant transmission probability between adjacent electrodes, independent of the distance between them, is assumed. In addition, the physical mechanism behind the inter-scattering is yet unknown. Therefore, more dedicated theoretical and experimental work may be required in the future to resolve the underlying microscopic inter-scattering mechanism.

At this point, there is need to make a remark regarding the validity of our *four-band model* (cf. Sec. 5.1) considering the possible inter-scattering of n-type and p-type states. In all three cases, namely quantum Hall edge states propagating exclusively in the same direction, an equal number of counter-propagating edge states, and an unequal number of counter-propagating QH edge states, the transverse conductivity measured in the experiment is equal to $(N_f - N_b)e^2/h$. Hence, the conductance of the 3D TI system as a whole is only determined by the difference between the numbers of occupied n-type and p-type states. This result facilitates the applicability of the *four-band model*, since our model basically also counts the numbers of populated electron and hole systems and adds them up[2] to identify the total filling factor at a given magnetic field.

In this chapter, we were able to develop a toy model, the so-called *four-band model*, allowing us to reconstruct experimentally obtained Landau level fan-charts. In addition, the model enables us to assign each LL to its underlying topological or massive state and to determine the contribution of all populated carrier systems to transport. Thus, we could identify the re-entrant quantum Hall effect observed for the first time in three-dimensional topological insulator samples as an interplay of n-type topological and p-type massive surface states. In Mn-doped devices, an early onset of the $\nu = -1$ QH plateau giving rise to a particularly pronounced $-1 \rightarrow -2 \rightarrow -1$ re-entrant quantum Hall effect was observed. This observation is discussed in Ref. [15] in the context of the parity anomaly.

In addition, it was shown that due to imposed opposite chirality of electrons and holes, inter-scattering occurs between counter-propagating n-type and p-type quantum Hall edge states. By using a simplified scattering model based on the Landauer-Büttiker formalism, we were able to demonstrate that the strength of inter-scattering depends on the numbers of occupied electron and hole systems. It was found that an equal amount of n-type and p-type edge channels cancel each other and the transport properties of the 3D TI system as a

[2]Note that p-type states are given a negative sign.

whole are determined solely by the unpaired QH edge states. In this context, the possibility of independent manipulation of the populations of the surface states of top and bottom surfaces by means of the dual-gate configuration was demonstrated as well.

Based on the investigation of macroscopic Hall bars, this chapter has documented the gained knowledge that has fundamentally enhanced our understanding of magneto-transport measurements of three-dimensional topological insulator samples. We are now able to accurately describe the experimentally obtained results and have access to previously unexplained transport phenomena (e.g. re-entrant quantum Hall effect). The next step is the analysis of our high-quality heterostructures in terms of transport properties, for which the mean free path or the spin relaxation length of the charge carriers are decisive. Since these values are typically only a few micrometers, microscopic devices are required for this purpose. Chapter 6 presents the lithographic realization of such structures.

6. Lithography of three-dimensional HgTe-based microstructures

Since the charge carriers in the surface states are subject to spin-momentum locking (cf. Subsec. 2.1.2), the investigation of our devices regarding spin-associated transport phenomena is also of particular interest. However, macroscopic structures, which can be fabricated using easy-to-use optical lithography (cf. Chap. 3) and which are not susceptible to sample impurities[1], are inapplicable for this purpose. The reason for this is that to be able to observe these phenomena experimentally, the dimensions of the devices should not exceed the spin relaxation length λ_s of the charge carriers. Given that λ_s is typically in the range of a few micrometers, structures of several hundred micrometers in size cannot be used. Therefore, the lithographic processing of microscopic three-dimensional HgTe-based devices is to be introduced. In analogy, such structures can be used to study the ballistic transport regime of our high-quality samples, as in clean systems the mean free path of the charge carriers is comparable to their spin relaxation length [87].

The detailed steps required for the lithographic fabrication of microstructures are described in Sec. 6.1. Particular emphasis is given to the definition of the mesa via etching, as this is the most demanding lithography step. In Sec. 6.2, wet etching (WE) and inductively coupled plasma etching (ICP)[2] are discussed alongside their advantages and disadvantages. It is noted that all developments and improvements which have been developed for the fabrication of macroscopic devices (cf. Sec. 3.2), are also applied to the processing of microstructures as far as they are applicable.

6.1. Processing steps for the fabrication of microscopic samples

Analogous to the lithography of macroscopic devices, the lithography of microscopic structures uses masks so that only intended areas of the sample are affected by a certain fabrication step. Since each step involves the usage of a mask, its application process is described first. Given that the inaccuracy of our optical mask-aligner is around one micron, which is approximately the dimension of microstructures, optical lithography cannot be used. Instead, electron beam lithography (EBL) is utilized. The procedure, however, is similar: First, a drop

[1] Due to the large size of macroscopic devices, the measurements are independent of isolated defects and impurities affecting the transport only locally.

[2] The reason why ion beam etching is excluded from the beginning is given in this section as well.

of polymethyl methacrylate (PMMA) e-beam resist is spin-coated homogeneously across the sample surface. The spin-coating is done for 40 s and the revolutions per minute depend on the underlying PMMA resist. For microscopic sample fabrication, we use either PMMA 950K 3 % or PMMA 600K 6 %. The first number indicates the molar mass, while the second one describes the solids content. PMMA 950K 3 % is spin-coated at 7000 rpm and PMMA 600K 6 % at 5000 rpm. After spin-coating, the resist is baked at 80 °C for 8 min (PMMA 950K 3 %) or 10 min (PMMA 600K 6 %) to evaporate the solvent. Now, the electron beam exposure takes place in a high vacuum chamber. Both resists consist of long molecule chains, which decay under e-beam exposure. Note that only positive electron beam resists are used in our group. As a result, the e-beam designs have to be adapted accordingly. The exact parameters used for exposure are given in Appx. C. The resist at the exposed areas of the device is then stripped during the 1 min (PMMA 950K 3 %) or 1 min 10 s (PMMA 600K 6 %) development in *AR 600-56*, which is diluted in isopropyl alcohol (IPA) at a ratio of 1:1. Resist at non-exposed areas remains. Analogous to the optical photoresists, we assume that e-beam resists are mechanically and chemically stable, i.e. anything done to the sample surface only affects the non-covered parts. After dissolving the remaining resist, the formerly covered parts of the device are unaffected. Acetone is used to dissolve both PMMA 950K 3 % as well as PMMA 600K 6 % chemically. Since the exposure using a focused electron beam is time-consuming, only designs within a 204.8 x 204.8 µm^2 writing field are exposed. In the following, we refer to all structures within this writing field as inner part of the sample. The width of the contacts of the inner part of the device is only about 50 µm, which is not enough for reliable wedge-wedge bonding. For this reason, the contacts are expanded and enlarged within an area of 2 x 2 mm^2, the outer part of the sample, using optical lithography.

The lithographic steps for the fabrication of microscopic devices presented below are exemplified using optical images of H-bars that are shaped like the capital letter “H”. This particular sample design has been chosen, because such structures are ideally suitable for the investigation of spin-associated transport phenomena (cf. Chap. 7).

Definition of the inner mesa:
The first step to fabricate a microscopic device is the definition of the inner mesa. During this step, an arbitrary mesa design is transferred from a computer onto a sample piece using PMMA 950K 3 %, e-beam exposure, and either wet etching or inductively coupled plasma etching. As described above, the combined usage of PMMA resist and electron beam exposure creates a polymethyl methacrylate mask. While in the case of WE, this mask can be used directly as an etch mask, in the case of ICP etching, the PMMA mask is required to fabricate an etch mask consisting of 100 nm BaF_2 and 10 nm Ti. Hence, the same sample design requires different e-beam designs for each of the two etching techniques. In a simple picture, the electron beam design used for WE is the negative one used for ICP etching. In addition, both etching techniques require different processing steps:

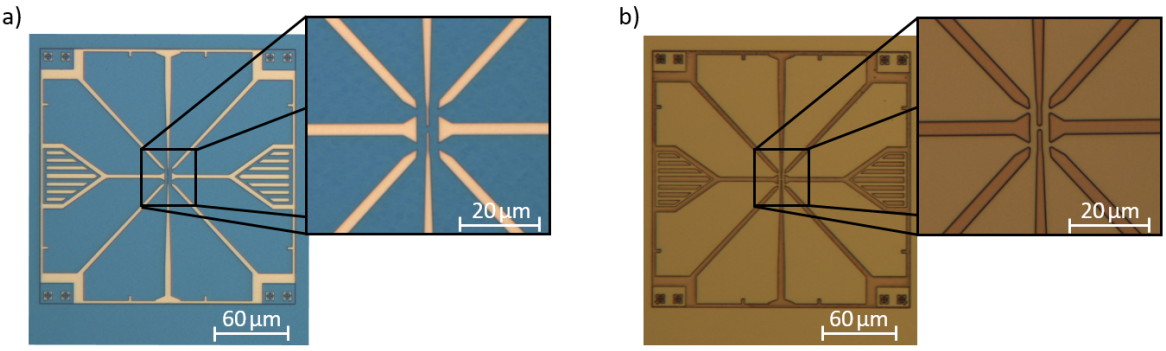

Figure 6.1.: Optical microscope images showing a) the PMMA etch mask (blue) and b) the etched inner mesa. Brighter areas present mesa, while darker ones are etched. The contrast lines are mesa rims. The insets of both pictures display the H-bar in the center of the 204.8 x 204.8 µm^2 writing field in higher magnification. The so-called alignment marks, which are required for the correct alignment of the sample in subsequent e-beam exposures, are visible in all four corners of the writing field.

After applying the PMMA mask and just before wet etching, the sample piece has to be dipped for 50 s in hydrofluoric acid, which is diluted in deionized water at a ratio of 1:400, in order to remove any oxidations from the device surface. The sample is then wet etched using a KI:I_2:HBr solution and the pumping method (cf. Subsec. 3.1.2). The desired inner mesa is protected by the polymethyl methacrylate mask, which can be removed with acetone post etching. Optical images showing the PMMA mask and the etched inner mesa are presented in Fig. 6.1a) and b), respectively.

In the case of inductively coupled plasma etching, after application of the PMMA mask, the sample is transferred into a high vacuum chamber. There, the sequential deposition of 100 nm barium fluoride and 5 nm titanium is accomplished via thermal and e-gun evaporation, respectively. The subsequent lift-off process is carried out for 5 min in acetone at 50 °C. Then, the device is etched in an ICP tool (cf. Subsec. 3.1.2). The stripping of the BaF_2/Ti etch mask happens by putting the sample in deionized water (DIW) for 15 min at 50 °C. Optical images displaying the PMMA mask, the BaF_2/Ti etch mask, and the etched inner mesa are presented in Fig. 6.2a), b) and c), respectively. It is noted that the polymethyl methacrylate mask in Fig. 6.2a) possesses a different color compared to the PMMA mask in Fig. 6.1a). This can be explained by the different modes, in which the optical microscope was operated in each case. Since the polymethyl methacrylate is unsuitable as an etch mask for ICP etching, additional lithography steps, namely the application of the BaF_2/Ti etch mask and removal of the PMMA mask, are required.

A detailed consideration of both etching techniques and the requirements for the respective e-beam designs is given in Sec. 6.2. In this context, the advantages and disadvantages of wet and inductively coupled plasma etching to define the inner mesa structures of microscopic three-dimensional devices are specified as well.

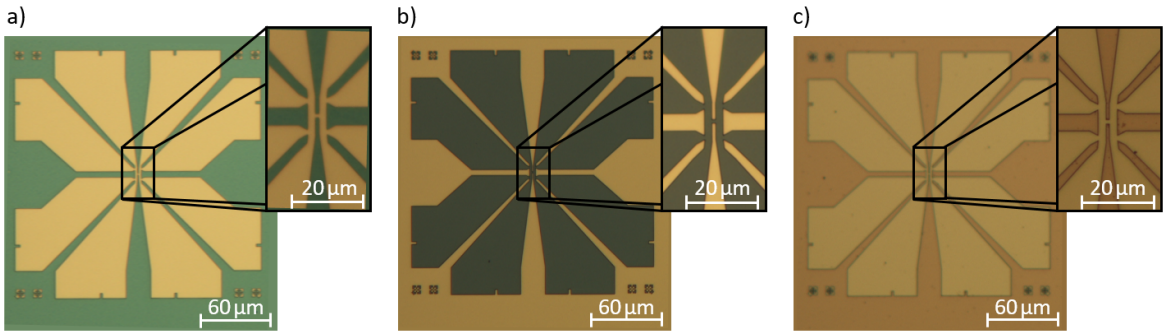

Figure 6.2.: Optical microscope images showing a) the PMMA mask (green), b) the BaF_2/Ti etch mask (dark gray), and c) the etched inner mesa, which stands out clearly from the darker etched areas. The insets in all three pictures present the H-bar in higher magnification.

Definition of the outer mesa:

Since the PMMA mask is directly used as an etch mask for WE, only the inner mesa within the 204.8 x 204.8 µm^2 writing field is etched. The outer part of the sample is covered with polymethyl methacrylate and therefore remains unetched. For this reason, the extensions of the contacts have to be defined in an additional step. To protect the already etched inner mesa and the desired outer mesa, a photomask consisting of positive resist *ECI 3012* is used. The application of photoresist and the etching process is carried out as described in Sec. 3.1. After etching, the mask is removed with acetone. Optical images presenting the photomask and the etched outer mesa are shown in Fig. 6.3a) and b), respectively. The mask which is utilized to define the outer mesa features 18 contacts. However, all of the inner mesa structures presented in this thesis (H-bars and microscopic 6-terminal Hall bars) possess only nine contacts. The nine contacts consist of eight ohmics (cf. Fig. 6.1 and Fig. 6.2) and one additional contact to contact the top-gate-electrode, which will be fabricated later. Hence, two inner structures can be contacted simultaneously. When defining the inner mesa, the two desired structures have to be written next to each other at a distance of 200 µm. By using the same inner structure twice, one is able to receive a backup device, whereas the definition of different inner mesa structures allows two diverse samples on the same wafer piece to be positioned. The device shown in Fig. 6.3, for instance, features two differently sized H-bars: The lengths of the connecting pieces between the two legs of the H-bars are 1 µm and 500 nm, respectively.

In the case of inductively coupled plasma etching, not the PMMA but a BaF_2/Ti mask is used as an etching mask. Hence, the polymethyl methacrylate mask is removed before etching and the whole wafer piece, exclusive of the two inner mesa structures, is etched in the process. Therefore, it is not necessary to define an outer mesa in an additional fabrication step.

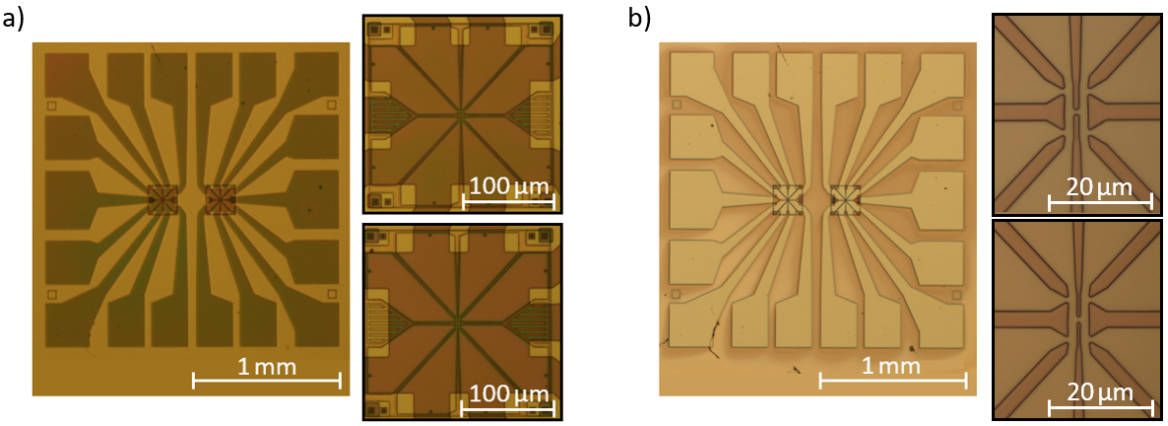

Figure 6.3.: Optical microscope images showing a) the photomask (dark areas) and b) the etched outer mesa. A shadow-like pattern around the outer mesa is formed during the wet etching process (cf. Subsec. 3.1.2). The insets present the inner structures in higher magnification. The inner mesa on the left corresponds to the upper inset and the one on the right to the lower inset. In a), it can be seen that the inner mesa is protected by photoresist during etching. In b), the different lengths of the connecting pieces between the two legs of the H-bars (1 µm and 500 nm) are visible.

Fabrication of the inner contacts:

The last three fabrication steps (fabrication of the inner contacts, application of gate-dielectric and top-gate-electrode, and fabrication of the outer contact leads) are identical for both etching techniques. Thus, in the following, no distinction is required and optical images of inductively coupled plasma etched samples are used for visualization purposes.

To fabricate the inner contacts, a polymethyl methacrylate mask consisting of PMMA 600K 6 % is used. Afterwards, a short miniclean step (cf. Subsec. 3.1.4) is performed to remove any resist residues from the device surface. Except for one adjustment, the ion milling step as well as the in-situ metallization with 50 nm AuGe and 50 nm Au are carried out as described in Subsec. 3.1.3. To prevent discontinuities of the metal layers over the mesa edges, the contact metals are deposited under an alternating angle of ±40 °. The angle is altered every 10 nm of deposited metal. The subsequent lift-off process takes place in acetone at 50 °C for 5 min. Optical images showing the PMMA mask and the metallized ohmic contacts are presented in Fig. 6.4a) and b), respectively.

It is noted that during this lithography step, since nearly arbitrarily shaped masks can be created using PMMA resists and e-beam exposure, one can determine how close the metallized contacts should be positioned to the microscopic structure in the center of the writing field, depending on the investigations to be carried out on the sample. The device shown in Fig. 6.4, for instance, possesses a distance of 8 µm between H-bar and metallized contacts. This distance enables an overlapping as well as a non-overlapping top-gate-layout to be achieved (cf. Sec. 4.2), depending on the dimensions of the top-gate-electrode that is

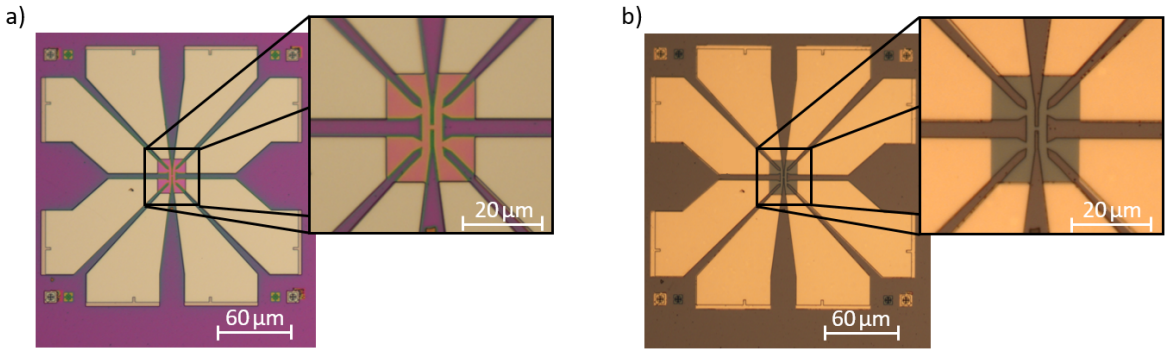

Figure 6.4.: Optical microscope images showing a) the PMMA mask (purple) and b) the metallized inner contacts. The insets of both pictures present the H-bar in higher magnification.

applied in the next fabrication step.

Application of gate-dielectric and top-gate-electrode:
Just before the application of gate-dielectric and top-gate-electrode, the sample piece has to be placed in methyl isobutyl ketone (MIBK) at 50 °C for one night in order to remove resist residues from the surface, which might have remained after the mesa etch and the fabrication of the ohmics. This step is necessary to ensure that the device surface is as clean as possible before the gate insulator is applied. After application of a polymethyl methacrylate mask consisting of PMMA 600K 6 %, a short miniclean step is performed. Then, the sample piece can be taken to the high vacuum atomic layer deposition (ALD) chamber. The growth of 90 cycles HfO_a insulator as well as the subsequent metallization with 5 nm Ti and 100 nm Au in another high vacuum chamber are carried out as described in Subsec. 3.1.4. The deposition of the top-gate metals titanium and gold is performed utilizing angular deposition to prevent discontinuities of the metal layers over the mesa edges. The angle is altered for every 10 nm of deposited metal from +40 ° to -40 ° and vice versa. The following lift-off process is accomplished for 30 min in acetone at 50 °C. Optical images of a sample showing the PMMA mask, the 15 nm thick HfO_a insulator layer, and the metallized top-gate-electrode are presented in Fig. 6.5a), b) and c), respectively. Depending on the dimensions of the e-beam design for the top-gate-electrode, one can define whether the top-gate overlaps with the metallized contacts or not (cf. Sec. 4.2). Both cases are presented in Fig. 6.6a). This picture is made up of two optical images of H-bars, which are put together in the middle of the H-bar structures. To make it more convenient to distinguish between the two devices, the brightness of the upper H-bar has been increased slightly. The upper structure features an overlapping top-gate layout, while the lower one displays the non-overlapping design.

At this point, it should be mentioned that an overlapping top-gate layout in microstructures increases the chances of a short circuit between the gate-electrode and the ohmic contacts. When a top-gate voltage is applied, the electrical field strengths are particularly high at

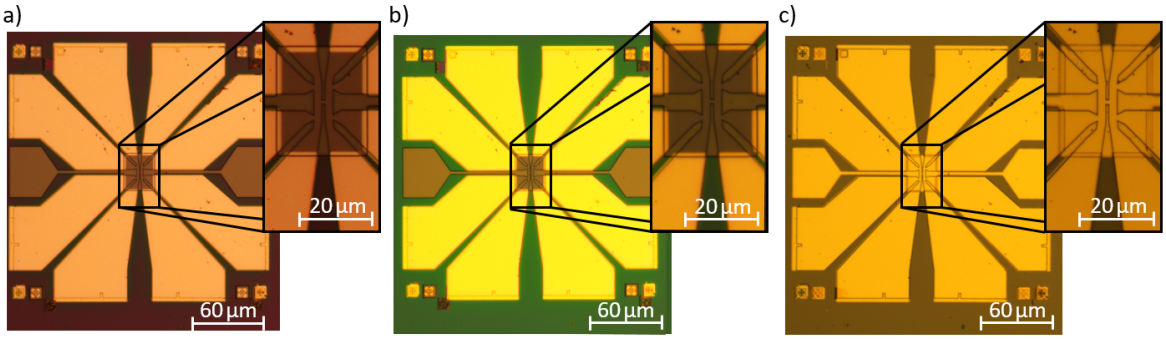

Figure 6.5.: Optical microscope images showing a) the PMMA mask covering the whole sample except for the area of the top-gate-electrode and its leads (light brown), b) the sample after the growth of 15 nm HfO_a insulator, and c) the metallized top-gate after removal of the PMMA mask. The insets of the pictures present the H-bar in higher magnification. The device displayed possesses an overlapping top-gate design.

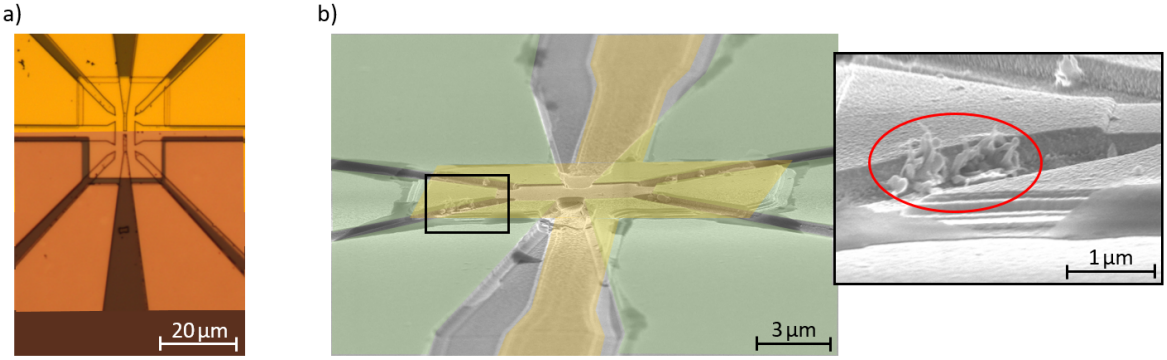

Figure 6.6.: a) presents optical images of two H-bar structures, which are put together in the middle of the H-bars. The top-gate-electrode of the upper structure has the dimensions 24 x 28 µm^2, while the size of the top-gate of the lower one is only 18 x 22 µm^2. b) displays an SEM image of a microscopic Hall bar (3 x 1 µm^2) possessing an overlapping top-gate design. The metallized ohmic contacts are marked in green, while the top-gate-electrode and its leads are highlighted in yellow. The black rectangle indicates the area of the device shown in higher magnification in the inset. It can be recognized that parts of the gate metals have peeled off from the sample (marked by a red oval), which has led to a short circuit between top-gate and ohmic contacts. b) was kindly provided by Pragya Shekhar and adapted afterwards.

the corners and edges of the top-gate-electrode. At these positions, the high electric field strengths can cause parts of the gate metals, including the insulator underneath, to be blown off the sample. This may allow gate metals and contact metals to come into direct contact, which in turn leads to a short circuit. In such a case, the device can no longer be gated. This phenomenon occurs more frequently in microscopic samples, since the dimensions of their top-gate-electrodes are smaller and thus higher electric field strengths are present. It is noted, however, that these short circuits are not a direct consequence of the lithographic processing of microstructures, but happen in the laboratory during mounting of the devices into the measurement-setups or during measurement. An SEM image of a relevant sample is shown in Fig. 6.6b). This figure shows a microscopic 6-terminal Hall bar structure. Such structures represent the microscopic equivalents of the macroscopic Hall bars which were considered in Chap. 3, 4, and 5. In order to reduce the risk of a short circuit, the overlapping design should only be used when necessary, for instance if the device is going to be measured at high magnetic fields ($B > 4\,\mathrm{T}$) and extremely low temperatures ($T \ll 1\,\mathrm{K}$). Under these conditions, an overlapping top-gate-electrode should be used so that the issues related to the magnetoresistance signals described in Chap. 4 do not occur.

Fabrication of the outer contact leads:
During the last fabrication step, the ohmic contacts are expanded and enlarged within an area of 2 x 2 mm^2 to enable wedge-wedge bonding. For this purpose, a photomask consisting

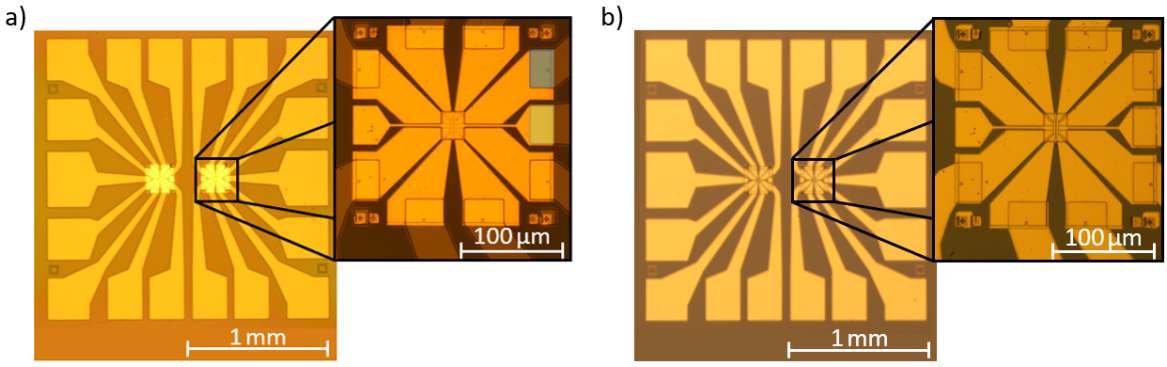

Figure 6.7.: Optical microscope images showing a) the photomask (darker areas) and b) the metallized outer contact leads after removal of the photomask. The insets present one of the inner mesa structures in higher magnification. In a), one of the eight interfaces between inner ohmic contacts and outer contact leads is marked in blue, while the interface between inner top-gate lead and outer contact lead is highlighted in light green.

of negative resist *ARN 4340* is utilized. Before metallization, a short miniclean step is carried out to remove resist residues. Afterwards, an additional cleaning of the interfaces between inner ohmic contacts and outer contact leads as well as inner top-gate lead and outer contact lead is performed in a high vacuum chamber. There, an ion gun is operated at 0.4 kV and

a total current of 8 mA for about 10 s to remove any contaminations from the interfaces. The subsequent in-situ metallization with 80 nm AuGe and 80 nm Au happens using angular deposition to prevent discontinuities of the metal layers over the mesa edges. The lift-off process is carried out for 5 min in acetone at 50 °C. Optical images showing the photomask and the metallized outer contact leads are presented in Fig. 6.7a) and b), respectively. Now, the samples can be glued into a chip carrier, bonded, and measured.

These five fabrication steps provide the necessary tools for the lithographic processing of microscopic devices. In this context, two different etching techniques (wet and inductively coupled plasma etching) are considered as well. The advantages and disadvantages of both techniques and the resulting limitations for the envisaged microscopic designs are specified in Sec. 6.2. The fabrication steps described in Sec. 6.1 are summarized in the form of two sample recipes for WE and ICP etching in Appx. C.1 and Appx. C.2, respectively.

6.2. Etching techniques for defining microscopic mesa structures

In Chap. 3, three etching techniques, namely ion beam etching, wet etching, and inductively coupled plasma etching, to define the mesas of macroscopic devices are presented. To fabricate microscopic samples, however, only WE and ICP etching are suitable. In Subsec. 3.1.2, it is found that the quality of ion beam etched structures strongly depends on the device size. More precisely, the carrier mobility scales with sample size. Larger structures exhibit higher mobilities and vice versa. It has been shown that the mobilities of macroscopic and microscopic ion beam etched HgTe-based devices built of the same wafer material differ by up to eight times [14]. For this reason, we will focus exclusively on wet and inductively coupled plasma etching in the following.

First, the dependence of charge carrier mobility on device size of WE and ICP etched samples is to be investigated to determine if a similar correlation exists for these etching techniques as for IBE etched structures. In Fig. 6.8, the mobilities of six devices built of the same wafer material QC0461 (cf. Appx. A.2) are plotted versus charge carrier density. All samples are structured into 6-terminal Hall bars and two each possess the dimensions 600 x 200 µm^2, 30 x 10 µm^2, and 6 x 2 µm^2. The devices fabricated using WE and ICP etching are presented in Fig. 6.8a) and b), respectively. One is able to recognize that the mobilities vary slightly with sample size. This applies to wet etching as well as to inductively coupled plasma etching. However, neither of the two etching techniques shows a systematic dependency of μ on the device size. In fact, the medium-sized structures (30 x 10 µm^2) exhibit the maximum mobilities ($\mu^{30\,\mathrm{x}\,10}_{\mathrm{WE,max}} = 10.7 \cdot 10^4\ \frac{\mathrm{cm}^2}{\mathrm{Vs}}$, $\mu^{30\,\mathrm{x}\,10}_{\mathrm{ICP,max}} = 9.9 \cdot 10^4\ \frac{\mathrm{cm}^2}{\mathrm{Vs}}$). Hence, we assume that the carrier mobility of WE and ICP etched microscopic devices does not depend on the size of the structures, but rather depends on the impurity density of the

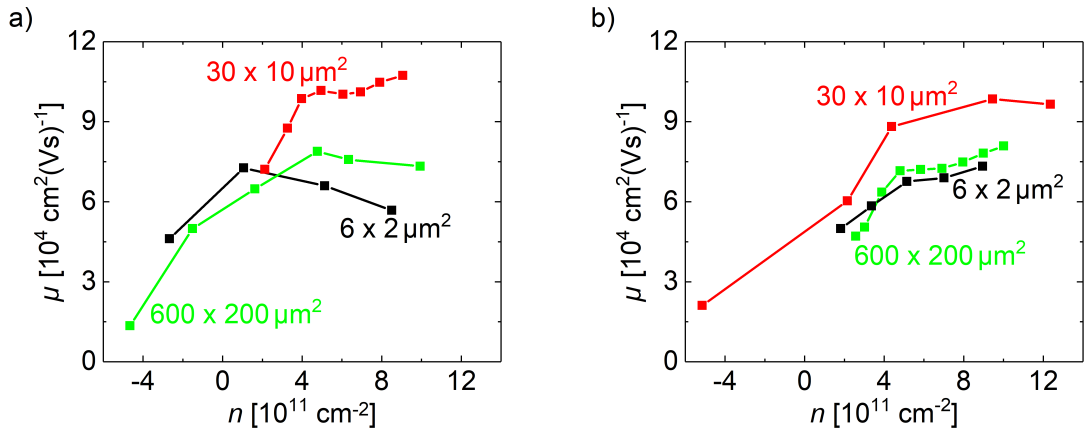

Figure 6.8.: Charge carrier mobilities μ of a) wet etched and b) inductively coupled plasma etched 6-terminal Hall bar devices of different sizes as a function of carrier density n. The data points are connected by linear interpolation. To ensure comparability, all samples were fabricated of the same wafer QC0461 (cf. Appx. A.2) and measured at $T \approx 1.5\,\mathrm{K}$.

underlying sample piece. A higher impurity density leads to lower mobilities and vice versa. Since this density is not homogeneous across the whole wafer, devices fabricated of the same wafer can exhibit different mobilities. The two 30 x 10 µm² Hall bar structures were built from adjacent pieces of wafer material QC0461. Thus, a particularly low impurity density in the corresponding region of the wafer may possibly explain the relatively high μ of these two samples. The comparison of wet and inductively coupled plasma etched devices shows that the usage of both etching techniques results in similar charge carrier mobilities. In principle, WE samples should exhibit slightly higher charge carrier mobilities, since ICP etching involves a physical etching component, which may damage the side surfaces of the active layer during the process and therefore might reduce μ (cf. Subsec. 3.1.2). The energy of the Ar^+-ions used for physical ICP etching, however, is much lower than the energy of the argon ions used for IBE, resulting in a more gentle process and less damage to the sample. If we compare the maxima of the remaining two Hall bar sizes, we find $\mu_{\mathrm{WE,max}}^{600\,\mathrm{x}\,200} = 7.9 \cdot 10^4\ \frac{\mathrm{cm}^2}{\mathrm{Vs}}$, $\mu_{\mathrm{ICP,max}}^{600\,\mathrm{x}\,200} = 8.0 \cdot 10^4\ \frac{\mathrm{cm}^2}{\mathrm{Vs}}$, $\mu_{\mathrm{WE,max}}^{6\,\mathrm{x}\,2} = 7.3 \cdot 10^4\ \frac{\mathrm{cm}^2}{\mathrm{Vs}}$, and $\mu_{\mathrm{ICP,max}}^{6\,\mathrm{x}\,2} = 7.3 \cdot 10^4\ \frac{\mathrm{cm}^2}{\mathrm{Vs}}$. In fact, there is hardly any difference between wet and inductively coupled plasma etched devices of the same size.

Since the results of the two etching techniques are comparable and independent of the size of the structure to be etched, we are able to state that wet etching as well as inductively coupled plasma etching can be used to define the inner mesas of microscopic samples. However, both etching techniques possess advantages and disadvantages, wherefore it depends on the envisaged experiment which technique is to be preferred. The wet and inductively coupled plasma etching techniques are considered in detail below.

Wet etching:
Since WE is an isotropic etching process, lateral etching under the PMMA mask occurs. For macroscopic samples, this phenomenon does not require any additional attention, as lateral etching in the order of a few hundred nanometer can be neglected compared to structure sizes of several hundred micrometer. In the case of microscopic devices, however, the lateral etching component has already to be taken into account when preparing the e-beam design. Fig. 6.9a) presents an SEM image of a wet etched H-bar mesa. This dummy sample was fabricated of wafer QC0460 (cf. Appx. A.2). The center of the 204.8 x 204.8 µm^2 writing field is shown in high magnification. Blue areas mark the e-beam design, which was used to define the mesa. Based on the isotropic nature of WE, lateral etching in the order of approximately 200 nm occurs (cf. inset in Fig. 6.9a)). For this reason, trenches featuring a width of less than 500 nm are difficult to realize, since the desired etch depth is also etched laterally. A trench 100 nm wide on the PMMA mask, for instance, is already about 500 nm wide after being etched 200 nm deep. Mesa structures between two trenches, on the other hand, can easily be processed to a width of 100 nm to 200 nm by taking advantage of the lateral etching of the adjacent trenches. In order to obtain precisely defined structural dimensions, the E-beam design has to be adapted accordingly. This may be necessary to ensure comparability between samples or to determine the exact length of edge channels. In our case, the design was chosen so that both legs of the H-bar and the connecting piece in between exhibit widths of 2 µm and 1 µm after etching, respectively.

In addition, it can be seen that corners and edges of the e-beam design are rounded off during etching and that the etch rate depends on the width of the structure to be etched. The reason for the latter is that wet etching is a diffusion-controlled process (cf. Subsec. 3.1.2). This means that the etch rate is determined by the width of the structure to be etched due to diffusive trenching. Wide structures exhibit a lower etch rate compared to narrow ones. This can be recognized, for instance, by the extent of the legs of the H-bar. While the legs are widest in the middle, their width decreases towards the outside as the etch rate, including the lateral component, increases there due to the pattern of the e-beam design (cf. Fig. 6.9a)). The diffusion-controlled nature of WE can also be observed by examining measurements of etching profiles. An optical image of the same dummy sample is shown in Fig. 6.9b). The etch depth was determined at six positions (marked by colored stripes), two of which possess the same width (approximately 20 µm, 10 µm, and 5 µm). Fig. 6.9c) presents the etching profiles at these six positions. One is able to observe that the etch rate strongly depends on the width of the trench. The narrowest structures exhibit an average etch depth of about 270 nm, the medium ones of 210 nm, and the widest of 160 nm. The combined thickness of buffer, active, and cap layer for wafer QC0460 is 146 nm. Therefore, during the etching process, care was taken to ensure that all structures within the 204.8 x 204.8 µm^2 writing field have an etch depth of at least 150 nm. By doing so, however, one has to take into account that the narrowest structures in the center of the writing field are possibly etched to

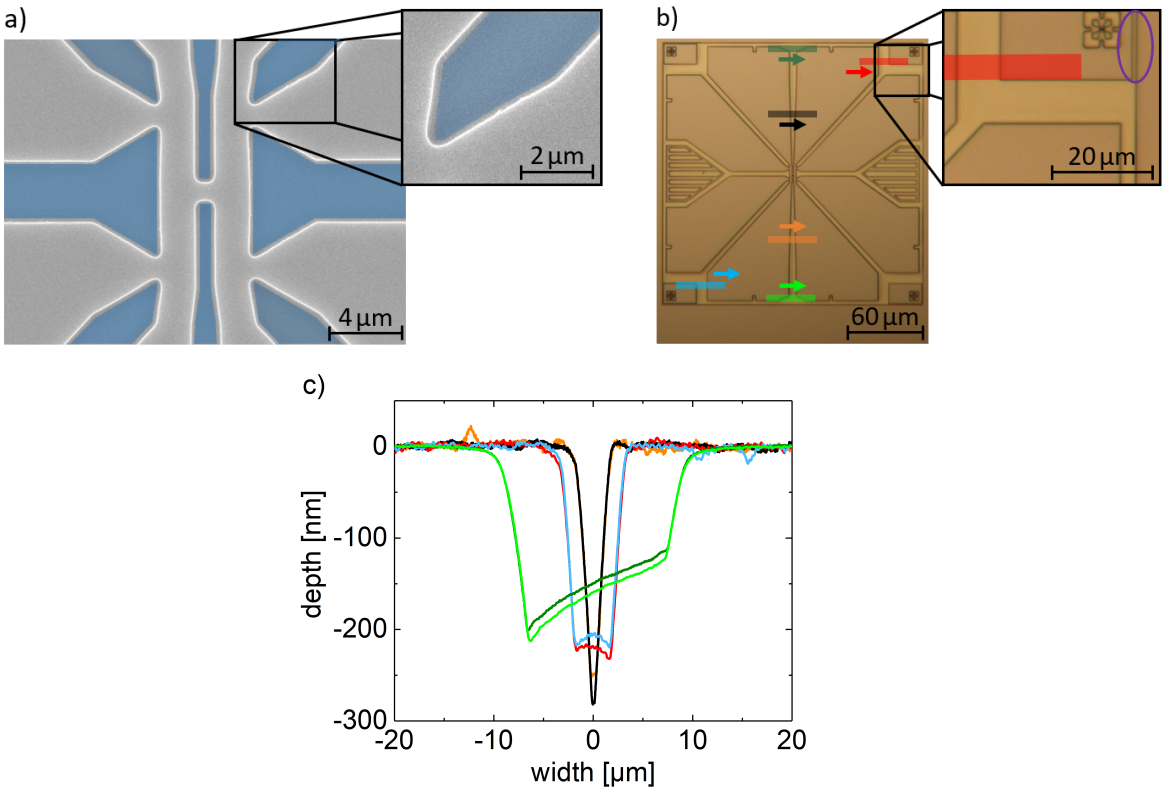

Figure 6.9.: a) SEM image of a wet etched H-bar mesa. Bright contrast lines represent mesa rims. The e-beam design used to create the PMMA etch mask is marked in blue, representing the areas where the WE happened. b) optical image of the same sample. The positions, at which the etch depths were measured, are indicated by colored stripes. Arrows specify the measuring direction. The insets in a) and b) show parts of the sample in higher magnification. The 300 nm wide frame defined around the 204.8 x 204.8 µm^2 writing field is marked by a purple oval. c) etch depth in dependence on the width of the structure to be etched. The same colors as in b) are used.

a depth of more than 300 nm. Hence, the top-gate metals should always be applied utilizing angular deposition (cf. Sec. 6.1), as otherwise discontinuities of the metal layers over such high mesa structures are likely to occur. The measurements of the narrowest (black and orange curves) and medium trenches (red and blue curves) shown in Fig. 6.9c) exhibit the typical etching profiles that result from wet etching described in Subsec. 3.1.2 and Fig. 3.5b). The asymmetrical appearances of the widest structures (olive and light green curves) are probably caused by the selected measuring direction and speed.

The two largest areas of the writing field to be etched are those on which the inner leads to the top-gate-electrode will later be metallized. Therefore, due to the diffusion-controlled nature of wet etching, these areas exhibit significantly lower etch rates. In order to obtain a similar etching result for the entire inner mesa structure, these areas should be divided into several separate strips (cf. Fig. 6.9b)), so that all trenches of the inner structure to be etched have comparable widths. Furthermore, based on Fig. 6.9c), one can see that wet etching is a process, which is difficult to reproduce. Even identical structures on the same sample exhibit slightly different etch depths and profiles. Throughout the development of the WE process, it has been shown that the active layer is an etch barrier [14]. This means that the Hg(Mn)Te layer exhibits a lower etch rate than the CMT buffer and cap layers. Selectively etched through the active layer in some spots, the underlying CMT buffer layer etches faster and an overhang remains. This effect is distinct, if the inner mesa is connected to the outer part of the device. In order to decouple the inner writing field from the outer part of the sample electrically, a 200 nm wide frame defined around the writing field is used. As the narrowest structure, the frame is etched first and deepest due to diffusive trenching. Since the inner writing field is now electrically decoupled, in the redox reaction, the electrons available from the oxidation remain within the to-be-etched Hg(Mn)Te layer of the inner mesa and participate in the reduction so that the active as well as the buffer layer are etched uniformly. As results, the Hg(Mn)Te layer is not outstanding, the rims are smooth, and the mesa edges sharp. The etched frame is visible in Fig. 6.9b) (marked by a purple oval). As wet etching is a process that is difficult to control precisely and all points mentioned above have to be considered, it is recommended to perform an etch test series for each wafer material and envisaged microscopic sample design in order to obtain the best possible result.

The main advantage of wet etching is its non-damaging process due to pure chemical etching. The resulting preservation of the crystal structure of the side surfaces of the active layer should result in the best overall sample qualities. This is particularly crucial for microscopic devices to be investigated regarding edge channel transport (e.g. observation of the quantum spin Hall effect). In addition, the polymethyl methacrylate mask can be used directly as an etch mask, leading to a reduced amount of lithographic treatment of the inner mesa structure.

Inductively coupled plasma etching:
Due to the anisotropic nature of ICP etching, no lateral component occurs during etching. Fig. 6.10a) shows an SEM image of an ICP etched H-bar mesa. The same dimensions of the H-bar and the same wafer material (QC0460) as for wet etching (cf. Fig. 6.9a)) were chosen to ensure the best possible comparability of both etching techniques. Again, blue areas mark the e-beam design used to define the inner mesa. This time, however, the e-beam design does not represent the areas where the etching happens, but displays the position of the BaF_2/Ti etch mask, i.e. the shape of the mesa structure. One is able to recognize that the e-beam design aligns perfectly with the mesa edges. Thus, due to the nonexistence of lateral etching, the desired microscopic sample structure can be realized without any adjustments to the e-beam design. Again, the electron beam design was chosen so that both legs of the H-bar and the connecting piece in between possess widths of 2 µm and 1 µm after etching, respectively. Since in the case of wet etching, trenches significantly narrower than 500 nm are hardly realizable, no trench structures having widths less than 500 nm have been investigated for inductively coupled plasma etching in the framework of this thesis. However, it may well be that narrower trenches can be fabricated using ICP etching. The limiting factor is probably the lift-off process of the BaF_2/Ti etch mask (cf. Sec. 6.1), which might run incompletely for structures that are too small in size or too close to each other.

Now, the dependence of the etch rate on the width of the microscopic structure to be etched for ICP etching is to be investigated. Fig. 6.10b) shows an optical image of the same dummy sample displayed in figure 6.10a). Using this inner mesa structure, the etching profiles were determined at six positions (marked by colored stripes). Again, two trenches each possess the same width. The widths are approximately 20 µm, 10 µm, and 5 µm. The result of the measurements are presented in Fig. 6.10c). All trenches exhibit the same etch depth independent of their width. Therefore, the etch depth does not depend on the design of inner the mesa structure, but solely on the etching time and the layer stack of the underlying wafer material. According to Appx. A.2, the thicknesses of buffer, active, and cap layer of wafer QC0460 are 70 nm, 62 nm, and 14 nm, respectively. Using the formula $t_{\mathrm{ICP}} \approx (2d_{\mathrm{cap}} + 2d_{\mathrm{buffer}} + d_{\mathrm{Hg(Mn)Te}})/5.76\,\frac{\mathrm{s}}{\mathrm{nm}}$ (cf. Subsec. 3.1.2), an etching time of about 40 s can be calculated. To ensure that etching is carried out through all three layers, the time was increased by five additional seconds, i.e. a total of 45 s. Fig. 6.10c) reveals that the mesa height of this sample is around 160 nm uniformly across the entire inner structure. Thus, the required etching time for arbitrarily shaped microscopic devices can be determined quite easily without having to perform etch tests beforehand. All measurements show the box-shaped profile typical for ICP etching described in Subsec. 3.1.2 and Fig. 3.6c). Due to the uniformity of ICP etching, large areas exhibit the same etch rate as narrow trenches. Therefore, the e-beam design of the inner structure does not require any adjustments in this regard. Furthermore, inductively coupled plasma etching is highly reproducible. Samples of the same wafer etched for the same amount of time will result in identical etching profiles.

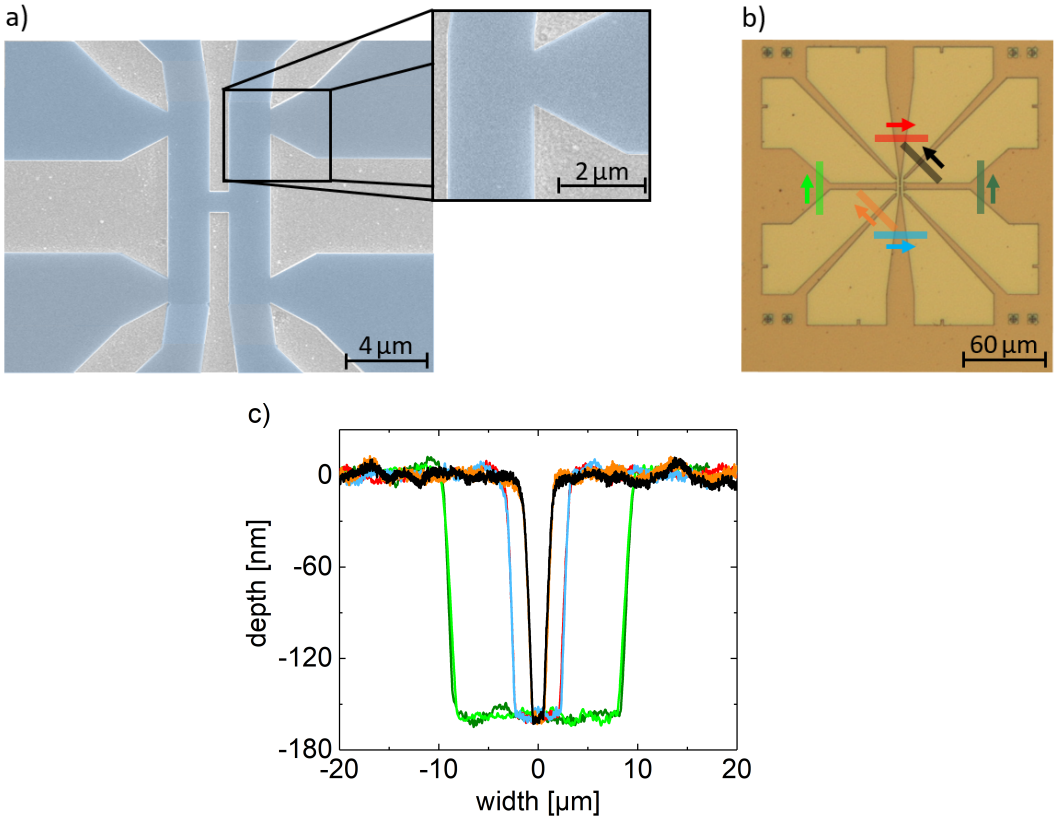

Figure 6.10.: a) SEM image of an inductively coupled plasma etched H-bar mesa. Bright contrast lines represent mesa rims. The e-beam design used to create the BaF_2/Ti mask and thus to define the inner mesa is highlighted in blue. The inset shows part of the device in higher magnification. b) optical image of the same sample. The positions, at which the etching profiles were measured, are indicated by colored stripes. Arrows give the measuring direction. c) etch depth in dependence on the width of the structure to be etched. The same colors as in b) are used.

Since the individual layers of devices (CMT buffer, Hg(Mn)Te, and CMT cap) are etched uniformly, no additional frame has to be added to the electron beam design. This makes inductively coupled plasma etching the more reproducible, controllable, and easier to handle etching technique compared to wet etching. In addition, increased structural fidelity can be achieved using ICP etching due to its anisotropic nature. This is of particular importance for samples used to study size-dependent effects.

The most noteworthy disadvantage of ICP etching is its physical etching component (cf. Subsec. 3.1.2). The resulting damage to the side surfaces of the active layer may lead to the formation of impurities along these surfaces. The impurities may disturb the potential landscape and introduce additional scattering of charge carriers in the surface states reducing their overall mobility. As the additional scattering may have a detrimental effect on edge channel transport, WE is the preferred etching technique for microscopic devices intended to be investigated in this regard. However, no detectable systematic reduction in charge carrier mobility could be found in ICP etched microstructures used for this thesis. Furthermore, an additional lithographic step is required for inductively coupled plasma etching, since the PMMA mask is not suitable as an etch mask. Due to the increased lithographic treatment of the surface of the inner mesa structure, the risk of sample contamination is increased as well.

In this chapter, the realization of microscopic three-dimensional HgTe-based topological insulator devices was discussed. Based on the described five fabrication steps and the etching procedures, in principle nearly any desired microscopic sample can be realized as long as no trenches significantly narrower than 500 nm are included in the design. In addition, it was found that wet and inductively coupled plasma etching result in comparable carrier mobilities for microstructures. It was observed that wet etching preserves the quality of the side surfaces of the active layer best, but is difficult to reproduce, and due to its isotropic nature, structural fidelity is hindered. ICP etching, on the other hand, is characterized by an easy handling, high reproducibility, and an excellent structural fidelity. However, a physical etching component is included, which may damage the crystal structure of the side surfaces, resulting in the formation of impurities. Since both etching techniques have important advantages and disadvantages, it is the task of the experimenter to make the more appropriate choice for the envisaged experiment.

The lithography described in this chapter is optimized for microscopic Hall bars and H-bars. This means that the recipes given in this thesis (cf. Appx C.1 and Appx. C.2) are only be considered as a basis for differently shaped three-dimensional HgTe-based microstructures. Each microscopic device may feature individual requirements that are specific to the underlying design and which may cause issues during lithographic realization. These issues might

be novel and unique and are therefore not covered in this thesis. Nevertheless, the knowledge gained in this chapter should represent an excellent starting point for the realization of future arbitrarily shaped microscopic 3D sample structures.

Using the H-bars presented in this chapter, the next chapter (Chap. 7) will focus on whether spin-associated transport phenomena can be detected in three-dimensional HgTe-based topological insulator devices.

7. Spin polarization induced non-local signals in microscopic H-bar structures

In order to be able to investigate our MBE grown heterostructures regarding spin-associated transport phenomena, a suitable sample design is required. In two-dimensional HgTe-based quantum wells, the existence of both the intrinsic spin Hall effect (SHE) and inverse spin Hall effect (ISHE) has been demonstrated using microscopic H-bar structures [88]. For this purpose, so-called non-local measurements were performed on H-shaped structures, i.e. a current was sent through one leg of the H-bar (current-carrying leg) and the resulting voltage difference on the other leg (detection leg) was measured. The non-local signal observed in the detection leg depending on applied top-gate voltage has been explained by the interplay of intrinsic SHE and ISHE.

Inspired by this observation from a decade ago, we also choose microscopic H-bars (cf. e.g. Fig. 6.5c)) to investigate spin transport in our 3D HgTe-based devices. The following section describes why microscopic H-bar structures are well-suited for the identification of this type of transport. In this context, two different measurement configurations are introduced, namely the so-called Hall-like (Subsec. 7.1.1) and non-local measurements (Subsec. 7.1.2). The explanation of the non-local signal detected in our three-dimensional samples is subject of Sec. 7.2. In the process, the different origins of the non-local signals in 2D and 3D H-bar devices are discussed as well.

7.1. Microscopic H-bar samples

H-bar structures are excellent for investigating non-local signals, since the H-shape strongly suppresses the spreading of the local signal (voltage drop) across the connecting piece [88]. Microscopic dimensions are required, as the size of the structures should not be larger than the spin relaxation length λ_s of the charge carriers (cf. Chap. 6). Fig. 7.1 shows SEM images of both H-bars located on sample Q2982 spindetection II (cf. Appx. A.1). The difference between the two structures is the length of the connecting piece, which is 1 µm and 0.5 µm, respectively. Fig. 7.1a) displays the larger H-bar and b) the smaller one. In order to obtain the most accurate structural fidelity and well-defined device dimensions, the inductively coupled plasma etching technique was chosen (cf. Sec. 6.2). In addition, both structures located on sample Q2982 spindetection II possess an overlapping top-gate design to enable the determination of magnetoresistances even in the presence of high magnetic fields (cf.

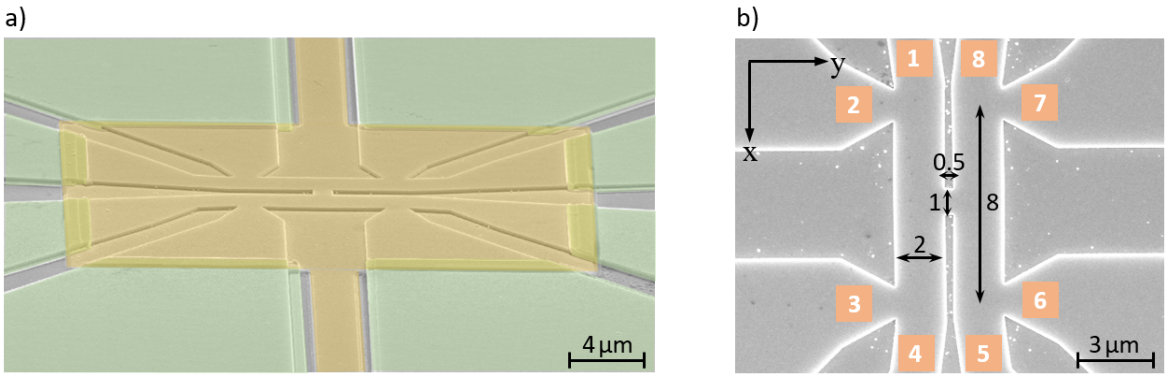

Figure 7.1.: SEM images of both H-bar structures located on sample Q2982 spindetection II. a) displays the H-bar possessing a 1 µm connecting piece from the side view. The metallized ohmic contacts are highlighted in green, while the top-gate-electrode and its leads are marked in yellow. b) presents the smaller structure (0.5 µm) from the bird's eye view. The dimensions of this H-bar are given in the unit of micrometer. The contact configuration used to describe the measurements is defined by consecutive numbering from 1 to 8.

Sec. 4.2). Using the contact configuration introduced in Fig. 7.1b), the H-shape suppresses, for instance, any residual voltage between contacts 8 and 5 resulting from spreading of the potential difference applied between contacts 1 and 4 and vice versa.

As the first step to evaluate the non-local measurements, Hall-like measurements were carried out in order to determine the electron and hole densities as well as their mobilities for each applied top-gate voltage. This knowledge is required to identify all carrier systems contributing to transport, giving us insight into the spin transport behavior of our devices.

It is noted that unless specified otherwise, all measurements shown in Chap. 7 were performed at $T = 1.5\,\mathrm{K}$, without applying an external magnetic field[1], and on sample Q2982 spindetection II using the H-bar possessing the shorter connecting piece. The dimensions of this structure are given in Fig. 7.1b).

7.1.1. Hall-like measurements

We can employ the H-bar structure to estimate the transverse resistance R_{xy} by a certain configuration. If we presuppose that the current I is homogenous in the current-carrying leg and is sent from contact 1 to contact 4, then R_{xy} can be obtained by a combination of $R_{14,28} = V_{28}/I$ and the longitudinal resistance $R_{\mathrm{xx}} = R_{14,23}$ as follows (cf. Fig. 7.1)

$$R_{\mathrm{xy}} = -R_{14,28} + \frac{R_{14,23}}{2}. \tag{7.1}$$

It is assumed that all contacts of the detection leg (5, 6, 7, and 8) are at the same potential during the magneto-transport measurement. The right side of the H-bar device can therefore

[1]The Hall-like measurements presented in Subsec. 7.1.1 were made with an applied external magnetic field.

be seen as one voltage probe. The negative sign of $R_{14,28}$ in Eq. 7.1 is a consequence of the direction of the magnetic field in our measurement-setup (cf. Subsec. 2.2.1 and Fig. 2.11). Since the transverse resistance in H-shaped structures cannot be determined directly, we refer to measurements performed in the configuration described above allowing us to estimate R_{xy} as Hall-like measurements. Fig. 7.2 shows the results of the magneto-transport measurements of sample Q2982 spindetection II at different values of top-gate voltage V_{TG}^{*}. It is noted that, analogous to Chap. 5, V_{TG}^{*} is introduced so that $V_{\mathrm{TG}}^{*} = 0\,\mathrm{V}$ applies to the transition point from n-type to p-type conductance. It is calculated by $V_{\mathrm{TG}}^{*} = V_{\mathrm{TG}} + 0.38\,\mathrm{V}$. One is able to observe that the transverse resistance R_{xy} calculated by means of $-R_{14,28}$ (Fig. 7.2a)), $R_{14,23}$ (Fig. 7.2b)), and Eq. 7.1 rests on several quantized values well at high magnetic fields (cf. Fig. 7.2c)). This can be seen, for instance, for a top-gate voltage of $V_{\mathrm{TG}}^{*} = -0.12\,\mathrm{V}$, where the $\nu = -4$ quantum Hall plateau is formed at $B = 3\,\mathrm{T}$. Meanwhile, R_{xy} is linearly dependent on B at lower fields and changes its sign at $B = 0$ ($R_{\mathrm{xy}}(B = 0) = 0$). All these evidences substantiate our method to extract an appropriate transverse resistance in a H-bar structure.

Using Fig. 7.2b), c), and a two-band Drude model [47], we are able to estimate the electron densities n_{E} and mobilities μ_{E} as well as those of the holes ($|n_{\mathrm{hole}}|$ and μ_{hole}) for each applied top-gate voltage V_{TG}^{*}. The results are presented in Fig. 7.2d). Note that for the aspect ratio of H-bar samples $AR = 4$ applies (cf. Fig. 7.1b)). Since the transition point between n-type and p-type conductance is at $V_{\mathrm{TG}}^{*} = 0\,\mathrm{V}$, the massive p-type Volkov-Pankratov state is not occupied for $V_{\mathrm{TG}}^{*} \geq 0.08\,\mathrm{V}$ and the transport is dominated by electrons. Starting from $V_{\mathrm{TG}}^{*} \leq -0.02\,\mathrm{V}$, however, the occupation of the p-type VPS and its contribution to transport is visible in the measurements. The number of holes in the system increases with decreasing top-gate voltage. The n-type charge carrier density in the bottom topological surface state (TSS,II) is approximately constant for all applied values of V_{TG}^{*} due to Dirac-screening (cf. Subsec. 2.2.3). The density in TSS,I increases linearly with increasing V_{TG}^{*} for $V_{\mathrm{TG}}^{*} > 0.08\,\mathrm{V}$ and is nearly constant as long as the Fermi energy is pinned to the p-type massive VPS ($V_{\mathrm{TG}}^{*} \leq -0.02\,\mathrm{V}$). For high p-type densities ($V_{\mathrm{TG}}^{*} < -0.4\,\mathrm{V}$), the same effect that has already been observed for the macroscopic Hall bar fabricated of the same wafer material Q2982 (cf. Subsec. 3.3.2 and Fig. 3.20b)) is visible: Due to the filling of the trap states with positive charge carriers, the energy potential of the top-gate is increasingly screened with increasing negative applied gate voltage until the effective top-gate voltage $V_{\mathrm{TG}}^{\mathrm{eff}}$, which the active layer perceives, takes a constant value. For this reason, the charge carrier density and mobility of the system no longer changes for $V_{\mathrm{TG}}^{*} < -0.4\,\mathrm{V}$. In this regime, the values of hole and electron densities are approximately $n_{\mathrm{hole}} = -5.7 \cdot 10^{11}\,\frac{1}{\mathrm{cm}^2}$ and $n_{\mathrm{E}} = 1.3 \cdot 10^{11}\,\frac{1}{\mathrm{cm}^2}$, respectively. The majority of these electrons is located in TSS,II. In addition, we find an average electron mobility of about $\mu_{\mathrm{E}} = 12.8 \cdot 10^{4}\,\frac{\mathrm{cm}^2}{\mathrm{Vs}}$ and an average hole mobility of around $\mu_{\mathrm{hole}} = 2.5 \cdot 10^{4}\,\frac{\mathrm{cm}^2}{\mathrm{Vs}}$.

From of Fig. 7.2d), we are able to specify electron and hole densities for each top-gate volt-

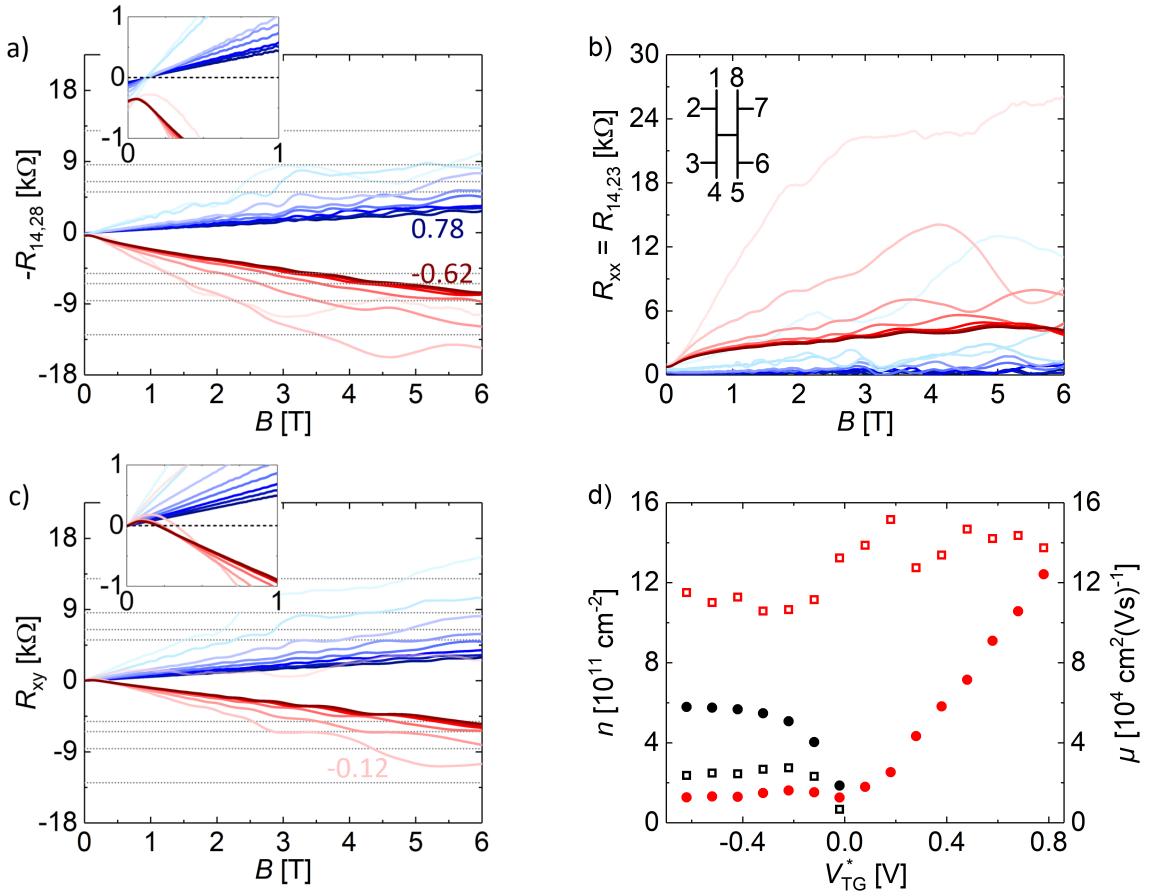

Figure 7.2.: Measured resistances a) $-R_{14,28}$ and b) $R_{14,23}$ are presented as a function of magnetic field B for different top-gate voltages V^*_{TG}. V^*_{TG} is stepped from -0.62 V (dark red) to 0.78 V (dark blue) in 0.1 V steps. The contact configuration used for the measurements is given as an inset in b). c) Hall resistance R_{xy} calculated according to Eq. 7.1. In a) and c), the theoretical values of the QH plateaus with filling factors $\nu = -5$, -4, -3, -2, 2, 3, 4, and 5 are indicated via dotted gray lines. The insets depict the low-field regime in higher magnification and use identical axis labels. $-R_{14,28} = 0$ and $R_{\mathrm{xy}} = 0$ are drawn by black dashed lines. d) Electron densities n_{E} and mobilities μ_{E} as a function of V^*_{TG} are shown as red circles and squares respectively. Hole densities $|n_{\mathrm{hole}}|$ and mobilities μ_{hole} are displayed using the same symbols in black.

age V_{TG}^{*}. This knowledge is an important part of understanding the non-local measurements presented in the following subsection.

7.1.2. Non-local measurements

A non-local transport measurement is the measurement of a potential difference between two electrodes, neither of which is on the current path. Using the contact configuration introduced in Fig. 7.1b), we send a current I from contact 1 to contact 4 and measure the non-local potential difference V_{85} between contacts 8 and 5. The resulting resistance $R_{14,85} = V_{85}/I_{14}$ is defined as the non-local signal R_{nl}. Fig. 7.3 presents the non-local signal $R_{14,85}$ (in blue) as a function of the applied top-gate voltage V_{TG}^{*}. It can be seen that $R_{14,85}$ is negative for all values of V_{TG}^{*} and develops a clear minimum at approximately $V_{\mathrm{TG}}^{*} = 0.2\,\mathrm{V}$. The signal strength at the minimum is about $-3.9\,\Omega$. Around $V_{\mathrm{TG}}^{*} = 0.2\,\mathrm{V}$, $|R_{\mathrm{nl}}|$ diminishes for increasing as well as for decreasing top-gate voltages. Since for $V_{\mathrm{TG}}^{*} < -0.4\,\mathrm{V}$, the effective top-gate voltage $V_{\mathrm{TG}}^{\mathrm{eff}}$, which the active layer perceives, no longer changes (cf. Subsec. 7.1.1), the non-local signal is also nearly constant in this regime. Furthermore, the non-local signal is more pronounced for n-type conductance ($V_{\mathrm{TG}}^{*} > 0\,\mathrm{V}$). Fig. 7.3 also

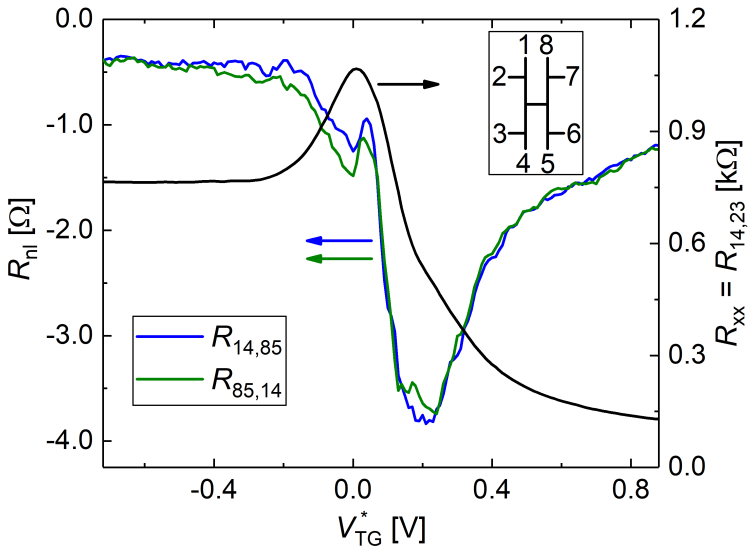

Figure 7.3.: Non-local signals R_{nl} (in blue and green) and longitudinal ("local") resistance R_{xx} (in black) as a function of top-gate voltage V_{TG}^{*}. The inset displays the contact configuration.

shows the longitudinal ("local") resistance $R_{\mathrm{xx}} = R_{14,23}$ (in black) as a function of top-gate voltage V_{TG}^{*}. The longitudinal resistance is rather typical for a three-dimensional topological insulator as discussed in detail in Subsec. 2.2.3. Again, due to an almost constant effective top-gate voltage $V_{\mathrm{TG}}^{\mathrm{eff}}$, the value of R_{xx} hardly changes for $V_{\mathrm{TG}}^{*} < -0.4\,\mathrm{V}$.

First, the robustness of the underlying experiment is to be tested. For this purpose, the so-called Onsager reciprocal relations for linear response can be used [89]. To verify the Onsager reciprocal relations, or more precisely to show the equality of the ratio between flow (non-local signal on the detection leg of the H-bar) and force (current sent through the current-carrying leg), the non-local measurement has to be performed with reversed contact configuration [90]: This time, the current is sent from contact 8 to contact 5 and the non-local potential difference is measured between contacts 1 and 4. The non-local signal $R_{85,14}$ (green curve) is also plotted in Fig. 7.3. It can be seen that the two non-local signals $R_{14,85}$ and $R_{85,14}$ match well. They exhibit the same characteristics at identical top-gate voltages (e.g. clear minimum at $V_{\mathrm{TG}}^{*} = 0.2\,\mathrm{V}$). Hence, the Onsager reciprocal relations for linear response are fulfilled and the system is in local equilibrium, demonstrating the robustness of our experiment.

The next step is to investigate the physical mechanism responsible for the non-local signals observed in microscopic three-dimensional HgTe-based topological insulators. In this context, the differences between 2D and 3D cases are to be discussed as well. Based on Ref. [88] (2D) and Fig. 7.3 (3D), it can be determined that in three-dimensional devices, the non-local signal is more pronounced for n-type conductance and shows a clear minimum, while in two-dimensional samples, the value of $|R_{\mathrm{nl}}|$ is larger in the p-type regime. Furthermore, the non-local signal does not exhibit an extremum but continues to rise as long as the number of holes in the system is increased, reaching signal strengths of more than $1\,\mathrm{k\Omega}$. Thus, in the two-dimensional case, the non-local resistance signal is about two orders of magnitude larger. For this reason, we assume that different physical mechanisms are responsible for the detected non-local signals in 2D and 3D H-bar devices. In the following section, we will focus on the origin of the non-local resistance signals found in our three-dimensional samples.

7.2. Non-local signals derived from spin-polarized charge carriers in topological surface states

We assume that a current-induced spin polarization of the topological surface states is responsible for the experimentally observed non-local resistance signal R_{nl}. As described in Chap. 2 (cf. Subsec. 2.1.2), the charge carriers in the topological surface states exhibit spin-momentum locking. Thus, the spin direction of a carrier is perpendicularly coupled to its momentum direction. To determine the spin polarization $\left\langle \overrightarrow{S} \right\rangle$ of the system, the integral along the Fermi circle $\mathcal{C}$ has to be calculated (cf. Fig. 2.5b)):

$$\left\langle \overrightarrow{S} \right\rangle = \left\langle \begin{pmatrix} S_{\mathrm{x}} \\ S_{\mathrm{y}} \\ S_{\mathrm{z}} \end{pmatrix} \right\rangle = \frac{1}{2\pi k_{\mathrm{F}}} \oint_{\mathcal{C}} \overrightarrow{S}(\overrightarrow{k})\,\mathrm{d}\overrightarrow{k}\,, \tag{7.2}$$

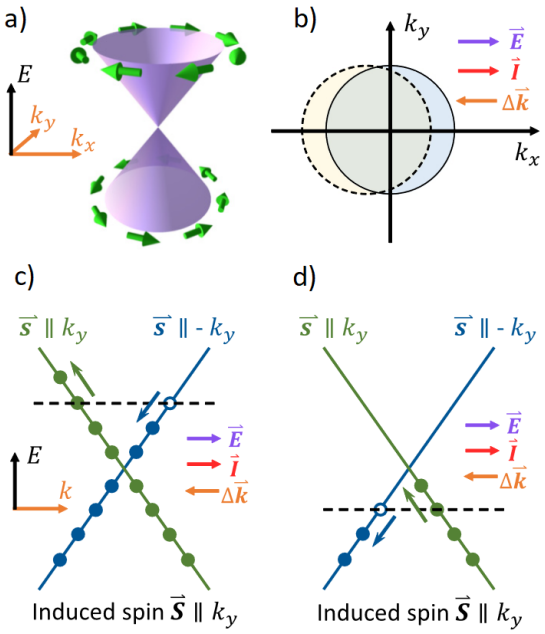

Figure 7.4.: a) illustrates the spin texture of the topological surface states having opposite helicities on both sides of the Dirac cone. b) An applied electric field $\vec{E}$ along k_x generates a charge current $\vec{I}$ in the same direction, shifting the Fermi surface by $\Delta\vec{k}$ in the $-k_x$-direction. The occupations of the Dirac cone states in the n-type and p-type regimes under the influence of charge currents are shown in c) and d), respectively. Irrespective of the carrier type, a current along k_x always makes the $\vec{S} \parallel k_y$ branch more populated, leading to a net spin polarization $\left|\left\langle \vec{S} \right\rangle\right| > 0$ in the k_y-direction. Adapted with permission from [91]. Copyright 2016 by the American Physical Society.

where the absolute value of the Fermi wave vector k_F is the radius of the Fermi circle, $\vec{S}$ the spin of a charge carrier located in the TSSs, and $\vec{k}$ the wave vector. If the system is in equilibrium, i.e. there is no driving current, then the many carrier spins point randomly in all directions as to cancel out as a whole. The consequence is a net spin polarization $\left|\left\langle \vec{S} \right\rangle\right|$ of zero. However, if the system is brought out of equilibrium, for instance by applying an external excitation voltage, then an imbalance in the orientation of the individual spins is created due to spin-momentum locking. This effect is demonstrated by sketches in Fig. 7.4. Note that in our devices the hole regimes of the TSSs are not accessible in the experiment (cf. Subsec. 2.1.2). From Fig. 7.4, it can be seen that a charge current along k_x-direction leads to a current-induced net spin polarization $\left|\left\langle \vec{S} \right\rangle\right| > 0$ in the k_y-direction. The next step is to consider a three-dimensional topological insulator, which has two topological surface states TSS,I and TSS,II localized at the opposite surfaces (top and bottom) of the TI (cf. Subsec. 2.1.3). As before, the normals to the surfaces are to point in the z-direction. In this case, the orientation of the spins $\vec{S}$ of the electrons perpendicular to their momentum can

be described by

$$\frac{\vec{S}(\vec{k})}{\left|\vec{S}(\vec{k})\right|} = \pm\frac{(\vec{k}\times\hat{z})}{\left|\vec{k}\right|}, \tag{7.3}$$

with $\vec{k} = (k_x, k_y)$ being the in-plane wave vector of the charge carriers and $\hat{z}$ the unit vector in z-direction [92]. The $\pm$-sign indicates the opposite helicities of TSS,I and TSS,II.

Now, the formalism described above is to be applied to sample Q2982 spindetection II. The two surfaces of this device are examined individually, since both topological surface states are assumed to contribute to conductance in parallel without interaction. At the top surface, when a current is sent from contact 1 to contact 4 (technical direction of current), the electrons located in the current-carrying leg of the H-bar structure receive a momentum change $\Delta\vec{k}$ in the $-k_x$-direction as illustrated in Fig. 7.5. According to Eq. 7.2 and Eq. 7.3,

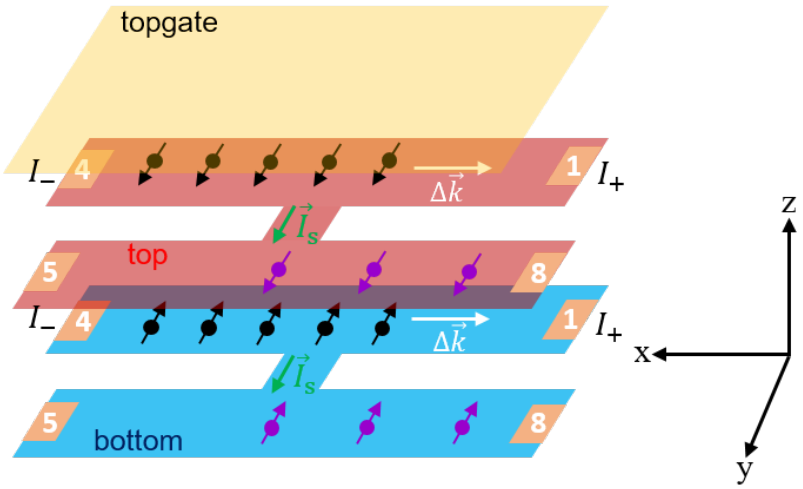

Figure 7.5.: Sketch of the origin of the negative non-local resistance signal observed in our 3D TI samples. Shown are the top-gate-electrode (in yellow), top surface (in red), bottom surface (in blue), technical direction of current (I_+ to I_-), and contact configuration introduced in Fig. 7.1 (1, 4, 5, 8). The spin-polarized electrons in the current-carrying leg due to the momentum change $\Delta\vec{k}$ are represented by black dots and arrows. The spin current $\vec{I}_s = I_s\hat{y}$ induced by this spin polarization is displayed in green. As a result of the spin current, a spin polarization is generated in the detection leg, leading to a net movement of electrons (purple dots and arrows) to contact 8.

the change in momentum leads to a current-induced spin polarization of this leg in the k_y-direction. As long as the length of the connecting piece is shorter than the spin relaxation length λ_s of the charge carriers, the spin polarization is transferred to the detection leg due to the magnetization of the electrons located in the connecting piece. This implies that a spin current I_s is induced between the two legs of the H-bar structure. In clean systems, λ_s can be determined based on the mean free path λ_{mfp} of the charge carriers, since both values

are comparable [87]. Using a Drude model, we can estimate the mean free path to be

$$\lambda_{\mathrm{mfp}} \approx \frac{\hbar}{e}\mu\sqrt{4\pi\,|n|}. \tag{7.4}$$

By means of the data from Fig. 7.2d), we are able to calculate that λ_{mfp} is in the range of a few micrometers for TSS,I. Note, however, that for microscopic devices, due to the unknown crystal structure, the determination of the mean free path using a Drude model should only be considered as an indicator and not as an exact measure of the actual value. Nevertheless, our result agrees well with Ref. [93]. There, the spin relaxation length λ_{s} of charge carriers in the topological surface state of a HgTe-based sample has also been estimated to be in the range of a few microns. As the length of the connecting piece (0.5 µm) is shorter than λ_{s}, we assume that a transfer of spin polarization from the current-carrying to the detection leg occurs via a spin current. Since the spin distribution in the latter is now also driven out of equilibrium, the electrons moving in the $-k_{\mathrm{x}}$-direction are favored over those moving in the k_{x}-direction due to spin-momentum locking. This leads to an inverse effect: in the detection leg, the spin polarization in the k_{y}-direction generates a charge current in the $-k_{\mathrm{x}}$-direction, finally resulting in a negative non-local voltage drop $V_{85} = V_8 - V_5 < 0$ between contacts 8 and 5. In combination with the defined direction of the current $I = I_{14} > 0$, the consequence is a negative non-local resistance signal $R_{\mathrm{nl}} = R_{14,85} = V_{85}/I < 0$.

The consideration of the bottom surface is carried out analogously. Again, the current sent from contact 1 to contact 4 (technical direction of current) causes the electrons located on the current-carrying leg to receive a change in momentum $\Delta\overrightarrow{k}$ in the $-k_{\mathrm{x}}$-direction (cf. Fig. 7.5). This time, due to the opposite helicities of the two surface states (cf. Eq. 7.3), $\Delta\overrightarrow{k}$ leads to a current-induced spin polarization of this leg in the $-k_{\mathrm{y}}$-direction. Using Eq. 7.4, $n_{\mathrm{TSS,II}} \approx 1 \cdot 10^{11}\,\frac{1}{\mathrm{cm}^2}$, and $\mu_{\mathrm{E}} \approx 13 \cdot 10^4\,\frac{\mathrm{cm}^2}{\mathrm{Vs}}$ (cf. Fig. 7.2d)), the mean free path of the charge carriers in TSS,II can be estimated to $\lambda_{\mathrm{mfp}} \approx 1\,\mu\mathrm{m}$. Since the mean free path is comparable to the spin realization length λ_{s}, we assume that at the bottom surface the spin polarization is also transferred from the current-carrying to the detection leg by means of a spin current I_{s} passing through the short connecting piece (0.5 µm). The spin polarization induced in the detection leg in the $-k_{\mathrm{y}}$-direction results in an accumulation of electrons at contact 8 due to the spin-momentum locking of charge carriers in a topological surface state. Thus, analogous to the top surface, a negative non-local resistance signal $R_{\mathrm{nl}} = R_{14,85} = V_{85}/I < 0$ is obtained. Since we only determine potential differences and not the spin orientation of the charge carriers, the opposite helicities of the electrons at top and bottom surfaces has no relevance for the measured non-local signal. One can say that the two topological surface states contribute independently to the non-local resistance signal with the same sign. Hence, the total effect is a combination of the contributions of TSS,I and TSS,II resulting in an enhanced $|R_{\mathrm{nl}}|$.

So far, we have generally considered which non-local signal to expect when two topological

surface states are involved in transport. Now, the influence of the top-gate-electrode is to be investigated, so that the non-local measurement of sample Q2982 spindetection II (cf. Fig. 7.3) can be described. Depending on the applied top-gate voltage, the level of the Fermi energy in the system changes and thus the populated transport channels. According to Subsec. 2.1.2, we know that the electron regime of our devices can be composed of the contributions of the TSSs (TSS,I and TSS,II) and n-type massive states (Volkov-Pankratov or bulk states). The p-type transport, on the other hand, is assigned exclusively to the p-type massive VPS. Furthermore, it is known that at the bottom surface only TSS,II is accessible in the experiment. Due to Dirac-screening (cf. Subsec. 2.2.3), this surface is assumed to be unaffected by a change in top-gate voltage, resulting in a constant contribution to R_{nl} during the non-local measurement. TSS,I is also occupied for all values of V_{TG}^{*} as a result of Fermi level pinning (cf. Sec. 5.1), however, the population of this state depends on applied TG voltage. To determine which massive states are occupied for each applied top-gate voltage and hence contribute to transport, several 8-orbital $k \cdot p$ calculations are performed for sample Q2982 spindetection II. The main results are shown in Fig. 7.6. Above a top-gate voltage of approximately $V_{\mathrm{TG}}^{*} \approx 0.6\,\mathrm{V}$, n-type bulk states are populated (cf. Fig. 7.6a)). In the gate voltage range $0.14\,\mathrm{V} < V_{\mathrm{TG}}^{*} < 0.6\,\mathrm{V}$, only electrons located in the topological surface states contribute to transport (cf. Fig. 7.6b)). Starting at a top-gate voltage of about 0.14 V, holes are introduced into the system (cf. Fig. 7.6c)). As soon as $V_{\mathrm{TG}}^{*} < 0\,\mathrm{V}$ applies, holes become the dominant carrier type. In this regime, the p-type massive VPS is occupied (cf. Fig. 7.6d)). An overview of which charge carrier systems contribute to transport at which top-gate voltages is shown in Fig. 7.7.

First, the voltage range $0.14\,\mathrm{V} < V_{\mathrm{TG}}^{*} < 0.6\,\mathrm{V}$ is to be considered. In this regime, solely the two topological surface states are populated. Since the occupation of TSS,I depends on the top-gate voltage, we assume that the magnitude of the net spin polarization of TSS,I obtained when an external electric field is applied depends on V_{TG}^{*} as well. A change in the magnitude of the net spin polarization should in turn affect the strength of the non-local resistance signal. According to Ref. [94], for a topological insulator surface in the xy-plane, the relation between electric current operator $\overrightarrow{j}$ and spin-density operator $\overrightarrow{s}$ can be decribed as

$$\overrightarrow{j} = e v_{\mathrm{F}} \overrightarrow{s} \times \hat{z}. \tag{7.5}$$

In the case of a current density j_{x} in the x-direction, we thus obtain

$$j_{\mathrm{x}} = e v_{\mathrm{F}} s_{\mathrm{y}}, \tag{7.6}$$

with s_{y} being the current-induced spin density in the k_{y}-direction. To obtain a figure of merit for the spin polarization of the charge carriers in a TSS, the ratio between the current-induced spin density s_{y} and carrier density n is taken. Now, the theoretical analysis described above is applied to our case. Since we only detect potential differences and not the spin orientation

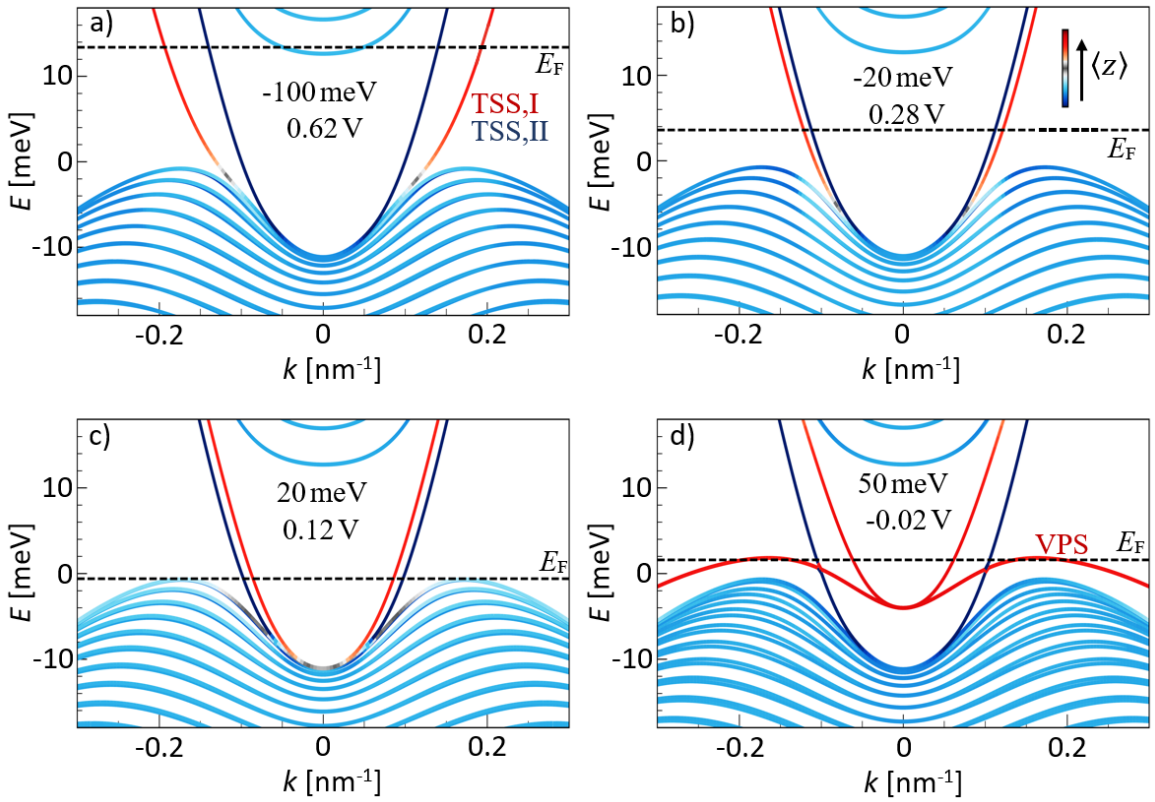

Figure 7.6.: Band structures from 8-orbital $k \cdot p$ calculations for sample Q2982 spindetection II at different applied electrostatic potentials U_i at the interface HgTe/cap layer. The energy potentials under consideration are a) -100 meV, b) -20 meV, c) 20 meV, and d) 50 meV. The corresponding values of V_{TG}^* are also noted. In addition, indicated are top and bottom surface states (TSS,I and TSS,II), the Volkov-Pankratov state (VPS), the Fermi energy E_F via a dashed black line, and a color code (legend in b)), which depicts the wave function location (expectation value $\langle z \rangle$): top surface (red), bottom surface (dark blue) or elsewhere (light blue).

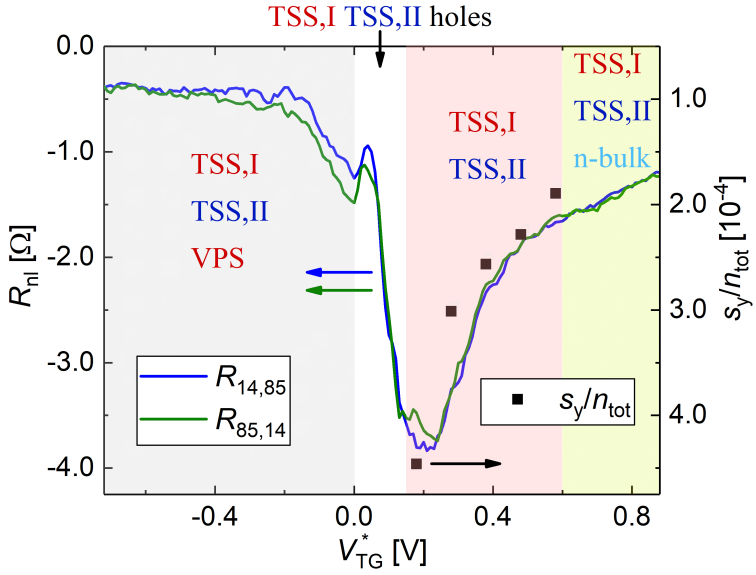

Figure 7.7.: The data of the non-local measurement of Fig. 7.3 are re-presented. The top-gate voltage V^*_{TG} is subdivided into regions in which certain charge carrier systems contribute to transport. These regions are: n-bulk states, TSS,I and TSS,II (marked in yellow), TSS,I and TSS,II (marked in red), and p-type VPS, TSS,I and TSS,II (marked in gray). Between the red and gray region is the region where holes are introduced into the system. The ratio between the current-induced spin density s_y and the total charge carrier density n_{tot} calculated according to Eq. 7.7 is displayed by black squares for different values of V^*_{TG}.

of the charge carriers, we combine the opposite orientations of the spin polarizations in $\pm k_y$-direction of TSS,I and TSS,II simply as polarization perpendicular to the current direction. Due to this simplification, the total electron density n_{tot} comprising the densities of top $n_{TSS,I}$ and bottom surface states $n_{TSS,II}$ ($n_{tot} = n_{TSS,I} + n_{TSS,II}$) can be used as input density. Furthermore, the current density can be derived from the total current I_{14} flowing through the sample. Utilizing $j_x = I_{14}/w$, where $w = 2\,\mu m$ is the width of the current-carrying leg of the H-bar (cf. Fig. 7.1b)), we are able to determine the ratio between current-induced spin density and total electron density by the relation

$$\frac{s_y}{n_{tot}} = \frac{I_{14}}{e w v_F n_{tot}}. \tag{7.7}$$

Eq. 7.7 is only applicable in the case of pure topological surface state transport, i.e. in the voltage range under consideration ($0.14\,V < V^*_{TG} < 0.6\,V$). Using the Hall-like measurements (cf. Fig. 7.2), n_{tot} can be determined for several top-gate voltages in this regime. This allows us to calculate the ratio s_y/n_{tot}, which provides a good estimate for the magnitude of spin polarization of the TSSs, as a function of V^*_{TG}. Analogous to Subsec. 2.1.3 and Sec. 5.1, we set $v_F = 5 \cdot 10^5 \frac{m}{s}$. The results are shown in Fig. 7.7. As expected, one is able to

recognize that a larger magnitude of spin polarization also leads to a more pronounced non-local resistance signal R_{nl}. Overall, it can be stated that the curves of spin polarization and $|R_{\mathrm{nl}}|$ are quite comparable, suggesting a tight connection. This strengthens our assumption that the experimentally observed non-local signal is caused by spin-polarized electrons in the topological surface states. At this point, it should be mentioned that the TSSs are much more effective spin polarization generators than a regular two-dimensional electron gas. For a Rashba-coupled 2DEG, the current-induced spin density can be calculated by the relation

$$s_{\mathrm{y}} = 2\delta \frac{j_{\mathrm{x}}}{e v_{\mathrm{F}}}, \tag{7.8}$$

with $\delta = \Delta_{\mathrm{so}}/E_{\mathrm{F}} \ll 1$ being the ratio between spin-orbit energy Δ_{so} and Fermi energy E_{F} [95]. The comparison of Eq. 7.6 and Eq. 7.8 results in a current-induced spin density being larger by a factor of $1/(2\delta) \gg 1$ for a topological surface state. Even stronger spin polarizations can be obtained in ferro/normal hybrid systems [94]. However, these systems do not offer the possibility of gate voltage control.

We next, consider the range of top-gate voltage ($V_{\mathrm{TG}}^{*} < 0.14\,\mathrm{V}$) where holes are present in the system. To identify whether current-induced spin polarization also occurs in the Volkov-Pankratov state when an external excitation voltage is applied, the spin texture of this state has to be determined. The spin texture of the surface states at the Fermi level for a top-gate voltage of $V_{\mathrm{TG}}^{*} = -0.02\,\mathrm{V}$ for sample Q2982 spindetection II is shown in Fig. 7.8. The black dashed line in this figure coincides with the black dashed line in Fig. 7.6d). It can be seen that the topological surface states TSS,I and TSS,II exhibit large spin expectation values (represented by blue and green arrows, respectively) due to spin-momentum locking. The spin expectation values of the populated VPS (turquoise arrows), on the other hand, are significantly smaller in the regions of the Fermi contour. Indeed, the Rashba effect imposed by the electrostatic top-gate (inversion symmetry breaking) can lift the spin degeneracy of the massive Volkov-Pankratov states. However, these states are very flat and close in energy. This leads to a considerable inter-band scattering, giving rise to much smaller spin expectation values in comparison to the topological surface states. Therefore, we expect only a weak current-induced spin polarization of the VPS to occur when an external electric field is applied to the device. Since holes possess a lower mobility, their mean free path and thus λ_{s} are reduced. Using Eq. 7.4, $n_{\mathrm{hole}} \approx -5 \cdot 10^{11}\,\frac{1}{\mathrm{cm}^2}$, and $\mu_{\mathrm{hole}} \approx 2.5 \cdot 10^{4}\,\frac{\mathrm{cm}^2}{\mathrm{Vs}}$ (cf. Fig. 7.2d)), the mean free path of the holes can be estimated to $\lambda_{\mathrm{mfp}} \approx 0.4\,\mu\mathrm{m}$, which is shorter than the length of the connecting piece. Hence, it can be supposed that the weak current-induced spin polarization of the Volkov-Pankratov state is not transferred to the detection leg. Hence, due to the connection between spin polarization and non-local signal, we assume that the contribution of the VPS to the experimentally observed R_{nl} is negligible. On the contrary, based on Sec. 5.2 we know that inter-scattering between n-type and p-type states can occur in our samples. The possibility of inter-scattering largely enhances the

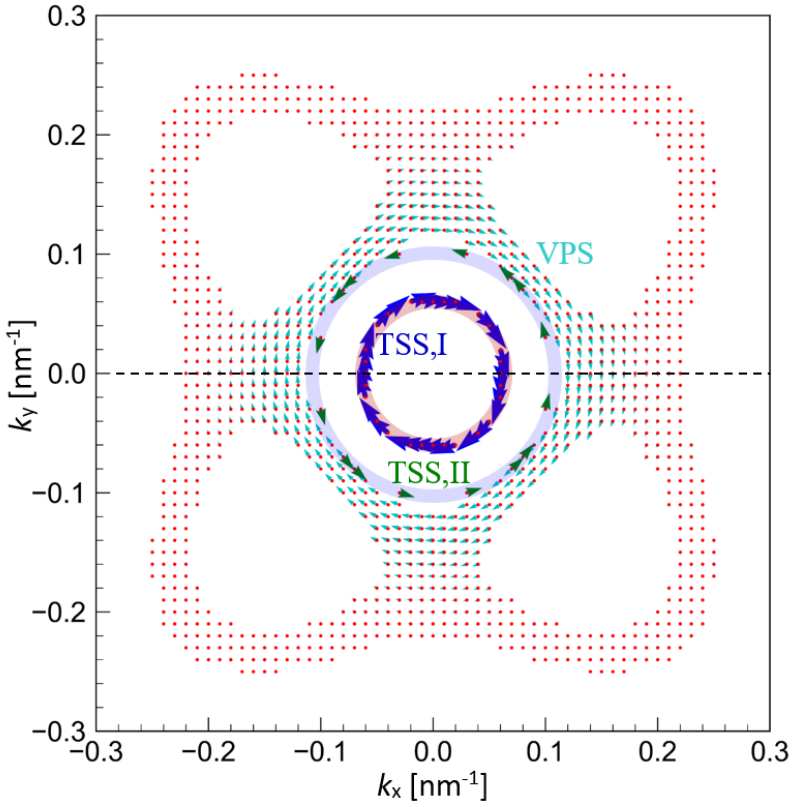

Figure 7.8.: Spin texture of topological and massive surface states at the Fermi level E_F for an applied top-gate voltage of $V^*_{TG} = -0.02\,V$. The occupied surface states in the momentum space are marked by red dots. To facilitate the differentiation, the TSSs are highlighted via circles in the colors also used in Fig. 7.6d): TSS,I (in red) and TSS,II (in blue). All other populated states are assigned to the p-type massive VPS. The spin expectation value for each point in the momentum space is indicated by an arrow: TSS,I (in blue), TSS,II (in green), and VPS (in turquoise). Larger arrows specify higher values and vice versa. $k_y = 0$ is drawn as a dashed black line.

likelihood of spin-flipping of electrons in the topological surface states. The more holes are present in the system, the more pronounced this effect becomes. The result is a reduction of the spin polarization of the TSSs and therefore a smaller non-local signal. We expect effects of inter-scattering to become discernable as soon as holes are introduced into the system. Thus, $|R_{nl}|$ should decrease significantly starting from a top-gate voltage of approximately 0.14 V. This behavior can in fact be observed in the non-local measurement (cf. Fig. 7.7).

Lastly, the region of high electron densities ($V^*_{TG} > 0.6\,V$) is considered. In this region, n-bulk states, TSS,I and TSS,II contribute to transport. According to Subsec. 2.1.2, the bulk states in the n-type regime are spin-degenerate. Therefore, these states cannot exhibit current-induced spin polarization and are not expected to contribute to the non-local resistance signal R_{nl}. Furthermore, we assume that, in a simple picture, the addition of electrons without spin polarization into the system dilutes the contributions of spin-polarized electrons

from TSS,I and TSS,II as a whole. This means that the n-bulk states provide a large unpolarized electron background, resulting in a decrease in the non-local signal $|R_{\mathrm{nl}}|$ as soon as the bulk states are occupied [96]. The behavior described above can be observed in Fig. 7.7 as well.

It is noted that the non-local measurement of sample Q2982 spindetection II (Fig. 7.7) exhibits additional features such as another local maximum in $|R_{\mathrm{nl}}(V_{\mathrm{TG}}^{*})|$ at $V_{\mathrm{TG}}^{*} = 0\,\mathrm{V}$. A complete explanation of all details of the measurement curves may require further dedicated research.

It can be concluded that the non-local measurement of sample Q2982 spindetection II can be well described by our assumption that spin-polarized topological surface states are responsible for the observed non-local resistance signal. The massive states (p-type VPS and n-type bulk states) can hardly contribute to R_{nl} in our proposed mechanism. On the contrary, due to possible inter-scattering or the addition of an unpolarized electron background, $|R_{\mathrm{nl}}|$ decreases as the Fermi energy is moved into the valence band or conduction band, respectively. To verify our assumption to a greater extent, the behavior of the non-local signal is investigated as a function of temperature, the length of the connecting piece, and in the presence of an external magnetic field. When the temperature is increased in the system of a three-dimensional topological insulator, two effects are observed [97]: First, the bulk conduction increases due to thermally activated bulk dopants. As already discussed above, this leads to an enhanced unpolarized electron background diluting the contributions of the spin-polarized topological surface states. Second, an increase in temperature results in an enhancement of inelastic scatterings such as phonon scatterings. This in turn increases the likelihood of spin-flipping events, leading to a decrease in spin polarization of the TSSs. Thus, we assume that both effects cause a reduction of the non-local resistance signal $|R_{\mathrm{nl}}|$. The temperature-dependent non-local measurements are presented in Fig. 7.9a). As expected, the peak strength decreases continuously with increasing temperature from $|R_{\mathrm{nl}}(T = 1.5\,\mathrm{K})| \approx 3.9\,\Omega$ to $|R_{\mathrm{nl}}(T = 46\,\mathrm{K})| \approx 2.0\,\Omega$.

As the length of the connecting piece increases, the magnitude of induced spin polarization in the detection leg decreases, since the magnetization of the electrons declines over the extent of the connecting piece. This reduced spin polarization immediately gives rise to a weaker non-local voltage drop. To verify this statement, two identical H-bars were fabricated on the same sample piece (Q2982 spindetection II) at a distance of 400 µm, differing only in the length of their connecting piece (0.5 µm and 1 µm). The non-local measurement on the smaller structure can be found in Fig. 7.7. The equivalent measurement on the larger H-bar is shown in Fig. 7.9b). In general, it can be observed that the two non-local resistance signals exhibit similar characteristics as a function of top-gate voltage V_{TG}^{*}. The maximum of $|R_{\mathrm{nl}}|$ is taken when only the topological surface states TSS,I and TSS,II are occupied and therefore contribute to transport. As soon as holes are introduced into the system, the non-local

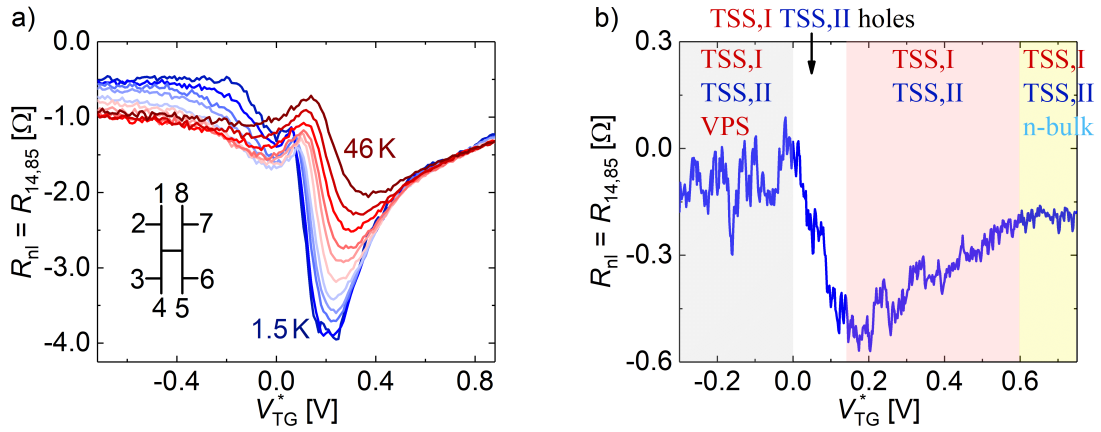

Figure 7.9.: a) temperature dependence of the non-local resistance signal R_{nl} determined using the H-bar structure possessing a length of the connecting piece of 0.5 µm. The temperature ranges from $T = 1.5\,\mathrm{K}$ (dark blue) to $T = 46\,\mathrm{K}$ (dark red) in steps of about 4.5 K. The inset depicts the contact configuration. b) non-local measurement of the H-bar having a 1 µm connecting piece at $T = 1.5\,\mathrm{K}$. The top-gate voltage V^*_{TG} is subdivided into regions in which certain charge carrier systems contribute to transport. These regions are: n-bulk states, TSS,I and TSS,II (marked in yellow), TSS,I and TSS,II (marked in red), and p-type VPS, TSS,I and TSS,II (marked in gray). Between the red and gray region is the region where holes are introduced into the system.

resistance signal decreases significantly as a result of possible inter-scattering. By populating the n-bulk states, a smaller non-local signal is likewise obtained due to the addition of an unpolarized electron background. However, a distinct difference can be recognized regarding the strength of the non-local resistance signal. While the extreme value of R_{nl} for the H-bar structure having a connecting piece length of 0.5 µm reaches about $-3.9\,\Omega$, the extremum for the H-bar with the 1 µm connecting piece approaches only approximately $-0.6\,\Omega$. Hence, as expected, the larger structure possesses a weaker non-local resistance signal due to a stronger relaxation of electron spins over the extent of the connecting piece.

Without magnetic perturbation [68, 98], the topological surface states are protected by time-reversal symmetry (TRS), which causes backscattering to be forbidden [99]. However, in the presence of an external magnetic field B, the time-reversal symmetry will be broken [100], allowing backscattering in the TSSs [101, 102]. The possibility of backscattering leads to a reduction in the magnitude of the current-induced spin polarization of the topological surface states. In addition, according to Ref. [103], the spin-momentum locking in the TSSs of a three-dimensional topological insulator can be cancelled when the TRS is broken. This would also result in a decreased current-induced spin polarization. Thus, we expect a decrease in net spin polarization and, consequently, a smaller non-local resistance signal $|R_{\mathrm{nl}}|$ when an external magnetic field B is applied to our H-bar structures. To verify this assumption, the non-local resistance signal of sample Q2982 spindetection II was examined regarding its

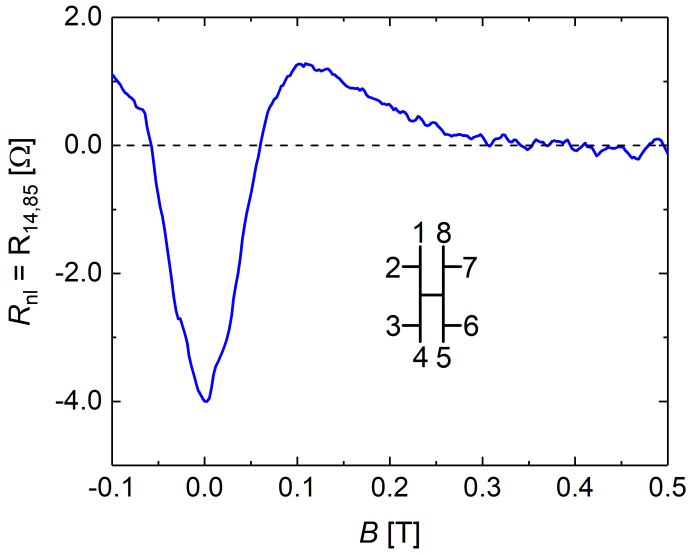

Figure 7.10.: Non-local resistance signal R_{nl} of sample Q2982 spindetection II (0.5 µm long connecting piece) as a function of magnetic field B at applied top-gate voltage $V_{\mathrm{TG}}^{*} = 0.2\,\mathrm{V}$. $R_{\mathrm{nl}} = 0$ is shown as a black dashed line. The inset depicts the measurement configuration.

magnetic field dependence. In order to obtain the most pronounced non-local signal, V_{TG}^{*} was set to 0.2 V, since the maximal $|R_{\mathrm{nl}}|$ can be detected at this top-gate voltage (cf. Fig. 7.7). The result is presented in Fig. 7.10. One is able to observed that the non-local resistance signal $|R_{\mathrm{nl}}|$ decreases strongly with increasing magnetic field $|B| > 0$. At a magnetic field of about $\pm 60\,\mathrm{mT}$, the non-local signal becomes zero. Hence, as assumed, an externally applied magnetic field reduces the magnitude of the current-induced spin polarization, causing a significant decrease in $|R_{\mathrm{nl}}|$. However, the non-local resistance signal does not remain zero but increases with increasing field until a positive maximum is formed. We find that the position of this maximum is approximately at $B \approx 0.1\,\mathrm{T}$. At even stronger magnetic fields, R_{nl} approaches zero again. For $B \gtrsim 0.3\,\mathrm{T}$, no non-local signal is detectable anymore. A possible explanation for the occurrence of the positive maximum might be given by geometrical effects. It has been shown that in a ballistic narrow-channel multiprobe conductor penetrated by a weak perpendicular magnetic field, so-called bend resistances, which are associated with current passing around the corner at a junction, can be observed [104]. By a similar effect, in the presence of a weak magnetic field B, electrons may pass from the current-carrying leg of a H-bar structure through the connecting piece into the detection leg, affecting the measured non-local resistance signal. In order to resolve the underlying mechanism causing this phenomenon, future studies may require the consideration of various sample geometries and computationally intensive simulations.

The investigations of temperature dependence, dependence on the length of the connect-

ing piece, and magnetic field dependence of the non-local resistance signal support our assumption that a current-induced spin polarization of the topological surface states, which is generated by electrons in these states obeying spin-momentum locking, is responsible for the experimentally observed R_{nl}. Thus, in the three-dimensional case, the non-local voltage is caused by a surface effect. In contrast, the intrinsic spin Hall effect creating the non-local resistance signal in the 2D case is a bulk effect: By applying an increasingly negative top-gate voltage, the Fermi level is gated deeper and deeper into the valence band, resulting in a strong enlargement in spin-orbit splitting. The magnitude of the non-local signal ultimately depends on the difference in the populations of the two spin-orbit split subbands [88].

In this chapter, spin-associated transport phenomena of three-dimensional HgTe-based topological insulators were investigated using microscopic H-bar devices. Based on top-gate voltage-dependent, temperature-dependent, and magnetic field-dependent measurements as well as by utilizing H-bar structures of different sizes, we were able to demonstrate that a current-induced spin polarization of the two topological surface states is responsible for the occurrence of non-local signals. It was found that this spin polarization is generated by the spin-momentum locking to which the electrons in the TSSs are subjected and can be transferred from the current-carrying to the detection leg by means of a spin current passing through the short connecting piece in between. In the detection leg, the imposed spin polarization induces a charge current, leading to the non-local signal.

In addition, it could be shown that in our proposed mechanism, neither n-type bulk states nor p-type Volkov-Pankratov states provide a detectable contribution to the non-local signal. On the contrary, the population of these massive states resulted in a decrease of the non-local voltage due to the addition of a large unpolarized electron background and the possible inter-scattering between n-type TSSs and p-type VPSs. Thus, we were able to determine a clear distinction between 3D and 2D HgTe-based H-bar samples regarding the origin of the observed non-local signals. In three-dimensional H-bar structures, the non-local signal is caused by a surface effect. In two-dimensional devices, however, this signal is generated by the intrinsic spin Hall effect being a result of the difference in population of the valence band spin-orbit subbands and therefore by a bulk effect.

8. Summary

The subject of this thesis is the investigation of the transport properties of topological and massive surface states in the three-dimensional topological insulator Hg(Mn)Te. These surface states give rise to a variety of extraordinary transport phenomena, making this material system of great interest for research and technological applications. In this connection, many physical properties of the topological insulator Hg(Mn)Te still require in-depth exploration. The overall aim of this thesis is to analyze the quantum transport of HgTe-based devices ranging from hundreds of micrometers (macroscopic) down to a few micrometers in size (microscopic) in order to extend the overall understanding of surface states and the possibilities of their manipulation.

In order to exploit the full potential of our high-quality heterostructures, it was necessary to revise and improve the existing lithographic fabrication process of macroscopic three-dimensional Hg(Mn)Te samples. A novel lithographic standard recipe for the fabrication of the HgTe-based macrostructures was developed. This recipe includes the use of an optimized Hall bar design and wet etching instead of etching with high-energy Ar^+-ions, which can damage the samples. Further, a hafnium oxide insulator is applied replacing the SiO_2/Si_3N_4 dielectric in order to reduce thermal load. Moreover, the devices are metallized under an alternating angle to avoid discontinuities of the metal layers over the mesa edges. It was revealed that the application of gate-dielectric and top-gate metals results in n-type doping of the devices. This phenomenon could be attributed to quasi-free electrons tunneling from the trap states, which form at the interface cap layer/insulator, through the cap into the active layer. This finding led to the development of a new procedure to characterize wafer materials. It was found that the optimized lithographic processing steps do not unintentionally react chemically with our heterostructures, thus avoiding a degradation of the quality of the Hg(Mn)Te layer. The implementation of new contact structures Ti/Au, In/Ti/Au, and Al/Ti/Au did not result in any improvement compared to the standard structure AuGe/Au. However, a novel sample recipe could be developed, resulting in an intermixing of the contact metals (AuGe and Au) and fingering of metal into the mesa. The extent of the quality of the ohmic contacts obtained through this process has yet to be fully established.

This thesis further deals with the lithographic realization of three-dimensional HgTe-based microstructures measuring only a few micrometer in size. Thus, these structures are in the order of the mean free path and the spin relaxation length of topological surface state electrons. A lithographic process was developed enabling the fabrication of nearly any desired

microscopic device structure. In this context, two techniques suitable for etching microscopic samples were realized, namely wet etching and the newly established inductively coupled plasma etching. While wet etching was found to preserve the crystal quality of the active layer best, inductively coupled plasma etching is characterized by high reproducibility and excellent structural fidelity. Hence, the etching technique employed depends on the envisaged type of experiment.

Magneto-transport measurements were carried out on the macroscopic HgTe-based devices fabricated by means of improved lithographic processing with respect to the transport properties of topological and massive surface states. It was revealed that due to the low charge carrier density present in the leads to the ohmic contacts, these regions can exhibit an insulating behavior at high magnetic fields and extremely low temperatures. As soon as the filling factor of the lowest Landau levels dropped below a critical value ($\nu_c \approx 0.8$), the conductance of the leads decreased significantly. It was demonstrated that the carrier density in the leads can be increased by the growth of modulation doping layers, a back-gate-electrode, light-emitting diode illumination, and by the application of an overlapping top-gate layout. This overlapping top-gate and a back-gate made it possible to manipulate the carrier density of the surface states on both sides of the Hg(Mn)Te layer independently. With this setup, it was identified that topological and massive surface states contribute to transport simultaneously in 3D Hg(Mn)Te. A model could be developed allowing the charge carrier systems populated in the sample to be determined unambiguously. Based on this model, the process of the re-entrant quantum Hall effect observed for the first time in three-dimensional topological insulators could be explained by an interplay of n-type topological and p-type massive surface states. A well-pronounced $\nu = -1 \rightarrow \nu = -2 \rightarrow \nu = -1$ sequence of quantum Hall plateaus was found in manganese-doped HgTe-based samples. It is postulated that this is the condensed-matter realization of the parity anomaly in three-dimensional topological insulators. The actual nature of this phenomenon can be the subject of further research. In addition, the measurements have shown that inter-scattering occurs between counter-propagating quantum Hall edge states. The good quantization of the Hall conductance despite this inter-scattering indicates that only the unpaired edge states determine the transport properties of the system as a whole. The underlying inter-scattering mechanism is the topic of a publication in preparation.

Furthermore, three-dimensional HgTe-based microstructures shaped like the capital letter "H" were investigated regarding spin transport phenomena. The non-local voltage signals occurring in the measurements could be attributed to a current-induced spin polarization of the topological surface states due to electrons obeying spin-momentum locking. It was shown that the strength of this non-local signal is directly connected to the magnitude of the spin polarization and can be manipulated by the applied top-gate voltage. It was found that in these microstructures, the massive surface and bulk states, unlike the topological

surface states, cannot contribute to this spin-associated phenomenon. On the contrary, it was demonstrated that the population of massive states results in a reduction of the spin polarization, either due to the possible inter-scattering of massive and topological surface states or due to the addition of an unpolarized electron background. The evidence of spin transport controllable by a top-gate-electrode makes the three-dimensional material system mercury telluride a promising candidate for further research in the field of spintronics.

Zusammenfassung

Die vorliegende Dissertation beschäftigt sich mit der Untersuchung der Transporteigenschaften von topologischen und massiven Oberflächenzuständen in dem dreidimensionalen topologischen Isolator Hg(Mn)Te. Da diese Oberflächenzustände zu einer Vielzahl von außergewöhnlichen Transportphänomenen führen, ist dieses Materialsystem für die Grundlagenforschung und technologische Anwendungen von großem Interesse. Der Bereich der dreidimensionalen topologischen Isolatoren stellt ein relativ junges Forschungsgebiet dar. Daher bedürfen noch viele physikalische Eigenschaften des topologischen Isolators Hg(Mn)Te ein tiefergehendes Verständnis. Das übergeordnete Ziel dieser Arbeit ist die Analyse des Quantentransports von HgTe-basierten Proben, deren Abmessungen von mehreren hundert Mikrometern (makroskopisch) bis hin zu wenigen Mikrometern (mikroskopisch) reichen. Auf diese Weise soll das allgemeine Verständnis der Oberflächenzustände und die Möglichkeiten ihrer Manipulation erweitert werden.

Um das volle Potential unserer hochqualitativen Heterostrukturen, welche durch Molekularstrahlepitaxie gewachsen werden, ausschöpfen zu können, musste das bestehende lithographische Herstellungsverfahren für makroskopische dreidimensionale Hg(Mn)Te-Proben überarbeitet und verbessert werden. Es konnte ein neuartiges lithographisches Standardrezept für die Herstellung von HgTe-basierten Makrostrukturen entwickelt werden. Dieses Rezept beinhaltet die Verwendung eines optimierten Probendesigns und verwendet nasschemisches Ätzen anstelle von Ätzen mit hochenergetischen Ar^+-Ionen, welches die Proben beschädigen kann. Außerdem wird ein Isolator aus Hafniumoxid verwendet, der das SiO_2/Si_3N_4-Dielektrikum ersetzt, um die thermische Belastung der Proben zu verringern. Darüber hinaus werden die Proben unter einem veränderlichen Winkel metallisiert, um Diskontinuitäten der Metallschichten entlang der Ränder der Mesa zu vermeiden. Es zeigte sich, dass das Aufbringen des Isolators und der Feldeffektelektrode zu einer Erhöhung der Elektronendichte in der Hg(Mn)Te-Schicht führt. Dieses Phänomen konnte darauf zurückgeführt werden, dass quasifreie Elektronen aus sogenannten Fallenzuständen, welche sich an der Grenzfläche zwischen der $Cd_{0.7}Hg_{0.3}Te$ Deckschicht und dem Dielektrikum bilden, durch die Deckschicht in die aktive Schicht tunneln können. Dieser neue Einblick führte zu der Entwicklung einer neuen Prozedur zur Charakterisierung von Wafermaterialien. Es stellte sich heraus, dass die optimierten lithographischen Prozessschritte nicht unbeabsichtigt mit unseren Heterostrukturen chemisch reagieren, was eine Verringerung der Qualität der Hg(Mn)Te-Schicht verhindert. Die Implementierung der neuen Kontaktstrukturen Ti/Au, In/Ti/Au und Al/Ti/Au führ-

te zu keiner Verbesserung im Vergleich zur Standardstruktur AuGe/Au. Es konnte jedoch ein neuartiges Probenrezept entwickelt werden, dessen Anwendung zu einer Vermischung der Kontaktmetalle (AuGe und Au) und zu einem Eindiffundieren von Metall in die Mesa führt. Das Ausmaß der Qualität der ohmschen Kontakte, welche durch dieses Verfahren erhalten werden, muss noch vollständig ermittelt werden.

Zudem befasst sich diese Dissertation mit der lithographischen Realisierung dreidimensionaler HgTe-basierter Mikrostrukturen, die nur wenige Mikrometer groß sind. Somit liegen diese Strukturen in der Größenordnung der mittleren freien Weglänge und der Spinrelaxationslänge von Elektronen, welche sich in den topologischen Oberflächenzuständen befinden. Es wurde ein lithographischer Prozess entwickelt, der die Herstellung nahezu jeder gewünschten mikroskopischen Struktur ermöglicht. In diesem Zusammenhang wurden zwei für das Ätzen mikroskopischer Proben geeignete Techniken vorgestellt, nämlich nasschemisches Ätzen mit einer flüssigen KI:I_2:HBr Lösung und das Ätzen unter Verwendung eines induktiv gekoppelten Methan-Plasmas. Während nasschemisches Ätzen die Kristallqualität der Hg(Mn)Te-Schicht am besten erhält, zeichnet sich das Plasmaätzen durch eine hohe Reproduzierbarkeit und ausgezeichnete Strukturtreue aus. Die Wahl der zu bevorzugenden Ätztechnik hängt daher von der Art des geplanten Experiments ab.

An den makroskopischen Bauelementen auf HgTe-Basis, welche durch Anwendung der verbesserten lithographischen Prozessierung hergestellt wurden, wurden magnetfeldabhängige Transportmessungen hinsichtlich der Transporteigenschaften von topologischen und massiven Oberflächenzuständen durchgeführt. Es zeigte sich, dass die Zuleitungen zu den ohmschen Kontakten bei hohen Magnetfeldern ($B > 4\,\mathrm{T}$) und extrem tiefen Temperaturen ($T \ll 1\,\mathrm{K}$) ein isolierendes Verhalten aufweisen können. Eine geringe Ladungsträgerdichte in diesen Bereichen wurde als Ursache identifiziert. Sobald der Füllfaktor der untersten Landau-Niveaus unter einen kritischen Wert fiel, nahm die Leitfähigkeit der Zuleitungen deutlich ab. Es wurde festgestellt, dass der Betrag dieses kritischen Füllfaktors für alle untersuchten Proben ungefähr 0,8 beträgt und unabhängig davon ist, ob die untersten Landau-Niveaus elektronen- oder lochartig sind. Darüber hinaus konnte gezeigt werden, dass die Ladungsträgerdichte in den Zuleitungen durch das Wachstum von Modulationsdotierschichten, eine unterhalb des Bauelements angeordnete Feldeffektelektrode, die Bestrahlung mit einer Leuchtdiode und das Aufbringen einer mit den ohmschen Kontakten überlappenden Feldeffektelektrode erhöht werden kann. Diese beiden Feldeffektelektroden, welche sich unter- und oberhalb der Heterostruktur befinden, ermöglichten es die Ladungsträgerdichte der Oberflächenzustände auf beiden Seiten der Hg(Mn)Te-Schicht unabhängig voneinander zu manipulieren. Mit diesem Aufbau wurde festgestellt, dass topologische und massive Oberflächenzustände gleichzeitig zum Transport in 3D Hg(Mn)Te beitragen. Es konnte ein Modell entwickelt werden, welches die eindeutige Bestimmung der in der Probe besetzten Ladungsträgersysteme ermöglicht. Auf der Grundlage dieses Modells konnte ein magnetfeldabhängiger Prozess, welcher sich durch

wiedereinkehrende Plateaus im Rahmen des Quanten-Hall-Effekts auszeichnet, erklärt werden. Dieser erstmals in dreidimensionalen topologischen Isolatoren beobachtete Prozess ist das Resultat des Zusammenspiels von zwei elektronenartigen topologischen Oberflächenzuständen und einem lochartigen massiven Oberflächenzustand. Eine besonders deutlich ausgeprägte $\nu = -1 \rightarrow \nu = -2 \rightarrow \nu = -1$ Abfolge von Plateaus konnte in mit Mangan dotierten dreidimensionalen HgTe-basierten topologischen Isolatoren gefunden werden. Es wird postuliert, dass es sich dabei um die Realisierung der Paritätsanomalie in kondensierter Materie handelt. Die tatsächliche Natur dieses Phänomens kann Gegenstand weiterer Forschung sein. Darüber hinaus haben die Messungen gezeigt, dass entgegengesetzt verlaufende elektronen- und lochartige Randzustände miteinander streuen. Die gute Quantisierung der Hall-Leitfähigkeit, welche ungeachtet dieser Streuung beobachtet werden kann, deutet darauf hin, dass nur die ungepaarten Randzustände die Transporteigenschaften des Gesamtsystems bestimmen. Der zugrundeliegende Streumechanismus ist das Thema einer Publikation, welche sich in der Vorbereitung befindet.

Des Weiteren wurden dreidimensionale HgTe-basierte Mikrostrukturen, die wie der Großbuchstabe "H" geformt sind, hinsichtlich Spintransportphänomene untersucht. Die bei den Messungen auftretenden nichtlokalen Spannungssignale konnten auf eine strominduzierte Spinpolarisation der topologischen Oberflächenzustände zurückgeführt werden. Ursache für diese strominduzierte Spinpolarisation ist die starke Kopplung des Elektronenspins an den Elektronenimpuls. Es wurde gezeigt, dass die Intensität dieses nichtlokalen Signals direkt mit der Stärke der Spinpolarisation zusammenhängt und durch eine Feldeffektelektrode manipuliert werden kann. Es wurde festgestellt, dass in diesen Mikrostrukturen die massiven Oberflächen- und Bulkzustände, im Gegensatz zu den topologischen Oberflächenzuständen, nicht zu diesem mit dem Spin assoziierten Phänomen beitragen können. Es wurde im Gegenteil gezeigt, dass eine Besetzung der massiven Zustände zu einer Verringerung der Spinpolarisation führt. Die verantwortlichen Mechanismen sind das Streuen von massiven und topologischen Oberflächenzuständen und das Hinzufügung eines großen Hintergrunds an unpolarisierten Elektronen. Der Nachweis des durch eine Feldeffektelektrode kontrollierbaren Spintransports macht das dreidimensionale Materialsystem Quecksilbertellurid zu einem vielversprechenden Kandidaten für weitere Forschungen auf dem Gebiet der Spintronik.

Bibliography

[1] W. S. Boyle and G. E. Smith: *Charge Coupled Semiconductor Devices*, Bell System Technical Journal, **49**(4), 587-593 (1970).

[2] V. Lathinen and J. Pachos: *A Short Introduction to Topological Quantum Computation*, SciPost Physics, **3**, 021 (2017).

[3] J. Wiedenmann, E. Bocquillon, R. S. Deacon, S. Hartinger, O. Herrmann, T. M. Klapwijk, L. Maier, C. Ames, C. Brüne, C. Gould, A. Oiwa, K. Ishibashi, S. Tarucha, H. Buhmann, and L. W. Molenkamp: *4π-periodic Josephson supercurrent in HgTe-based topological Josephson junctions*, Nature Communications, **7**, 10303 (2016).

[4] D. E. Kharzeev and Q. Li: *The Chiral Qubit: quantum computing with chiral anomaly*, arXiv:1903.07133 [quant-ph] (2019).

[5] O. Vafek and A. Vishwanath: *Dirac Ferminons in Solids: From High-T_c Cuprates and Graphene to Topological Insulators and Weyl Semimetals*, Annual Review of Condensed Matter Physics, **5**, 83-112 (2014).

[6] C. L. Kane and E. J. Mele: *Quantum Spin Hall Effect in Graphene*, Physical Review Letters, **95**, 226801 (2005).

[7] M. König, S. Wiedmann, C. Brüne, A. Roth, H. Buhmann, L. W. Molenkamp, X. L. Qi, and S. C. Zhang: *Quantum Spin Hall Insulator State in HgTe Quantum Wells*, Science, **318**(5851), 766-770 (2007).

[8] D. Hsieh, D. Qian, L. Wary, Y. Xia, Y. S. Hor, R. J. Cava, and M. Z. Hasan: *A topological Dirac insulator in a quantum spin Hall phase*, Nature, **452**, 970-974 (2008).

[9] C. Brüne, C. X. Liu, E. G. Novik, E. M. Hankiewicz, H. Buhmann, Y. L. Chen, X. L. Qi, Z. X. Shen, S. C. Zhang, and L. W. Molenkamp: *Quantum Hall Effect from the Topological Surface States of Strained Bulk HgTe*, Physical Review Letters, **106**, 126803 (2011).

[10] B. A. Volkov and O. A. Pankratov: *Two-dimensional massless electrons in an inverted contact*, Journal of Experimental and Theoretical Physics Letters, **42**, 178-181 (1985).

[11] L. Fu and C. L. Kane: *Superconducting Proximity Effect and Majorana Fermions at the Surface of a Topological Insulator*, Physical Review Letters, **100**, 096407 (2008).

[12] M. O. Goerbig: *Quantum Hall Effects*, arXiv:0909.1998 [cond-mat.mes-hall] (2009).

[13] C. Liu, X. Qi, X. Dai, Z. Fang, and S. Zhang: *Quantum Anomalous Hall Effect in $Hg_{1-y}Mn_yTe$ Quantum Wells*, Physical Review Letters, **101**, 146802 (2008).

[14] M. K. Bendias: *Quantum Spin Hall Effect - A new generation of microstructures*, doctoral thesis, Julius-Maximilians-Universität Würzburg (2017).

[15] L. Wang, F. Schmitt, W. Beugeling, L. Lunczer, J. Mayer, H. Buhmann, E. Hankiewicz, and L. W. Molenkamp: *Parity anomaly, spectral asymmetry and reentrant quantum Hall effect in a topological insulator*, Manuscript in preparation (2021).

[16] J. K. Furdyna: *Electrical, optical, and magnetic properties of $Hg_{1-x}Mn_xTe$*, Journal of Vacuum Science and Technology, **21**, 220 (1982).

[17] J. Chu and A. Sher: *Physics and Properties of Narrow Gap Semiconductors*, Springer-Verlag New York, 1st edition (2008).

[18] M. Regnet: *Hochauflösende Röntgenbeugung zur Charakterisierung gestörter Heterostrukturen auf der Basis von II-VI-Halbleitermaterialien*, doctoral thesis, Julius-Maximilians-Universität Würzburg (1993).

[19] J. Ruan, S. Jian, H. Yao, H. Zhang, S. Zhang, and D. Xing: *Symmetry-protected ideal Weyl semimetal in HgTe-class materials*, Nature Communications, **7**, 11136 (2016).

[20] L. Voon and M. Willatzen: *The k·p Method - Electronic Properties of Semiconductors*, Springer-Verlag Berlin Heidelberg, 1st edition (2009).

[21] E. O. Kane: *Band structure of indium antimonide*, Journal of Physics and Chemistry of Solids, **1**(4), 249-261 (1957).

[22] D. J. Chadi, J. P. Walter, M. L. Cohen, Y. Petroff, and M. Balkanski: *Reflectivities and Electronic Band Structures of CdTe and HgTe*, Physical Review B, **5**, 3058 (1972).

[23] M. Stuiber: *Dreidimensionale Topologische Isolatoren*, master's thesis, Julius-Maximilians-Universität Würzburg (2011).

[24] L. Fu, C. L. Kane, and E. J. Mele: *Topological Insulators in Three Dimensions*, Physical Review Letters, **98**, 106803 (2007).

[25] L. Fu and C. L. Kane: *Topological insulators with inversion symmetry*, Physical Review B, **76**, 045302 (2007).

[26] P. Capper: *Properties of Narrow Gap Cadmium-based Compounds*, INSPEC, the Institution of Electrical Engineers, London (1994).

[27] C. Thienel: *Exploring the transport properties of the three-dimensional topological insulator material HgTe*, doctoral thesis, Julius-Maximilians-Universität Würzburg (2014).

[28] I. M. Tsidilkovski, G. I. Harus, and N. G. Shelushinina: *Impurity states and electron transport in gapless semiconductors*, Advances in Physics, **34**(1), 43-174 (1985).

[29] R. Schlereth: *New techniques and imrpovements in the MBE growth of Hg-containing narrow gap semiconductors*, doctoral thesis, Julius-Maximilians-Universität Würzburg (2019).

[30] J. Moore: *Topological insulators: The next generation*, Nature Physics, **5**(6), 378-380 (2009).

[31] C. Liu, G. Bian, T. Chang, K. Wang, S. Xu, I. Belopolski, I. Miotkowski, H. Cao, K. Miyamoto, C. Xu, C. Matt, T. Schmitt, N. Alidoust, M. Neupane, H. Jeng, H. Lin, A. Bansil, V. Strocov, M. Bissen, A. Fedorov, X. Xiao, T. Okuda, Y. Chen, and M. Hasan: *Tunable spin helical Dirac quasiparticles on the surface of three-dimensional HgTe*, Physical Review B, **92**, 115436 (2015).

[32] D. Mahler, J. Mayer, P. Leubner, L. Lunczer, D. Di Sante, G. Sangiovanni, R. Thomale, E. M. Hankiewicz, H. Buhmann, C. Gould, and L. W. Molenkamp: *Interplay of Dirac Nodes and Volkov-Pankratov Surface States in Compressively Strained HgTe*, Physical Review X, **9**, 031034 (2019).

[33] S. Tchoumakov, V. Jouffrey, A. Inhofer, E. Bocquillon, B. Placais, D. Carpentier, and M. Goerbig: *Volkov-Pankratov states in topological heterojunctions*, Physical Review B, **96**, 201302(R) (2017).

[34] A. Inhofer, S. Tchoumakov, B. Assaf, G. Feve, J. Berroir, V. Jouffrey, D. Carpentier, M. Goerbig, B. Placais, K. Benidas, D. Mahler, E. Bocquillon, R. Schlereth, C. Brüne, H. Buhmann, and L. W. Molenkamp: *Observation of Volkov-Pankratov states in topological HgTe heterojunctions using high-frequency compressibility*, Physical Review B, **96**, 195104 (2017).

[35] D. Mahler: *Surface states in the topological material HgTe*, doctoral thesis, Julius-Maximilians-Universität Würzburg (2021).

[36] C. W. J. Beenakker and H. v. Houten: *Quantum Transport in Semiconductor Nanostructures*, Solid State Physics, **44**, 1-228 (1991).

[37] K. v. Klitzing, R. Gerhardts, and J. Weis: *25 Jahre Quanten-Hall-Effekt*, Physik Journal, **4**(6), 37-44 (2005).

[38] L. Ghenim, R. G. Mani, J. R. Anderson, and J. T. Cheung: *Shubnikov-de Haas oscillations in HgTe/CdTe superlattices grown by laser molecular-beam epitaxy*, Physical Review B, **39**(2), 1419-1421 (1989).

[39] J. Analytis, R. McDonald, S. Riggs, J. Chu, G. Boebinger, and I. Fisher: *Two-dimensional surface state in the quantum limit of a topological insulator*, Nature Physics, **6**, 960-964 (2010).

[40] M. Willatzen, M. Cardona, and N. E. Christensen: *Spin-orbit coupling parameters and electron g factor of II-VI zinc-blende materials*, Physical Review B, **51**(24), 17992-17994 (1995).

[41] B. Büttner, C. X. Liu, G. Tkachov, E. G. Novik, C. Brüne, H. Buhmann, E. M. Hankiewicz, P. Recher, B. Trauzettel, S. C. Zhang, and L. W. Molenkamp: *Single valley Dirac ferminons in zero-gap HgTe quantum wells*, Nature Physics, **7**, 418-422 (2011).

[42] P. Leubner, L. Lunczer, C. Brüne, H. Buhmann, and L. W. Molenkamp: *Strain Engineering of the Band Gap of HgTe Quantum Wells Using Superlattice Virtual Substrates*, Physical Review Letters, **117**, 086403 (2016).

[43] M. Kessel: *HgTe-CdTe Heterostrukturen verschiedener Dimensionalität und Topologie*, master's thesis, Julius-Maximilians-Universität Würzburg (2012).

[44] J. J. Dubowski, T. Dietl, W. Szymanska, and R. R. Galazka: *Electron scattering in $Cd_xHg_{1-x}Te$*, Journal of Physics and Chemistry of Solids, **42**(5), 351-362 (1981).

[45] C. Brüne, C. Thienel, M. Stuiber, J. Böttcher, H. Buhmann, E. Novik, C. Liu, E. M. Hankiewicz, and L. W. Molenkamp: *Dirac-Screening Stabilized Surface-State Transport in a Topological Insulator*, Physical Review X, **4**, 041045 (2014).

[46] X. Lu and M. Goerbig: *Magneto-optical signatures of Volkov-Pankratov states in topological insulators*, Europhysics Letters, **126**(6), 67004 (2019).

[47] C. Liu, F. Wei, K. Premasiri, S. Liu, S. Ma, Z. Zhang, and X. Gao: *Non-Drude Magneto-Transport Behavior in a Topological Crystalline Insulator/Band Insulator Heterostructure*, Nano Letters, **18**(10), 6538-6543 (2018).

[48] D. Mahler, V. Müller, C. Thienel, J. Wiedenmann, W. Beugeling, H. Buhmann, and L. W. Molenkamp: *Massive and Topological Surface States in Tensile-Strained HgTe*, Nano Letters, **21**(23), 9869-9874 (2021).

[49] L. J. v. d. Pauw: *A Method of Measuring the Resistivity and Hall Coefficient on Lamellae of Arbitrary Shape*, Philips Technical Review, **20**, 220-224 (1958).

[50] P. M. Hemenger: *Measurement of High Resistivity Semiconductors Using the van der Pauw Method*, Review of Scientific Instruments, **44**(6), 698-700 (1973).

[51] J. L. Elkind: *Ion mill damage in n-HgCdTe*, Journal of Vacuum Science & Technology B, **10**, 1460 (1992).

[52] E. Belas, P. Höschl, R. Grill, J. Franc, P. Moravec, K. Lischka, H. Sitter, and A. Toth: *Ultrafast diffusion of Hg in $Hg_{1-x}Cd_xTe$ ($x \approx 0.21$)*, Journal of Crystal Growth, **138**, 940-943 (1994).

[53] P. W. Leech, P. J. Gwynn, and M. H. Kibel: *A selective etchant for $Hg_{1-x}Cd_xTe$, CdTe and HgTe on GaAs*, Applied Surface Science, **37**(3), 291-298 (1989).

[54] P. W. Leech, M. H. Kibel, and P. J. Gwynn: *The Chemical Etching of II-VI/GaAs Heterostructures in Aqueous I:KI:HBr Solutions*, Journal of The Electrochemical Society, **137**(2), 705 (1990).

[55] R. Tenne, R. Brener, and R. Triboulet: *Chemical modifications of $Hg_{0.1}Cd_{0.9}Te$ surfaces: Analysis with Auger electron spectroscopy*, Journal of Vacuum Science & Technology A, **7**, 2570 (1989).

[56] H. K. Kuiken, J. J. Kelly, and P. H. Notten: *Etching Profiles at Resist Edges: I. Mathematical Models for Diffusion-Controlled Cases*, Journal of The Electrochemical Society, **133**(6), 1217 (1986).

[57] V. Müller: *Transport signatures of topological and trivial states in the three-dimensional topological insulator HgTe*, doctoral thesis, Julius-Maximilians-Universität Würzburg (2021).

[58] P. Capper and J. W. Garland: *Mercury Cadmium Telluride: Growth, Properties and Applications*, John Wiley & Sons Ltd, United Kingdom, 1st edition (2011).

[59] G. Davis, W. Beck, M. Kelly, N. Tache, and G. Margaritondo: *Deposition of the unreactive metal Au onto sputtered and cleaved $Hg_{1-x}Cd_xTe$ surfaces*, Journal of Applied Physics, **60**, 3157-3161 (1986).

[60] A. Ciani, S. Ogut, I. Batra, and S. Sivananthan: *Diffusion of gold and native defects in mercury cadmium telluride*, Journal of Electronic Materials, **34**, 868-872 (2005).

[61] R. Wirth: *Focused Ion Beam (FIB): A novel technology for advanced application of micro- and nanoanalysis in geosciences and applied mineralogy*, European Journal of Mineralogy, **16**(6), 863-876 (2004).

[62] Z. Huang, T. Feuchtwang, P. Cutler, and E. Kazes: *Wentzel-Kramers-Brillouin method in multidimensional tunneling*, Physical Review A, **41**(1), 32-41 (1990).

[63] J. Hinz: *Rashba-Effekt in II-VI-Halbleiterheterostrukturen*, master's thesis, Julius-Maximilians-Universität Würzburg (2005).

[64] C. Ames: *Molecular Beam Epitaxy of 2D and 3D HgTe, a Topological Insulator*, doctoral thesis, Julius-Maximilians-Universität Würzburg (2015).

[65] N. Braslau, J. B. Gunn, and J. L. Staples: *Metal-semiconductor contacts for GaAs bulk effect devices*, Solid-State Electronics, **10**(5), 381-383 (1967).

[66] S. Datta: *Electronic Transport in Mesoscopic Systems*, Cambridge University Press, United Kingdom, 1st edition (1995).

[67] F. D. M. Haldane: *Model for a Quantum Hall Effect without Landau Levels: Condensed-Matter Realization of the "Parity Anomaly"*, Physical Review Letters, **61**(18), 2015-2018 (1988).

[68] Y. Xu, I. Mitokowski, C. Liu, J. Tian, H. Nam, N. Alidoust, J. Hu, C. Shih, M. Z. Hasan, and Y. P. Chen: *Observation of topological surface state quantum Hall effect in an intrinsic three-dimensional topological insulator*, Nature Physics, **10**, 956-963 (2014).

[69] D. V. Khveshchenko: *Magnetic-Field-Induced Insulating Behavior in Highly Oriented Pyrolitic Graphite*, Physical Review Letters, **87**, 206401 (2001).

[70] L. Jing, J. Velasco Jr., P. Kratz, G. Liu, W. Bao, M. Bockrath, and C. N. Lau: *Quantum Transport and Field-Induced Insulating States in Bilayer Graphene pnp Junctions*, Nano Letters, **10**(10), 4000-4004 (2010).

[71] A. Shuvaev, G. Astakhov, C. Brüne, H. Buhmann, L. W. Molenkamp, and A. Pimenov: *Terahertz magneto-optical spectroscopy in HgTe thin films*, Semiconductor Science and Technology, **27**(12), 124004 (2012).

[72] T. Ihn: *Semiconductor Nanostructures: Quantum States and Electronic Transport*, Oxford University Press, New York, 1st edition (2010).

[73] M. Dittmar: *Lichtinduzierte Ladungsträger in HgTe-Quantentrog-Strukturen*, bachelor's thesis, Julius-Maximilians-Universität Würzburg (2020).

[74] M. Dyakonov, A. Efros, and D. Mitchell: *Magnetic Freeze-Out of Electrons in Extrinsic Semiconductors*, Physical Review, **180**(3), 813-818 (1969).

[75] A. Laszcz, A. Czerwinski, J. Ratajczak, A. Szerling, F. Phillipp, P. A. v. Aken, and J. Katcki: *Transmission electron microscopy characterization of Au/Pt/Ti/Pt/GaAs ohmic contacts for high power GaAs/InGaAs semiconductor lasers*, Journal of Microscopy, **237**(3), 347-351 (2010).

[76] M. Yakunin, S. Krishtopenko, W. Desrat, S. Podgornykh, M. Popov, V. Neverov, S. Dvoretsky, N. Mikhailov, F. Teppe, and B. Jouault: *Unconventional reentrant quantum Hall effect in a HgTe/CdHgTe double quantum well*, Physical Review B, **102**, 165305 (2020).

[77] S. Shamin, W. Beugeling, J. Böttcher, P. Shekhar, A. Budewitz, P. Leubner, L. Lunczer, E. M. Hankiewicz, H. Buhmann, and L. W. Molenkamp: *Emergent quantum Hall effects below 50 mT in a two-dimensional topological insulator*, Science Advances, **6**, 26 (2020).

[78] N. B. Brandt and V. V. Moshchalkov: *Semimagnetic semiconductors*, Advances in Physics, **33**(3), 193-256 (1984).

[79] C. Chang, J. Zhang, X. Feng, J. Shen, Z. Zhang, M. Guo, K. Li, Y. Ou, P. Wei, L. Wang, Z. Ji, Y. Feng, S. Ji, X. Chen, J. Jia, X. Dai, Z. Fang, S. Zhang, K. He, Y. Wang, L. Lu, X. Ma, and Q. Xue: *Experimental Observation of the Quantum Anomalous Hall Effect in a Magnetic Topological Insulator*, Science, **340**(6129), 167-170 (2013).

[80] C. Ma: *Parity Anomaly and Duality Web*, Fortschritte der Physik - Progress of Physics, **66**, 1800045 (2018).

[81] M. Büttiker: *Four-Terminal Phase-Coherent Conductance*, Physical Review Letters, **57**(14), 1761-1764 (1986).

[82] L. Wang, F. Schmitt, V. Müller, D. Mahler, L. Lunczer, W. Beugeling, H. Buhmann, and L. W. Molenkamp: *Selective equilibration of counter-propagating edge states in a topological insulator*, Manuscript in preparation (2021).

[83] A. Roth, C. Brüne, H. Buhmann, L. W. Molenkamp, J. Maciejko, X. Qi, and S. Zhang: *Nonlocal Transport in the Quantum Spin Hall State*, Science, **325**(5938), 294-297 (2009).

[84] B. A. Bernevig, T. Hughes, and S. Zhang: *Quantum Spin Hall Effect and Topological Phase Transition in HgTe Quantum Wells*, Science, **314**(5806), 1757-1761 (2006).

[85] J. Väyrynen, M. Goldstein, and L. Glazman: *Helical Edge Resistance Introduced by Charge Puddles*, Physical Review Letters, **110**, 216402 (2013).

[86] H. Liu, H. Jiang, Q. Sun, and X. C. Xie: *Dephasing Effect on Backscattering of Helical Surface States in 3D Topological Insulators*, Physical Review Letters, **113**, 046805 (2014).

[87] R. raimondi, C. Gorini, P. Schwab, and M. Dzierzawa: *Quasicalssical approach to the spin Hall effect in the two-dimensional electron gas*, Physical Review B, **74**, 035340 (2006).

[88] C. Brüne, A. Roth, E. G. Novik, M. König, H. Buhmann, E. M. Hankiewicz, W. Hanke, J. Sinova, and L. W. Molenkamp: *Evidence for the ballistic intrinsic spin Hall effect in HgTe nanostructrues*, Nature Physics, **6**, 448-454 (2010).

[89] L. Onsager: *Reciprocal Relations in Irreversible Processes. I.*, Physical Review, **37**(4), 405-426 (1931).

[90] P. Jacquod, R. S. Whitney, J. Meair, and M. Büttiker: *Onsager relations in coupled electric, thermoelectric, and spin transport: The tenfold way*, Physical Review B, **86**, 155118 (2012).

[91] F. Yang, S. Ghatak, A. Taskin, K. Segawa, Y. Ando, M. Shiraishi, Y. Kanai, K. Matsumoto, A. Rosch, and Y. Ando: *Switching of charge-current-induced spin polarization in the topological insulator $BiSbTeSe_2$*, Physical Review B, **94**, 075304 (2016).

[92] S. S. Pershoguba and V. M. Yakovenko: *Spin-polarized tunneling current through a thin film of a topological insulator in a parallel magnetic field*, Physical Review B, **86**, 165404 (2012).

[93] A. Kadykov, S. Krishtopenko, B. Jouault, W. Desrat, W. Knap, S. Ruffenach, C. Consejo, J. Torres, S. Morozov, N. Mikhailov, S. Dvoretskii, and F. Teppe: *Temperature-Induced Topological Phase Transition in HgTe Quantum Wells*, Physical Review B, **120**, 086401 (2018).

[94] D. Pesin and A. H. MacDonald: *Spintronics and pseudospintronics in graphene and topological insulators*, Nature Materials, **11**, 409-416 (2012).

[95] V. M. Edelstein: *Spin polarization of conduction electrons induced by electric current in two-dimensinoal asymmetric electron systems*, Solid State Communications, **73**(3), 233-235 (1990).

[96] C. H. Li, O. M. J. v. 't Erve, J. T. Robinson, Y. Liu, L. Li, and B. T. Jonker: *Electrical detection of charge-current-induced spin polarization due to spin-momentum locking in Bi_2Se_3*, Nature Nanotechnology, **9**, 218-224 (2014).

[97] J. Tang, L. Chang, X. Kou, K. Murata, E. S. Choi, M. Lang, Y. Fan, Y. Jiang, M. Montazeri, W. Jiang, Y. Wang, L. He, and K. L. Wang: *Electrical Detection of Spin-Polarized Surface States Conduction in $(Bi_{0.53}Sb_{0.47})_2Te_3$ Topological Insulator*, Nano Letters, **14**(9), 5423-5429 (2014).

[98] Y. Chen, J. Chu, J. Analytis, Z. Liu, K. Igarashi, H. Kuo, X. Qi, S. Mo, R. Moore, D. Lu, M. Hashimoto, T. Sasagawa, S. Zhang, I. Fisher, Z. Hussain, and Z. Shen: *Massive Dirac Fermion on the Surface of a Magnetically Doped Topological Insulator*, Science, **329**(5992), 659-662 (2010).

[99] W. Lee, C. Wu, D. Arovas, and S. Zhang: *Quasiparticle interference on the surface of the topological insulator Bi_2Te_3*, Physical Review B, **80**, 245439 (2009).

[100] C. Chang, P. Wei, and J. S. Moodera: *Breaking time reversal symmetry in topological insulators*, MRS Bulletin, **39**(10), 867-872 (2014).

[101] T. Zhang, P. Cheng, X. Chen, J. Jia, X. Ma, K. He, L. Wang, H. Zhang, X. Dai, Z. Fang, X. Xie, and Q. Xue: *Experimental Demonstration of Topological Surface States Protected by Time-Reversal Symmetry*, Physical Review Letters, **103**, 266803 (2009).

[102] S. Piatrusha, E. Tikhonov, Z. Kvon, N. Mikhailov, S. Dvoretsky, and V. Khrapai: *Topological Protection Brought to Light by the Time-Reversal Symmetry Breaking*, Physical Review Letters, **123**, 056801 (2019).

[103] M. Deng, R. Ma, W. Luo, R. Shen, L. Sheng, and D. Y. Xing: *Time-reversal invariant resonant backscattering on a topological insulator surface driven by a time-periodic gate voltage*, Scientific Reports, **8**, 12338 (2018).

[104] C. W. J. Beenakker and H. v. Houten: *Billiard model of a ballistic multiprobe conductor*, Physical Review Letters, **63**(17), 1857-1860 (1989).

Appendices

A. List of samples and wafer materials used in this thesis

The first section (Appx. A.1) of Appx. A lists all macroscopic and microscopic samples presented in this thesis. This excludes the devices investigated in Chap. 3 to explore the unintentional lithography-induced doping of our heterostructures. Since a total of 17 different wafer materials are considered in this chapter, each of which was used to build at least two samples, it is not meaningful to list all the devices fabricated for this project. Instead, Appx. A.2 simply provides the wafers examined and indicates how many samples were built of each material.

A.1. Details about the devices presented in this thesis

All samples displayed in this thesis are listed in Tab. A.1. The name of the device, the recipe used for fabrication, the sample design, the type of insulator applied, and whether the sample possesses a back-gate-electrode are specified. It is noted that details of the wafer materials used to build the devices listed in Tab. A.1 can be found in Appx. A.2.

sample name	used sample recipe	sample design	insulator type	back-gate
Q2982 II	Appx. B.2	macroscopic Hall bar	HfO_a	no
Q2982 spindetection II	Appx. C.2	microscopic H-bar with overlapping TG	HfO_a	no
QC0461 I	Appx. B.1	macroscopic Hall bar	HfO_a	yes
QC0464 OG I	Appx. B.4	macroscopic Hall bar with overlapping TG	HfO_a	yes
Q3097 II	Appx. B.5	macroscopic Hall bar	HfO_a	no
Q3097 VI	Appx. B.2	macroscopic Hall bar	HfO_a	no

Table A.1.: List of all devices presented in this thesis. The first component of the name always indicates the underlying wafer material. Unless otherwise specified, the samples possess a non-overlapping top-gate design.

A.2. Details about the wafer materials used to explore the lithography-induced increase of the n-type density

All wafers involved in the evaluations of chapter 3 are listed in Tab. A.2. It is noted that in addition to the devices featuring SiO_2/Si_3N_4 and HfO_a insulators, a reference specimen without top-gate-electrode was fabricated of each wafer material.

wafer	substrate	layer stack	layer thicknesses [nm]	SiO_2/Si_3N_4 insulator	HfO_a insulator
Q2843	GaAs	CMT/HgTe/CMT	100/60/100	1	1
Q2982	CdTe	CMT/HgTe/CMT	50/100/30	1	1
Q3097	CdTe	CMT/CMT:I/CMT/ HgTe/CMT/CMT:I/CMT	86/9/43/ 13/41/9/25	-	2
Q3119	GaAs	CMT/HgTe/CMT	59/78/59	1	2
Q3138	CdTe	CMT/HgTe/CMT	134/13/38	-	1
QC0438	CdTe	CMT/HgTe/CMT	81/61/10	1	-
QC0441	GaAs	CMT/HgTe/CMT	150/9/50	-	1
QC0460	GaAs	CMT/ HgMn(2.5 %)Te/CMT	70/62/14	1	1
QC0461	GaAs	CMT/ HgMn(1.1 %)Te/CMT	100/81/14	1	1
QC0464	GaAs	CMT/ HgMn(1.7 %)Te/CMT	100/73/15	1	2
QC0478	CdTe	CMT/HgTe/CMT	94/65/12	1	1
QC0479	CdTe	CMT/HgTe/CMT	98/73/12	1	-
QC0500	CdTe	CMT/HgTe/CMT	86/76/45	2	-
QC0501	CdTe	CMT/CMT:I/CMT/ HgTe/CMT	18/9/65/ 67/50	2	-
QC0502	CdTe	CMT/CMT:I/CMT/ HgTe/CMT	19/10/67/ 67/50	3	1
QC0568	CdTe	CMT/HgTe/CMT	13/63/13	-	1
QC0573	CdTe	CMT/ HgMn(2.4 %)Te/CMT	147/12/49	-	1

Table A.2.: List of wafer materials used in this thesis. GaAs is used as a short form for a substrate consisting of n-doped GaAs, a ZnTe interlayer, and CdTe. Layer stack is composed of buffer/active layer/cap. If the active layer possesses manganese doping, the Mn content is given in brackets. Both the buffer and the cap layer may contain a CMT:I modulation doping layer. The last two columns indicate how many devices having a top-gate were fabricated of each wafer and how often each of the two gate-dielectrics was used.

B. Recipes for the fabrication of macroscopic three-dimensional HgTe-based device structures

In Appx. B, the sample recipes for the lithographic processing of three-dimensional structures measuring a few hundred micrometers in size are presented. These are: The outdated standard recipe (Appx. B.1), the current standard recipe for devices with top-gate-electrode (Appx. B.2), the current standard recipe for samples without top-gate (Appx. B.3), the recipe used to obtain an overlapping top-gate layout (Appx. B.4), and the recipe leading to an intermixing of contact metals and fingering of metal into the mesa (Appx. B.5). In order to avoid interrupting these recipes within the description of a fabrication step, the presentation of each sample recipe always starts on a new page.

B.1. Old 6-terminal standard recipe

Appx. B.1 presents the recipe that was used as standard for the fabrication of macroscopic HgTe-based samples in our group "Experimental Physics III" during the period from 2016 to 2019. The knowledge gained in the course of this PhD project contributed significantly to the replacement of the *old 6-terminal standard recipe* by an improved standard recipe, which can be found in Appx. B.2, in 2019. It is noted that the *old 6-terminal standard recipe* shown below is taken from the database of our group.

Hall-Bar Process (BaF_2 mask) Stand: 26.4.2016, V.01

I. The Mesa

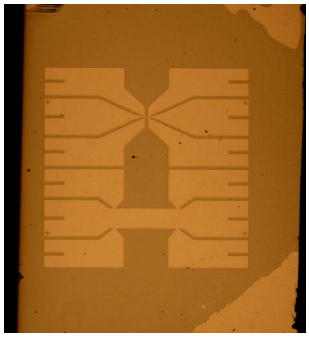

I.1 The negative lift-off resist ARN 4340

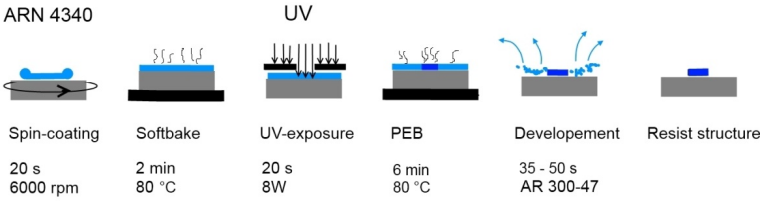

Spin Coating: ARN 4340, 6000 rpm / 20 s
Softbake: 2 min / 80 °C
Exposure: 20 s (8 W) with the Mesa mask
Post-Exposure-Bake: 6 min / 80 °C
Development: 40s in AR 300-47

I.2 BaF_2 deposition in the "Käseglocke"

Deposit a layer of BaF_2, which will later form the etch mask.
Etch rate of BaF_2: <0.25nm/s (1kV IBE process), i.e. 100nm should be sufficient for most processes
Emission current: <10mA (be careful not to go higher!), use sweep!
Deposition rate: should be approx. 0.8nm/s

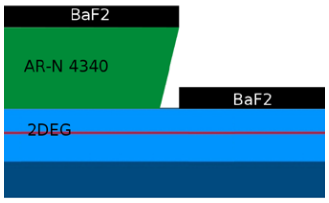

I.3 Lift-off

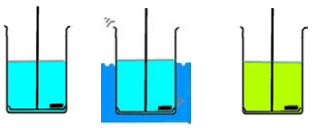

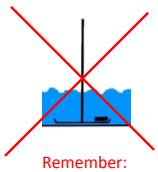

Carefully inspect the etch mask in Nomarski mode. If you see lines, rinse with Isopropanol and Acetone and check again.

I.4 The Ar^+-etch step

Etch through the 2DEG or the bulk HgTe-layer.
!! Mount sample on central position on sample holder !!

I.5 Stripping

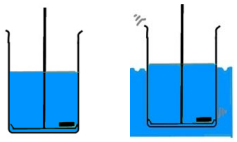

Schematic of the sample

Hall-Bar Process (BaF_2 mask) Stand: 26.4.2016, V.01

II. The insulator

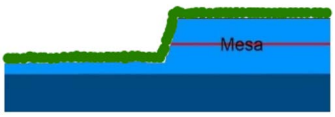

II.1 RIE

Do a short O_2 step in the RIE to remove AR-N4340 residues
Program: "Miniclean" (program number 70)
Duration: 2s (starting when the reflected power drops to zero)

II.2 PECVD

Deposit 110 nm of the Si_2O-Si_3N_4 superlattice, use the SiO-SiN-Lattice recipe.

III. The Gate

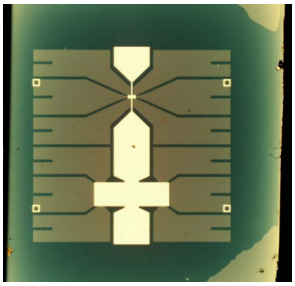

III.1 The negative lift-off resist ARN 4340

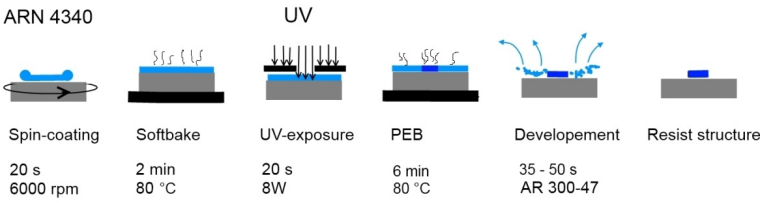

Spin Coating: ARN 4340, 6000 rpm / 20 s
Softbake: 2 min / 80 °C
Exposure: 20 s (8 W) with the Gate-Metallization-mask
Post-Exposure-Bake: 6 min / 80 °C
Development: 35-50 s in AR 300-47

!! The development time has to be adapted to the sample properties (weak insulator etc.). 30 s is developing through, every second more increases the undercut of the resist. !!

III.2 The metallization

Evaporation of 5 nm Ti and 100 nm Au (Käseglocke or UHV-evaporation chamber, NOT in cluster)
!! If the mesa is higher than 150 nm a thicker metal layer should be considered to prevent gate rip-offs over the edges. !!

Hall-Bar Process (BaF_2 mask) Stand: 26.4.2016, V.01

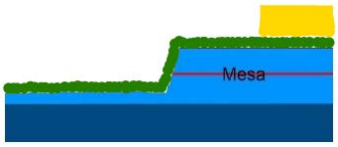

III.3 Lift-off

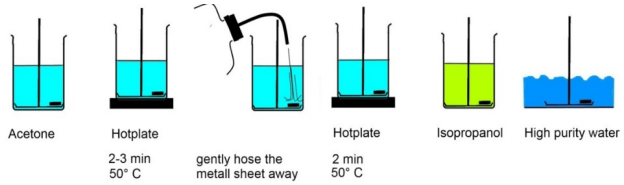

III. Insulator Etch

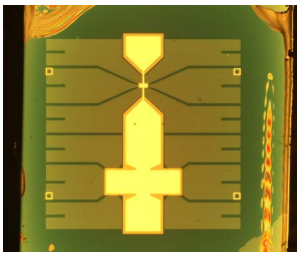

III.1 The wet-etch shield

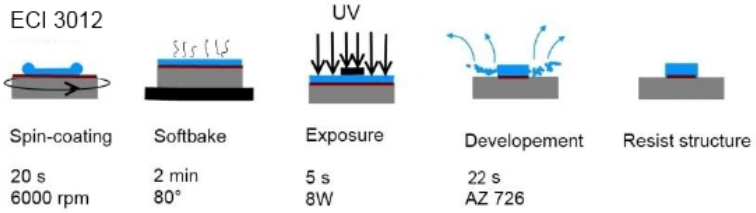

Spin Coating: ECI 3012, 6000 rpm / 20 s

Softbake: 2 min / 80 °C
Exposure: 7 s (8 W) with the Insulator-mask
Development: 22 s in AZ 726 MIF

!! The exposure time of this step can be higher because we do not care too much about the angle of the resist edge for wet-etching and to get rid of eventual resist mountains on the edges of the sample. !!

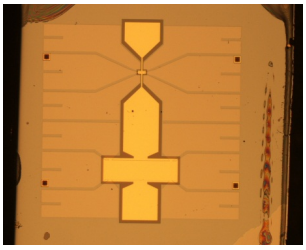

Either etch trough the CMT layer, or use the big Insulator mask with H-Bar and pad coverage.

III.2 The HF-Dip and wet-etch shield stripping

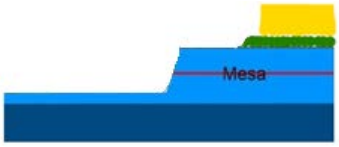

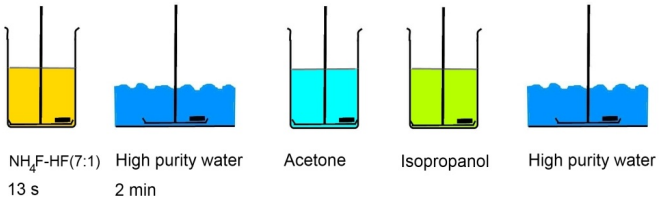

Hall-Bar Process (BaF_2 mask) Stand: 26.4.2016, V.01

IV. Contacts — Contact etch & - metallization

IV.1 The negative lift-off resist ARN 4340

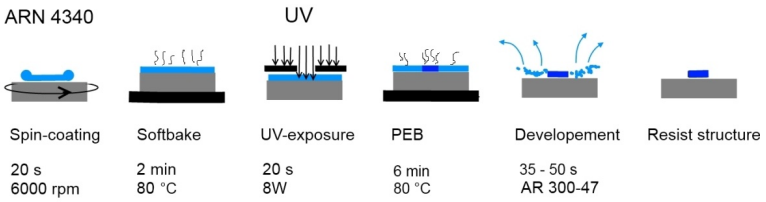

Spin Coating: ARN 4340, 6000 rpm / 20 s
Softbake: 2 min / 80 °C
Exposure: 20 s (8 W) with the Metallization-mask
Post-Exposure-Bake: 6 min / 80 °C
Development: 35-50 s in AR 300-47

IV.2 The Ion Beam Contact Etch

Etch partly through the CdHgTe-Cap about 20 nm close to the 2DEG or the Bulk HgTe-layer. Beam voltage 400 V!
!! Mount sample on central position on sample holder !!

IV.3 The Metallization (in situ)

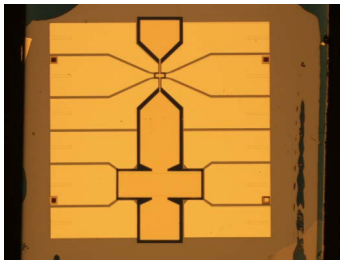

Evaporation of 50 nm AuGe and 50 nm Au on the sample.
!! If the mesa is higher than 150 nm a thicker metal layer should be considered to prevent gate rip-offs over the edges. !!

IV.4 Lift-off

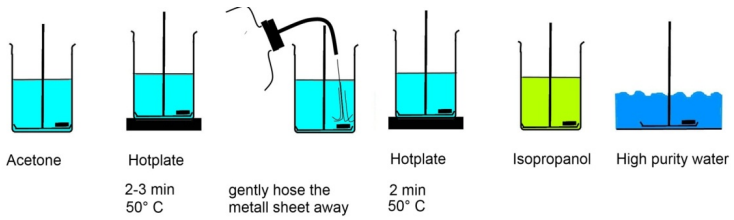

B.2. New 8-terminal standard recipe

In Appx. B.2, the revised version of the *old 6-terminal standard recipe*, which became the new standard recipe for the fabrication of macroscopic HgTe-based devices in our group as of October 2019, is displayed. The enhancements developed in this thesis regarding the lithographic processing of macrostructures, which ultimately led to the introduction of the *new 8-terminal standard recipe*, can be found in chapter 3. It is noted that the *new 8-terminal standard recipe* presented hereafter is taken from the database of our group.

8-terminal Hall bar process

Mask: 8-TERMINAL HALLBARS2019
Recipe version 1.3.1 (24.10.2019)

1. Cleaving

- Inspection of wafer: choose a piece without visible issues
- Use a Petri dish with a mm paper standard. Immerse sample in ultra-pure water (UPW) and use a new scalpel. Sample in water "face-up".
- Sample dimensions should be at least 3x3 mm^2 (you might need to remove resist edge beads when using small samples),
- Blow dry using N_2
- Carefully inspect sample using Nomarski microscope. Document surface quality. Eventually cleaning with acetone, IPA, rinse in UPW, blow dry (N_2).
- Update sample database

2. Cleaning sample backside (GaAs substrates only)

- Spin coating: ECI 3012 resist, 20 s @ 5000 rpm
- Softbake: 2 min @ 80 °C
- HCl etching (see recipe in cleanroom folder)
- Resist removal: Acetone, US bath, 5 min @ 80 kHz (100 %), rinse 1 min in IPA and 1 min in UPW, blow dry using N_2

3. Mesa

a) Prepare wet etch solution

- Prepare wet etch solution. The details of the preparation procedure are described at the end of this recipe
- Wait for 2 hours

b) Etch mask for wet etching

- Spin coating ECI 3012 resist, 20 s @ 6000 rpm
- Softbake: 2 min @ 80 °C
- Exposure: 7 s (8 W, mesa mask)
- Clean the mask right after exposure: acetone, IPA, UPW, blow dry.
- Development: 22 s in AZ MIF-726, rinse 1 min in UPW, blow dry.

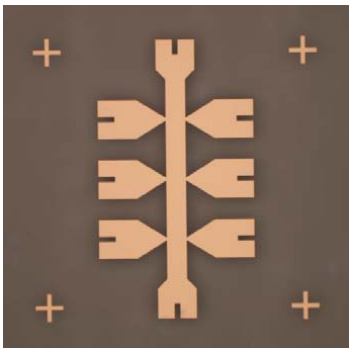

c) Wet etching process (KI: I_2: HBr + H_2O)(1:4)

- Use the pumping method
- Adjust the etch time according to the targeted etch depth. In case you do not know the etch rate of your sample, you need to do a calibration.
- In general, you need to etch through the 2DEG or the bulk HgTe-layer.
- When done, bring the pump back in initial condition (water-cleaned and empty pipes!)

d) Resist mask removal

- Acetone, US bath, 5 min @ 80 kHz (100 %)
- Rinse 1 min in IPA and 1 min in UPW, blow dry (N_2)
- Carefully inspect and document the etched mask in Nomarski microscope
- Measure the height of etched mesa (Dektak)
- Report etch rate on network log.

4. Gate

a) Lift-off resist mask

- Spin coating ARN 4340, 20 s @ 6000 rpm
- Softbake: 2 min @ 80 °C
- Exposure: 20 s (8 W, gate mask)
- Post-Exposure-Bake (PEB): 6 min @ 80 °C
- Development: 40 s in AR 300-47
- Rinse 1 min in UPW, blow dry (N_2)
- Inspection using Nomarski microscope (use yellow light filter!)

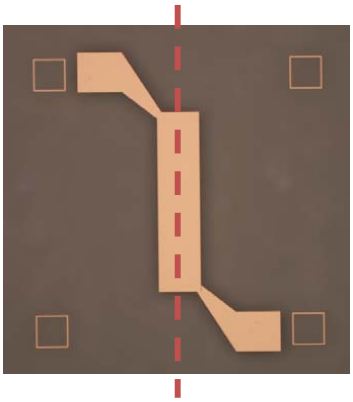

b) Descumming (ICP)

- O_2 plasma cleaning: 100 sccm O_2, 100 W ICP power, 50 µbar, 3 min => ICP program “EP3 miniclean photolitho”
- Mount sample into ALD chamber immediately
- Add a piece of Si for characterization purposes

c) Gate insulator (ALD)

- Run the HfO_x 90 cycles program @ 30 °C
- Update the excel sheet

d) Metallization of gate electrode

- Evaporate 5 nm Ti and 100 nm Au (UHV-evaporator)
- Always do angle deposition (to prevent gate rip-offs)! Mount sample so that sample is tilted around the long axis (Hall bar direction) as indicated by dashed line on the image.
- Angle: ±40°, Au deposition 10 nm in turns (leave the evaporator on)

e) Lift-off

- Acetone, 30 min @ 50 °C
- Gently hose the metal sheet away
- Acetone, 2 min @ 50 °C
- Rinse 1 min in IPA, 1 min in UPW
- Blow dry (N_2)

5. Contacts

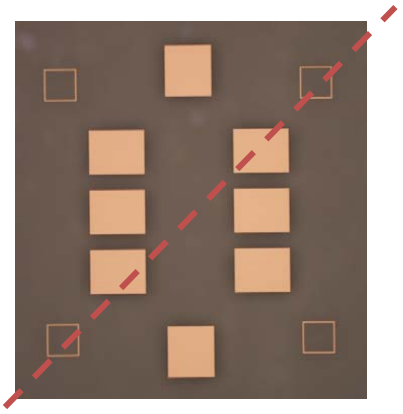

a) Lift-off resist mask

- Spin coating ARN 4340, 20 s @ 6000 rpm
- Softbake: 2 min @ 80 °C
- Exposure: 20 s (8 W, overlapping contacts mask)
- PEB: 6 min @ 80 °C
- Development: 40 s in AR 300-47
- Rinse 1 min in UPW, blow dry (N_2)
- Inspection using Nomarski microscope (use yellow light filter!)
- O_2 plasma cleaning: 100 sccm O_2, 100 W ICP power, 50 µbar, 3 min. => ICP program "EP3 miniclean photolitho"

b) Ion beam contact etch

- Mounting the sample to the moly block: Due to the angle deposition of the contacts, the sample needs to be mounted so that sample can be tilted around the diagonal of the device as indicated by dashed line on the image. Mount the sample on central position
- Etch partly through the top CdHgTe-Cap about 20 nm close to the HgTe-layer.
- Dry etching parameters (cluster IBE): beam/extractor voltages ±0.4 kV, beam current 8 mA, 3.5 sccm Ar, use rotation.

c) Contact metallization (in-situ)

- Evaporate 50 nm AuGe and 50 nm Au
- Always angle deposition (to prevent rip-offs)!
- Angle: ±40°, deposition 10 nm in turns (leave the evaporator on)

d) Lift-off

- Acetone, 10 min @ 50 °C
- Gently hose the metal sheet away
- Acetone, 2 min @ 50 °C
- Rinse in 1 min in IPA and 1 min in UPW, blow dry (N_2)

6. Mounting sample on chip carrier

a) Sample with backgate

- Use silver glue: Use really small amount of the 1:10 silver glue
- Take care for glue creeping up the sides of the sample!

b) Sample without backgate

- Use diluted GE varnish: Use a spatula which fits (width of spatula ca. width chip carrier), take a small amount at the edge of the spatula and then put it in the chip carrier by scratching with the edge over the chip carrier.
- This procedure is part of the bonder introduction
- Wait for glue to dry

7. Bonding

- Use wedge bonding
- Bonds should be placed on the outer part of the bonding pad sitting on substrate (not on Mesa)
- Update sample database

Preparation of wet etch solution [(KI: I_2: HBr: $H_2O)_{50mL}$: H_2O_{200mL}] (1:4)

- Measure 37.5ml of H_2O
- Carefully measure 4.15 g of Potassium Iodide (KI) on the weighing scale and add in H_2O.
- Measure 0.1 g of I_2 (avoid large pieces as it is difficult to dissolve) and add in KI- H_2O solution.
- Mix the solution with magnetic stirrer.
- Measure 12.5 mL of HBr with pipette and add in the above mixture.
- Mix the solution with magnetic stirrer and check if the solution is homogeneous. Now the total solution is 50 mL.
- Measure 200 mL of H_2O and add it to the above prepared 50 mL solution to make 1: 4 solution.

B.3. 8-terminal characterization Hall bar recipe

Appx. B.3 shows the *8-terminal characterization Hall bar recipe*, which is identical to the *new 8-terminal standard recipe* except for the omission of the top-gate. Ungated devices are ideal for characterizing wafer materials, since the unintentional n-type doping of our samples due to the application of gate-dielectric and top-gate-electrode described in Chap. 3 does not occur. As a result, the intrinsic properties of the molecular beam epitaxy grown wafers can be determined, providing important feedback for the growers. It is noted that the *8-terminal characterization Hall bar recipe* presented in the following is taken from the database of our group.

8-terminal Hall bar process for growth characterization (NO GATE)

Mask: 8-TERMINAL HALLBARS2019

Recipe version 1.3.1 (24.10.2019)

1. Cleaving

- Inspection of wafer: choose a piece without visible issues
- Use a Petri dish with a mm paper standard. Immerse sample in ultra-pure water (UPW) and use a new scalpel. Sample in water "face-up".
- Sample dimensions should be at least 3x3 mm^2 (you might need to remove resist edge beads when using small samples),
- Blow dry using N_2
- Carefully inspect sample using Nomarski microscope. Document surface quality. Eventually cleaning with acetone, IPA, rinse in UPW, blow dry (N_2).
- Update sample database

2. Cleaning sample backside (GaAs substrates only)

- Spin coating: ECI 3012 resist, 20 s @ 5000 rpm
- Softbake: 2 min @ 80 °C
- HCl etching (see recipe in cleanroom folder)
- Resist removal: Acetone, US bath, 5 min @ 80 kHz (100 %), rinse 1 min in IPA and 1 min in UPW, blow dry using N_2

3. Mesa

a) Prepare wet etch solution

- Prepare wet etch solution. The details of the preparation procedure are described at the end of this recipe
- Wait for 2 hours

b) Etch mask for wet etching

- Spin coating ECI 3012 resist, 20 s @ 6000 rpm
- Softbake: 2 min @ 80 °C
- Exposure: 7 s (8 W, mesa mask)
- Clean the mask right after exposure: acetone, IPA, UPW, blow dry.
- Development: 22 s in AZ MIF-726, rinse 1 min in UPW, blow dry.

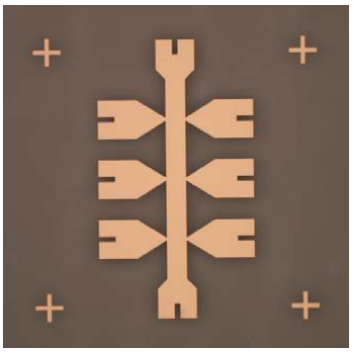

c) Wet etching process (KI: I_2: HBr + H_2O)(1:4)

- Use the pumping method
- Adjust the etch time according to the targeted etch depth. In case you do not know the etch rate of your sample, you need to do a calibration.
- In general, you need to etch through the 2DEG or the bulk HgTe-layer.
- When done, bring the pump back in initial condition (water-cleaned and empty pipes!)

d) Resist mask removal

- Acetone, US bath, 5 min @ 80 kHz (100 %)
- Rinse 1 min in IPA and 1 min in UPW, blow dry (N_2)
- Carefully inspect and document the etched mask in Nomarski microscope
- Measure the height of etched mesa (Dektak)
- Report etch rate on network log.

4. Contacts

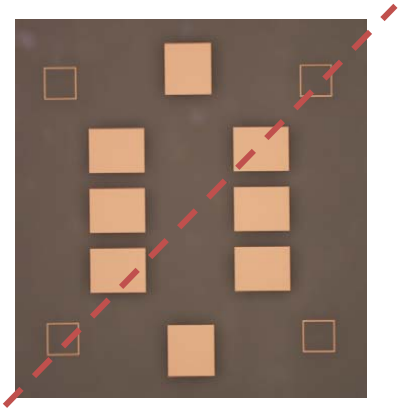

a) Lift-off resist mask

- Spin coating ARN 4340, 20 s @ 6000 rpm
- Softbake: 2 min @ 80 °C
- Exposure: 20 s (8 W, overlapping contacts mask)
- PEB: 6 min @ 80 °C
- Development: 40 s in AR 300-47
- Rinse 1 min in UPW, blow dry (N_2)
- Inspection using Nomarski microscope (use yellow light filter!)
- O_2 plasma cleaning: 100 sccm O_2, 100 W ICP power, 50 µbar, 3 min. => ICP program "EP3 miniclean photolitho"

b) Ion beam contact etch

- Mounting the sample to the moly block: Due to the angle deposition of the contacts, the sample needs to be mounted so that sample can be tilted around the diagonal of the device as indicated by dashed line on the image. Mount the sample on central position
- Etch partly through the top CdHgTe-Cap about 20 nm close to the HgTe-layer.
- Dry etching parameters (cluster IBE): beam/extractor voltages ±0.4 kV, beam current 8 mA, 3.5 sccm Ar, use rotation.

c) Contact metallization (in-situ)

- Evaporate 50 nm AuGe and 50 nm Au
- Always angle deposition (to prevent rip-offs)!
- Angle: ±40°, deposition 10 nm in turns (leave the evaporator on)

d) Lift-off

- Acetone, 10 min @ 50 °C, Gently hose the metal sheet away
- Acetone, 2 min @ 50 °C
- Rinse in 1 min in IPA and 1 min in UPW, blow dry (N_2)

5. Mounting sample on chip carrier

a) Sample with backgate

- Use silver glue: Use really small amount of the 1:10 silver glue
- Take care for glue creeping up the sides of the sample!

b) Sample without backgate

- Use diluted GE varnish: Use a spatula which fits (width of spatula ca. width chip carrier), take a small amount at the edge of the spatula and then put it in the chip carrier by scratching with the edge over the chip carrier.
- This procedure is part of the bonder introduction
- Wait for glue to dry

6. Bonding

- Use wedge bonding
- Bonds should be placed on the outer part of the bonding pad sitting on substrate (not on Mesa)
- Update sample database

Preparation of wet etch solution [(KI: I_2: HBr: $H_2O)_{50mL}$: H_2O_{200mL}] (1:4)

- Measure 37.5ml of H_2O
- Carefully measure 4.15 g of Potassium Iodide (KI) on the weighing scale and add in H_2O.
- Measure 0.1 g of I_2 (avoid large pieces as it is difficult to dissolve) and add in KI- H_2O solution.
- Mix the solution with magnetic stirrer.
- Measure 12.5 mL of HBr with pipette and add in the above mixture.
- Mix the solution with magnetic stirrer and check if the solution is homogeneous. Now the total solution is 50 mL.
- Measure 200 mL of H_2O and add it to the above prepared 50 mL solution to make 1: 4 solution.

B.4. 6-terminal overlapping top-gate recipe

The *6-terminal overlapping top-gate recipe* displayed in Appx. B.4 represents a modified version of the *new 8-terminal standard recipe* to achieve an overlapping top-gate layout. By using this layout, the top-gate-electrode also covers parts of the ohmic contacts. An overlapping top-gate may be necessary to record the magnetoresistance signals of devices that are to be measured at high magnetic fields ($B > 4\,\mathrm{T}$) and extremely low temperatures ($T \ll 1\,\mathrm{K}$) in a meaningful way (cf. Chap. 4). Since the new 8-terminal Hall bar design lacks a suitable gate-mask for the fabrication of an overlapping top-gate-electrode, the old 6-terminal design is used for this purpose. It is noted that the *8-terminal characterization Hall bar recipe* presented below is taken from the database of our group.

6-terminal Hall bar process "overlapping gate"

Mask: HB MASK 2018 NEW

Recipe version 1.3.1 (24.10.2019)

1. Cleaving

- Inspection of wafer: choose a piece without visible issues
- Use a Petri dish with a mm paper standard. Immerse sample in ultra-pure water (UPW) and use a new scalpel. Sample in water "face-up".
- Sample dimensions should be at least 3x3 mm^2 (you might need to remove resist edge beads when using small samples),
- Blow dry using N_2
- Carefully inspect sample using Nomarski microscope. Document surface quality. Eventually cleaning with acetone, IPA, rinse in UPW, blow dry (N_2).
- Update sample database

2. Cleaning sample backside (GaAs substrates only)

- Spin coating: ECI 3012 resist, 20 s @ 5000 rpm
- Softbake: 2 min @ 80 °C
- HCl etching (see recipe in cleanroom folder)
- Resist removal: Acetone, US bath, 5 min @ 80 kHz (100 %), rinse 1 min in IPA and 1 min in UPW, blow dry using N_2

3. Mesa

a) Prepare wet etch solution

- Prepare wet etch solution. The details of the preparation procedure are described at the end of this recipe
- Wait for 2 hours

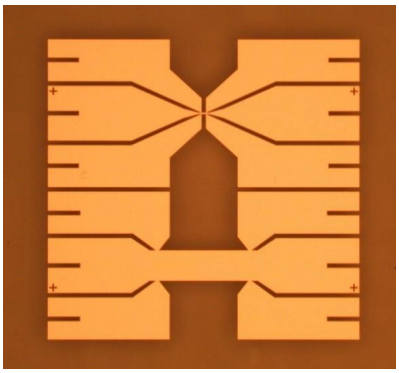

b) Etch mask for wet etching

- Spin coating ECI 3012 resist, 20 s @ 6000 rpm
- Softbake: 2 min @ 80 °C
- Exposure: 7 s (8 W, mesa mask)
- Clean the mask right after exposure: acetone, IPA, UPW, blow dry.
- Development: 22 s in AZ MIF-726, rinse 1 min in UPW, blow dry.

c) Wet etching process (KI: I_2: HBr + H_2O)(1:4)

- Use the pumping method
- Adjust the etch time according to the targeted etch depth. In case you do not know the etch rate of your sample, you need to do a calibration.
- In general, you need to etch through the 2DEG or the bulk HgTe-layer.
- When done, bring the pump back in initial condition (water-cleaned and empty pipes!)

d) Resist mask removal

- Acetone, US bath, 5 min @ 80 kHz (100 %)
- Rinse 1 min in IPA and 1 min in UPW, blow dry (N_2)
- Carefully inspect and document the etched mask in Nomarski microscope
- Measure the height of etched mesa (Dektak)
- Report etch rate on network log.

4. Contacts

a) Lift-off resist mask

- Spin coating ARN 4340, 20 s @ 6000 rpm
- Softbake: 2 min @ 80 °C
- Exposure: 20 s (8 W, non-overlapping contacts mask)
- PEB: 6 min @ 80 °C
- Development: 40 s in AR 300-47
- Rinse 1 min in UPW, blow dry (N_2)
- Inspection using Nomarski microscope (use yellow light filter!)
- O_2 plasma cleaning: 100 sccm O_2, 100 W ICP power, 50 µbar, 3 min. => ICP program “EP3 miniclean photolitho”

b) Ion beam contact etch

- Mounting the sample to the moly block: Due to the angle deposition of the contacts, the sample needs to be mounted so that sample can be tilted around the diagonal of the device as indicated by dashed line on the image. Mount the sample on central position
- Etch partly through the top CdHgTe-Cap about 20 nm close to the HgTe-layer.
- Dry etching parameters (cluster IBE): beam/extractor voltages ±0.4 kV, beam current 8 mA, 3.5 sccm Ar, use rotation.

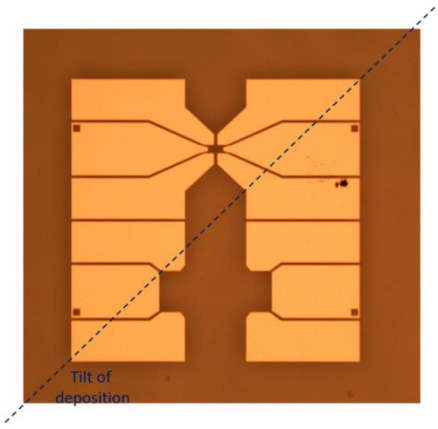

c) Contact metallization (in-situ)

- Evaporate 50 nm AuGe and 50 nm Au
- Always angle deposition (to prevent rip-offs)!
- Angle: ±40°, deposition 10 nm in turns (leave the evaporator on)

d) Lift-off

- Acetone, 10 min @ 50 °C
- Gently hose the metal sheet away

- Acetone, 2 min @ 50 °C
- Rinse in 1 min in IPA and 1 min in UPW, blow dry (N_2)

5. Gate

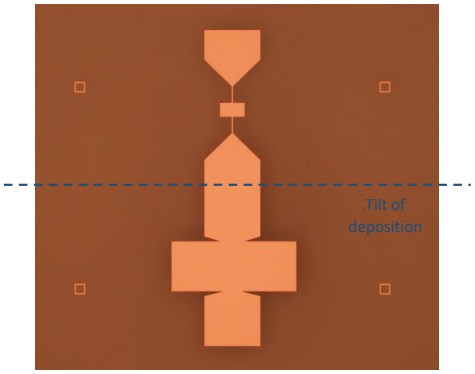

a) Lift-off resist mask

- Spin coating ARN 4340, 20 s @ 6000 rpm
- Softbake: 2 min @ 80 °C
- Exposure: 20 s (8 W, gate mask)
- Post-Exposure-Bake (PEB): 6 min @ 80 °C
- Development: 40 s in AR 300-47
- Rinse 1 min in UPW, blow dry (N_2)
- Inspection using Nomarski microscope (use yellow light filter!)

b) Descumming (ICP)

- O_2 plasma cleaning: 100 sccm O_2, 100 W ICP power, 50 µbar, 3 min => ICP program "EP3 miniclean photolitho"
- Mount sample into ALD chamber immediately
- Add a piece of Si for characterization purposes

c) Gate insulator (ALD)

- Run the HfO_x 90 cycles program @ 30 °C
- Update the excel sheet

d) Metallization of gate electrode

- Evaporate 5 nm Ti and 100 nm Au (UHV-evaporator)
- Always do angle deposition (to prevent gate rip-offs)! Mount sample so that sample is tilted around the long axis (Hall bar direction) as indicated by dashed line on the image.
- Angle: ±40°, Au deposition 10 nm in turns (leave the evaporator on)

e) Lift-off

- Acetone, 30 min @ 50 °C
- Gently hose the metal sheet away
- Acetone, 2 min @ 50 °C
- Transfer to IPA in a petri-dish and check the result using Nomarski microscope. If the lift-off is not successful, transfer to a beaker with Acetone and repeat the steps so far until the lift-off is successful.
- If the lift-off is successful, Rinse 1 min in IPA, 1 min in UPW
- Blow dry (N_2)

6. Mounting sample on chip carrier

a) Sample with backgate

- Use silver glue: Use really small amount of the 1:10 silver glue
- Take care for glue creeping up the sides of the sample!

b) Sample without backgate

- Use diluted GE varnish: Use a spatula which fits (width of spatula ca. width chip carrier), take a small amount at the edge of the spatula and then put it in the chip carrier by scratching with the edge over the chip carrier.
- This procedure is part of the bonder introduction
- Wait for glue to dry

7. Bonding

- Use wedge bonding
- Update sample database

Preparation of wet etch solution [(KI: I_2: HBr: H_2O)$_{50mL}$: H_2O $_{200mL}$] (1:4)

- Measure 37.5ml of H_2O
- Carefully measure 4.15 g of Potassium Iodide (KI) on the weighing scale and add in H_2O.
- Measure 0.1 g of I_2 (avoid large pieces as it is difficult to dissolve) and add in KI- H_2O solution.
- Mix the solution with magnetic stirrer.
- Measure 12.5 mL of HBr with pipette and add in the above mixture.
- Mix the solution with magnetic stirrer and check if the solution is homogeneous. Now the total solution is 50 mL.
- Measure 200 mL of H_2O and add it to the above prepared 50 mL solution to make 1: 4 solution.

B.5. 8-terminal Hall bar clustering metals recipe

In Appx. B.5, the sample recipe leading to an intermixing of the contact metals gold germanium and gold as well as fingering of metal into the mesa structure is presented. Since contact structures that exhibit both intermixing and fingering of metal are referred to as clustering metals, this recipe is called *8-terminal Hall bar clustering metals recipe*. The *8-terminal Hall bar clustering metals recipe* provides an excellent starting point for future research concerning the ohmic contacts of HgTe-based devices. It is noted, however, that clustering metals can only occur in samples whose layer stacks possess a CMT:I modulation doping layer above the active layer.

Recipe 8-terminal Hall bar (clustering metals)

I. Sample preparation:

- Cleave sample piece (≈ 3 x 3 mm^2) and clean it with Acetone in ultrasonic bath (USB)
  - wash sample with Isopropyl (IPA) and ultra-pure water (UPW)
  - blow dry with Nitrogen (N_2) gun
- *PECVD*: 10 nm SiO_2 sacrificial layer (SL)

II. SL removal at the contact areas:

- HMDS + ECI 3012; 6000 rpm for 20 s; bake 2 min @ 80 °C
- Expose 7 s with contact mask
- Development: 22 s AZ MIF 726
- Dip for 10 s in BOE 7:1
  - wash sample for ≈ 3 min in UPW → blow dry with N_2
- Lift-off: 5 min Acetone @ 50 °C → IPA → UPW → N_2

III. Mesa etch:

- ARN 4340; 6000 rpm for 20 s; bake 2 min @ 80 °C
- Expose 20 s with mesa mask
  - 6 min post exposure bake @ 80 °C
- Development: 40 s AR 300-47
- Metallization of 15 nm Ti in *Cluster*
- Lift-off: 5 min Acetone @ 50 °C → IPA → UPW → N_2
- SL etch in *ICP* ("SiN_x etch" for 30 s + "mini-clean" for 3 min)
- Mesa etch in *Cluster*: ± 1 kV; 8 mA; 1.62 sccm
  - etch through buffer layer down to the substrate
- Stripping of Ti etch mask: 45 s in 1:10 diluted HF (use USB!)
  - wash sample for ≈ 3 min in UPW → N_2
- Measure mesa height with *Dektak*

IV. Contacts:

- ARN 4340; 6000 rpm for 20 s; bake 2 min @ 80 °C
- Expose 20 s with contact mask

  - 6 min post exposure bake @ 80 °C
- Development: 42 s AR 300-47
- Contact etch in *Cluster*: ± 0.4 kV; 8 mA; 3.5 sccm
  - etch about 20 nm close to the HgTe layer
- In-situ metallization: AuGe / Ti / Au (50 nm / 5 nm / 50 nm)
  - use angle deposition (± 40 °, deposition 10 nm in turns)
- Lift-off: 5 min Acetone @ 50 °C
  - gently hose the metal sheet away
  - 2 min Acetone @ 50 °C → IPA → UPW → N_2

V. ALD insulator and Gate:

- ARN 4340; 6000 rpm for 20 s; bake 2 min @ 80 °C
- Expose 20 s with gate mask
  - 6 min post exposure bake @ 80 °
- Development: 42 s AR 300-47
- *ICP* ("mini-clean" for 3 min)
- *ALD* (90 cycles of HfO_x @ 30 °C)
- Gate metallization in *UHV*: Ti / Au (5 nm / 100 nm)
  - use angle deposition (± 40 °, deposition 10 nm in turns)
- Lift-off: ≈ 30 min Acetone @ 50 °C
  - gently hose the metal sheet away
  - 3 min Acetone @ 50 °C → IPA → UPW → N_2

VI. Mounting sample on chip carrier and bonding:

- Use diluted GE Varnish
  - wait one day for glue to dry
- bond the sample

C. Recipes for the fabrication of microscopic three-dimensional HgTe-based device structures

In Appx. C, the sample recipes for the lithographic processing of three-dimensional structures measuring a few micrometers in size are presented. These microstructures usually require more demanding lithographic techniques, such as the use of electron beam lithography instead of optical lithography, but are necessary when ballistic or spin-associated transport phenomena are to be investigated. To define the microscopic mesa two different etching techniques can be applied. The recipe involving wet etching with a KI:I_2:HBr solution is shown in Appx. C.1, while the recipe using inductively coupled plasma etching with reactive methane can be found in Appx. C.2. The lithographic processing steps of both recipes are optimized for microscopic Hall bar and H-bar structures. However, based on these recipes, the realization of nearly any desired sample design should be facilitated. Again, in order to avoid interrupting these recipes within the description of a fabrication step, the presentation of each sample recipe always starts on a new page.

C.1. Recipe for the fabrication of microstructures (wet etching)

Appx. C.1 presents the recipe used for the fabrication of microscopic three-dimensional HgTe-based samples by means of wet etching. This recipe is referred to as *recipe for the fabrication of microstructures (wet etching)*. Wet etching preserves the crystal structure of the active layer best due to pure chemical etching, but possesses an isotropic nature. Therefore, trench structures significantly narrower than 500 nm should be avoided.

µ-structure-process *KI:I:HBr etch* Date: 25.04.2020

I. EBL Mesa

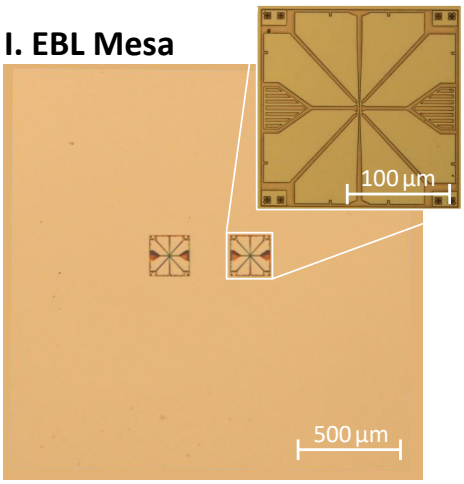

Resist
- PMMA 950K 3 %, 40 s @ 7000 rpm, 8 min @ 80 °C

Exposure
- 2.5 kV; 204.8 µm 388X; 70 µC/cm²; 12.5 nm = 4 px; 30 µm aperture; 7 mm working distance

Development
- 1 min in AR 656:IPA 1:1 -> isopropanol (≈ 60 s)

HF-dip
- 50 s in HF:DIW 1:400 [1:200 with HF(50 %)] -> DIW (right before etching)

Wet etch
- ≈ 40 to 60 s (depending on layer stack)

Stripping
- acetone -> IPA -> DIW –> measure etch depth via Dektak

II. Optical Mesa

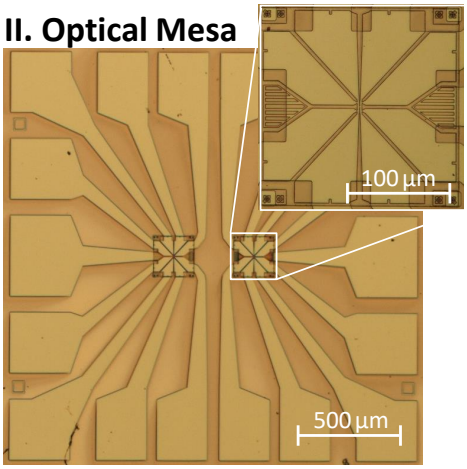

Positive resist
- ECI 3012; 20 s @ 6000 rpm; 2 min @ 80 °C

Exposure
- 7 s development
- 22 s in AZ 726 MIF -> DIW

Wet etch
- 60 to 80 s (depending on layer stack)

Stripping
- acetone -> IPA-> DIW –> measure etch depth via Dektak

III. Inner Contacts

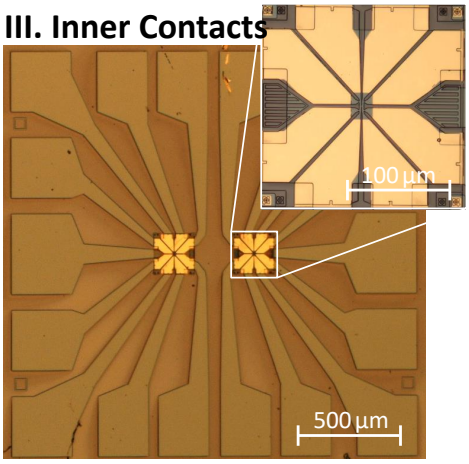

Resist
- PMMA 600K 6 %; 40 s @ 6000 rpm, 10 min @ 80 °C

Exposure
- 6.5 kV; 204.8 µm 387X; 310 µC/cm²; 6.25 nm = 2 px; 30 µm aperture; 10 mm working distance

Development
- 1 min 10 s in AR 656:IPA 1:1 -> IPA (≈ 60 s)

Oxygen plasma miniclean
- execute a oxygen plasma miniclean in ICP or RIE

Ion milling contacts
- etch 20 nm close to active layer; 400 V, 400 V, 8 mA, 3.5 sccm; in situ transfer ->

Metallization contacts
- 50 nm AuGe; 50 nm Au (use angular deposition) -> lift-off in acetone -> IPA -> DIW

MIBK cleaning: One night in MIBK @ 50 °C right before the topgate application.

IV. EBL ALD Topgate

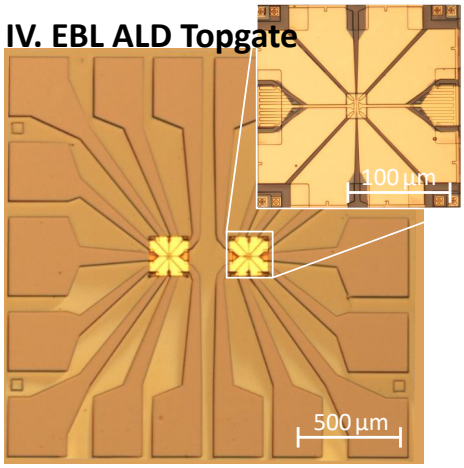

Resist
- PMMA 600K 6 %; 40 s @ 6000 rpm, 10 min @ 80 °C

Exposure
- 6.5 kV; 204.8 µm 387X; 310 µC/cm²; 6.25 nm = 2 px; 30 µm aperture; 10 mm working distance

Development
- 1 min 10 s in AR 656:IPA 1:1 -> IPA (≈ 60 s)

Oxygen plasma miniclean
- execute a oxygen plasma miniclean in ICP or RIE

ALD HfO_x H_2O Hf
- Pulse 200 ms; 50 ms; Purge 200 s; Sat. 10 s; 90 cyc. (standard 30 °C process)

Metallization gate
- 5 nm Ti; 100 nm Au (use angular deposition) -> lift-off in acetone -> IPA -> DIW

V. Outer Contacts

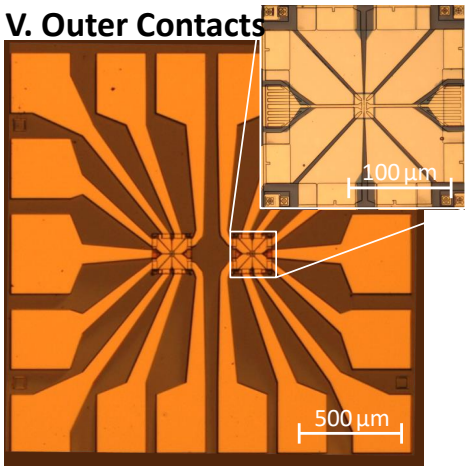

Negative resist
- ARN 4340; 20 s @ 6000 rpm; 2 min @ 80 °C

Exposure
- 20 s; post exposure bake 6 min @ 80 °C

Development
- 42 s in AR 300-47 -> DIW

Oxygen plasma miniclean
- execute a oxygen plasma miniclean in ICP or RIE

Ion Milling cleaning
- ≈ 10 s; 400V, 400 V, 8 mA, 3.5 sccm; in situ transfer ->

Metallization leads
- 80 nm AuGe; 80 nm Au (use angular deposition) -> lift-off in acetone -> IPA -> DIW

C.2. Recipe for the fabrication of microstructures (inductively coupled plasma etching)

In Appx. C.2, the recipe for the fabrication of microscopic three-dimensional HgTe-based devices using inductively coupled plasma etching is displayed. This recipe is referred to as *recipe for the fabrication of microstructures (inductively coupled plasma etching)*. Inductively coupled plasma etching features a weak physical etching component that can damage the side surfaces of the HgTe layer, but is characterized by its ease of use, high reproducibility, and excellent structural fidelity.

µ-structure-process *ICP etch* Date: 26.04.2020

I. EBL Mesa

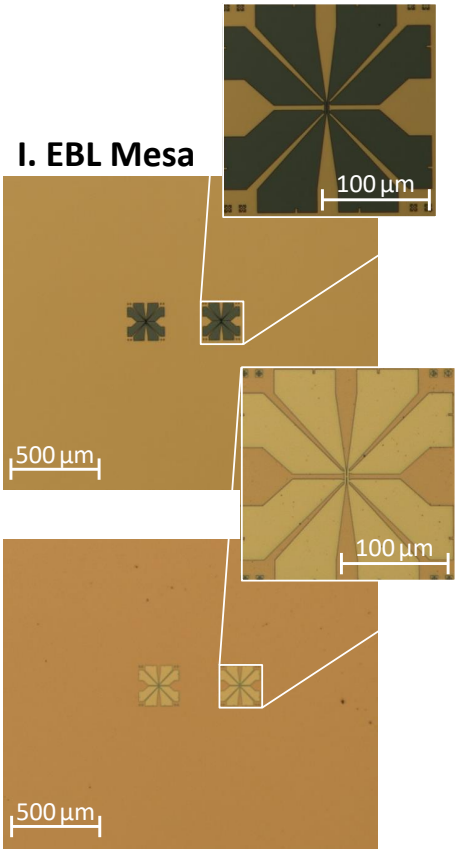

Resist
- PMMA 950K 3 %, 40 s @ 7000 rpm, 8 min @ 80 °C

Exposure
- 2.5 kV; 204.8 µm 388X; 70 µC/cm^2; 12.5 nm = 4 px; 30 µm aperture; 7 mm working distance

Development
- 1 min in AR 656:IPA 1:1 –> isopropanol (≈ 60 s)

Etch mask
- deposit 100 nm BaF_2 + 10 nm Ti (in situ) in Käseglocke

Lift-off
- 5 min acetone with ultrasonic excitation (50 °C, 37 kHz, 100 % power) –> IPA (no DIW!)

ICP etching
- glue sample to carrier wafer with Crystal Bond 509
- etch in ICP for a suitable amount of time
- remove sample from carrier wafer

Stripping
- 15 min in DIW (50 °C, 37 kHz, 100 % power) –> acetone –> IPA –> DIW –> measure etch depth via Dektak

II. Inner Contacts

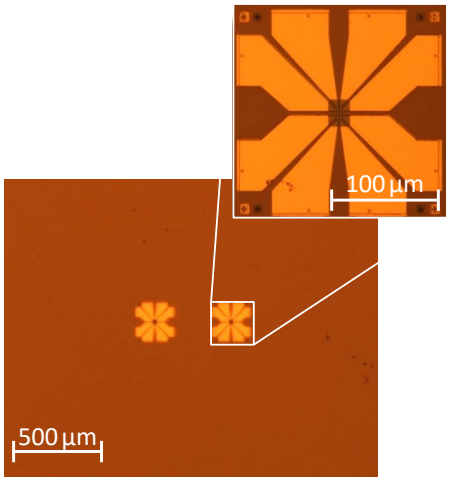

Resist
- PMMA 600K 6 %; 40 s @ 6000 rpm, 10 min @ 80 °C

Exposure
- 6.5 kV; 204.8 µm 387X; 310 µC/cm^2; 6.25 nm = 2 px; 30 µm aperture; 10 mm working distance

Development
- 1 min 10 s in AR 656:IPA 1:1 -> IPA (≈ 60 s)

Oxygen plasma miniclean
- execute a oxygen plasma miniclean in ICP or RIE

Ion milling contacts
- etch 20 nm close to active layer; 400 V, 400 V, 8 mA, 3.5 sccm; in situ transfer ->

Metallization contacts
- 50 nm AuGe; 50 nm Au (use angular deposition) -> lift-off in acetone -> IPA -> DIW

MIBK cleaning: One night in MIBK @ 50 °C right before the topgate application.

III. EBL ALD Topgate

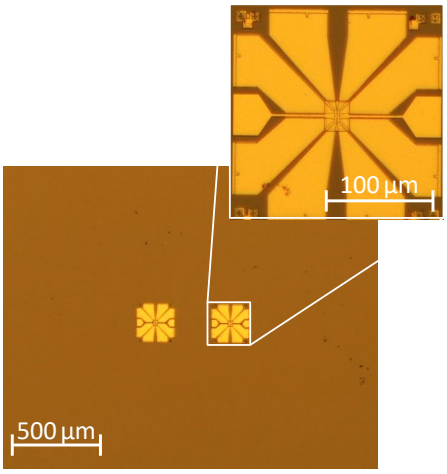

Resist
- PMMA 600K 6 %; 40 s @ 6000 rpm, 10 min @ 80 °C

Exposure
- 6.5 kV; 204.8 µm 387X; 310 µC/cm^2; 6.25 nm = 2 px; 30 µm aperture; 10 mm working distance

Development
- 1 min 10 s in AR 656:IPA 1:1 -> IPA (≈ 60 s)

Oxygen plasma miniclean
- execute a oxygen plasma miniclean in ICP or RIE

ALD HfO_x H_2O Hf
- Pulse 200 ms; 50 ms; Purge 200 s; Sat. 10 s; 90 cyc. (standard 30 °C process)

Metallization gate
- 5 nm Ti; 100 nm Au (use angular deposition) -> lift-off in acetone -> IPA -> DIW

IV. Outer Contacts

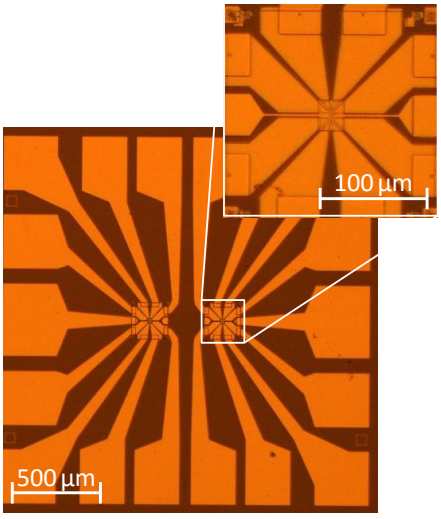

Negative resist
- ARN 4340; 20 s @ 6000 rpm; 2 min @ 80 °C

Exposure
- 20 s; post exposure bake 6 min @ 80 °C

Development
- 42 s in AR 300-47 -> DIW

Oxygen plasma miniclean
- execute a oxygen plasma miniclean in ICP or RIE

Ion milling cleaning
- ≈ 10 s; 400 V, 400 V, 8 mA, 3.5 sccm; in situ transfer ->

Metallization leads
- 80 nm AuGe; 80 nm Au (use angular deposition) -> lift-off in acetone -> IPA -> DIW

Danksagung

Zum Abschluss möchte ich mich bei all denjenigen Menschen bedanken, die mich während meiner gesamten Promotion unterstützt und damit maßgeblich zur Verwirklichung dieser Dissertation beigetragen haben. Mein ganz besonderer Dank gilt

- Prof. Laurens Molenkamp für die Möglichkeit mein Promotionsstudium am Lehrstuhl "Experimentelle Physik III" durchzuführen. Du hast dir immer Zeit für Fragen und Diskussionen genommen, was ich sehr zu schätzen weiß.

- Prof. Harmut Buhmann, meinem Doktorvater, für das erfahrene Leiten meiner Projekte, für die vielen interessanten Diskussionen und für ein stets offenes Ohr für meine Fragen. Aufgrund meiner Arbeit mit dir in den vergangenen Jahren hat sich mein physikalischer Horizont extrem erweitert. Nicht vergessen werde sollte deine sympathische, freundliche Art, mit der du all deinen Studenten begegnest. Es war mir wirklich eine Freude mein Promotionsstudium unter deiner Anleitung durchführen zu dürfen.

- Dr. Micheal Gbordzoe für das aufmerksame, ausdauernde Gegenlesen meiner Thesis und für die vielen äußerst nützlichen Hinweise und Anmerkungen.

- Dr. Li-Xian Wang für die tolle Zusammenarbeit bei vielen Projekten, für unsere perfekt abgestimmte Koordination und Arbeitsteilung von Reinraum- und Laborarbeiten und für das Gegenlesen meiner Dissertation. Du hast mir beim Sammeln von Daten und Ergebnissen sehr geholfen. Besonders freue ich mich, dass unsere gemeinsame Arbeit zu drei Publikationen geführt hat (oder noch führen wird).

- Dr. Tanja Borzenko für die Beantwortung aller etwaiger Fragen im Reinraum und für deine Hilfestellungen hinsichtlich lithographischer Prozesse und Abläufe.

- Dr. David Mahler und Dr. Saquib Shamim für die Einführung in die Arbeitsabläufe im Labor und für eure Erfahrung, von der meine Ratlosigkeit des Öfteren profitierte.

- den Molekularstrahlepitaxie-Experten, die mich mit ausreichend Probenmaterial zur Herstellung von unzähligen makroskopischen sowie mikroskopischen Proben versorgt haben. Ihr habt im wahrsten Sinne des Wortes die Basis für alle in dieser Dissertation präsentierten Ergebnisse gelegt. Zu erwähnen sind diesbezüglich Dr. Phillip Leubner, Dr. Raimund Schlereth, Lukas Lunczer und Lena Fürst.

- den Personen, die oft unbemerkt im Hintergrund ihre Arbeiten verrichten, aber ohne die ein reibungslosen Arbeiten im Reinraum nicht möglich wäre: Ich danke Volkmar Hock für die ganz besondere Fähigkeit wirklich jedes Problem im Reinraum lösen zu können und für seinen ausgeprägten Sinn für Humor, der so manchen tristen Tag aufzuheitern vermochte. Außerdem danke ich Carmen Bundschuh und Petra Wolf-Müller für das Aufrechterhalten eines produktiven Arbeitsflusses im Reinraum.

- Roland Ebert und Cornelius Ziga für die Bereitstellung von flüssigem Helium und für die Hilfestellungen bei Fragen hinsichtlich der Tieftemperaturphysik und Kryostatentechnik.

- Angelika Berger für deine Unterstützung bei allen organisatorischen Herausforderungen, welche mir als Mitarbeiter der Universität im Laufe meines Promotionsstudiums begegnet sind. Ohne dich wäre ich sicherlich das eine oder andere Mal mit den ganzen Formularen überfordert gewesen.

- all meinen anderen Kollegen am Lehrstuhl, die zu zahlreich sind, um alle einzeln aufzuzählen. Es war mir eine Ehre einen kurzen Abschnitt meines Lebens mit euch teilen zu dürfen. Besonders die geselligen Grillfeste im Sommer werden mir in Erinnerung bleiben.

Zu guter Letzt möchte ich mich noch bei meiner Familie bedanken. Danke für eure uneingeschränkte Unterstützung bei all meinen Entscheidungen. Danke, dass ihr mich durch die Höhen und Tiefen der letzten Jahre begleitet habt und stets hinter mir standet. Danke, dass ihr mich immer, wenn nötig, an das wirklich Wichtige im Leben erinnert habt. Ich kann mich glücklich schätzen, Teil einer so tollen Familie zu sein!